UNIVERSITY OF OXFORD

ROLE OF CARBONIC ANHYDRASE CATALYSIS AND GAP JUNCTIONAL COUPLING IN REGULATING pH IN PANCREATIC DUCTAL ADENOCARCINOMA (PDAC)



Tobias Højgaard Dovmark

Linacre College

Thesis submitted for the degree of Doctor of Philosophy

Michaelmas Term 2017

Acknowledgements

I wish to thank my supervisor Professor Pawel Swietach (Oxford) for his extraordinary supervision and the opportunity to work in his laboratory. I am sincerely grateful for the thorough supervision, constructive criticism and guidance I have received along the way. I would like to thank Professor Pawel Swietach for the exceptional and friendly daily supervision and for the intellectual challenges that have been fundamental for the scientific and personal progress I have experienced during the years in Oxford. For that, I will be forever indebted. I owe a special thank you to Alzbeta Hulikova (Oxford), who has been a tremendous and always kind help with cell and molecular biological techniques. Without her tremendous knowledge, guidance in technical setups and help with troubleshooting, my research would not have been as fruitful. Her kindhearted help and expertise has been inspiring. I wish to thank Professor Frauke Alves for the kind opportunity to work at her laboratory for Molecular Imaging in Oncology at the Max-Planck-Institute for Experimental Medicine at the University of Göttingen, Germany. Furthermore, I would like to thank Dr. Mara Saccomano (Göttingen) for a fruitful collaboration at the Max-Planck Institute on the *in vivo* studies presented in chapter 9. I thank Vicky Ball (Oxford) for the kind help with lactate and glucose measurements presented in figure 8.2.7.1. In addition, I would like to thank my family, my mother Lise-Lotte Højgaard and especially my sister Nina-Marie Højgaard Dovmark and my father Johan Dovmark for their scientific support along the way. I would like to thank all my friends at the Marie Curie IonTraC network, Linacre College, Linacre College Boat Club and my friends from other oxford colleges for their great friendship and memorable moments.

This work has been possible thanks to the generous funding from the Ion Transport in Pancreatic Cancer (IonTraC) Marie Skłodowska-Curie Actions Innovative Training Network, Framework Program 7, European Union.

Abbreviations

AM	Acetoxymethyl
ATZ	Acetazolamide
CA	Carbonic Anhydrase
CA_e	Exofacial carbonic anhydrase
CA_i	Intracellular carbonic anhydrase
CBX	Carbenoxolone
Cx	Connexin
D_H^{eff}	Effective H^+ diffusivity
DMA	5(*N*-*N*-dimethyl)amiloride
DOG	2-deoxy D-glucose
cSNARF1	5-(and-6)-Carboxy-seminaphthorhodafluor-1
DIDS	4,4'diisothiocyano-2,2'-stilbenedisulfonic acid
DMOG	Dimethyloxalylglycine
eGFP	Enhanced green fluorescent protein
EGFR	Epidermal growth factor receptor
FRAP	Fluorescence recovery after photobleaching

FS_e	Extracellular fluorescein sulfonic acid
GLUT	Glucose transporter
Hepes	N-2-hydroxyethylpiperazine-N-2-ethanesulphonic acid
HIF	Hypoxia Inducible Factor
LAMP-2	Lysosomal associated membrane protein-2
LDH	Lactate dehydrogenase
HRE	HIF-responsive element
MAPK	Mitogen-activated protein kinase
MCT	H^+-linked monocarboxylate cotransporter
NBC	Na^+-HCO_3^- cotransporter
PDAC	Pancreatic ductal adenocarcinoma
PHD	Prolyl Hydroxylase Domain
pH_e	Extracellular pH
pH_i	Intracellular pH
PK	Pyruvate kinase
RISC	RNA induced silencing complex
R_{max}	Maximum fluorescence ratio

R_{min}	Minimum fluorescence ratio
ROI	Region of interest
ROS	Reactive oxygen species
shRNA	Short hairpin RNA
SSH	Sonic hedgehog
vHL	von Hippel Lindau
WGA	Wheat germ agglutinin

Table of contents

1 ABSTRACT 1

2 GENERAL INTRODUCTION 3

2.1 Pancreatic ductal adenocarcinoma (PDAC) epidemiology 3

2.2 Pathology and oncogenes 5

2.3 Invasion and metastasis 8

2.4 Tumour hypoxia 8

2.5 Interplay between hypoxia and the PDAC tumour stroma 10

2.6 Reprogramming of cancer cell metabolism 11

2.7 Oxidative lactate metabolism 16

2.8 Tumour acidity and pH homeostasis 18

2.9 Canonical models of acid venting mechanisms 20

2.10 Microenvironment acidity as a selection pressure 23

2.11 Current therapies and future treatment of pancreatic cancer 28

2.12 Rationale for the study and original hypotheses 34

3 GENERAL METHODS 36

3.1 Cell lines 36

3.2 Gene expression databases 40

3.3 Monolayer and spheroid culture 41

3.4 Cell-Titer-Blue assay 43

3.5 Knockdown of *GJA1*, the gene coding for Cx43 44

3.6 Western blotting 48

3.7 Solutions and superfusion 50

3.8 Confocal fluorescence microscopy 53

3.9 Fluorescent indicators of pH 56

3.10 Fluorescence recovery after photobleaching (FRAP) 60

3.11 Photolytic uncaging of H^+ ions using 6-nitroveratraldehyde (NVA) 62

3.12 Mathematical algorithms and statistics 67

3.13 Biochemical lactate assay 70

3.14 Orthotopic xenografting experiments 73

3.15 Immunohistochemistry 75

3.16 Statistics 77

4 METABOLIC PROFILING OF PDAC CELL LINES 78

4.1 Background 78

4.2 Methods 81

4.3 Results 82

4.4 Summary of findings 88

5 H^+ BUFFERING CAPACITY OF PDAC CELL LINES 89

5.1 Background 89

5.2 Methods 90

5.3 Results 93
5.4 Summary of findings 96

6 CO_2/HCO_3^- HANDLING BY CARBONIC ANHYDRASES IN PDAC CELL LINES 98
6.1 Background 98
6.2 Results 99
6.3 Summary of findings 123

7 METABOLIC ALTRUISM AND REMOTE HCO_3^- TRANSPORT 124
7.1 Background 124
7.2 Results 125
7.3 Summary of findings 155

8 LACTATE HANDLING PATHWAYS 156
8.1 Background 156
8.2 Results 157
8.3 Summary of findings 199

9 IN VIVO INVESTIGATION OF CX43 IN ORTHOTOPIC XENOGRAFT MOUSE MODELS 200
9.1 Background 200
9.2 Results 201
9.3 Summary of findings 215

10 GENERAL DISCUSSION 216
10.1 Metabolic profiling of cancer cells 216
10.2 H^+ Buffering capacity of PDAC cell lines 218
10.3 CO_2/HCO_3^- handling by carbonic anhydrases in PDAC cell lines 219
10.4 Metabolic altruism and remote HCO_3^- transport 220
10.5 Lactate handling pathways 223
10.6 *In vivo* investigation of Cx43 and LAMP2 in orthotopic xenografts 225
10.7 Future directions 227

11 REFERENCES 228

12 Appendices 260

1 ABSTRACT

The Role of Carbonic Anhydrase Catalysis and Gap Junctional Coupling in Regulating pH in Pancreatic Ductal Adenocarcinoma (PDAC)

Tobias Højgaard Dovmark
Linacre College
Submitted for the degree of D.PHIL, Michaelmas Term 2017

Pancreatic ductal adenocarcinoma (PDAC) develops from the acinar cells of the exocrine pancreas. PDAC tumours are hypoxic and produce a characteristically acidic microenvironment hypothesised to favour more aggressive phenotypes. My thesis work concerned the acid-handling mechanisms in 2-D (monolayer) or 3-D (spheroid) PDAC culture, to underpin survival advantages under acid-stress. The dependence on aerobic glycolysis was assessed in PDAC cells to appreciate the metabolic lactic acid-production. Fluorescence imaging revealed variances in H^+ buffering capacity between PDAC cell lines. Activity of intra- and extracellular carbonic anhydrase (CA) enzymes facilitating CO_2/HCO_3^- buffer equilibration revealed the highest extracellular CA-activity in glycolytic Colo357 cells. Interestingly, fluorescence recovery after photobleaching (FRAP) revealed strong connexin 43 (Cx43)-mediated cell-to-cell diffusive coupling in Colo357 cells. Photolytic H^+-uncaging producing local acid-disturbances at the hypoxic core of Colo357 spheroids, revealed a major Cx43-mediated acid neutralising HCO_3^- flux towards the core. The secondary-active HCO_3^- uptake was shown to take place in the spheroid rim, rather than at the core, because NBCe1 inhibition by DIDS only affected acid-handling at the core of Cx43-coupled spheroids, but not of Cx43-uncoupled spheroids. Normoxic cells in the spheroid rim thereby demonstrated metabolic altruism by donating actively imported HCO_3^- ions to hypoxic cells via gap junctions. Cx43 channels were also shown to transmit lactate, and in Colo357 spheroids, 80% of lactate at the core was vented via Cx43 channels compared to canonical MCT transport. Moreover, Cx43-coupling confers a survival advantage to cells at the proliferating spheroid rim, as demonstrated by co-culturing wild type (Cx43 positive) cells with GFP-expressing Cx43 knockdowns. Furthermore, orthotopic MiaPaCa2 xenografts models showed increased Cx43 staining at invasive sites, indicating the enrichment of a more aggressive phenotype in Cx43-positive cells. Overall, my studies have confirmed the importance of HCO_3^- as a base for neutralising cancer-derived acids and demonstrated novel pathways for venting glycolytic products.

My thesis work was part of two publications where I am first author. These papers are appendix to this thesis as supporting material, but excluded from the word-count.

2 GENERAL INTRODUCTION

2.1 Pancreatic ductal adenocarcinoma (PDAC) epidemiology

Pancreatic cancer is the fourth leading causes of deaths due to cancer in the United States and Europe, and affected an estimated 367,000 diagnosed patients worldwide in 2015 (1-3). For cases diagnosed between 2005 and 2011, the five-year survival rate was only 8%, which is among the lowest survival rates documented among all types of cancers (2). Despite on-going research efforts, the mortality due to pancreatic cancer has not decreased over the past several decades; moreover, recent data suggest that the incidence is continuing to rise in the United Kingdom and in North America, which may be related to an ageing population demography (1).

Although there are several forms and origins of pancreatic cancer, the most common form of the disease, accounting for over 90% of all pancreatic malignancies, is pancreatic ductal adenocarcinoma (PDAC), which arises in the acinar cells of the exocrine pancreas (4, 5). Research has shown that the acinar cells undergo an acinar-to-ductal metaplasia which can progress to PDAC (6, 7). The resemblance of PDAC cells to the ductal morphology of the pancreas led to the previous paradigm that PDAC arose in the ductal cells of the exocrine pancreas (1, 5). In the United States, the incidence of pancreatic cancer is projected to increase steadily and become the third leading cause of cancer-associated deaths in males and females by the year 2030 (8). In Europe, the number of deaths related to pancreatic cancer increased steadily between 2009 and 2015, by 5% in women and 4% in men (3). Between 2005 and 2011, 53% of all pancreatic cancer patients in the United States were diagnosed with cancer

at a distant metastatic stage (2). The five-year survival rate of patients with pancreatic cancer diagnosed at this advanced stage is as low as 2%, which is among the lowest survival rates of all metastatic cancers (2). Only 9% of cancers are detected at a localised tumour stage; this low detection rate is attributable to the limited diagnostic ability of contemporary clinical tests. These patients have a five-year survival rate of 27% (2). Regional tumour spread accounts for 8% of diagnosed cases, with an associated five-year survival rate of 11%. Not all diagnosed cases are included in these statistics, due to inadequate staging information (2).

The majority of pancreatic cancer patients are diagnosed when they are older than 50 years of age (9). Smoking and the use of tobacco products have been estimated to contribute to up to 30% of cases (10). Smokers over the age of 35 years have a more than two-fold greater risk of pancreatic cancer-associated death, compared to age-matched non-smokers (11). Furthermore, smokeless tobacco products, such as snus, increase the risk of pancreatic cancer, which is likely related to the consumption of *N*-nitrosamine toxins (12). Whereas moderate alcohol consumption does not increase the risk of pancreatic cancer, evidence suggests that heavy alcohol consumption is a risk factor (13, 14). The inflammatory disease pancreatitis, which is commonly induced by heavy alcohol drinking, is an additional risk factor for pancreatic cancer (9). Patients with chronic pancreatitis lasting at least five years have a 14-fold greater risk of developing pancreatic cancer (9).

Some evidence suggests that obesity and low physical activity contribute to an increased risk of pancreatic cancer (15-17), but other studies appear to contradict this assertion (18, 19). Up to 80% of pancreatic cancer patients experience glucose

intolerance or diabetes. Whilst some evidence suggests that diabetes can have a causal relationship with pancreatic cancer, the metabolic disorder may be a consequence of early, sub-clinical pancreatic cancer (20). Indeed, it is common in clinical practice to diagnose glucose intolerance concomitantly with pancreatic cancer (20). This could suggest that diabetes is in fact a comorbidity triggered by pancreatic cancer, since the malignancy typically evolves over many years prior to clinical diagnosis. The link between diabetes and pancreatic cancer appears to be consistent with the observation that, in some pancreatic cancer patients, peripheral insulin resistance is reversed upon resection of the pancreatic tumour (21). The onset of diabetes may therefore be an early and traceable sign of developing pancreatic cancer. This hypothesis is supported by the observation that diabetic patients have a 2.1-fold greater risk of developing pancreatic cancer (22).

Thus, in summary, pancreatic cancer is a major health concern that is likely to become more prevalent worldwide, due to a combination of ageing demography and increased incidence of diabetes. Whilst early diagnosis would greatly reduce late-stage disease incidence, effective therapies for this metastatic disease are required to improve overall survival. A promising avenue for treatment relates to addressing the specific pathological features of pancreatic malignancies.

2.2 Pathology and oncogenes

Despite a common location of origin, pancreatic cancers are highly heterogeneous (23). Even though some frequently mutated genes have been identified, genotypic discrepancies between patients highlight the complexity of PDAC

tumours and the challenge in managing the disease. A characterisation of 100 different tumours was able to classify PDAC tumours into four subgroups, based on the integrity of the genome (23). According to this classification system, 50% of PDAC tumours harbour either structural genomic changes of between 50 and 200 events, or unstable genomes with more than 200 rearrangements. Another 30% of tumours harbour locally rearranged genomes with a large number of events in one to three chromosomes. Only 20% of PDAC tumours contain stable genomes with less than 50 mutations (23).

In terms of oncogenesis and pathology, PDAC evolves through a series of non-invasive neoplastic lesions, typically intraepithelial neoplasia, but also at a lower frequency, intra-ductal papillary mucinous neoplasms (24). Pathological examination of morphological changes in the diseased pancreas is routinely used to identify the stage of the lesions (25). In intraepithelial neoplasia, the cuboidal cells change to a columnar morphology (**Fig 2.2.1**) (24, 26, 27). The epithelial cells lose apical-basolateral polarity and become papillary, after which they become highly mitotic and then begin to bud off and form an adenocarcinoma (**Fig 2.2.1**) (24, 27). The time-frame for the evolution of metastatic PDAC tumours from non-neoplastic lesions has been estimated to be a period of ~10 years (**Fig 2.2.1**) (28). Successive mutations or epigenetic silencing leads to the development of PDAC tumours from the non-invasive neoplasms (29). Oncogenic activating mutations in the genes *KRAS* and *ERBB2* are frequently observed upon sequencing and occur at an early stage in PDAC tumour development (27, 29). For example, activating oncogenic mutations in *KRAS* are found in over 90% of PDAC tumours (30-33). Inactivation of common tumour suppressor genes, such as

TP53, *SMAD4, CDKN2A* (encoding p16) or *BRCA2,* is proposed to take place at later stages of tumour formation (27). Inactivating mutations in *TP53, SMAD4* and *CDKN2A* occur in 50 to 80% of tumours (31-33). Evidence obtained from genetically engineered mouse models has revealed that oncogenic *KRAS* alone is sufficient for the initiation of pancreatic intraepithelial lesions, as well as their progression towards metastatic and invasive PDAC tumours (34). The tumorigenic process can be further accelerated by additional mutations in *TP53 (35)*, *CDKN2A (36)* or *SMAD4* (37).

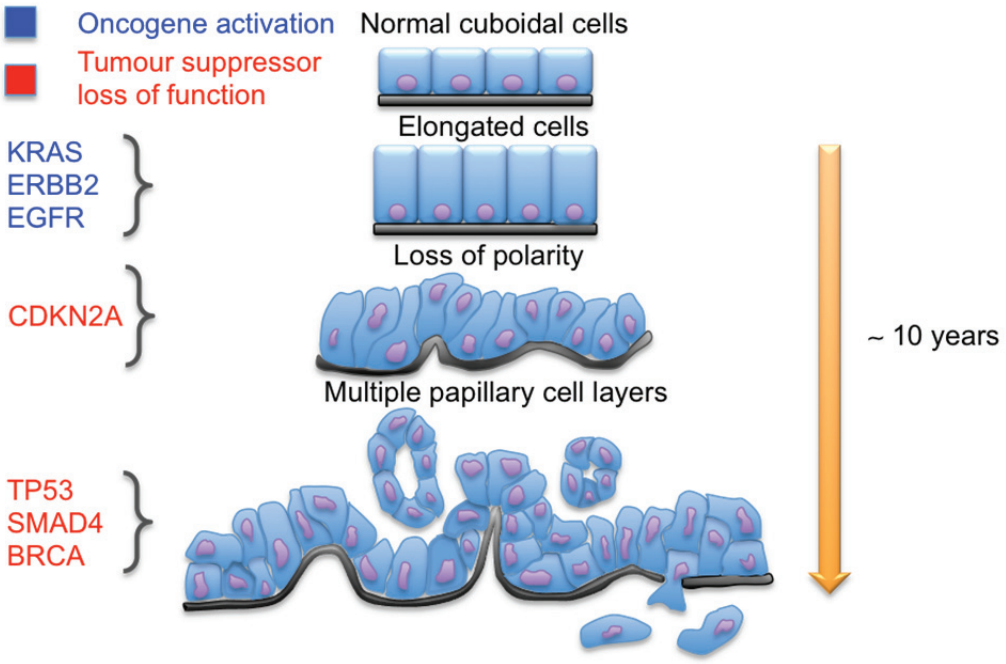


Figure 2.2.1 Genetic and morphologic evolution of pancreatic ductal adenocarcinoma (PDAC). *Normal cuboidal cells line the basement membrane (black) of the exocrine pancreas. Early mutations in KRAS, ERBB2 or EGFR, render the epithelial cells elongated. Later, the cells lose polarity in a process thought to occur due to the loss of function of tumour suppressor genes such as CDKN2A. Further loss of tumour suppressor genes such as TP53, SMAD4 and BRCA2 is thought to lead to the development of multiple papillary cell layers, leading to invasive PDAC. The process of PDAC evolution is estimated to take ~10 years.*

2.3 Invasion and metastasis

PDAC tumours are characteristically highly invasive and metastatic. The process of PDAC cell invasion and metastasis occurs late in the process of carcinogenesis, and this is estimated to require several years to take place (28). The metastatic potential of PDAC is illustrated by the observation that upon diagnosis, less than 20% of pancreatic tumours are confined to the pancreas itself (1). Common targets of PDAC cell invasion are areas dorsal to the pancreas and the distal regions of the stomach (38). Invasion in the proximity of the coeliac trunk, hepatic and superior mesenteric arteries and veins has also been reported, which complicates and obstructs surgical resection (1). PDAC tumours arising in the head of the pancreas may cause jaundice by obstructing bile ducts. Jaundice symptoms are, however, much less common in tumours originating in the distal areas of the pancreatic tail (1). Invasion of cancer cells into the adjacent endocrine pancreas can cause diabetes, explaining the link between these neoplastic and metabolic diseases (20). Metastatic spread is most frequently reported in the lymph nodes, liver, lungs and peritoneal cavity (39).

2.4 Tumour hypoxia

Hypoxia is a state of low ambient oxygen partial pressure (40, 41). Despite fully oxygenated arterial blood, tissues can experience hypoxia as a result of insufficient capillary flow or densities and diffusion-limited oxygen supply (40, 42-44). Pancreatic tumours experience inadequate capillary function due to aberrant angiogenic

signalling (1, 45), uncontrolled proliferation (42, 43), and high interstitial pressure in the tumour (43, 46-49). Actively respiring cancer cells can use oxygen rapidly despite its fast tissue diffusion (40, 42). Oxidative phosphorylation in cells near the blood vessel delivering the oxygen can thus use up the oxygen and prevent distant cancer cells from an adequate supply (41, 42). Chronic hypoxia therefore develops in areas more than 100 – 150 μm from blood vessels, where the distance is inversely correlating the rates of oxidative phosphorylation undergoing in the tissue (41, 42). Acute or intermittent hypoxia may also arise as a consequence of fluctuations in blood flow in areas of a tumour leading to periods of decreased oxygen tension (41).

Pancreatic tumours belong to the most hypoxic human tumours (44). Tissue oxygenation can be measured with a polarographic electrode needle measuring the partial pressure of oxygen (pO_2) (44). Tissue hypoxia is typically categorised as <10 mmHg, <5 mmHg or <2.5 mmHg (41, 44). The majority of pancreatic tumours measured have revealed a median tissue oxygenation of <2.5 mmHg (43, 44). In contrast, normal pancreas oxygenation has been measured as 59 mmHg (43), whereas normal arterial blood has been measured as 200 mmHg (44). A ranked comparison of different independent studies using the same oxygen measuring method in solid tumours prior to treatment suggests that pancreatic cancers are among the most hypoxic, with only prostate cancers showing a similar median pO_2 in one study (44, 50). It should be noted that this information is based on a review of different published studies that may not be directly comparable. Metastases from breast, head and neck cancers show a similar oxygenation status of the primary tumour, which may indicate

that the metastatic cells evolve to withstand a certain level of oxygen depletion while situated within the primary tumour (44).

Evidence from mouse models of pancreatic cancer shows that the metastatic spread of cancer cells correlate with the levels of hypoxia found in the primary tumour of the orthotopic PDAC xenograft (51). These results suggest that a hypoxic environment result in a selection of a more aggressive phenotype in a Darwinian-like manner (52). Hypoxia is among the most prominent selection pressures that can render the subpopulations of malignant tumour cell phenotype resistant to the absence of oxygen by Darwinian-like somatic evolution (53-56). The effects of hypoxia on cancer cell biology and metabolism are described more fully in Sections 2.5 and 2.6, respectively.

2.5 Interplay between hypoxia and the PDAC tumour stroma

Previous studies have shown that tumour hypoxia can stimulate the formation of desmoplastic stroma (57). Indeed, the accumulation of large amounts of fibrous desmoplastic tissue is a specific hallmark of pancreatic cancer (1). Under hypoxia, PDAC cells stimulate stromal fibroblasts to increase their deposition of extracellular matrix (57). This fibrous deposition is mediated by secretion of the sonic hedgehog (SHH) ligand by cancer cells upon stabilisation of HIF 1-α. In PDAC tumours, the pancreatic stellate cells contribute to the formation of desmoplastic stroma which confers chemo-resistance and contributes to a poor clinical outcome of pancreatic cancer (1, 58-60). Intriguingly, in mice, pancreatic stellate cells are capable of migrating

with tumour cells from the primary tumour site to metastatic sites, where they may continue to facilitate tumour growth locally (61).

The desmoplastic reaction of PDAC tumours and the proliferation of stromal cells *per se* can exacerbate hypoxia by imposing an additional barrier to gas diffusion (57). Additionally, the deposition of extracellular matrix around capillary networks and expansion of the stromal compartment could push cancer cells further way from the failing supply of oxygen, towards more extreme hypoxic niches (62). In many cases of PDAC tumours, the volume occupied by stromal components exceeds that of cancer cells (48). Thus, hypoxia and desmoplasia may form a vicious feedback loop that could further amplify the strength of the selection pressure favouring hypoxia-resistant phenotypes (57). This could then contribute to increased metastasis and unfavourable prognosis (51, 53).

2.6 Reprogramming of cancer cell metabolism

2.6.1 Role of hypoxia in metabolic reprogramming

Hypoxia exerts many of its effects genomically via the transcriptional activity of hypoxia inducible factor-1 (HIF-1) (63). Among the key genomic effects of HIF-1 are responses relating to metabolic reprogramming that favour survival under hypoxic stress (63). The HIF-1 molecule is a heterodimeric protein consisting of an α and β subunit (63) and in the presence of molecular oxygen, the constitutively expressed HIF-1α subunit is hydroxylated by prolyl-hydroxylase domain (PHD) enzymes (64). This chemical modification targets HIF-1α for proteasomal degradation, mediated by the

von Hippel Lindau protein and E3 ubiquitin ligase (**Fig 2.6.1.1 A**) (65, 66). In contrast, in the absence of adequate oxygen, HIF-1α is not degraded and remains active (63, 64). This leads to rapid dimerisation with HIF-1β and subsequent binding of the protein complex to its consensus nucleotide sequence on DNA: 5'-RCGTG-3 (where R is a purine) (**Fig 2.6.1.1 B**) (67).

Genes coding for proteins involved in glycolysis and pH regulation are among those up-regulated by HIF-1α, and are highly relevant to the metabolic adaptation of hypoxic cancer cells (63, 68). For example, HIF-1 induces the expression of glucose transporters GLUT1 and -3, as well as a majority of the glycolytic enzymes (63). This hypoxic response underlies the transition from oxidative to glycolytic metabolism of glucose at an elevated rate, in order to sustain ATP generation in the absence of oxidative metabolism (42, 69). GLUT-1 (and HIF-1α) up-regulation at protein level are associated with lymph node metastasis and advanced tumour stage in PDAC tumours (70). HIF-1-dependent induction of lactate dehydrogenase A (LDH-A) and pyruvate kinase of the glycolytic pathway are both upregulated in PDAC tumours and associated with poor clinical outcome (71). Similarly, H^+-monocarboxylate transporter isoform 4 (MCT4), which mediates cellular lactate export, along with a co-transported H^+ ion, is upregulated in PDAC and correlates with poor clinical outcome as does increased lactate concentrations in the blood (72, 73). In addition, one study showed that the *GJA1* gene coding for the gap junction protein connexin 43 (Cx43) is up-regulated by hypoxia, where it could thus mediate cell-to-cell passage of small metabolites (68). It is, however, likely that at least some hypoxic responses of gene expression are cell-line specific.

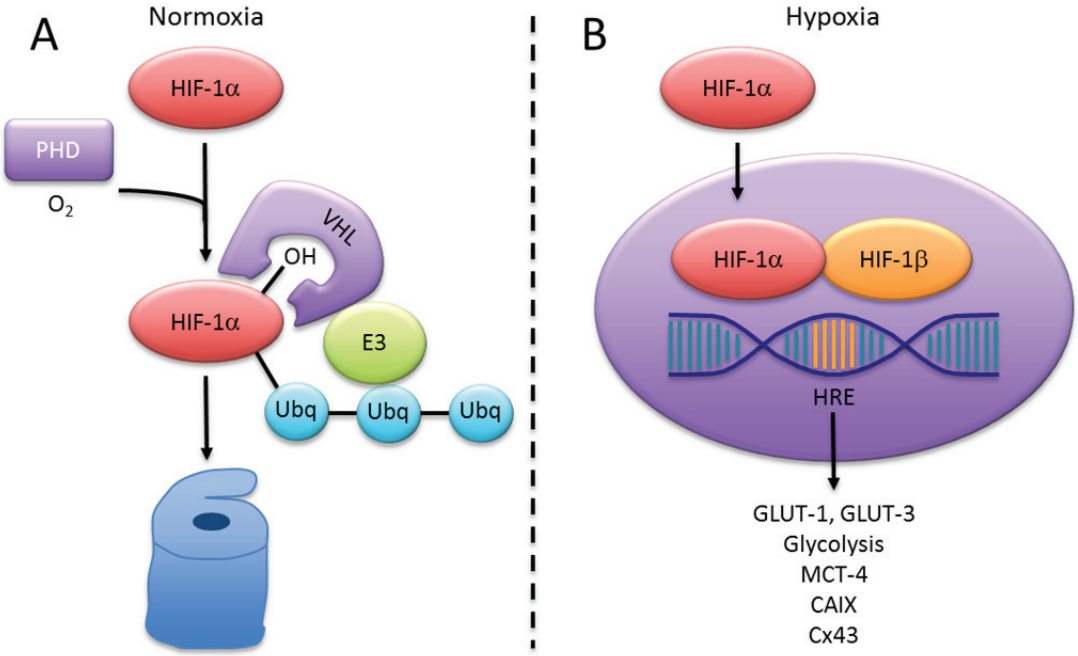


Figure 2.6.1.1 Oxygen-mediated degradation of hypoxia inducible factor 1α (HIF-1α). ***(A)*** *In the presence of oxygen, HIF-1α is hydroxylated by prolyl hydroxylase domain enzymes (PHD). Hydroxylated HIF-1α is then targeted for proteasomal degradation upon binding by von Hippel Lindau protein (VHL) and ubiquitinylation by E3 ubiquitin ligase.* ***(B)*** *In the absence of oxygen, HIF-1α dimerises with HIF-1β and translocate to the nucleus, where they binds the HIF response elements (HRE). HIF mediates the transcription of glucose transporters (GLUT-1, GLUT-3), glycolytic intermediates, monocarboxylate transporter 4 (MCT4), carbonic anhydrase IX (CAIX) and connexin 43 (Cx43).*

2.6.2 Role of oncogenes in metabolic reprogramming

Oncogenic activation of *KRAS* leads to profound metabolic changes in glutamine and glucose metabolism (74-76). The protein product Kras supports enhanced tumour cell growth by up-regulating micropinocytosis and glutamine utilisation for anabolic synthesis of non-essential amino acids (76, 77). In this process,

the NADPH/$NADP^+$ ratio is increased and contributes to the detoxification of reactive oxygen species (ROS), thereby helping to maintain a favourable cellular redox state (76). In conjunction with regulating glutamine metabolism, Kras mediates growth by regulating glucose metabolism (74). This effect includes the up-regulation of ribose biogenesis in a MAPK-dependent manner and the directing of glycolytic intermediates into the non-oxidative (anaerobic) arm of the pentose phosphate pathway thereby facilitating the supply of ribose intermediates for DNA and RNA synthesis (74).

Kras mutations are also associated with an up-regulated glycolytic flux (74), which is important in PDAC tumours because it allows cancer cells to adapt to the ambient micro-environmental stress characterised by hypoxia (75). Glycolysis provides a rapid and responsive generator of ATP, both in the presence and absence of oxygen and renders cancer cells less susceptible to fluctuations in oxygen causing acute hypoxia (42). In addition to producing ATP, glycolysis can yield important anabolic derivatives, which support cancer cell proliferation (42, 69). The expression of the pyruvate dehydrogenase kinase isoform M-2, a kinetically slow isoform, would allow the build-up of glycolytic intermediates to steady-state concentrations that engage collateral anabolic pathways such as the pentose phosphate shunt (71, 78). In combination with enhanced glutamine metabolism (76), oncogenic KRAS activity may favour glycolysis as a balance between ATP production and supply of intermediates for the synthesis of macromolecules in PDAC cells.

In summary, metabolic reprogramming in PDAC cells involves up-regulated anabolic and catabolic processes that, overall, permit cells to replicate, manage ROS and supply ATP, even under stress conditions of the tumour milieu (**Fig 2.6.2.1**).

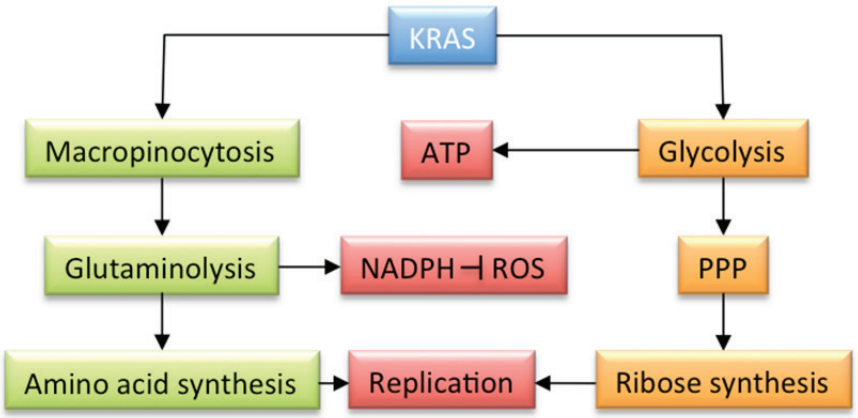


Figure 2.6.2.1 The role of oncogenic KRAS in metabolic reprogramming. *KRAS activation facilitates macropinocytosis and enhanced glutaminolysis. Glutaminolysis prevents the formation of reactive oxygen species (ROS) and provides building blocks for amino acid synthesis. Upregulation of glycolysis generates energy in the form of ATP and facilitates replication by providing intermediates for ribose synthesis through the pentose phosphate pathway (PPP).*

2.6.3 The Warburg effect

The metabolic reprogramming of cancer cells towards glycolysis can persist even at levels of oxygen normally deemed sufficient for mitochondrial oxidative phosphorylation (42). This so-called aerobic glycolysis is commonly referred to as the Warburg effect, and was first discovered by Otto Warburg in the 1920s (79). Early work on a range of different cancer cells demonstrated that cells may derive as much as half of their energy from glycolysis (80). Furthermore, Warburg showed that 10 times more glucose is used for glycolytic fermentation than for oxidative phosphorylation under aerobic conditions, which can be explained in terms of the necessary flux of glucose to

ensure an adequate turnover of ATP (79). This observation has been exploited for diagnostic purposes. On the basis that increased glucose uptake is a near universal phenomenon in cancer, PET imaging for fluorodeoxyglucose has been used successfully for the purpose of detecting tumours *in vivo*, including in patients (42, 69). Capitalising on the notion of metabolic imaging, recent studies have shown that lactate production from glycolytic flux can similarly be used for the detection of tumours through the use of hyperpolarised ^{13}C-labelled pyruvate or glucose in conjunction with nuclear magnetic resonance technology (81).

2.7 Oxidative lactate metabolism

Although lactate cannot be metabolised further in the absence of oxidative phosphorylation in hypoxic cells, it can be committed to the Krebs cycle in more oxic cells, such as those nearer to blood vessels along the route of lactate diffusion (82). For this process to take place, lactate released by hypoxic tumour cells must be avidly taken up by oxidative cancer cells via H^+-monocarboxylate transporters (MCTs), as the lipid matrix of membranes has a very low permeability to lactic acid (the un-ionised form) (**Fig 2.7.1**) (83, 84). The enzyme lactate dehydrogenase B (LDH-B) in the recipient cell then catalyses the conversion of lactate to pyruvate, which feeds into the Krebs cycle for oxidative decarboxylation to CO_2 (85). Oxidative metabolism of lactate may thus provide an additional pipeline for energy supply to normoxic cancer cells, which may therefore take up less glucose (42, 83). In this model of metabolic symbiosis, hypoxic tumour cells feed lactate to normoxic cancer cells, which in turn utilise less

glucose (83). As a consequence, this could increase the bio-availability of glucose for hypoxic cells. Lactate may thus sustain a metabolic symbiosis between normoxic and hypoxic cancer cells (83). Analogously, some stromal cells of some cancers primarily express enzymes involved in lactate metabolism, whereas cancer cells express glycolytic enzymes (86).

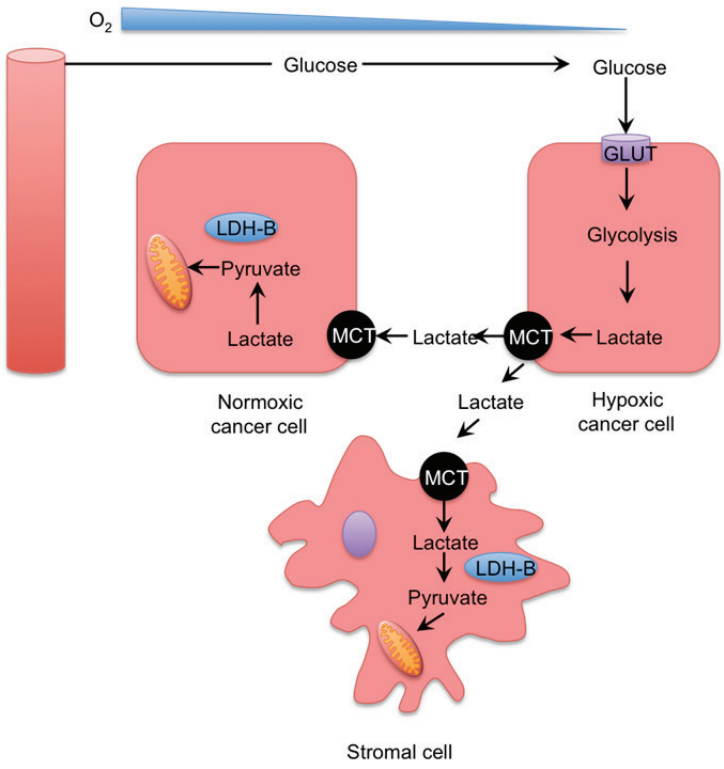


Figure 2.7.1 Metabolic symbiosis of lactate in tumours. *Normoxic cancer and stromal cells expressing lactate dehydrogenase B (LDH-B) can metabolise lactate upon oxidative phosphorylation. By taking up lactate via monocarboxylate transporters (MCT), the cells become less reliant on glucose uptake. This spares the glucose for hypoxic tumour cells that are unable to respire lactate, which instead up-regulate glucose transporters in the plasma membrane. This forms the basis of a metabolic symbiosis between hypoxic and normoxic cells.*

In addition to acting a substrate for catabolic metabolism to generate ATP, lactate may also contribute to the anabolic growth of cancer cells by providing carbon for macromolecule synthesis. Recent evidence in cancer cells has shown that LDH-B is predominantly present in mitochondria, rather than in the cytosol (82). The study also demonstrated the incorporation of carbon atoms from exogenously-labelled lactate into proteins and lipids in HeLa and H460 cancer cells.

The existence of this symbiotic mechanism in PDAC cells is subject to studies (75, 83) as the therapeutic targeting of this juxtaposition of two contrasting cell phenotypes could prove useful in delivering efficacy in a cancer-specific setting (i.e. achieving synthetic lethality).

2.8 Tumour acidity and pH homeostasis

The aberrant blood perfusion caused by abnormal pancreatic cancer vasculature challenges the removal of the acidic end-products in solid PDAC tumours (45, 49) and contributes to the heterogeneity and high levels of hypoxia observed in PDAC tumours (43). The glycolytic reprogramming of cancer cells imposes a challenge for the lactate producing cell (42, 83). The ATP production per glucose molecule is markedly reduced compared to oxidative phosphorylation (42). Whereas glycolysis produces 2 moles of ATP per mole of glucose, full oxidative phosphorylation produces 36-38 moles of ATP per mole of glucose (42, 79). Therefore, the rate of glucose consumption in glycolytic cells would need to be increased accordingly in order to produce adequate amounts of ATP for normal cellular function and proliferation (69).

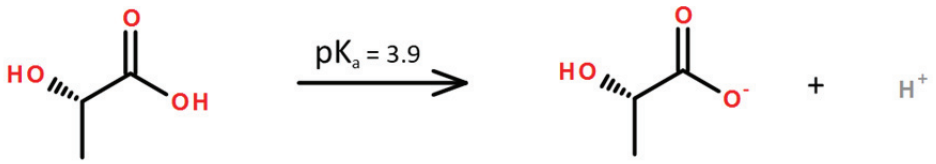
In addition, the lactic acid produced by glycolysis and ATP hydrolysis is fully ionised at physiological pH and far less membrane permeant compared to CO_2, the end-product of oxidative phosphorylation (84, 87). In contrast, CO_2 is vented rapidly from tissues due to its high diffusivity in the aqueous compartments and high permeability across biological membranes (87). Furthermore, the diffusive path-length of CO_2, produced by aerobic respiration, is as short as that of the O_2 delivered to sustain oxidative phosphorylation (i.e. the distance from the blood vessel to the cell). This is not the case for lactate produced by hypoxic cells growing distantly from the blood vessels, i.e. much expanded distances (43, 88). Therefore, PDAC tumour cells rely on adequate acid venting systems to curtail the accumulation of H^+ ions and lactate (84) which would ultimately lead to acid retention.

Since cellular physiology is sensitive to intracellular pH (pH_i) changes, the homeostatic mechanisms of the cells must be deployed in regulating pH_i (89, 90). In order to reach a steady state, trans-membrane H^+ ion (or H^+ ion equivalent) venting must be equal to the flux of H^+ generation. Furthermore, H^+ venting flux must be regulated to fine-tune pH_i in the mildly alkaline range (91). The magnitude of the homeostatic importance of pH_i regulation imposes an energetic burden on the cancer cells since the extrusion of H^+ ions (or their chemical equivalents, such as HCO_3^- ions) into the acidic extracellular space requires ATP consumption for primary or secondary active transport across the cell membrane (84, 89, 92).

2.9 Canonical models of acid venting mechanisms

As a result of metabolic reprogramming and the frequent hypoxic areas, PDAC tumours generally produce large quantities of lactate (42). When oxygen levels are insufficient to sustain oxidative phosphorylation, lactate becomes a waste product that the cell must extrude (83). Since glycolysis produce lactate and hydrolysis of the ATP formed generates H^+ ions (the determining factor of pH) (84), it reduces pH. These H^+ ions can be chelated by buffers that are weak acids or bases (84, 93). However, as buffers are a saturable "reservoir" for H^+ ions, the cell is required, in the end, to deploy active mechanisms for acid extrusion in order to restore this reservoir for on-going acid-production (84, 90, 92). Effective H^+ and lactate venting mechanisms are thus a prerequisite for sustaining a high metabolic rate required for cancer cell proliferation and invasion.

In order for lactate and H^+ ions to be vented across tissue, it must be transported across the cell membrane and diffuse across the intra- and extracellular compartments (84). Lactic acid exists in a dynamic equilibrium with lactate and H^+ ions:



Lactic acid Lactate$^-$

The uncharged lactic acid molecule can cross the cell membrane but has remarkably lower lipid:water partition coefficient than CO_2 and is thus not as membrane permeant (84). Due to its low pK_a of 3.9, more than 99% of the lactic acid is dissociated into lactate and H^+ ions at physiological pH (94). Lactic acid permeation across the cell

membrane unaided by transporters is thus insufficient to allow adequate venting from glycolysis. Therefore, lactate and H^+ ions require the assistance of membrane-spanning transport proteins in order to sufficiently facilitate transport across the cell membrane (84).

The extracellular diffusion of small molecules such as lactate and H^+ ions are affected by the tortuosity imposed by impenetrable barriers. Cell membranes and other macromolecules constitute such diffusion barriers (84, 87, 95). Tortuosity is a description of the elongation of the path-length that a molecule needs to diffuse in order to circumnavigate the impenetrable barriers (84, 87). In addition to the tortuosity, the viscosity of the extracellular compartment affects the solute diffusion coefficient (96). Also, the effective diffusivity of a molecule depends on its binding onto other molecules. As H^+ ions are highly reactive, their diffusion is greatly affected by binding to H^+ buffers (84). The concentration of H^+ buffers markedly exceeds the H^+ ion concentration, therefore, the effective diffusivity of H^+ ions (D_H^{eff}) is governed by the diffusivity of the H^+ buffers (84). Poorly perfused tumours with a low D_H^{eff} will thus be vulnerable to producing large pH gradients in the direction point to blood vessels, whereas any means of increasing D_H^{eff} will reduce the pH gradient. The D_H^{eff} can be accelerated by the presence of mobile buffers that compete for the H^+ ion binding with fixed buffers such as membrane bound proteins (97). The carbonic buffer CO_2/HCO_3^- constitutes the major extracellular mobile buffer, but the efficiency of this buffer is dependent on the activity of carbonic anhydrases (CAs), as the spontaneous reactions are slow (84, 89). The activity of exofacial CAs (with an extracellularly facing catalytic site) contributes to pH_i regulation by facilitating the diffusion of CO_2 in tumour

spheroid growths (98). In muscle cells, the exofacial CAs facilitate lactate venting by enhancing CO_2/HCO_3^- buffering of H^+ ions extruded by MCTs (99) and might thus serve similar functions in cancer cells. However, carbonic anhydrases cannot themselves facilitate the lactate venting across the cell membrane without the transmembrane flux of lactate and H^+ ions via MCT. Since glycolysis produces lactate and H^+ ions in close to 1:1 stoichiometry when the ATP generated by glycolysis is hydrolysed (84), it would be desirable for their venting if the diffusivities for lactate and H^+ were similar. In biological solutions, lactate shows a diffusion rate of 1,000 $\mu m^2/s$ (100). Carbonic anhydrase activity may be necessary to increase the D_H^{eff} to a similar level (84, 101).

The canonical pathway for lactate venting occurs through monocarboxylate transporters (MCTs). The MCTs are membrane bound proteins which translocate lactate and H^+ ions across the membrane in a 1:1 stoichiometry (83, 102-104). The MCT1 and MCT4 isoforms are commonly expressed in cancer as well as normal cells (103). MCT4 is induced by hypoxia whereas MCT1 is not (102). However, since lactate anions are co-transported with H^+ via MCT, the extracellular acidity developing in tumours (**section 2.10**) would tend to reduce, or even reverse, the driving force for lactate venting out of cells (84, 88, 105-110). Furthermore, the extracellular acidity reduces D_H^{eff} by shifting buffering capacity towards fixed buffers (84). It is thus unclear whether MCT transport alone is sufficient to ensure adequate lactate efflux from glycolytic cells in acidic niches, and alternative mechanisms for lactate venting may be needed. Full elucidation of the pathways involved in lactate traffic is therefore of importance for the development of effective therapeutic strategies targeting cancer cell metabolism (111).

2.10 Microenvironment acidity as a selection pressure

Micro-environmental acidity has been suggested to be a strong selection pressure governing the process of somatic evolution in carcinogenesis, analogous to the established role of hypoxia in somatic evolution (52, 56, 109, 112). In order for epithelial cells to evolve into invasive cancer, they must overcome a set of physiological and anatomical barriers set out by the environment (52). Normal pancreatic ductal cells secrete HCO_3^- into the lumen (113). This physiological transport activity produces an alkaline extracellular pH (pH_e) luminally and an acidic pH_e basolaterally; consequently, ductal cells are normally adapted to extracellular acid-base challenges (113). This compartment-specific pH milieu has been suggested to precondition the pancreatic ductal cells to adapt under pH-stress, which may precondition transformed cells to survive in more acidic environments (88, 113).

The lumen that epithelial cells line provides a space into which the epithelial cells can grow (52). In normal epithelial cells, growth into the luminary space is prevented by contact inhibition and detachment-induced cell death, a process called anoikis (114, 115). In the somatic evolution of cancer cell populations, normal epithelial cells must acquire a phenotype that can overcome the barriers of contact inhibition and anoikis (52, 114-117). As the developing tumour population grows, the microenvironment also changes (52). Upon proliferation away from the basement membrane, diffusion distances increase, making transport processes more prone to becoming diffusion-limited. This subjects the developing cancer cells to lower oxygen partial pressures, forcing their biology to adapt to the ensuing local hypoxia (52, 118).

Only those cellular phenotypes that can survive to this microenvironmental growth barrier can continue to proliferate (52). This process will undoubtedly change the phenotypic constitution of a tumour (52). Additionally, the hypoxic up-regulation of glycolysis and intensified production of lactic acid lead to a profound acidification of the extracellular environment (42). This hallmark of cancer confers an additional selection pressure on developing tumour cells that may work synergistically with hypoxia. Acidity will select clones that are resistant to acid-induced cell death (119, 120); however, the precise mechanisms of this have not yet been described fully at the molecular level. The ability of a cancer cell to maintain an alkaline (favourable) pH_i independently of the extracellular acid-base chemistry would allow it to survive acid-selection pressures (42). Thus, the accumulation of metabolic acids in the tumour interstitium may feedback on the phenotypic landscape of cancer cells via a process of selection and somatic evolution (54, 108, 121).

2.10.1 Genetic mechanisms of environmental selection

According to Darwinian principles of evolution, individual phenotypes interact with environmental selection pressures that determine the fitness of a phenotype (121). The fitness of a cancer phenotype is its ability to proliferate as the tumour growth is determined by the ratio of proliferating cells and dying cells (55). Novel phenotypes can evolve through both genetic and epigenetic changes. The rate of cancer cell evolution depends on the phenotypic heterogeneity of the tumour population and the selection pressure exerted by the microenvironment (**Fig 2.10.1.1**)

(55, 122). Thus, increasing the phenotypic heterogeneity and a more powerful and specific environmental selection pressure will tend to increase the rate of somatic evolution of cancer cell sub-populations (55). Since somatic mutations are generally random, cancer cell populations may utilise different, but functionally-equivalent strategies adapt to the same micro-environmental growth barrier (52). Resistance to acidosis may either be attained through up-regulation of acid-extruding transporter proteins at the cell membrane or through resistance to acid-induced cell death (42, 52, 108). Although these strategies may be genetically distinct, they lead to adaptation to the same growth barrier (42). Thus, the phenotype, rather than genotype, is the parameter by which tumour cells are selected (42, 52, 55, 121).

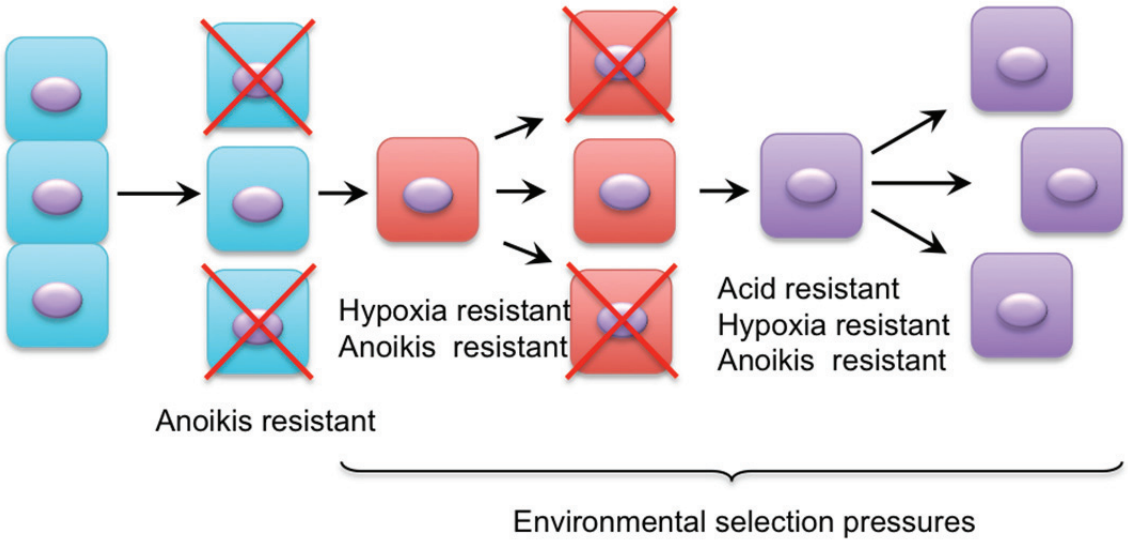


Figure 2.10.1.1 Darwinian evolution of tumour cells via environmental selection. *Environmental selection pressures such as hypoxia and developing extracellular acidity force the cancer cells to adapt to novel microenvironments. As the cells become resistant to detachment-induced cell death and expand, phenotypes adapted to the arising microenvironmental constraints are selected over phenotypes unable to survive (red crosses).*

2.10.2 Acidic extracellular pH in invasion and metastasis

For tumours to become invasive, they must breach the basement membrane (42). A low pH_e facilitates invasion by promoting migration and extracellular proteolysis (109, 112, 123, 124). Cathepsin B mediated degradation of the basement membrane constituent collagen IV is enhanced at acidic pH_e in MDA-MB-231 breast cancer cells (123). An acidic pH_e of 6.8 increases the levels of total and pericellular cysteine cathepsins in comparison to levels existing at physiological pH of 7.4 (123). Similarly, melanoma cells grown under an acidic pH_e enhance the excretion of matrix metalloproteinases, cysteine cathepsins and angiogenic factors that collectively contribute to an invasive phenotype (125). Measurements of peritumoural pH_e of HCT116 colon cancer xenografts show that tumour cells grow into areas with a low pH_e whereas limited or no growth was observed in peritumoural areas with a more alkaline pH_e (112). The invasive areas of these tumours were enriched in the glucose transporter GLUT-1 and the sodium/hydrogen exchanger NHE-1 (112).

Pre-treating tumour cells at a low pH_e prior to tail vein injection increase experimental metastases in mice (125). An acidic extracellular pH_e of tumours can lead to increased migration and invasion. Melanoma cells cultured under acidic conditions increase their secretion of activated gelatinase B, leading to the degradation of collagen IV (126). Metabolic generation of acid is sufficient to induce gelatinase B secretion (126).

The importance of extracellular acidity as a tumour selection pressure is highlighted by experimental manoeuvres that have attempted to normalise the pH_e of

tumours (127). For instance, the oral administration of the pH buffer bicarbonate can increase tumour pH_e. Such systemic buffering inhibits carcinogenesis in the C57BL/6 TRAMP mouse model of prostate tumour formation (127). Whereas some oxidative cell lines are resistant to buffer therapy, tumour cells with a glycolytic phenotype respond to buffer therapy, which also inhibits their migration (124, 126, 128). Early oral administration of 200 mmol/L sodium bicarbonate via drinking water to C57BL/6 TRAMP mice at four weeks of age resulted in a decreased tumour size and increased survival upon increasing tumour pH_e (127). Administration of sodium bicarbonate at later stages had no effect on tumour formation, indicating that acidic tumour pH_e plays a role in the invasive step of carcinogenesis (127). Metastasis formation of prostate and breast cancer cells can be inhibited by pH buffers in mice as a result of decreased extravasation (129). Increased tumour pH buffering has also been attained experimentally with oral administration 2-imidazole-1-yl-3ethoxycarbonyl-propionic acid and lysine in mouse models (130, 131). These buffers have pK_as of 6.9 and 10, respectively, compared to the pK_a of 6.1 of CO_2/HCO_3^- (130-132). The buffers are therefore likely to show optimal buffering at that range. The optimal pK_a for systemic buffering of the tumour pH has been suggested to be 7.1 – 7.2 in order to maintain the blood pH within normal levels of pH 7.3 – 7.4 while raising tumour pH_e to 7.2 – 7.4 (128). Buffer therapy could potentially be applicable in humans, although the mouse dosing regimen extrapolated to an adult human would require a very high intake of bicarbonate, of around 50 g per day which challenges patient compliance (128).

2.11 Current therapies and future treatment of pancreatic cancer

Tumour resection is, at present, considered the only curative option for pancreatic cancer (1). However, resectable tumours account for only 10 - 20% of all diagnosed patients (1). This is because most pancreatic tumours are discovered at a late stage and are therefore deemed as non-resectable, often because of extensive invasion and metastasis (133, 134). In current clinical practice, patients with either resectable or non-resectable tumours receive chemotherapy (1). The standard chemotherapy targets DNA replication, mitosis, or inhibits tyrosine kinases. Aside from being an important factor in metabolic adaptation, hypoxia is also important in the context of tumour therapy because it contributes to resistance to chemotherapeutic drugs such as gemcitabine, as well as resistance to radiotherapy (135-137).

2.11.1 Resectable tumours

Complete resection increases the overall survival rate to 15 – 25% (138-140), with a median survival rate of only 11 - 18 months (38). The resection procedure varies depending on the location of the PDAC tumour. For example, tumours in the head of the pancreas are resected via a partial pancreaticoduodenectomy, with a possible need for resection of the distal stomach (141). In contrast, tumours in the pancreatic tail are resected by distal pancreatectomy in conjunction with splenectomy (1), although this procedure is debated (142). A total pancreatectomy is rare, but may be necessary when the tumour is discovered to occupy the entire pancreas (143).

Despite improvements in surgical techniques, most resections are not complete and leave PDAC cells in the system (144). To target these residual cells, adjuvant chemotherapy is recommended to mitigate the risk of disease recurrence and metastasis. For resectable PDAC tumours, the standard adjuvant therapies use the nucleoside analogues gemcitabine or 5-fluorouracil which increase median survival to ~23 months with no detectable difference in efficacy between gemcitabine and 5-fluorouracil (138, 139).

2.11.2 Locally advanced tumours

A large fraction of PDAC tumours are diagnosed at an already advanced stage and thus deemed non-resectable. Between 30 and 40% of diagnosed patients show borderline resectable PDAC tumours, or locally advanced and non-resectable tumours (133, 145). The resectability of the tumour is governed by the invasion in the proximity of the celiac trunk artery, hepatic artery and superior mesenteric artery, as well as portal and superior mesenteric vein (1, 145). For these advanced pancreatic cancers that are not recommended for resection, standard therapies are based on nucleoside analogues (gemcitabine or 5-fluorouracil) (139, 146). Neoadjuvant chemotherapeutic treatment with drug combinations such as FOLFIRINOX can in some instances decrease the tumour size and render borderline resectable or locally advanced PDAC tumours resectable contributing to a lower operative morbidity (147, 148). FOLFIRINOX combines 5-fluorouracil, oxaliplatin, a platinum-containing drug targeting DNA replication and transcription (149), folinic acid and irinotecan, a topoisomerase inhibitor (31).

2.11.3 Metastatic cancers

Metastases are present in 50 – 60% of patients upon diagnosis (1). In this context, gemcitabine has been shown to be more effective than 5-fluorouracil, and is thus the preferred treatment (146). Combining gemcitabine (or 5-fuorouracil) with other chemotherapeutics, however, has been shown to increase median survival (150-152). FOLFIRINOX is more effective than gemcitabine, and increases life expectancy from 6.5 - 11.1 months (152). However, FOLFIRINOX has many side effects and is only administered to individuals younger than 76 years of age and of good performance status (152).

The combination of gemcitabine with the mitotic spindle inhibitor Paclitaxel has shown an improvement in median survival from 6.7 to 8.5 months, when compared to gemcitabine alone (151). A combination of gemcitabine and erlotinib, a tyrosine kinase inhibitor, has shown a modest increase in median survival of ~2 weeks, compared to gemcitabine alone (153) but due to toxic side effects, erlotinib is not administered frequently (1, 154).

2.11.4 Future modifications to current therapeutic strategies

Patients may respond differently to any given therapy due to the molecular and genetic heterogeneity of pancreatic tumours (23, 155, 156). Precision medicine, predicting patient response to therapy, may be necessary for identifying the most efficacious treatment in the context of a given patient (1). Medicine tailored to target the pathways that are mutated in the patient may have particular promise in therapy

(156). In addition, inclusion of PDAC-subtypes in clinical trials may provide the information necessary to characterise therapeutic responses in subsets of PDAC patients.

2.11.5 Sub-types of PDAC tumours and their responses to therapy

Through genome-wide expression analysis of micro-dissected tumour PDAC biopsies, classical and quasi-mesenchymal sub-types of PDAC tumours have been identified (155, 157-159). The former sub-type expresses epithelial- and adhesion-associated genes, whereas the latter expresses mesenchymal-associated genes (155). These patient-derived sub-types have shown that the classical sub-type show significantly better erlotinib responsiveness and survival compared to the quasi-mesenchymal sub-type that instead had a higher gemcitabine response (155, 159).

To illustrate the utility of stratifying pancreatic cancers by specific genetic signatures, a small minority (3%) of PDAC tumours have found cells harbouring a mutation in the RAS effector protein BRAF (156) likely sensitising them to BRAF inhibitors (160). In addition, a subset of PDAC patients harbouring tumours with unstable genomes or mutations in double-stranded break repair genes has shown sensitivity to platin-based drugs and PARP-inhibitors (23).

In summary, the identification of PDAC sub-types may serve as a tool for predicting therapy responses. This may be further facilitated by the development of high-throughput *in vitro* drug-screening assays of cultures derived from biopsies (161).

2.11.6 Potential for the therapeutic targeting of reprogrammed metabolism

Emerging lines of evidence supporting metabolic reprogramming in PDAC cancer and stromal cells have drawn attention to therapy targeting metabolic pathways. The rise in extracellular acidity resulting from up-regulated glycolysis is a hallmark of cancer (42, 162). Severely hypoxic PDAC tumours are dependent on glycolysis for growth and may thus benefit from therapy targeting glycolytic metabolism (43). Targeting of glycolytic lactate production, lactate export and the stromal reaction contributing to the hypoxic environment have been suggested (48).

Glycolytic enzymes are up-regulated in PDAC tumours when compared to normal pancreatic tissue (163). LDH and pyruvate kinase M2 are among the genes upregulated in PDAC cells that have been proposed as therapeutical targets (48, 164, 165). The pyruvate kinase M2 isoform regulates the Warburg effect in tumours, leaving it as an attractive therapeutical target (48, 78, 166). LDH is upregulated by HIF-1 and controls the rate-limiting step in glycolysis conversion of pyruvate to lactate (165, 167). Mutations in the *LDHA* gene are not lethal and affected patients only exhibit myopathy under strenuous anaerobic exercise (168). Therefore LDH inhibition could act as a safe target to impede PDAC cell proliferation and reduce extracellular tumour acidity.

The classical and quasi-mesenchymal sub-types of PDAC have been shown to differ metabolically (158). The classical epithelial sub-type primarily metabolise glucose through oxidative phosphorylation to synthesise lipids, whereas the quasi-mesenchymal sub-type is glycolytic. Glycolytic quasi-mesenchymal cells show high

sensitivity towards inhibition of the glycolytic enzyme LDH-A, whereas classical lipogenic PDAC cells show sensitivity to inhibitors of lipid synthesis (158).

The acidic end product of glycolysis and ATP hydrolysis must be extruded from cells in order for the cell not to succumb to acidosis (83, 111). MCT inhibitors are currently in Phase I clinical trial (48, 111) and have been suggested to target glycolytic cancer cells by decreasing their pH_i and inducing cell death while sparing normal oxidative cells (75, 83, 111, 169, 170).

2.11.7 Therapy targeting the PDAC stroma

The strong stromal reaction in PDAC tumours promotes hypoxia and reduces chemotherapeutic efficiency (1, 46, 47, 171) as the dense stroma increases the interstitial fluid pressure, limiting the trans-capillary flow through the tumour (172). The interstitial fluid pressure is increased by the water-attracting glycosaminoglycan hyaluronan present in the desmoplastic stroma of PDAC tumours (172) but this can be counteracted by the administration of PEGylated hyaluronidase enzymes which break down the extracellularly-deposited hyaluronan (47). A clinical phase Ib study assessing PEGylated hyaluronidase enzymes in PDAC treatment found a positive effect on the overall survival (173).

2.12 Rationale for the study and original hypotheses

The overarching aim of my research project was to produce an improved model of acid handling in PDAC cells, with the ambition to understand how cancer cells adapt to their specific challenges and propose new targets for therapy. The targeting of reprogrammed metabolism offers tangible therapeutic potential in the treatment of pancreatic cancer, particularly after stratification based on the metabolic profile, such as reliance on glycolysis. Our current understanding of metabolism has focused on the handling of substrates, and our appreciation of how metabolic end-products are removed is less clear, yet critical for a complete model of reprogrammed cancer metabolism. For example, our understanding of the mechanisms that handle metabolic end-products has been focused primarily on the transport processes occurring across the surface membrane of cancer cells. This may be the dominant and rate-limiting mechanism in monolayer monocultures, but does not account for how products are vented over long diffusion path-lengths between the cell and its nearest blood vessel. Using a combination of imaging and assays performed on cell monolayers, spheroids and xenograft mouse models, I addressed the following hypotheses:

1. Carbonic anhydrase enzymes accelerate the extracellular H^+ venting in spheroid tissue structures of PDAC cells upon long diffusional distances.
2. Cancer cells can obtain HCO_3^- ions by direct uptake across the membrane from the extracellular space, but also through a novel pathway assembled from connexin channels that permit cell-to-cell transmission.

3. The Cx43-assembled pathway conducts lactate anions, thus producing a novel pipeline for venting glycolytic products that is particularly important under conditions where extracellular lactic acid may hinder H^+-monocarboxylate transport.

3 GENERAL METHODS

3.1 Cell lines

AsPC1, BxPC3, Capan1, Colo357, PANC1 and MiaPaCa2 cells were a kind gift by Holger Kalthoff (Kiel, Germany). BxPC3, MiaPaCa2 and PANC1 cells were originally established from primary PDAC tumours, whereas AsPC1 was established from ascites. Colo357 and Capan1 were established from metastatic lesions (174, 175). **Table 3.1.1** shows a schematic representation of oncogenic and tumour suppressor mutations in the PDAC cell lines used in this study. Previous morphological examinations of the cell lines showed no correlations among the mutational statuses of *KRAS*, *TP53*, *CDKN2A* and *SMAD4* when compared to the ultra-structural grade of the cell lines when classified according to the WHO guidelines (176).

PDAC cell lines can be categorised into classical epithelial-like, quasi-mesenchymal and exocrine-like sub-types as described in **Section 2.11.5**. The sub-type classification of the cell types used for this study can be found in **Table 3.1.1**. Cells belonging to the classical PDAC sub-type show an epithelial-like phenotype, whereas cells of the quasimesenchymal sub-type express mesenchymal genes (177). The exocrine-like sub-type over-express exocrine digestive enzymes. Quasimesenchymal PDAC cell lines are typically associated with a glycolytic metabolism, whereas the classical epithelial sub-type is associated with a lipogenic metabolism (158).

	KRAS	*TP53*	*CDKN2A*	*SMAD4*	Morphological subtype
AsPC1	Mut	Mut	Mut	Mut	Exocrine-like
BxPC3	WT	Mut	Mut	Mut	Classical
Capan-1	Mut	Mut	Mut	Mut	Exocrine-like
Colo357	Mut	WT	WT	Mut	Quasimesenchymal
MiaPaCa2	Mut	Mut	Mut	WT	Quasimesenchymal
PANC-1	Mut	Mut	Mut	WT	Quasimesenchymal

Table 3.1.1 Genetic and morphologic states of pancreatic ductal adenocarcinoma (PDAC) cell lines used in this study. *Representation of wild type (WT) or mutations (Mut) in oncogenic KRAS or in tumour suppressor genes TP53, CDKN2A and SMAD4 in PDAC tumour cell lines (176, 178-180).*

3.1.1 AsPC1

AsPC1 cells harbour point-mutated *KRAS* and *SMAD4,* and frameshift-mutated *TP53* and *CDKN2A (176, 181)*. Activation of the pentose phosphate shunt has been detected via the activity of the glucose-6-phosphate dehydrogenase enzyme(182). The doubling time of the cell line is 38 – 40 h (182). The AsPC1 cell line originates from ascites collected from a 62-year-old woman. The primary PDAC tumour originated in the head of the pancreas, with metastatic spread to several abdominal organs. The patient was treated with radiotherapy and 5-fluorouracil chemotherapy prior to establishment of the cell line. Ascites developed after therapy and the patient suffered from abdominal swelling before dying two weeks after therapy (182).

3.1.2 BxPC3

BxPC3 cells contain wild type *KRAS* (178, 180) and mutated *TP53* (180), *CDKN2A* (179) and *SMAD4* (183). The pentose phosphate shunt enzyme glucose-6-phosphate dehydrogenase is present in BxPC3 cells (184). The cell line originates from the primary PDAC tumour in the central body of the pancreas of a 61-year-old woman, who died six months after diagnosis. Resection of the tumour was not possible due to local tumour invasion. The patient received radiation and chemotherapy prior to establishment of the cell line, and no metastases were discovered. Histological similarities to the primary tumour were found in mouse xenografts of the cell line, showing moderately to well-differentiated tumour cells (184). BxPC3 cells have been described as belonging to the classical PDAC sub-type, although showing some overlap with the quasimesenchymal sub-type (158, 177).

3.1.3 Capan1

Capan1 cells harbour mutations in *KRAS* (178, 180), *TP53* (180), *P16* (179) and *SMAD4* (181) genes. Capan1 cells are derived from a liver metastasis originating from a PDAC primary tumour situated in the pancreatic head of a 40-year-old male (185). Morphological and biochemical similarities exist between the tumour of origin and mouse xenografts of the cell line.

3.1.4 Colo357

Colo357 cells show mutated *KRAS* (178) and *SMAD4* (181), but contain wild type alleles for *TP53* (178) and *CDKN2A* (179). Colo357 cells show an abnormal karyotype with 20 marker chromosomes (175). Chromosome 1 has been rearranged

into three chromosomes and break points are found in chromosome 5. The pentose phosphate shunt is active in Colo357 cells, detected based on glucose-6-phosphate dehydrogenase activity (175). Colo357 cells belong to the quasi-mesenchymal sub-type, showing an *in vitro* response to erlotinib and gemcitabine (155). The Colo357 cell line originates from a lymph node metastasis derived from a primary tumour (175). The primary tumour was found in the head of the pancreas of a 77-year-old female. Resection of the tumour was not possible, and the patient succumbed to metastatic adenocarcinoma three months after diagnosis. Celiac lymph nodes, from which the cell line was established, were partially replaced by well-differentiated mucinous ducts (175).

3.1.5 MiaPaCa2

MiaPaCa2 cells contain mutated *KRAS*, *TP53* and *CDKN2A* genes, but wild type *SMAD4* (176). Pentose phosphate pathway activity is indicated by the presence of the glucose-6-phosphate dehydrogenase enzyme. MiaPaCa2 cells belong to the quasimesenchymal sub-type. *In vitro*, these cells are sensitive to gemcitabine, but less so to erlotinib (155). MiaPaCa2 cells are derived from the primary PDAC tumour mass of a 65-year-old man (186). The PDAC tumour occupied the tail and body of the pancreas with invasion into peri-aortic areas and showed an undifferentiated phenotype. MiaPaCa2 cells show fibrinolytic activity and significant clonogenic colony formation on agar plates indicating a malignant invasive potential (186).

3.1.6 PANC1

PANC1 cells harbour mutated *KRAS, TP53* and *CDKN2A* genes, but contain wild type *SMAD4* (176). Chromosomal rearrangements are present among chromosomes 1, 5 and 15, in addition to the presence of a ring chromosome (187). Presence of pentose phosphate pathway has been indicated by glucose-6-phosphate dehydrogenase expression. PANC1 cells originate from the undifferentiated primary PDAC tumour of a 56-year-old male which was situated in the head of the pancreas and had a diameter of 1.5 cm. Duodenal invasion and metastatic spread to peripancreatic lymph nodes was found (187).

3.2 Gene expression databases

Microarray data showing gene expression in 22 PDAC cell lines derived from either primary tumours or metastases (listed in **Table 3.2.1**) were obtained from BioGPS (http://biogps.org; dataset: E-GEOD-21654). The dataset was examined for gene expression of connexin and carbonic anhydrase isoforms.

Primary tumour		Metastasis
BxPC3	Panc 3.27	AsPC1
CaPan-2	Panc 5.04	CFPAC
MiaPaCa2	Panc 6.03	Colo357
Nor-P1	Panc 8.13	HPAF-II
PANC1	Panc 10.05	HS766t
Panc 2.03	PL45	L3.6 pl
Panc 2.13	SU86.86	Mpanc-96
Panc 3.3		

Table 3.2.1 Pancreatic ductal adenocarcinoma (PDAC) cell lines used for gene expression analysis. *Gene expression data from pancreatic tumour biopsies was retrieved from the Pancreatic Expression Database (http://www.pancreasexpression.org/; Datasets: Bandea, Buchholz and Segara).*

3.3 Monolayer and spheroid culture

AsPC1, BxPC3, Capan1, Colo357, MiaPaCa2 and PANC1 cells were cultured in 44mM bicarbonate-buffered DMEM (Sigma-Aldrich) containing 10% FBS (Sigma-Aldrich; except Capan1 cells in 20%), 2mM L-glutamine, 0.1 mg/ml Normocin (InvivoGen), 20 U/mL penicillin and 20 µg/ml streptomycin (Sigma-Aldrich). Cells were passaged twice/week using 0.1% Trypsin (Gibco).

Monolayers were plated in LabTek or IBIDI chambers at a density of 70,000 or 50,000 cells per well, respectively, and grown for four days. For immunoblotting,

1,200,000 cells were seeded in 6 cm petri dishes and grown for three days. Cells for biochemical monolayer analyses were seeded at 600,000 cells per 6 cm petri dish and grown for four days. For xenograft experiments, MiaPaCa2 cells were cultured in DMEM/F12 containing Glutamax, 10% FCS and 2.5% horse serum whereas PANC1 cells were cultured in 25 mM glucose DMEM containing 10% FCS.

Spheroids were cultured for three days using the hanging-drop method as described previously (188). Four hundred Colo357 cells were seeded per 20 µl drop and hanging from the lid of a petri dish (**Fig 3.3.1**). Ten ml PBS were then placed in the bottom of the petri dish to avoid evaporation from the hanging drops. For spheroid co-culture experiments, wild type Colo357 cells were mixed 1:1 with shRNA-transfected cells and seeded at 400 cells per drop.

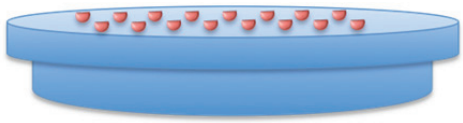


Figure 3.3.1 Spheroid formation via the hanging drop method. *Four hundred cells are seeded in 20 µl drops hanging from the lid of a petri dish.*

For biochemical experiments concerning lactate retention (**Section 3.13**), 5,000,000 cells were seeded in a 250 ml spinner flask (Techne), stirred at 42 rpm and grown in culture medium for up to 120 h at 37°C. Spheroids were generated upon constant rotation of a mercury-filled glass pendulum, which was controlled by a magnetic stirrer rotating it around a convex flask bottom (**Fig 3.3.2**).

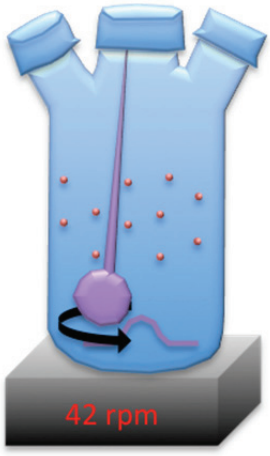


Figure 3.3.2 Spheroid formation in spinner flasks. *A Colo357 cell suspension forms spheroids upon continuous circulation in a spinner flask. A magnet stirrer controls the rotation of an Hg-filled glass pendulum.*

3.4 Cell-Titer-Blue assay

Cellular viability was assessed using Cell-Titer-Blue assay (Promega) (189, 190). Cell-Titer-Blue provides a measure of the reductive potential of viable cells (189). It contains the cell permeable dye resazurin, which is reduced to resorufin in viable cells (189). Resazurin shows a maximal absorbance at 600 nm, whereas resorufin has a maximal absorbance at 570 nm as visualised in **figure 3.4.1** (190). This change in absorbance can be measured with a spectrophotometer. Reduction of resazurin into resorufin is proportional to cell number and has been used to assess the cell viability of cancer cells (191). Both resazurin and resorufin is cell permeable and non-toxic to the cells (189-192).

For metabolic profiling, 60,000 AsPC1, BxPC3 and Capan1 cells, and 45,000 Colo357, MiaPaCa2 and PANC1 cells were plated per well in a 96-well plate to reach

similar confluency levels. For toxicity measurements, 40,000 Colo357 cells were seeded per well. Three hours prior to measurement, 20 µl of the Cell-Titer-Blue reagent was added to 100 µl medium and incubated at 37°C. Cell viability was then measured by determining the ratiometric absorbance at 562 nm/595 nm on a spectrophotometer.

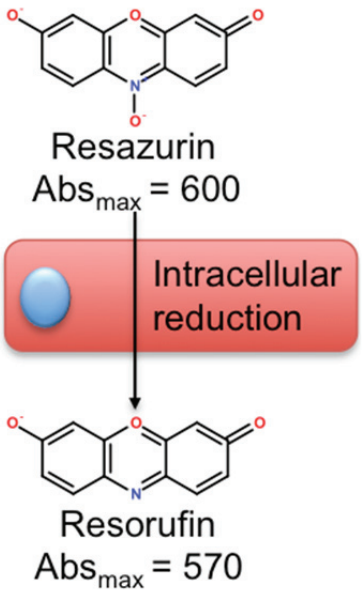


Figure 3.4.1 Cell-Titer-Blue mechanism of action. *The resazurin compound comprising the Cell-Titer-Blue assay is reduced to resorufin by viable cells. The reduction of resazurin to resorufin leads to a change in fluorescence, which expresses cell viability (192).*

3.5 Knockdown of *GJA1*, the gene coding for Cx43

Expression of genes can be genetically silenced by binding to antisense RNA which can be in the form of short hairpin RNA (shRNA). The binding of the shRNA to its antisense region of a target mRNA prevents the translation of the target mRNA into protein (193). ShRNA comprises an RNA strand of 21 - 25 nucleotides folding back on

itself to form a stem-loop hairpin structure (194). The shRNA-mediated degradation of mRNA is initiated by the binding of the DICER ribonuclease enzyme expressed in human cells. DICER recruits the RNA-induced silencing complex (RISC), which targets the mRNA for degradation. The RISC contains a helicase that unwinds the RNA hairpin. The exposure of the antisense sequence then leads the RISC to match the introduced antisense shRNA with its corresponding mRNA. A perfect sequence match leads to mRNA degradation, whereas a partial match promotes translational repression similar to the function of micro-RNA (193). Human cells can be transduced to stably express shRNA. Such transduction can be facilitated by lentiviruses. Lentiviral vectors for infection of human cells are retroviral, derived from Human Immunodeficiency Virus (HIV). These vectors can be used to integrate reverse transcribed RNA from the virus into DNA that can be trans-genetically inserted into the human host genome. The lentiviral particles are capable of infecting dividing cells, making them suitable transduction vectors for cancer cells (193).

HEK293T cells were used as packaging cells for the production of replication-deficient lentiviral particles (**Fig 3.5.1**). The HEK293 cells were grown for two days to 50% confluency in a T25 tissue culture flask prior to plasmid transfection, as recommended for optimal transfection criteria. The pSPAX2 and pMD2.G plasmids (kindly provided by Professor Adrian Harris, Oxford) were transfected together with one of four constructs encoding shRNA against *GJA1* or a scrambled control (scrambled control: CSHCTR001-LVRU6GP; shRNA against GJA1: HSH007411-1-LVRU6GP, HSH007411-2-LVRU6GP, HSH007411-3-LVRU6GP and HSH007411-4-LVRU6GP; Genecopoiea). Transfection into HEK293T packaging cells was performed using the

calcium phosphate method, driving and enhancing the cellular uptake of the plasmids (195). The pSPAX2 plasmid contains the viral *Gag*, *Rev*, *Pol* and *Tat* genes, essential lentiviral genes that encode reverse transcriptase and regulatory and structural proteins. The pMD2.G plasmid encodes another essential lentiviral gene, *Env*, encoding the production of the viral envelope. Co-transfection of these plasmids leads to the production of replication deficient lentiviral particles as the gene encoding the envelope packaging is not transferred to the viral particles. Lentivirus-containing media from transfected HEK293 cells were collected 24 and 48 h after infection, when viral titres are highest, and filtered through a 0.45µm syringe in order to isolate lentiviral particles from HEK293 cell remnants. Medium containing lentiviral particles was added to Colo357 cells and incubated for 72 h. A dose of 6µg/ml puromycin was used, as previously described (196), and validated as efficient to select transfected Colo357 cells. shRNA-mediated knockdown of the product of *GJA1*, Cx43, was evaluated by western blotting.

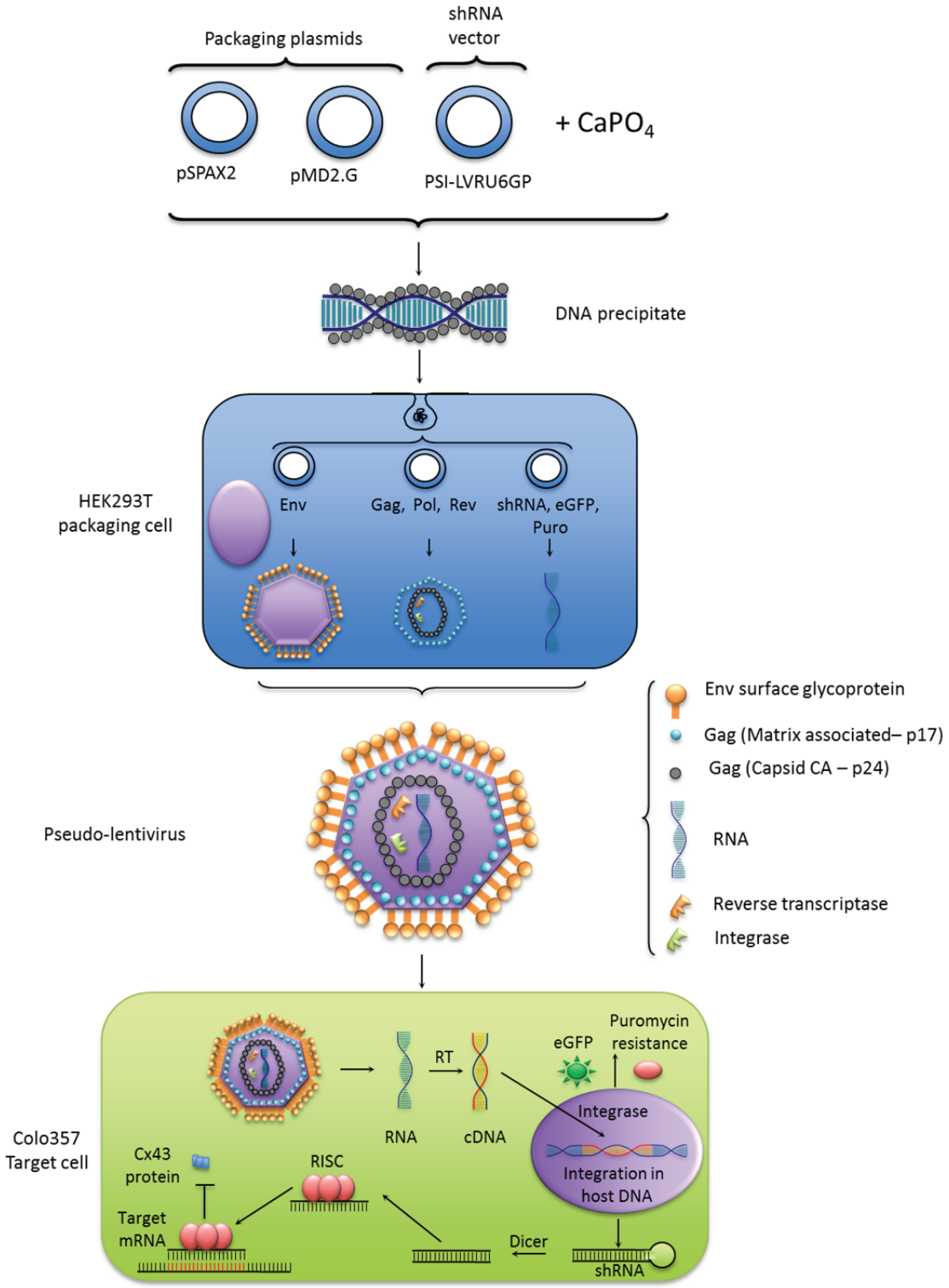


Figure 3.5.1 Lentiviral transfection of short hairpin RNA. *Packaging and short hairpin (shRNA) plasmids are transfected into HEK293T cells via the $CaPO_4$ method. The mixture of DNA and $CaPO_4$ leads to precipitation of the DNA and increased DNA uptake by the packaging*

cells. Pseudo-lentiviral structural proteins, enzymes and RNA molecules are synthesised from the plasmids transfected into HEK293T cells. Pseudoviral particles containing RNA coding for the shRNA against GJA1 (or scrambled for control) are secreted into the culture medium of the HEK293T cells. Incubation of Colo357 cells with filtrated pseudoviral containing medium leads to lentiviral infection with the shRNA against GJA1. The lentiviral RNA is then reverse transcribed into cDNA, which is inserted into the Colo357 genome. Successful transfection leads to the constitutive synthesis of anti-GJA1 (or scrambled control) shRNA molecules. Puromycin resistance genes and eGFP production ensure the capability of selection and recognition of transfected cells. The shRNA duplex generated in the transfected Colo357 cells is recognised by the Dicer ribonuclease. Dicer recruits the RNA induced silencing complex (RISC) complex, which leads to the binding of the shRNA to the target mRNA, leading to degradation or suppression of translation.

3.6 Western blotting

Western blotting is a technique used to assess the global presence of a protein in a pool of cells. By exploiting antibodies raised against an epitope in the protein of interest, its presence can be recognised in a cell lysate.

PDAC cells were grown for 24 h and subsequently treated for 48 h with 0.1% DMSO (control), in 2% O_2 hypoxia or in the presence of 1mM dimethyloxalylglycine (DMOG), a chemical inducer of hypoxic signalling (68). DMOG is a chemical 2-oxoglutarate analogue that works as an inhibitor of dioxygenase enzymes (68). The 2-oxoglutarate-dependent prolyl-hydroxylase domain enzymes that target HIF-1α for proteasomal degradation are among the enzymes inhibited by DMOG. A comparison of the expression pattern of cells incubated in either hypoxia or DMOG shows that DMOG

regulates gene expression in a similar manner to hypoxia, in that a majority of the regulated genes coincide, despite some differences (68).

Cells were lysed in RIPA buffer including protease inhibitors and spun for 20 min at 15,000×g. The supernatant was extracted and protein concentration was measured using a Pierce TM BCA Protein Assay Kit, according to the manufacturer's protocol. Next, 55µg of total protein was loaded in each lane and proteins were separated according to size by 10% SDS polyacrylamide gel electrophoresis. Proteins were transferred to a PVDF membrane, and subsequently blocked in 5% skimmed milk. Membranes were exposed to primary antibodies (**table 3.6.1**) and hereafter to secondary HRP-conjugated secondary antibodies (Novus) and developed with ECL (Pierce, Thermo).

Antibody	Animal	Company	Catalogue number
CAII	Rabbit monoclonal	Novus	NBP1-95903
CAIV	Mouse polyclonal	Novus	H00000762-B02
CAIX	Mouse monoclonal	Gift from Professor Silvia Pastorekova	M75
CAXII	Goat polyclonal	R&D	AF2190
CAXIV	Rabbit polyclonal	Novus	NBP1-55973
Cx26	Rabbit polyclonal	Abcam	AB65969
Cx43	Rabbit polyclonal	Cell Signaling Technologies	3512
Cx45	Mouse monoclonal	Abcam	AB78408
MCT1	Rabbit polyclonal	Millipore	AB3538P,
MCT4	Rabbit polyclonal	Novus	NBP1-00920
NBCe1	Mouse monoclonal	Novus	H00008671-M01
β-actin-HRP	Rabbit monoclonal	Cell Signaling Technologies	5125

Table 3.6.1 Primary antibodies used for western blotting. *The table indicates animal of origin, company and catalogue number.*

3.7 Solutions and superfusion

3.7.1 Solution composition

The osmolarity of solutions were measured to 300mOsm/kg on a Roebling osmometer (Camlab).

Physiological CO_2/HCO_3^- buffered solution:

125 mM NaCl, 22 mM $NaHCO_3^-$, 11 mM glucose, 4.5 mM KCl, 1 mM $MgCl_2$, 1 mM $CaCl_2$. The solution was bubbled with 5% CO_2 for > 30 min to obtain a pH of 7.4.

5% CO_2/11 mM HCO_3^--buffered solution

135 mM NaCl, 11 mM $NaHCO_3^-$, 11 mM glucose, 4.5 mM KCl, 1 mM $MgCl_2$, 1 mM $CaCl_2$. The solution was bubbled with 5% CO_2 for > 30 min to reach a pH of 7.1. Solutions containing 30 mM NH_4Cl were kept iso-osmotic upon an equimolar reduction of NaCl.

Lactate containing CO_2/HCO_3^--buffered solution:

85 mM NaCl, 40mM NaLactate, 22 mM $NaHCO_3^-$, 11 mM glucose, 4.5 mM KCl, 1 mM $MgCl_2$, 1 mM $CaCl_2$.

5% CO_2/2.2 mM HCO_3^--buffered solution

105 mM NaCl, 2.2 mM $NaHCO_3^-$, 11 mM glucose, 4.5 mM KCl, 1 mM $MgCl_2$, 1 mM $CaCl_2$. The solution was bubbled with 5% CO_2 for > 30 min to reach a pH of 6.4.

20 mM Hepes-buffered solution:

135 mM NaCl, 20 mM Hepes, 11 mM glucose, 4.5 mM KCl, 2 mM $CaCl_2$, 1 mM $MgCl_2$.

The pH of the solution was adjusted to 7.4 at 37°C with 4 M NaOH.

1 mM Hepes-buffered solution:

145 mM NaCl, 1 mM Hepes, 11 mM glucose, 4.5 mM KCl, 2 mM $CaCl_2$, 1 mM $MgCl_2$.

The pH of the solution was adjusted to 7.4 at 37°C with 4 M NaOH.

20 mM Hepes buffered solution containing ammonium or acetate:

(135 mM – X) NaCl, X mM NH_4Cl or Na-Acetate, 20 mM Hepes, 11 mM glucose, 4.5 mM KCl, 2 mM $CaCl_2$, 1 mM $MgCl_2$. X is defined in section 5.2. The added NH_4Cl or Na-Acetate was substituted at the expense of equimolar amounts of NaCl. Solutions were adjusted to a pH of 7.4 at 37°C with 4 M NaOH.

3.7.2 Superfusion of monolayers and spheroids

Monolayers were grown and superfused on IBIDI or LabTek plates **(Fig 3.7.2.1)**. IBIDI chambers were superfused at 37°C at a rate of 1.25 ml/min. The superfusate was passed through the 30 µl chamber containing the imaged cells **(Fig 3.7.2.1 A)**. Superfusate was delivered through a female elbow luer (IBIDI) sealing the superfusion chamber. LabTek chambers were superfused at 37°C at a rate of 4ml /min between an elbow luer and a suction device **(Fig 3.7.2.1 B)**. Solution input and output was kept to one side of the chamber to avoid artefacts from superfusion turbulence.

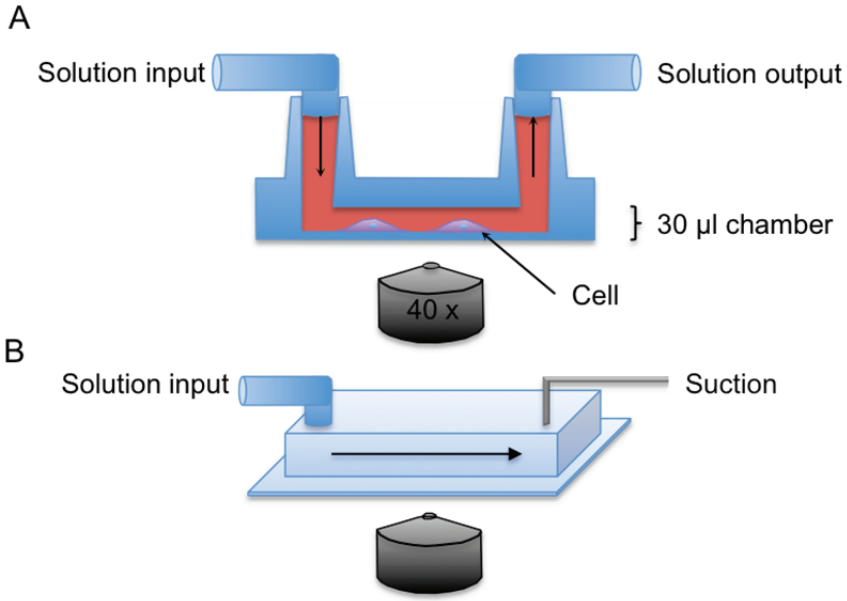


Figure 3.7.2.1 Superfusion of monolayers in IBIDI and LabTek chambers. *(A) Monolayers grown and imaged in a 30 µl IBIDI chamber are superfused through a female elbow luer sealing the superfusion chamber.* ***(B)*** *LabTek chambers are superfused continuously between an elbow luer delivering solution and a suction device.*

Spheroids were superfused at 37°C in a poly-L-lysine coated Perspex chamber containing a coverslip bottom (**Fig 3.7.2.2**). The superfusate was delivered via a tube mounted in one end removed by constant suction at the opposite end.

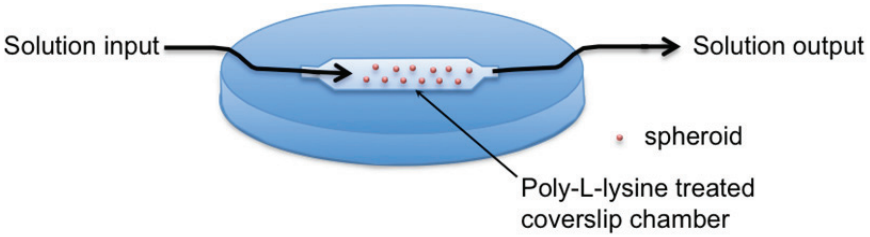


Figure 3.7.2.2 Superfusion of spheroids in a Perspex chamber. *Spheroids are seeded on a poly-L-lysine-treated coverslip, forming the bottom of a superfusion chamber in a Perspex dish. Superfusate is delivered through a tube in one end and removed by constant suction at the opposite end.*

Dual microsuperfusion of Colo357 monolayers was performed in LabTek chambers. The superfusate solution was delivered by a double-barrelled micropipette, as described previously (197). The flow of the microstream was driven by gravity. The integrity of the interstream boundary was assessed by the addition of fluorescein to one of the two microstreams as visualised in **figure 3.7.2.3**.

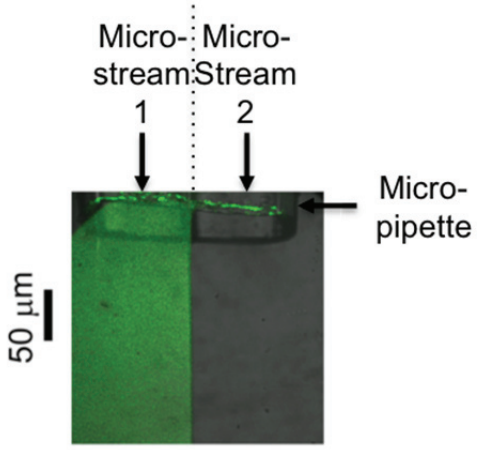


Figure 3.7.2.3 Principles of dual microsuperfusion. *Two solutions are forced through a two-barrel micropipette giving rise to a sharp inter-stream separation visualised by the boundary of fluorescent green (30 µM fluorescein, microstream 1) and non-fluorescence (microstream 2).*

3.8 Confocal fluorescence microscopy

3.8.1 Confocal imaging

Confocal microscopy is a technique that allows acquisition of high-resolution fluorescent images of a focal plane of a specimen. Depth discrimination in the z-axis plane is attained, by allowing only in-focus emitted light to pass through a pinhole aperture (**Fig 3.8.8.1**). In this way, out-of-focus light from sources above and below the focal plane is omitted, giving rise to a better signal-to-noise ratio compared to non-

confocal fluorescence microscopy (198). A model of confocal microscopy is presented in **figure 3.8.1.1**.

The axial resolution along the z-axis depends on the excitation wavelength (λ_{ex}), the refraction index of the immersion medium (n) and the numerical aperture of the objective (NA). The maximal theoretical axial resolution (198) can be estimated according to the function for the axial full width at half maximum:

$$\mathrm{FWHM_{axial}} = 0.88 \times \lambda_{ex}/\mathrm{n} - \sqrt{\mathrm{n}^2 - \mathrm{NA}^2}$$

The maximal theoretical lateral resolution in the x-y-plane describes the minimal resolvable distance between two sources of light (198). This can be estimated by the function describing full width at half maximum for the lateral x-y dimension:

$$\mathrm{FWHM_{lateral}} = 51 \times \lambda_{ex}/\mathrm{NA}^2$$

Confocal imaging was performed on a Carl Zeiss inverted Axiovert microscope supplied with a Carl Zeiss 700 confocal scanning module containing 405nm, 488nm and 555nm lasers. The laser intensity was kept as low as possible (<2%) to protect cells from cell death induced by photo bleaching. As a high pixel resolution of each recorded image compromises the corresponding scan speed, a satisfying compromise between spatial and temporal resolution was obtained for individual experiments. Both spatial image resolution and frequency of image acquisition was controlled manually within the Zeiss Zen 2010 software interface.

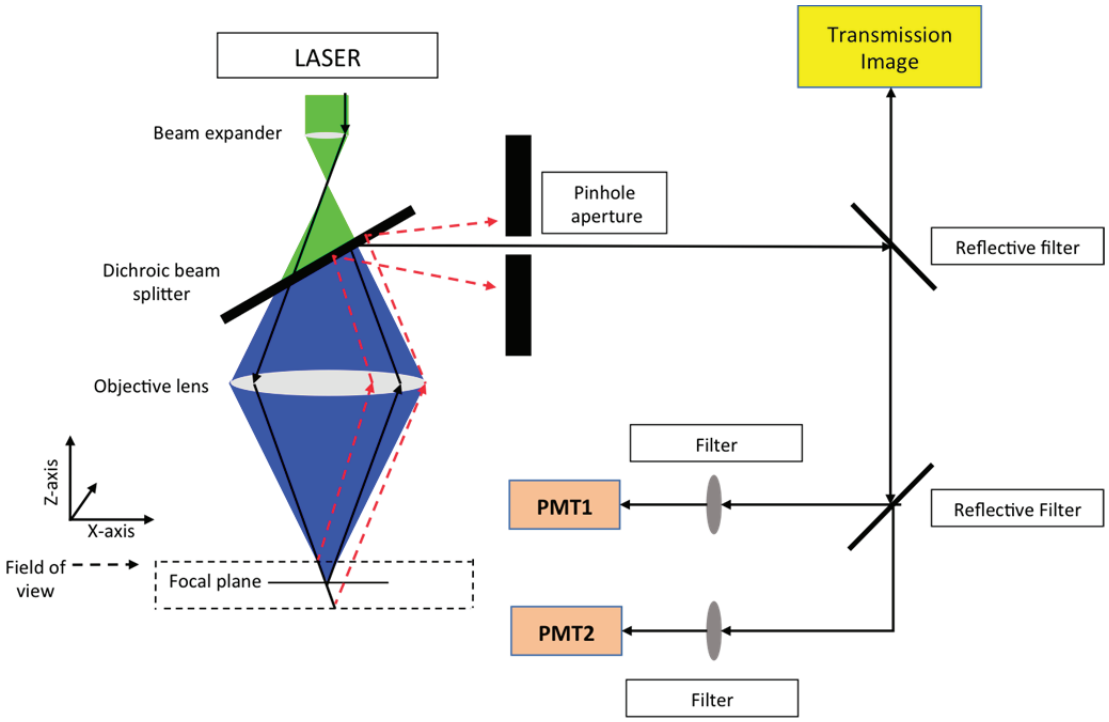


Figure 3.8.1.1 Principles of confocal microscopy. *A laser beam is expanded onto an objective lens and focused on a fluorescent sample. Emitted fluorescent light is reflected on the dichroic beam splitter and passed through a pinhole aperture. The pinhole ascertains that only light emitted from the focal plane is transferred to the photomultipliers (PMT), whereas light emitted from out-of-focus regions is blocked by the pinhole aperture. Thus, confocal microscopy allows the collection of light from a narrow focal plane of a fluorescent sample.*

3.8.2 Data analysis of confocal images

Mean fluorescence within regions of interest was quantified and converted to text files using Image J software (NIH). Data analysis of quantified fluorescent images was then performed using MATLAB (MathWorks®). Codes were written by Professor Pawel Swietach.

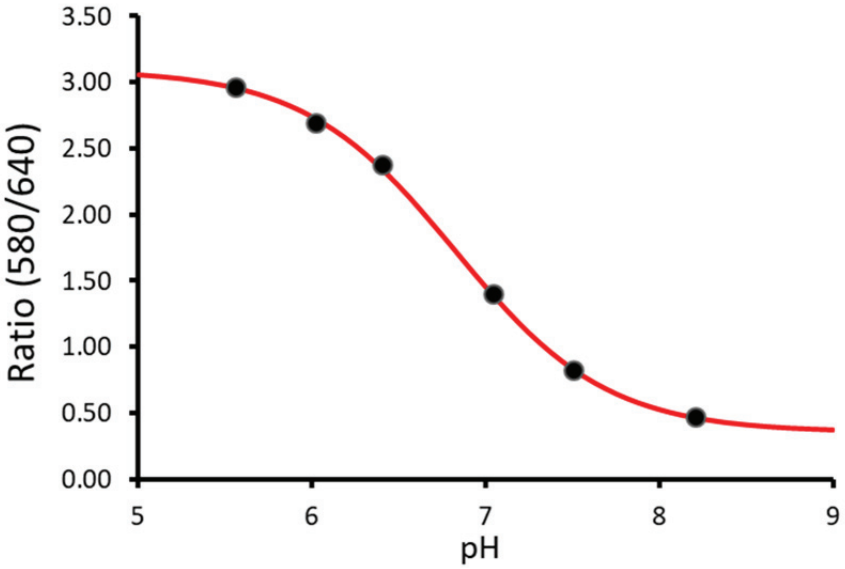
3.9 Fluorescent indicators of pH

3.9.1 cSNARF1

Fluorescence is a phenomenon describing the ability of a chemical substance to absorb light of a certain wavelength and subsequently release a smaller quantum of light of a higher wavelength (199). This technique can be used to measure pH, by using fluorescent probes that change emission fluorescence spectrum upon protonation and deprotonation. In order to detect pH within the physiological range, the fluorophore must have a pK_a within the physiological pH range (200). This ensures that the fluorescent molecule is most sensitive to protonation and deprotonation within the span of the recorded pH (199, 200).

In this study, cSNARF1 was used as an indicator of pH_i (199, 200). cSNARF1-AM is a cell permeable ester derivative of cSNARF1 molecule that is cleaved by intracellular acetoxymethyl esterases, whereupon it becomes cell impermeable and trapped inside cells, emitting intracellular fluorescence (200, 201). It is a non-toxic molecule and can thus be used without major interference in cellular processes. cSNARF1 has a pK_a of ca. 7.35 at 37°C and is thus ideal for measuring pH in the range of pH 6.0 – 8.0. This makes it optimal for measuring pH_i, which is typically around pH 7.2 (89). cSNARF1 possesses a dual emission spectrum with emission peaks at 580 nm and 640 nm. The pH can thus be determined based on the ratio of emitted light of 580 nm/640 nm (200). The ratiometric determination of pH from cSNARF1 has the advantage of being independent of variations in the intracellular concentration of cSNARF1. The pH_i indicator cSNARF1 was loaded into cell monolayers for 5 min at room temperature.

Spheroids were loaded with 20 µg/ml cSNARF1-AM for 3 h on a non-adhesive surface. cSNARF1 fluorescence was excited using a 555 nm laser and emission was recorded using ET580/40 and HQ640/40 band pass filters. (202). The ratio of 580 nm/640 nm fluorescence was transformed into pH using the nigericin calibration method as previously described (202). Monolayers were magnified with a 40x objective lens with a numerical aperture of 1.3. Colo357 spheroids were magnified with a 10x objective lens with a numerical aperture of 0.45. For monolayers, the pinhole was set to 2.9 airy units, corresponding to a 2.7 µm section of the specimen along the z-axis. Imaging of cSNARF1-loaded Colo357 spheroids was performed with a pinhole of 1.77 airy units, corresponding to a 12.4 µm section along the z-axis. A pH calibration curve for intracellular cSNARF1 is presented in **figure 3.9.1.1** along with a table of maximum fluorescence ratio, R_{max}, minimum fluorescence ratio, R_{min}, and pK for the calibration curves of cSNARF1 determined in PDAC cell lines imaged with 40x or 10 magnification lenses. Despite cSNARF1 acting as a buffer of H^+ ions upon protonation, the low intracellular concentration is too small to remarkably affect the pH_i (203).



	AsPC1 (40x)	BxPC3 (40x)	MiaPaCa2 (40x)	PANC1 (40x)	Colo357 (40x)	Colo357 (10x)
pK	6.7805	6.7545	6.7798	6.7601	6.8241	6.8211
Rmax	3.2559	3.3213	3.2020	3.1341	3.0966	3.7764
Rmin	0.2643	0.3515	0.3260	0.3320	0.3544	0.2609

Figure 3.9.1.1 The pH_i calibration of cSNARF1. (Top) *intracellular cSNARF1 pH calibration curve experimentally determined in Colo357 cells imaged with a 40x objective. Intracellular pH was clamped to the pH of extracellular buffers of known pH using the proton ionophore nigericin method. Data points represent mean ± SEM. The red curve represents the fitted pH calibration curve.* ***(Bottom)*** *Table of the determined pK, R_{max} and R_{min} for the intracellular cSNARF1 calibration curves of PDAC cells imaged with 40x or 10x magnification lenses as indicated.*

3.9.2 Fluorescein and derivatives

Extracellular pH was measured using fluorescein sulfonic acid which has a pK_a of ca. 6.4 (200) hence, the emission spectrum of fluorescein sulfonic acid is sensitive to changes in pH (**Fig 3.9.2.1**). The quantum yield of fluorescence emission is reduced greatly upon protonation, giving rise to the change in the emission spectrum. Since fluorescein sulfonic acid is cell-impermeant, it can be used to determine the pH_e around cells. pH_e in the extracellular compartment of spheroids was measured using 3 µM fluorescein sulfonic acid included in the superfusion solutions. Excitation was performed at 488 nm and emitted fluorescence was detected through an ET525/40 band pass filter. Pinhole settings were identical to the settings described for cSNARF1-loaded spheroids (**Section 3.9.1**).

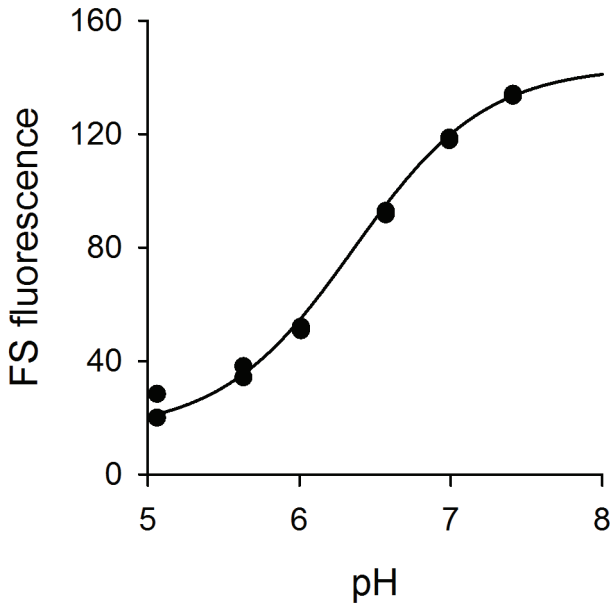


Figure 3.9.2.1 Fluorescence of fluorescein sulfonic acid as a function of pH. *The emission spectrum of fluorescein sulfonic acid at different pH values upon exposure to 488 nm laser. The*

emission spectrum changes upon changes in pH, giving the molecule the properties of a pH indicator. Fluorescence of fluorescein sulfonic acid was measured in Hepes buffered solution of various pHs, in order to produce a pH calibration curve.

Fluorescein-conjugated wheat germ agglutinin (WGA) was used for measurements of changes in local surface pH. Extracellular cell membranes were labelled for 4 min with 1 µg/ml fluorescein-conjugated WGA (molecular probes). WGA-coupled fluorescein was then excited using a 488 nm laser and emission was measured with an ET525/40 band pass filter. Pinhole settings were identical to the settings described for cSNARF1-loaded spheroids.

3.10 Fluorescence recovery after photobleaching (FRAP)

Fluorescence recovery after photobleaching (FRAP) is a technique that can be used to probe cell-to-cell communications mediated by connexins (204). After loading a confluent monolayer with a fluorescent dye (**Fig 3.10.1 A**), a cell is photobleached upon exposure to a high-intensity laser of a wavelength within the excitation spectrum of the fluorophore. The exposure to the high-intensity laser leads to degradation and thus a decrease in the concentration of the fluorophore in the photobleached cell (**Fig 3.10.1 B**). In the presence of gap junctional coupling, the difference in fluorophore concentration between coupled cells drives diffusion of the fluorophore from the connected donor cells into the photobleached cell (**Fig 3.10.1 C**) (204).

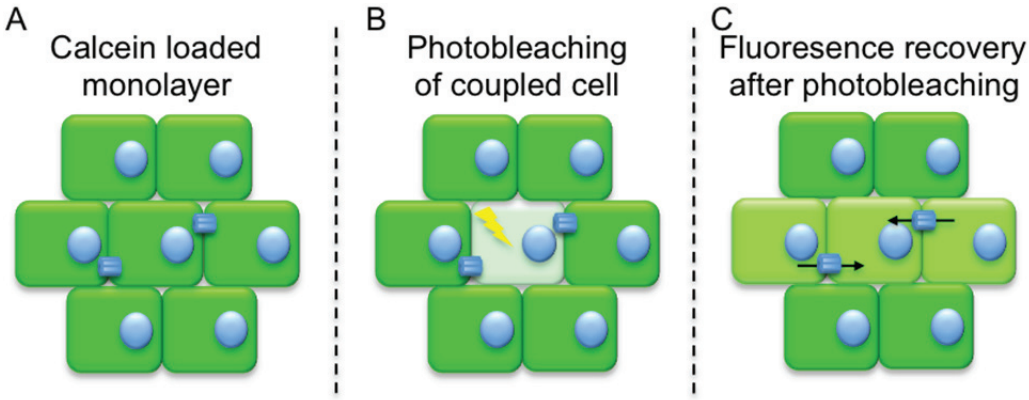


Figure 3.10.1 Concept of fluorescence recovery after photobleaching (FRAP). ***(A)*** *The fluorescein-derived fluorescent dye calcein-AM is loaded into a monolayer.* ***(B)*** *Calcein is photobleached by a high-intensity laser in a connexin-coupled cell.* ***(C)*** *The lower concentration of calcein in the photobleached recipient cell drives permeation of calcein from nearby coupled donor cells until equilibrium between donors and recipient cell is established.*

Because gap junctions are permeable to hydrophilic molecules of less than 1 kDa (204, 205), calcein, with a molecular weight of 622 Da, is small enough to permeate gap junctions (204). Confluent monolayers were exposed to 4 µM calcein-AM for 5 min and then calcein-AM-containing medium was replaced with calcein-AM-free medium to prevent further loading during the experimental procedure. Subsequent de-esterification of the dye inside cells leads to intracellular trapping. Calcein fluorescence was excited with a 488 nm laser and emission was measured using an ET525/40 band pass filter. Bleaching of calcein was performed at 100% laser power (488 nm) between each fluorescence recording until a 50% reduction in calcein fluorescence was obtained in the photobleached cell. The pinhole was set to 15 airy units, corresponding to a 12.5 µm section along the z-axis. The large pinhole was chosen to avoid

fluctuations along the z-axis, introducing artefacts to the signal collection of the fluorescence recovery.

3.11 Photolytic uncaging of H^+ ions using 6-nitroveratraldehyde (NVA)

Cellular pH can be manipulated via light-induced photolysis of a proton donor (206). The compound 2-nitrobenzaldehyde (NBA) has been used as such a photolytic proton donor in cardiomyocytes (206). Upon UV irradiation, NBA undergoes redox reactions within its nitryl and aldehyde groups, resulting in the release of a proton and the formation of 2-nitrobenzoic acid (pK_a = 2.2) (**Fig 3.11.1 A**) (206, 207)**.** Due to the low pK_a of the carboxylic acid in 2-nitrobenzoic acid, the molecule is dissociated into its ionic form at physiological pH. As NBA is an aldehyde, however, it shows fixative properties and is cytotoxic at high concentrations (206). In the attempt to find a less toxic proton donor, the cytotoxic effects and proton-labile properties of the NBA-related compound 6-nitroveratraldehyde (NVA) were assessed. The molecular structure of NVA resembles that of NBA (**Fig 3.11.1 A** and **B)**. The nitryl and aldehyde groups of NVA could therefore potentially react photolytically and work as a proton donor by forming 6-nitroveratric acid **(Fig 3.11.1 B)**. To assess the toxicity of the two compounds, Colo357 cell viability was measured using the Cell-Titer-Blue assay. Cells were grown and incubated with Cell-Titer-Blue, as described in **section 3.4**, and incubated with NVA or NBA for 5 h. The 5 h incubation time was chosen to ensure that the cytotoxic effects measured were within the timeframe of photolytic uncaging experiments (typically <1 h). The viability measurements were normalised to Colo357

cells grown in normal culture medium (100% viability) and those incubated for 5 h in the presence of the Ca^{2+} ionophore ionomycin (100 μM), inducing total cell death (0% viability). Cell viability was higher in cells incubated with NVA in comparison to those incubated with NBA at all concentrations, showing that NVA is less cytotoxic (**Fig 3.11.1 C**). NBA has previously been used at a concentration of 1mM, at which Colo357 cells are ~40% viable, in contrast to ~60% cell viability for 1mM NVA. In order to validate if a lower, and thus less cytotoxic, concentration of NVA can be used as a proton donor, photolytic uncaging was performed in the presence of 0.5 mM NVA. Upon four repeated flashes of 405 nm laser irradiation, the pH_i was observed to decrease, indicating the photolysis of NVA. As CO_2 can permeate membranes and thus short-circuit the intracellular accumulation of released protons, the membrane-impermeable Hepes buffer was chosen. The efficiency of the photolysis was close to 100% as evidenced by an increase in H^+ concentration of ~2 mM upon the four flashes (~0.5 mM H^+-injected per flash). Furthermore, this indicates that NVA does not become depleted or diffusion-limited after several consecutive flashes. Overall, these results suggest that NVA is an efficient photolytic proton donor and shows less cytotoxic side effects than does NBA.

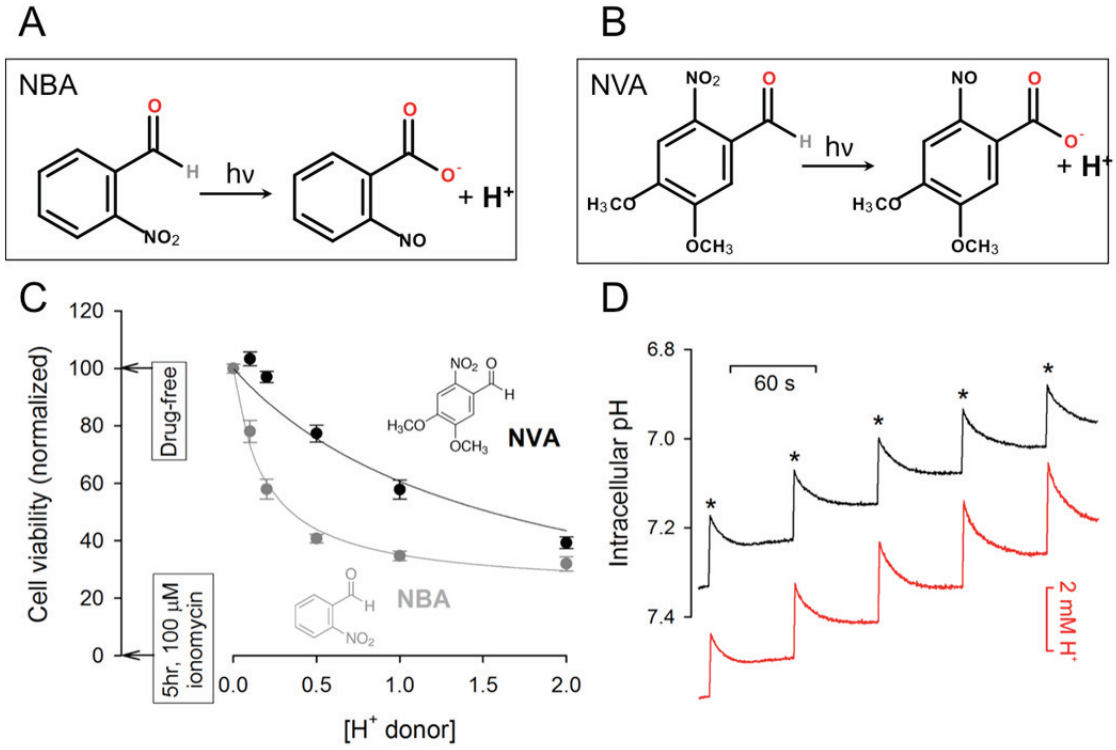


Figure 3.11.1 Proton uncaging properties and cytotoxic effects of 6-nitroveratraldehyde (NVA) compared to those of 2-nitrobenzaldehyde (NBA). ***(A)*** *Mechanism of photolytic uncaging from NBA. Energy from photons (hν) mediates a reaction between the nitryl and aldehyde group resulting in the release of a proton.* ***(B)*** *Proposed mechanism of H^+ uncaging from NVA. Photolysis results in a reaction between the nitryl and aldehyde group similar to the photolysis of NBA.* ***(C)*** *Cell viability of Colo357 cells incubated with NVA (black) or NBA (grey) for 5 h measured using the Cell-Titer-Blue assay. Molecular structures of NVA (black) and NBA (grey) are inserted. Cell-Titer-Blue measurements were normalised to Colo357 cells in drug-free medium (100% viable) and to Colo357 cells incubated in the presence of 100 µM ionomycin for 5 h inducing cell death (0% viable).* ***(D)*** *Validation of NVA as a photolytic proton donor. Intracellular pH (black) and H^+ concentration (red) in Colo357 cells in Hepes buffered medium containing 0.5 mM NVA. Photolysis of NVA, indicated with asterisks (*), was induced following four successive flashes of 405 nm. H^+ concentration was calculated based on the intracellular pH and the buffering capacity at the corresponding pH value.*

For measurements of intracellular H^+ diffusivity, cells loaded with cSNARF1 were placed in Hepes buffered (CO_2/HCO_3^--free) DMEM containing 1 mM NVA. Flash photolysis was then performed at intervals between each full-field acquisition at 555 nm for imaging pH. The flash photolysis was restricted to a defined region of interest within the field of view of the confocal fluorescence scan. Single cells were irradiated using a 405 nm laser to induce photolytic proton uncaging at a region of 1/5th of the length of the cell **(Fig 3.11.2)**. The pH_i was averaged in regions of $1/10^{th}$ of a cell length and converted to pH using the buffering capacity (**section 3.12.2**).

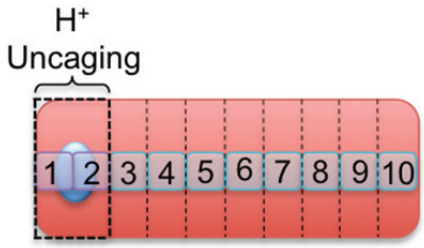


Figure 3.11.2 Proton uncaging in single cells. *Protons are uncaged in a region of $1/5^{th}$ of the length of the cell and pH measured in 10 consecutive regions throughout the cell.*

For H^+ permeability measurements in monolayers, cSNARF1-loaded cells were placed in Hepes buffered (CO_2/HCO_3^--free) DMEM containing 0.5 mM NVA. Protons were uncaged in the cell tested for gap junctional H^+ permeability. Proton uncaging was performed with a 405 nm laser restricted to a central area in the cell to avoid co-injection into neighbouring cells. The pH_i was measured in the central uncaged cell **(Fig 3.11.3, orange)**, in neighbouring cells **(Fig 3.11.3, red)** and in distant uncoupled cells **(Fig 3.11.3, grey)** using a 555 nm laser. Gap junctional H^+ permeability was calculated from the fall in pH_i in central and neighbouring cells as will be described in **section**

3.12.3. The area and perimeter of the central uncaged cell, and of the conglomerate of the central and neighbouring cells, were measured from confocal images, using Image-J to estimate cell volume.

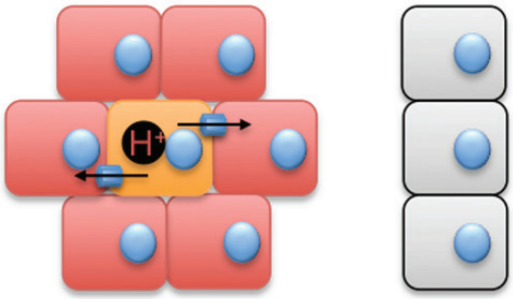


Figure 3.11.3 H^+ permeability measurements from proton uncaging in monolayers. *Flash photolysis of 6-nitroveratraldeyde (NVA) was restricted to a circular region (black region) within a central cell (orange cell) to test for H^+ permeability into neighbouring cells (red). The pH was measured in the central H^+-injected cell (orange), in the neighbouring cells (red) and in distant uncoupled cells (grey). Area and perimeter measurements of the central and surrounding cells were determined in order to estimate cell volume. The cellular permeability to H+ ions was calculated from the ΔpH in the central uncaged cell and neighbouring cells, and normalised to the pH of uncoupled cells (grey).*

Photolytic H^+-uncaging was used to measure the intracellular and extracellular radial H^+ redistribution in three-dimensional tissue structures. H^+ was uncaged centrally in a region of 1/10th of the spheroid radius **(Fig 3.11.4, region 1)**, and pH was measured and averaged in 10 concentric regions throughout the spheroid **(Fig 3.11.4, region 1 - 10)**. Flash photolysis was performed between each fluorescent confocal scan. Protons were injected at a rate of 20.6 ± 1.2 mM/min every 0.7 s over 4 min, calculated as $\Delta pH_i \times$ buffering capacity (see **section 3.12.4**). Intracellular $[H^+]_i$

redistribution was measured in cSNARF1-loaded spheroids at 555 nm whereas extracellular $[H^+]_e$ redistribution was measured in spheroids superfused with solution containing 30 µM fluorescein sulfonic acid, using a 488 nm laser.

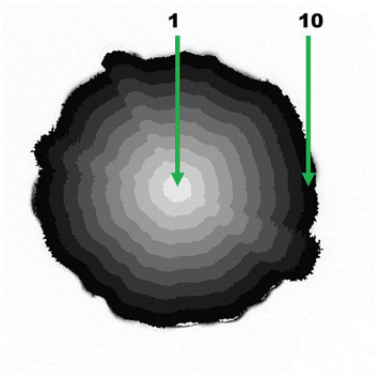


Figure 3.11.4 Proton uncaging in spheroids. *Protons are uncaged centrally in a region of 1/10th of the spheroid radius (region 1). Intracellular pH was measured in cSNARF1-loaded spheroids, whereas extracellular pH was measured in spheroids superfused with fluorescein sulfonic acid (30 µM). pH was measured and averaged in 10 concentric regions (1 – 10) throughout the cSNARF1-loaded spheroid.*

3.12 Mathematical algorithms and statistics

3.12.1 Fluorescence recovery after photobleaching

Calcein fluorescence in the photobleached and neighbouring cells was normalised to the fluorescence measured in cells at the edge of the field of view to correct for fluorescence fluctuations and fluorescence decay. To estimate the time constant for the fluorescence recovery, τ, the fluorescence in the bleached central cell (**Fig 3.10.1**), was best fitted to a mono-exponential function. The cellular permeability to calcein, $P_{junc,calcein}$ (µm/s), was then determined from:

area of central cell × perimeter of central cell/τ

3.12.2 Cytoplasmic H^+ diffusivity (D_H) determined from single cell proton uncaging

The pH was measured in 10 juxtaposed regions along the cell (**Fig 3.11.2**). $[H^+]$ was calculated from pH and buffering capacity and offset to baseline. The H^+ diffusivity, D_H (μm^2/s), was calculated from the $[H^+]$ and the rate of H^+-uncaging, *J*, over 30 – 40 s, and fitted to a constant-source H^+-injection diffusion equation:

$$d[H^+] / dt = D_H \times \partial^2[H^+] / \partial x^2 + J(x).$$

3.12.3 Gap junctional H^+ permeability ($P_{junc,H}$) in proton uncaged monolayers

The average $[H^+]$ concentration was measured in the H^+-uncaged (central) cell and in the neighbouring cells in direct contact with the uncaged cell (**Fig 3.11.3**). The cellular permeability to protons, $P_{junc,H}$ (μm/s), was determined upon solving and best-fitting the following differential equations for H^+ concentration in the central cell, ($[H^+]_{central}$), and the neighbour cells, ($[H^+]_{neighbour}$):

$$d[H^+]_{central} / dt = P_{junc,H} \times \rho_{central} \times ([H^+]_{neighbour} - [H^+]_{central}) + J(x)$$

$$d[H^+]_{neighbour} / dt = P_{junc,H} \times \rho_{neighbour} \times ([H^+]_{central} - [H^+]_{neighbour}$$

where J is the rate of proton injection, and $\rho_{central}$ and $\rho_{neighbour}$ describe the perimeter/area ratio of the central and neighbour cells, respectively, where perimeter

is the length of the boundary of contact. Best fitting was performed over a 60-second period.

3.12.4 Estimating proton uncaging upon NVA photolysis in spheroids

Measurements of pH_i relate to the concentration of free H^+ ions. As some protons are titrated onto buffers, the total quantity (Q) of injected H^+ ions upon photolytic uncaging can be estimated as the product of the measured ΔpH and buffering capacity (β). In the absence of CO_2/HCO_3^- (substituted with membrane impermeable 20mM Hepes), the cumulative Q can be measured from the ΔpH_i and the experimentally determined intrinsic buffering capacity (β_i) (presented in **Fig 5.3.1**). In the presence of CO_2/HCO_3^-, uncaged protons are titrated onto both intrinsic (β_i) and carbonic buffer (β_c). The rate of photolytic H^+-uncaging was estimated to 20.6 ± 1.2 mM/min based on the following integration across the spheroid:

$$\int_{t=0}^{t=T} \beta_i \times \left(\frac{dpH}{dt}\right)_{Hepes} dt$$

$$= \int_{t=0}^{t=T} \beta_i \times \left(\frac{dpH}{dt}\right)_{CO_2/HCO_3^-} dt + \int_{t=0}^{t=T} \beta_c \times \left(\frac{dpH}{dt}\right)_{CO_2/HCO_3^-}$$

$$\therefore \beta_c = \beta_i \times \left(\frac{(dpH)_{Hepes}}{(dpH)_{CO_2/HCO_3^-}} - 1\right)$$

This applies because the cellular acid extrusion in Colo357 cells is very low in the absence of CO_2/HCO_3^- (<1 mM/min within the applicable pH_i range; see **Fig 7.2.5.1 B**).

3.13 Biochemical lactate assay

Pentra 400 Lactate and glucose measurements for this experiment (presented in Fig 8.2.7.1) were kindly performed by Vicky Ball (Oxford). The remaining work was performed by me.

Monolayers and spheroids were grown as described in section 3.3. Spheroids were then collected and split into four vials. Vials were centrifuged for 5 min at 1000 rpm at 4°C for each size category in order to separate the spheroid cell mass from the extracellular medium. For each size category, a small spheroid aliquot was used for size measurements using Zeiss Zen software of transmission images. Extracellular medium was collected and spheroid pellets were lysed in 400 µl ice cold deionised water containing protease inhibitor (Sigma). Spheroid lysis was performed by alternating two freeze-thaw cycles with mechanical disruption with a pipette. All samples were kept on ice to block membrane transport and cellular metabolism. Intracellular and extracellular samples were then centrifuged at 15,000×g at 4°C for 20 min to remove cell debris from the intracellular and extracellular fractions.

Lactate and glucose concentrations were measured using a Pentra 400 (Horiba) supplied with LDH and PAP CP glucose cassettes respectively. Extracellular lactate concentration, $[lactate]_e$, and glucose concentration, $[glucose]_e$, were measured

directly in the extracellular supernatant fraction (culture medium). Since the spheroid lysate consists of intracellular fluid, added water and a remnant of extracellular fluid (**Fig 3.13.1**), these factors must be taken into consideration when determining the true intracellular lactate concentration, $[lactate]_i$. Thus, to calculate $[Lactate]_i$ from the lactate concentration measured in the lysate, $[Lactate]_L$, the measurement must be corrected for the amount of extracellular lactate present in the sample (measured from amount of extracellular glucose present in the intracellular fraction), the amount of dilution (measured by osmolarity) and the amount of spheroid mass (measured by protein content).

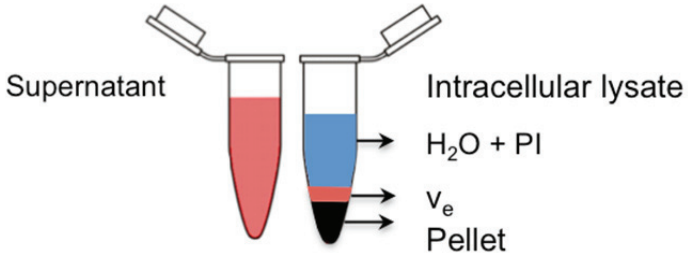


Figure 3.13.1 Lysate composition for intracellular measurements in spheroids*. Intracellular biochemical measurements of lactate and glucose concentrations were performed on spheroid lysates composed of a spheroid pellet, a remnant of extracellular medium (V_e) and 400 µl water containing protease inhibitors (PI). To calculate the true intracellular lactate concentration, the lysate measurement must be corrected for the amount of lactate contributed by the v_e fraction (estimated by glucose concentration), the spheroid mass (measured by protein concentration), and the dilution in water (measured by osmolarity) in order to determine v_i.*

Since most of the intracellular glucose is phosphorylated to glucose-1-phosphate, the glucose measured in the lysate can be used to estimate the extracellular volume, v_e, included in the lysate. The glucose concentration in the

spheroid lysate, $[Glucose]_L$, is thus equal to the product of the extracellular glucose concentration, $[Glucose]_e$, and the extracellular volume left in the intracellular fraction v_e. Thus, knowing the extracellular glucose concentration from direct measurements of the extracellular supernatant as well as the glucose concentration measured in the lysate, $[Glucose]_l$, v_e can be estimated:

$$[Glucose]_L \approx [Glucose]_e \times v_e$$

Similarly, the lactate concentration measured in the lysate is a mixture of intracellular lactate and extracellular lactate from the remnant of medium left in the pellet:

$$[Lactate]_L = [Lactate]_i \times v_i + [Lactate]_e \times v_e$$

The intracellular lactate in spheroids, $[Lactate]_i$ can thus be calculated as the lactate concentration of the lysate minus the product of the extracellular lactate concentration and the fraction of intracellular glucose and extracellular glucose:

$$[Lactate]_i = [Lactate]_L - [Glucose]_L \times [Lactate]_e / [Glucose]_e$$

To measure the dilution factor of intracellular lactate in the lysate and determine v_i, the osmolarities of the intra- and extracellular fractions were measured with a Roebling osmometer (Camlab). Osmotic equilibrium was assumed between intra- and extracellular fractions (cells and culture medium). As the lysate consists of

intra- and extracellular volumes in addition to added water ($v_i + v_e + v_w = 1$) v_i and v_e were determined by calculating the ratio of Osm_i / Osm_e.

The spheroid mass in each vial was estimated by determining the protein concentration using a BCA assay (Thermo). The lactate concentration normalised to protein concentration (mmol lactate/g protein) was converted into the unit of mM intracellular lactate by multiplying the result by the mass of soluble protein per unit of intracellular fluid, ρ, (g protein/L cell). The mass of soluble protein per unit of intracellular fluid was measured to 13.21 ± 1.78 g, based on the ratio of protein concentration (g protein/L) lysate and the intracellular volume (L cell/L lysate). The intracellular volume was calculated using the osmolarity and glucose measurements:

$$V_i = Osm_L / Osm_e - [Glucose]_L / [Glucose]_e$$

3.14 Orthotopic xenografting experiments

The orthotopic xenograft experiments presented here and in **Chapter 9** were performed during a secondment to Professor Frauke Alves' laboratory for Molecular Imaging in Oncology at the Max-Planck-Institute of Experimental Medicine at the University of Göttingen, Germany. The secondment was a part of the European Union Marie Curie Innovative Training Network (ITN) programme, Framework Programme 7. All orthotopic xenografts were grown and sectioned by Professor Frauke Alves' laboratory. Subsequent xenograft tissue staining and the analysis presented in **Chapter**

9 were performed in collaboration with Mara Saccomano, PhD at the Max-Planck-Institute of Experimental Medicine at University of Göttingen, Germany.

Orthotopic xenograft implantation of human PDAC cell lines into the pancreas of immuno-compromised mice has previously shown similarities to the development of pancreatic cancer in humans (208). When implanted into the proximal part of the mouse pancreas, the human xenografted cells invade and metastasise in a manner similar to the process observed in humans (1). The orthotopically-xenografted human cells predominantly spread into areas surrounding the pancreas, including the duodenum and stomach (208). Tumour obstruction of the bile ducts causes jaundice – a symptom also observed in the human disease (1). Histologically, such tumours show the formation of desmoplastic areas, similar to observations of human tumours (1). Similar to PDAC in humans, the xenografted cells metastasise to the lymph nodes, liver, peritoneum and lungs, amongst other sites (1).

In contrast to orthotopically-transplanted xenografts, subcutaneous xenografts of PDAC cells form remarkably different tumours in comparison to PDAC formation in humans (209). The invasive process of subcutaneously-transplanted xenografts obviously shows differences compared to human PDAC, due to the difference in location. In addition, the metastatic properties are different compared to human PDAC (209).

Overall, the invasive, metastatic and histological properties of orthotopically-xenografted PDAC cells show a higher similarity to human PDAC progression than do those from subcutaneous xenografts. Orthotopic xenografts were therefore chosen for this study.

MiaPaCa2 and PANC1 cells were compatible with orthotopic tumour formation in mice and were therefore chosen for the analysis. MiaPaCa2 and PANC1 cells were orthotopically xenografted into the proximal pancreas of NMRI Fox$^{nu/nu}$ nude mice (Charles River, Germany) that were 10 – 20 weeks of age. NMRI Fox$^{nu/nu}$ nude mice are T-cell deficient athymic hairless mice containing B-cells and NK cells. Mice were anesthetised with 75mg/kg ketamine and 15mg/kg xylazine as previously described (210). Upon traction of the stomach, the pancreas was exposed and 10^6 cells suspended in 20 µl PBS were injected into the orthotopic xenograft site. MiaPaCa2-bearing mice were terminated after ca. 90 days and PANC1-bearing mice were terminated after ca. 115 days. The pancreas, xenograft, duodenum, stomach, liver and lungs were excised and fixed for 16 h in 4% formalin in PBS. Fixed tissue was embedded in paraffin upon incubation in increasing concentrations of ethanol for 1.5 h (1 × 60%, 2 × 75%, 2 × 96% and 2 × 100%). The tissue was subsequently exposed to 2× xylol and 3x paraffin. Sections from four animals used for each epitope were tested via immunohistochemical staining. The mice were treated according to the national guidelines, license 33.9-42502-04-13/1085.

3.15 Immunohistochemistry

Paraffin-embedded mouse tissue was cut into 2-µm sections, deparaffinised and hydrated in xylol, ethanol and water, in the reverse order of that described for paraffin embedding in **Section 3.14**. Antigen retrieval was performed by incubation in citrate buffer (pH 6, Dako) at 98°C for 20 min. Peroxidase activity was inhibited by

incubation in 3% H_2O_2 for 10 min in order to reduce background staining. Sections stained for Cx43 were incubated for 20 min in SEA BLOCK buffer (Thermo Scientific) prior to incubation with anti-Cx43 antibody (**Table 3.15.1**) 1:100 overnight at 4°C. Primary Cx43 antibody was stained by v-histofine Simple Stain Rabbit Max PO (Nichirei Biosciences). Sections stained with monoclonal mouse antibodies were preincubated for 1 h with v-histofine Mousestain Kit Blocking Reagent A (Nichirei Biosciences) which prevents immunohistochemical background signals caused by endogenous mouse antibodies. Primary mouse monoclonal antibodies against anti-LAMP2 (**Table 3.15.1**) or anti-human EGFR antibody (**Table 3.15.1**) were incubated overnight at 4°C at 1:200 or 1:100 respectively. The slides were treated with v-histofine Mousestain Kit Blocking Reagent B and signal was detected with simple Stain Mouse Max PO reagent (Nichirei Biosciences) for 10 min. Antibody hybridisation was detected by 30 min AEC staining. Slides were washed in water and cells were counterstained with Meyers hematoxylin for 20 s. Between each step, tissue sections were washed twice for 5 min in TRIS buffer.

Adjacent Cx43- and EGFR-stained tumour sections were computationally overlaid using the ImageJ landmark correspondences rigid non-linear least squares method (http://imagej.net/Landmark_Correspondences). Histological sections were aligned upon selection of 10 – 20 landmarks. Staining patterns were assigned by filtering colour (https://imagej.nih.gov/ij/plugins/ihc-toolbox/index.html). Cx43- and EGFR- stained regions were pseudo-coloured red and blue, respectively. Purple pixels represent regions of Cx43 and EGFR colocalisation.

Antibody	Animal	Company	Catalogue no.
Cx43	Rabbit polyclonal	Cell Signaling Technologies	3512
LAMP2	Mouse monoclonal	Abcam	ab119124
EGFR	monoclonal rabbit	Life Technologies	MA5-16359

Table 3.15.1 Antibodies used for immunohistochemical staining. *The table shows animal of origin, company and catalogue number.*

3.16 Statistics

Two groups were compared using two tailed unpaired student's t-test. For comparisons of three or more groups, a one-way ANOVA was performed in conjunction with a Tukeys honest significant difference test or a Bonferroni correction post hoc test. Tukey and Bonferroni tests were used for comparisons of equal and unequal sample sizes respectively. The significance levels were set to *<0.05 **<0.01 and ***<0.001 unless stated otherwise. Error bars represent standard errors of the mean.

4 METABOLIC PROFILING OF PDAC CELL LINES

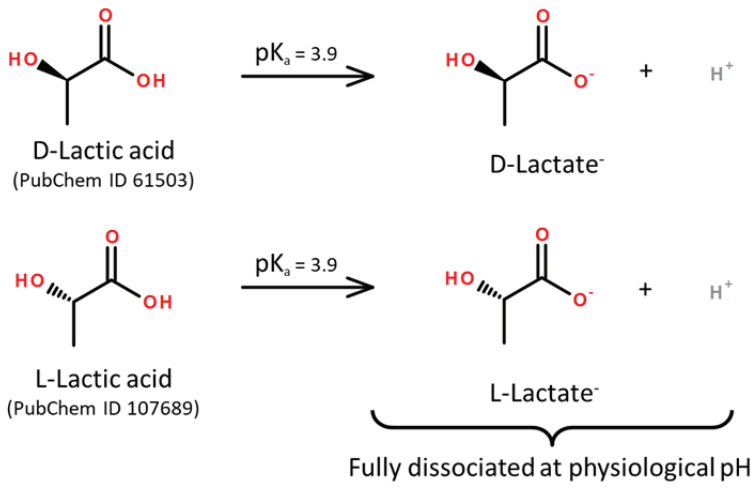
Objective: To determine the extent to which PDAC cell lines rely on glycolysis for the provision of energy.

4.1 Background

The end-products of glucose metabolism, lactic acid (formed upon ATP hydrolysis) and CO_2, are chemically acidic because they reduce pH in aqueous solution. CO_2 gas, generated as a by-product of oxidative phosphorylation, can influence ambient pH through the chemical reaction:

$$CO_2 + H_2O \rightleftharpoons HCO_3^- + H^+$$

(84). This reaction has a pK_a of 6.1 (128) and is slow, wherefore its equilibrium is facilitated by carbonic anhydrases located in both the intracellular and extracellular spaces (211). In contrast to the slow hydration of CO_2, lactic acid ionises rapidly without the need for enzymatic activity, due to its pK_a of 3.9. Lactic acid is therefore almost fully dissociated in most biological solutions (94) as per the following reaction:



Highly-proliferating cancer cells require increased levels of glucose consumption to support their growth demands, but this also burdens the tissue with a raised output of acidic products (45, 88). Without appropriate venting mechanisms, the accumulation of these acidic wastes will lower the intra- and extracellular pH (pH_i, pH_e) to levels that may no longer be conductive for growth (42).

As a result of the Warburg effect manifested in most types of cancers, a large fraction of glucose is metabolised through glycolysis into lactate, even in the presence of oxygen (42). Some types of cancer cells may convert as much as 90% of glucose into lactic acid (212). In hypoxic tumour regions observed in PDAC tumours, the absence of molecular oxygen forces cells to rely on glycolysis and the production of lactate, a phenomenon referred to as the Pasteur effect (42-44, 56, 75, 213). Despite the energetic disadvantage, the normoxic switchover to glycolytic metabolism renders cancer cells more capable of growing independently of the oxygen levels, rendering them resistant to fluctuating tensions (42). This adaptation equips cancer cell biology for colonisation of more hypoxic niches in regions that are more remote from the blood supply (42). Therefore, PDAC cells showing the Warburg effect can survive in the absence of mitochondrial oxidative phosphorylation, making it important to understand the extent of their glycolytic reliance, and how this relates to other aspects of malignant behaviour.

Lactate can be a metabolic substrate for oxidative phosphorylation in normoxic conditions as described in **Section 2.7**. Indeed, some pancreatic cancer cells have been shown to metabolise lactate under normoxic conditions (75). Two lactate enantiomers exist in nature (214, 215). Physiologically, mammalian glycolysis produces the L-lactate

enantiomer, whereas bacteria in the gut produce the D-lactate enantiomer (216). In relation to tumour cell metabolism, the L-lactate enantiomer is by far more common and relevant to cancer (215).

In addition to glucose and lactate glutamine and other amino acids present in serum (as well as common cell culture media) are viable substrates available for oxidative phosphorylation (217-219). By providing substrates for anabolism, glutamine is particularly important for enabling the growth of many types of cancer cells including PDAC cells (76). Through conversion into α-ketoglutarate, glutamine can be incorporated in the Krebs cycle and thus foster the generation of ATP in the presence of oxygen and may thus lead to the production of CO_2 (219).

In this chapter, cellular reliance on the Warburg effect was assessed to infer whether cells predominantly generated lactic acid or CO_2 as the end-product of metabolism. To investigate if glucose was the main substrate for PDAC cell growth, cell viability was assessed in the presence (glucose) and absence of hydrolysable carbohydrates (2-deoxy D-glucose; DOG) or carbohydrates that are not metabolised glycolytically (galactose). Some cancer cells prefer to metabolise lactate over glucose (83). Therefore, the PDAC cell viability sustained by lactate metabolism was assessed. Overall, the results informed a better model for the metabolic substrate preferences of PDAC cell lines. This information can better describe the nature and magnitude of the acid challenge that PDAC cells must handle in order to survive in diffusion-limited niches.

4.2 Methods

The cell's reliance on oxidative phosphorylation and glycolysis can be inferred experimentally from chemical modifications to the culture medium. By replacing cellular substrates, cells can be forced to rely on alternative metabolic pathways for their growth. The cell's ability to thrive in the long term under a particular substrate regime can be probed using indices of cell viability measured using Cell-Titer-Blue as described in **Section 3.4**. A distinction between oxidative phosphorylation and glycolysis can indicate whether cells will predominantly produce CO_2 or lactic acid as the acidic waste product of metabolism.

Cell viability in the presence of the non-metabolisable glucose derivative DOG was used to quantify the metabolic reliance of cells on non-carbohydrate sources of energy that may be present in the culture medium. The molecule DOG is readily taken up by glucose transporters at the membrane (220, 221). Intracellular DOG is then phosphorylated to 2-deoxy-D-glucose-6-phosphate by hexokinase, but this product cannot be processed further by the glycolytic pathway (222, 223). The enzyme phosphohexose isomerase, which normally converts glucose-6-phosphate to fructose-6-phosphate, is unable to metabolise phosphorylated DOG (222, 223).

The extent to which PDAC cells rely on normoxic glycolytic metabolism was inferred from cell viability in media containing 25 mM D-glucose (the control experiment), and results were compared with measurements in media containing 25 mM D-galactose or 25 mM DOG, without D-glucose. Metabolism of galactose yields no net ATP, and thus the cell viability becomes reliant on oxidative mitochondrial

respiration, if the enzymes and substrates are available to sustain cell growth (217, 224-226). Cultivation in galactose is an established method for determining Krebs cycle defects as the cells harbouring defects in respiratory chain proteins or pyruvate dehydrogenase cannot survive under conditions where glucose is replaced with galactose (225, 227-229). Measurements were performed on PDAC cell lines established from primary PDAC tumours (BxPC3, MiaPaCa2, PANC1), metastatic lesions (Colo357, Capan1) and ascites (AsPC1) (174, 175). Incubations with substituted carbohydrate-based substrates were performed for 24 h and Cell-Titre-Blue measurements were compared with time-matched controls in glucose-containing medium.

4.3 Results

The extent of metabolism that is supplied by non-carbohydrate fuels was derived from measurements in media containing 25 mM DOG. Under these conditions, PDAC cells may become reliant on substrates such as amino acids, which must be recruited into the Krebs cycle in order to yield energy. For normalisation purposes, the upper reference point for growth was taken as Cell-Titer-Blue readings in normal glucose-containing medium under normoxia. A model of the metabolism investigated is shown in **figure 4.3.1. A,** whereas **Figure 4.3.1. B** shows carbohydrate-independent cell viability of cells compared to cell viability in the presence of glucose. The growth of all cell lines under investigation was slowed substantially in DOG. Thus, the presence of glucose is necessary to enable a full extent of cell viability, as its substitution with DOG

leads to a 60 – 90% reduction in cell viability. PANC1 cells were the least responsive to this change, and Colo357 cell were the most sensitive. This finding may suggest that cells such as Colo357 rely most stringently on carbohydrate metabolism, perhaps as a result of a limited capacity to perform oxidative phosphorylation that is a prerequisite for using non-carbohydrate fuels. PANC1 cells, in contrast, were able to maintain higher cell viability in DOG, which may indicate a greater ability, compared to Colo357 cells, to obtain energy from non-carbohydrate sources via oxidative phosphorylation.

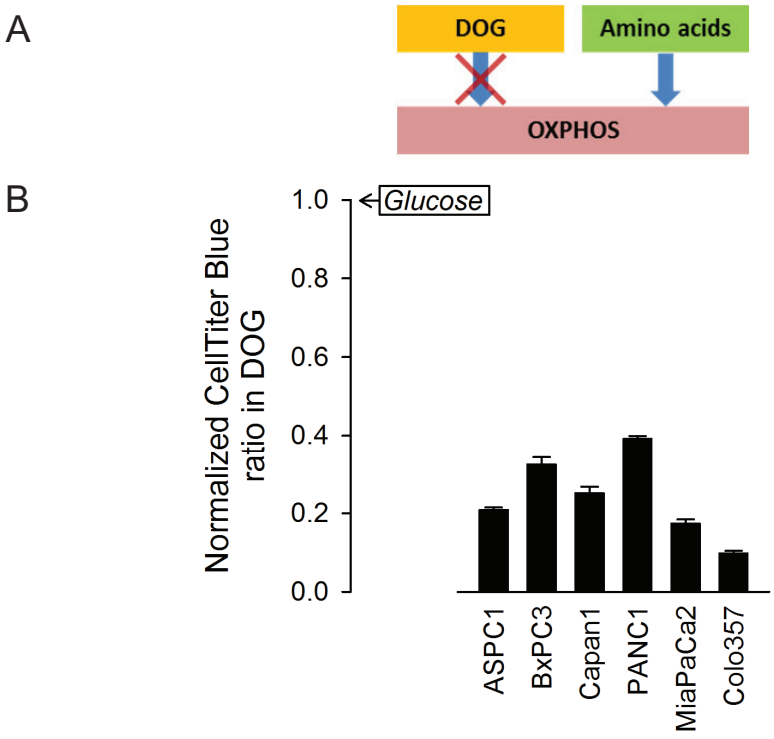


Figure 4.3.1 Cell viability of pancreatic ductal adenocarcinoma (PDAC) cell lines in the absence of carbohydrate metabolism. ***(A)*** *Model for the metabolic substrate utilisation in the presence of 2-deoxy-D-glucose.* ***(B)*** *PDAC cells were incubated in glucose-free media containing 2-deoxy-D-glucose, a substrate that does not commit to glycolysis or oxidative phosphorylation. Cell-Titer-Blue measurements were normalised to time-matched experiments performed in normal glucose containing media. All incubations were performed in normoxia. N = 9 – 15.*

The Cell-Titer-Blue measurements in the presence of DOG shown in **figure 4.3.1 B** served as a reference point indicating carbohydrate-independent respiration in **figures 4.3.2 - 4.3.3**. Since glucose-independent metabolism occurs through oxidative phosphorylation of amino acid substrates present in the medium, the carbohydrate-independent metabolism may predominantly lead to the production of CO_2.

In the presence of a hydrolysable carbohydrate substrate, the dependence of PDAC cell viability on oxidative phosphorylation versus glycolysis was inferred by comparing growth in glucose and galactose containing media. Unlike glucose, which yields ATP when respired glycolytically to lactate or oxidatively to CO_2, galactose must be committed to the Krebs cycle to provide the cell with ATP. Cell viability measured in the presence of galactose thus served as a measure for cellular reliance on oxidative phosphorylation. Cellular phenotypes that predominantly rely on glycolytic metabolism of carbohydrate fuels will be susceptible to the substitution of glucose for galactose, and thus show a reduced level of cell viability. For baseline normalisation, growth in DOG was used as the lower reference point. Growth in galactose-substituted media was substantially reduced in all PDAC cell lines, indicating that in all cases, there was a strong reliance on glycolysis to provide energy (**Fig 4.3.2**). This finding demonstrates that the Warburg effect (aerobic glycolysis) is engaged under normoxic conditions. In BxPC3, Capan1, PANC1 and MiaPaCa2 cells, the index of cell viability was reduced by a factor of two. Colo357 cells were the most sensitive to galactose substitution; hence, this cell line was the least reliant on mitochondrial respiration despite ample oxygen supply under normoxic conditions. AsPC1 cells, in contrast, had

the smallest response to galactose-substitution, indicating that under normoxia, these cells can harness the energy of carbohydrate fuels by engaging mitochondrial respiration, and hence, demonstrating the lowest instance of the Warburg effect.

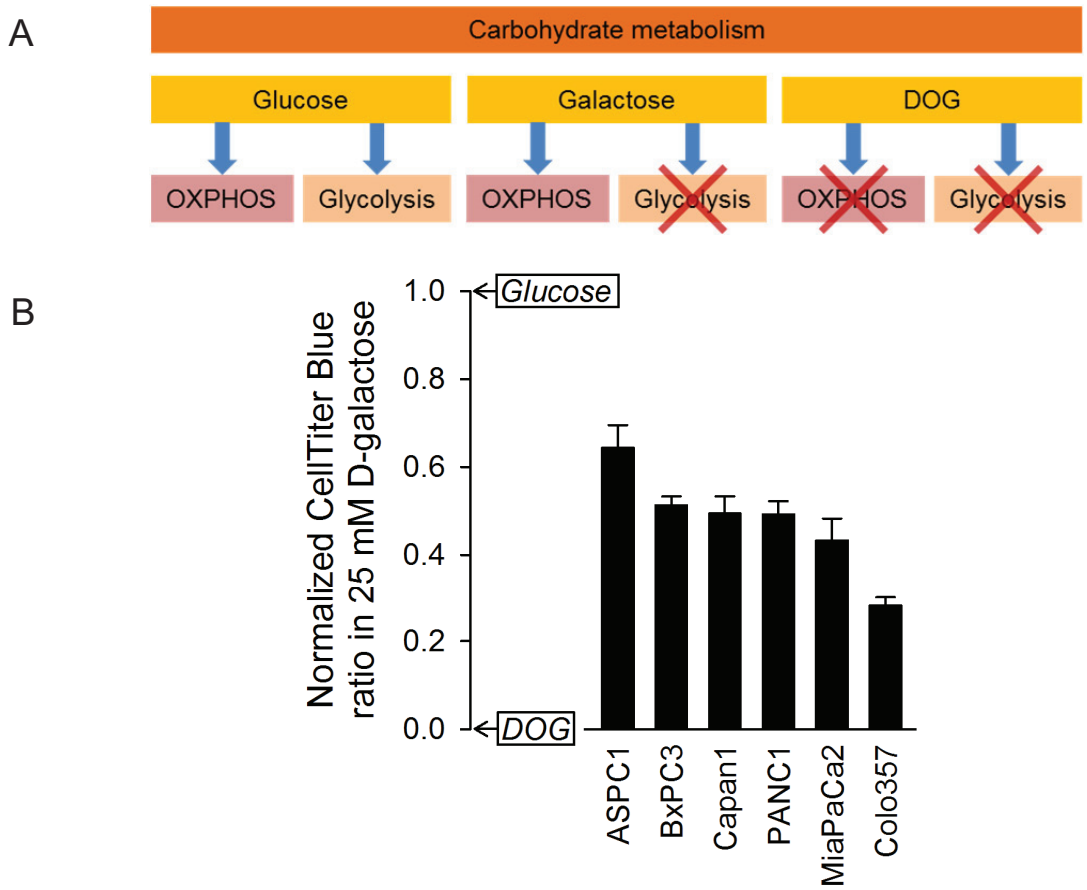


Figure 4.3.2 Estimating the reliance on oxidative phosphorylation in pancreatic ductal adenocarcinoma (PDAC) cell lines, as an index of the Warburg effect. ***(A)*** *Model of carbohydrate metabolic pathways sustained by glucose, galactose and 2-deoxy-D-glucose.* ***(B)*** *PDAC cells were incubated in glucose-free media containing 25 mM galactose, a substrate that produced ATP via mitochondrial respiration, but not glycolysis. Cell-Titer-Blue measurements were normalised to time-matched experiments performed in normal glucose-containing media (upper reference point) and in 2-deoxy-D-glucose substituted media (lower reference point). All incubations were performed in normoxia. N = 9 – 15.*

Lactate produced from glycolysis can be a metabolic fuel for some cancer cells (75, 83). To test if PDAC cell lines can utilise lactate as a metabolic fuel in the absence of carbohydrates, cells were grown in lactate-containing medium with no added glucose or galactose. Measurements were performed separately for the D- and L-enantiomers of lactate. Cell viability of cells grown in lactate was compared to the cell viability of those grown in galactose (which like lactate must be committed to oxidative phosphorylation) and DOG as a baseline for normalisation. All cell lines responded with an increased cell viability in media supplemented with L- or D-lactate, compared to DOG ($p<0.001$; Tukey HSD), but did not reach the level of cell viability measured in glucose (upper reference point; **Fig 4.3.3 B – G**). Thus, glucose is the preferable substrate, but L-lactate and D-lactate can, to some degree, fuel the growth of PDAC cells.

With the exception of Colo357 cells, cell viability in L-lactate was not significantly different from measurements made in galactose-containing medium (**Fig 4.3.3 B – F**). In Colo357 cells (**Fig 4.3.3 G**), L-lactate was less able to support growth compared to galactose. In contrast, metabolism of D-lactate led to a significant reduction in cell viability when compared to galactose in all PDAC cell lines, with the exceptions of BxPC3 and PANC1 (in which cases, there was no significant difference).

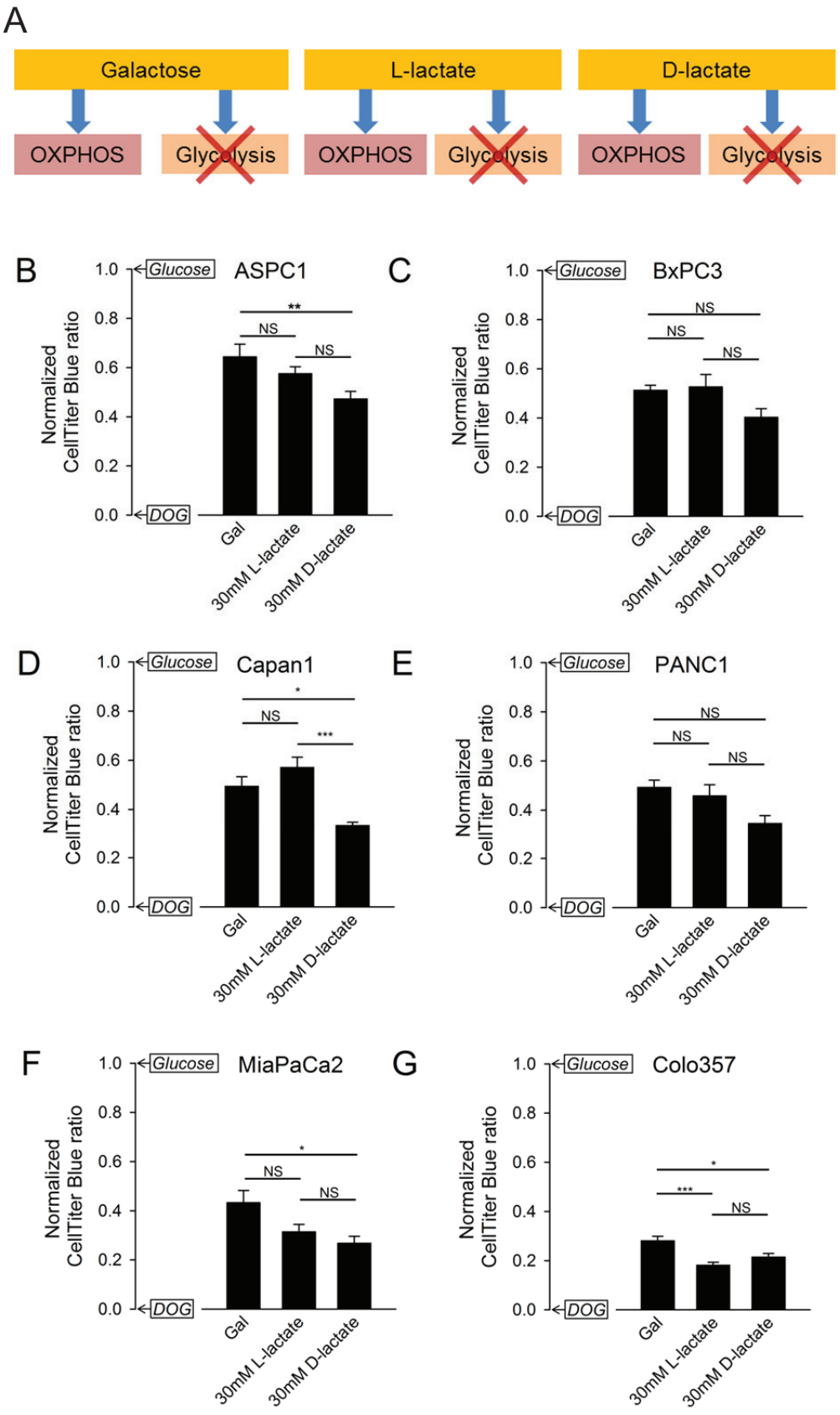

A
Galactose
L-lactate
D-lactate
OXPHOS
Glycolysis
OXPHOS
Glycolysis
OXPHOS
Glycolysis
B
ASPC1
C
BxPC3
D
Capan1
E
PANC1
F
MiaPaCa2
G
Colo357
Glucose
DOG
Normalized CellTiter Blue ratio
1.0
0.8
0.6
0.4
0.2
0.0
**
*
***
NS
Gal
30mM L-lactate
30mM D-lactate

Figure 4.3.3 Lactate dependent cell viability of pancreatic ductal adenocarcinoma (PDAC) cell lines in the absence of other carbohydrate energy sources. *(A) Model of metabolic pathways sustained in the presence of galactose, L-lactate and D-lactate.* ***(B-G)*** *PDAC cell lines were grown in glucose-free media containing either 25 mM galactose, as a measure of full cellular potential for oxidative phosphorylation, or 30 mM L- or D-lactate as substrates of oxidative phosphorylation. All measurements were performed under normoxic conditions. N = 9 – 15.*

4.4 Summary of findings

- Viability derived from carbohydrate-independent metabolism (**Fig 4.3.1**) ranged from 10 to 40% in the PDAC cell lines and ranked in the order:

  PANC1 > BxPC3 > Capan1 > AsPC1 > MiaPaCa2 > Colo357
- Glycolytic metabolism under normoxic conditions (**Fig 4.3.2**) demonstrated the manifestation of the Warburg effect in all PDAC cell lines.
- Cellular dependence on aerobic glycolysis (**Fig 4.3.2**) ranked in the order:

  Colo357 > MiaPaCa2 > PANC1 > Capan1 > BxPC3 > AsPC1
- Colo357 cells were chosen for further studies (**Chapters 6 – 8**) due to their high reliance on glycolysis.
- Lactate can be utilised to sustain viability, albeit not to the same level as glucose (**Fig 4.3.3**).

5 H^+ BUFFERING CAPACITY OF PDAC CELL LINES

Objective: To quantify the CO_2/HCO_3^- dependent and independent components of intracellular H^+ buffering capacity in PDAC cell lines.

5.1 Background

Lactic acid and CO_2 dissociate to H^+ and their conjugate base in aqueous solutions (84) and thus reduce pH. With abundant supply of glucose and hydrolysis of all ATP molecules generated by glycolysis, pancreatic cancer cells can produce 8 – 22 mmol of H^+ ions per min per litre tumour tissue (230, 231). Buffers cannot permanently remove H^+ ions, but merely serve as a finite and intermittent "reservoir" for H^+ ions that can reduce the amplitude of pH changes to protect cells from injurious deflections in pH (84).

Two types of buffers coexist in the cytoplasm: Intrinsic buffers consisting of protonatable residues on cytoplasmic molecules that do not permeate the plasma membrane and the extrinsic CO_2/HCO_3^- buffer (84, 93, 232). Due to the passive trans-membrane diffusion of CO_2, CO_2/HCO_3^- buffer is an "open" buffer that can readily cross the plasma membrane in the form of CO_2 (hence the label extrinsic) (232). The intrinsic buffers are heterogeneous and constitute a variety of protonatable groups such as inorganic phosphate molecules and the imidazole group of histidine showing a pK_a ~6.5 (203). The intrinsic buffering capacity (β_{int}) is dependent on cell type (through expression of different proteins and dipeptides) and must be determined

experimentally by the ammonium and acetate removal method (93). On the other hand, the CO_2/HCO_3^- buffering can be calculated as $\beta_c = 2.303 \times [HCO_3^-]_i$ (93). However, since its reaction kinetics is slow, the CO_2/HCO_3^- buffering system depends on catalysis from carbonic anhydrases for its rapid equilibration (84, 211).

As the majority of metabolically produced H^+ ions will be buffered in the cytoplasm, the H^+ diffusivity will depend on the mobility of the buffers that the H^+ ions bind (84, 203, 233). Buffers can either be fixed buffers or mobile, which is determined by their diffusivity in aqueous solutions (84, 97, 203, 233). Fixed buffers consist of protonatable histidine residues situated in immobile proteins (84, 90, 97). In contrast, mobile buffers such as dipeptides and phosphate ions act as chaperones transporting protons through the aqueous cytoplasm (203, 233, 234). Furthermore, mobile buffers can permeate gap junctions and thus chaperone H^+ ions between coupled cells down a H^+ concentration gradient (234).

5.2 Methods

The extrinsic buffering capacity attributed to the mobile CO_2/HCO_3^- system was calculated from $2.303 \times [HCO_3^-]_i$ as described above, assuming equilibrium (93). The intrinsic buffering capacity, in contrast, must be determined experimentally by imaging cSNARF1-loaded cells upon gradual removal ammonium (weak base, $pK_a = 9.03$) or acetate (weak acid, $pK_a = 4.53$) (235). The gradual removal of ammonium or acetate thus creates a set of step-wise acidifications and alkalinisations, respectively (**Fig 5.2.1**). Cells were superfused with solution containing 40 mM, 20, 10 and 5 mM NH_4Cl

or 80 mM, 40 mM, 20 mM and 10 mM sodium acetate substituted with equimolar amounts of NaCl to keep the osmolarity of the superfusate constant as described previously (**Section 3.7.1**) (235). Ammonium and acetate were used in conjunction in order to obtain intrinsic buffering capacity measurements within a broad-spectrum of pH_i values. A specimen time course of the NH_4Cl removal protocol is shown in **figure 5.3.1**. The step-wise change in superfusate NH_4Cl concentration and corresponding change in pH_i is shown in **figure 5.3.1 Ai** and **Aii**, respectively. The measurements were made in Hepes buffered (CO_2/HCO_3^- free) superfusate to exclude the extrinsic (CO_2/HCO_3^-) buffer system. To assure fast superfusion, experiments were performed in IBIDI chambers (see **section 3.7.2** and **Fig 3.7.2.1 A**). H^+ ion transport by the sodium hydrogen exchanger NHE was blocked with 30 µM 5(*N*-*N*-dimethyl)amiloride (DMA) whereas Cl^-/OH^- exchange was blocked with 50 µM 4,4'diisothiocyano-2,2'-stilbenedisulfonic acid (DIDS). For experiments using ammonium, the intrinsic buffering capacity was estimated by the change in intracellular $[NH_4^+]$ (assumed equal to the change in H^+) and the associated change in pH_i. The intracellular ammonium concentration can be estimated using the Henderson-Hasselbalch equation: $[NH_4^+]_i = [NH_4^+]_e \times 10^{pHe-pHi}$. The intrinsic buffering capacity β_{int} can be estimated by:

$$\beta_{int} = \frac{[NH_4^+]_i^{stop} - [NH_4^+]_i^{start}}{pH_i^{stop} - pH_i^{start}}$$ (235).

Similarly, buffering capacity measurements determined by the acetate removal method can be estimated by:

$$\beta_{int} = \frac{[Acetate^-]_i^{stop} - [Acetate^-]_i^{start}}{pH_i^{stop} - pH_i^{start}}$$

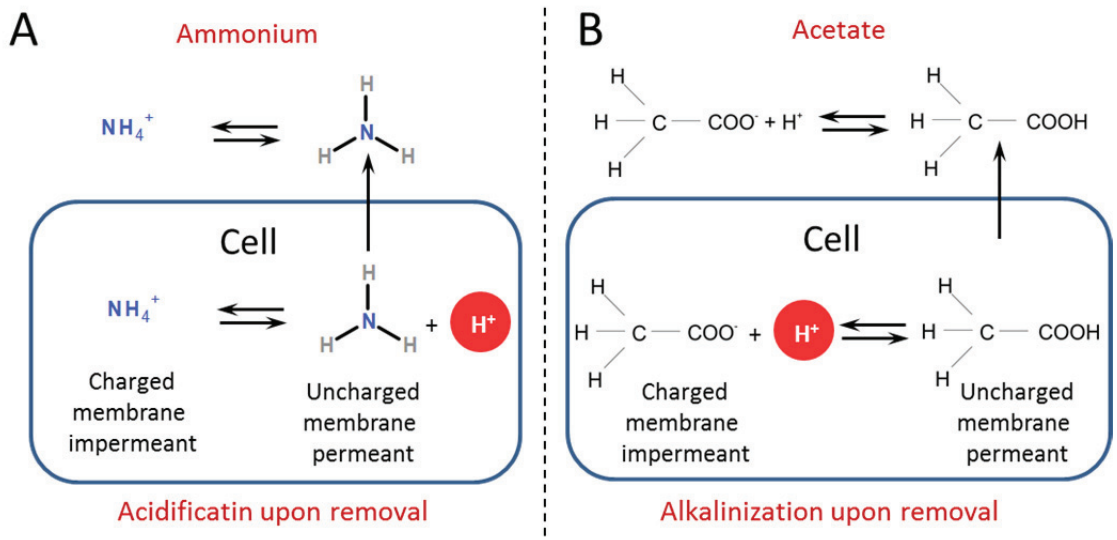


Figure 5.2.1 Mechanism of intracellular pH change upon removal of ammonium and acetate. ***(A)*** *Upon removal of ammonium, a new equilibrium between intracellular and extracellular ammonia (NH_3) is established. Since ammonia is uncharged, it can diffuse across the cell membrane. The diffusion of ammonia across the cell membrane disturbs the intracellular equilibrium of ammonium and ammonia. This leads to a release of H^+ ions into the cytoplasm.* ***(B)*** *Cells placed in an acetate containing solution develop an intracellular equilibrium between acetate and acetic acid. Upon removal of extracellular acetate, the concentration difference in intracellular and extracellular acetic acid leads to diffusion of the membrane permeant acetic acid from the intracellular to the extracellular compartment. Upon the reaction of acetate and H^+ ions to form acetic acid, the cytoplasm alkalinises.*

5.3 Results

Intrinsic buffering capacity was measured in five PDAC cell lines (**Fig 5.3.1 B – F**). In all cell lines, the intrinsic buffering capacity increased upon a decrease in pH_i. This indicates that the majority of intrinsic buffers show H^+ titratable groups with the pK_a in the acidic range. The pH at which the intrinsic buffering capacity is highest indicates the point at which the most abundant buffering moiety shows its ensemble pK_a (203). With a pKa of ~6.5, histidine is likely to be responsible for the majority of H^+ buffering in the acidic range in PDAC cells. The chemical composition of intrinsic buffers was not determined in this study, however.

As seen from **Fig 5.3.1 B – F** the majority of buffering at a normal pH_i of 7.0 – 7.2 was predicted to be mediated by CO_2/HCO_3^-. However, the estimate of CO_2/HCO_3^- buffering capacity, β_c, during rapid acid-base disturbances may be an overestimate as this assumes rapid CO_2 and HCO_3^- equilibrium which applies to a steady-state condition. Equilibrium may be attained in the presence of carbonic anhydrases. The time constant for CO_2 hydration is several seconds (K_h = 0.18 s^{-1}) (236) but it is accelerated by carbonic anhydrases (211).

In BxPC3 cells, the intrinsic buffering capacity was highest at acidic pH_i and decreased when pH_i increased (**Fig 5.3.1 B**). At a pH_i of 6.7, BxPC3 cells showed an intrinsic buffering capacity of 42 mM (**Fig 5.3.1 B,** dark grey). At that pH_i, the CO_2/HCO_3^--mediated buffering capacity was low, resulting in a total buffering capacity of 52 mM (**Fig 5.3.1 B,** light grey). At a pH_i of 7.2 the intrinsic buffering (**Fig 5.3.1 B,**

dark grey) constituted 38% (19mM) of the total buffering capacity of 50 mM, and CO_2/HCO_3^- was the major buffer.

In Colo357 cells, the intrinsic buffering capacity was lowest at alkaline pH and increased at acidic pH, reaching a plateau around pH_i of ~6.4 (**Fig 5.3.1 C,** dark grey). At this acidic pH_i, the intrinsic buffers constituted the majority (86%) of the total buffering capacity of 36 mM (**Fig 5.3.1 C,** light grey). At pH_i of 6.7, the intrinsic buffering capacity (**Fig 5.3.1 C,** dark grey) constituted 73% of the total buffering capacity of 37 mM (**Fig 5.3.1 C,** light grey). Among the five tested PDAC cell lines, Colo357 cells showed the lowest total buffering capacity in the acidic range. At pH_i 7.2, the intrinsic buffering capacity (**Fig 5.3.1 C,** dark grey) was 32% of the total buffering capacity (**Fig 5.3.1 C,** light grey). Thus, intrinsic buffers were dominant in Colo357 cells in the acidic range, whereas CO_2/HCO_3^- buffering dominated at an alkaline pH_i.

In MiaPaCa2 cells, the intrinsic buffers provided 79% of the total buffering power of 48 mM at pH_i 6.7 (**Fig 5.3.1 D,** dark and light grey, respectively). At pH_i 7.2, the intrinsic buffering capacity was reduced to 30% of the total buffering capacity. At alkaline pH_i, CO_2/HCO_3^- buffering was dominant.

In AsPC1 cells, the intrinsic buffers contributed to 80% of the total buffering capacity at pH_i 6.7 (**Fig 5.3.1 E**). At pH_i 7.2, AsPC1 cells showed an intrinsic buffering capacity of 20 mM, giving rise to a total buffering capacity of 51 mM.

In PANC-1 cells, the intrinsic buffering capacity constituted 76% of the total buffering capacity at an acidic pH_i of 6.7 (**Fig 5.3.1 F**). At pH_i 7.2, the intrinsic buffering capacity was further reduced to 30% of the total buffering capacity of 46 mM.

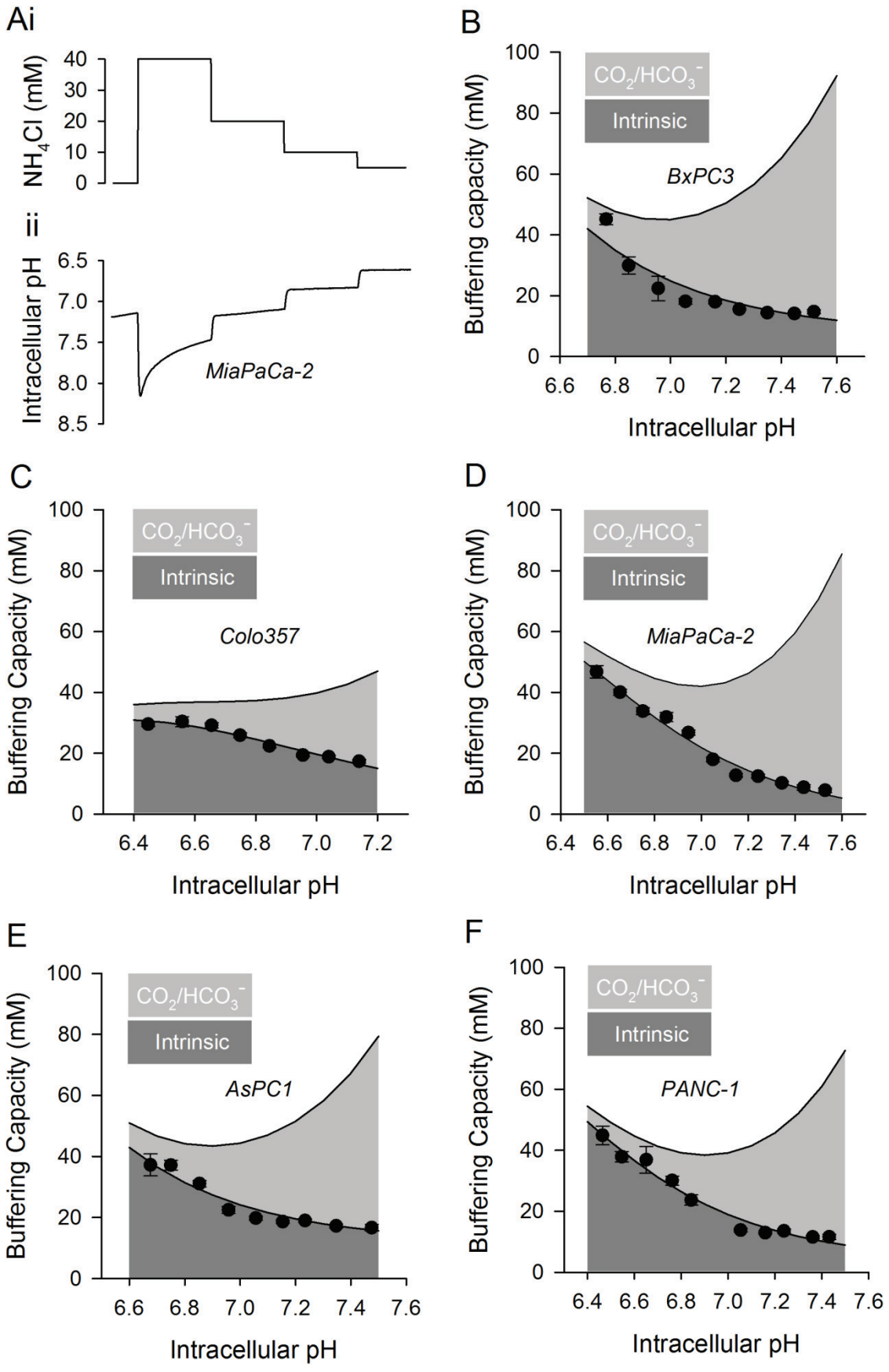

Ai
NH_4Cl (mM)
40
30
20
10
0
ii
Intracellular pH
6.5
7.0
7.5
8.0
8.5
MiaPaCa-2
B
Buffering capacity (mM)
100
80
60
40
20
0
CO_2/HCO_3^-
Intrinsic
BxPC3
6.6
6.8
7.0
7.2
7.4
7.6
Intracellular pH
C
Buffering Capacity (mM)
Colo357
6.4
6.6
6.8
7.0
7.2
Intracellular pH
D
Buffering Capacity (mM)
MiaPaCa-2
6.4
6.6
6.8
7.0
7.2
7.4
7.6
Intracellular pH
E
Buffering Capacity (mM)
AsPC1
6.6
6.8
7.0
7.2
7.4
7.6
Intracellular pH
F
Buffering Capacity (mM)
PANC-1
6.4
6.6
6.8
7.0
7.2
7.4
7.6
Intracellular pH

Figure 5.3.1 Measuring intrinsic buffering capacity. (Ai) *Time course of the ammonium concentration in the superfusate (top) and intracellular pH (pH_i; bottom) during the ammonium removal protocol. (**Aii)** Time course of the intracellular measured in a MiaPaCa2 monolayer superfused with Hepes-buffered CO_2/HCO_3^--free solution containing NH_4Cl, as indicated in (Ai). All solutions were kept at 300mOsm/kg via the isosmotic replacement of NH_4Cl with NaCl. The pH_i of MiaPaCa2 cells showed a rapid step-wise acidification concomitant with NH_4Cl removal. The intrinsic buffering capacity was inversely proportional to the ΔpH_i elicited by NH_4Cl removal. **(B)** BxPC3 cells. The intrinsic (dark grey, measured) and extrinsic CO_2/HCO_3^- mediated buffering capacity (light grey, calculated) as a function of pH_i. Each data point represents a mean ± SEM of 20 – 35 cells measured by acetate and ammonium removal. All intrinsic buffering capacity measurements were best-fitted. The CO_2/HCO_3^--mediated buffering capacity was calculated using the Henderson-Hasselbalch equation, $\beta_c = 2.303 \times [HCO_3^-]_i$ under the assumption of equilibrium between CO_2 and HCO_3^-. **(C)** Intrinsic (dark grey) and CO_2/HCO_3^- mediated (light grey) buffering capacity in Colo357 cells. **(D)** Intrinsic (dark grey) and CO_2/HCO_3^- mediated (light grey) buffering capacity in MiaPaCa-2 cells. **(E)** Intrinsic (dark grey) and CO_2/HCO_3^- mediated (light grey) buffering capacity in AsPC1 cells. **(F)** Intrinsic (dark grey) and CO_2/HCO_3^- mediated (light grey) buffering capacity in PANC1 cells.*

5.4 Summary of findings

- The majority of intracellular pH buffering in the physiological range of pH_i is due to CO_2/HCO_3^- under equilibrium conditions.
- The role of intrinsic buffers, relative to CO_2/HCO_3^-, increases at lower pH_i.

- The largest differences in the total buffering capacity among PDAC cell lines were observed at acidic pH_i, due to differences in intrinsic buffering, which is mainly determined by levels of protein expression.
- At pH_i of 6.7 and 7.2, the total buffering capacity decreased in the order: BxPC3 > MiaPaCa2 > AsPC1 > PANC1 > Colo357 and AsPC1 > BxPC3 > Colo357 > MiaPaCa2 ≈ PANC1, respectively.

6 CO_2/HCO_3^- HANDLING BY CARBONIC ANHYDRASES IN PDAC CELL LINES

Objective: To assess the functional activity of intracellular and exofacial carbonic anhydrases in PDAC cells, and address their role in and contribution to CO_2/HCO_3^- transport across three-dimensional diffusionally-restricted tissue growths.

6.1 Background

Carbonic anhydrases facilitate the chemical equilibration of CO_2/HCO_3^- (89, 211). As seen in **figure 5.3.1**, CO_2/HCO_3^- may be the most prominent cytoplasmic buffer within the neutral and alkaline range, provided the rate of CO_2 and HCO_3^- equilibrium is adequately fast. Due to the role of carbonic anhydrases in facilitating CO_2/HCO_3^- buffering, their inhibition may affect tumour pH and metabolism and could impede tumour growth and survival (42, 101, 211). Fifteen carbonic anhydrase isoforms have been identified in humans, differing in enzymatic activity, expression level and subcellular localisation (cytosolic, transmembrane, mitochondrial matrix associated and secreted) (211). The transmembrane CAIX and CAXII isoforms are upregulated by hypoxia (237) and have been heavily associated with cancer and poor prognosis (238-241). In contrast, low levels of the cytosolic CAII were linked with poor prognosis in pancreatic cancer in one study (242). This chapter seeks to elucidate the activity of carbonic anhydrases in PDAC cells and the roles they may play in facilitating CO_2 diffusion and H^+ venting in PDAC tumour growths.

6.2 Results

6.2.1 Expression profiling for carbonic anhydrase coding genes in PDAC cells

Introduction. To identify the carbonic anhydrase isoforms relevant to PDAC, mRNA expression microarray data were examined for expression of the fifteen CA isoforms.

Methods. A previously-published mRNA microarray dataset assessing 22 PDAC cell lines derived from either the primary tumour or metastases (243) was assessed for the expression of carbonic anhydrases encoding genes (**Fig 6.2.1.1**). The mRNA expression data were then categorised according to subcellular localisation.

Results. As seen in **figure 6.2.1.1 A**, the *CA2* gene was the most prominently expressed cytosolic isoform, whereas *CA9* and *CA12* expression dominated among the membrane associated isoforms. Based on differential gene expression of *CA2*, *CA9* and *CA12*, the cell lines AsPC1, MiaPaCa2, Colo357, PANC1 and BxPC3 were selected for further analysis (**Fig 6.2.1.1 B**). The gene expression of *CA2* decreased in the order of Colo357 > PANC1 > BxPC3 > MiaPaCa2 > AsPC1. Expression of the membrane-associated *CA9* and *CA12* ranked from AsPC1 > PANC1 ≈ Colo357 ≈ BxPC3 ≈ MiaPaCa2 and AsPC1 > BxPC3 > Colo357 ≈ MiaPaCa2 > PANC1 respectively.

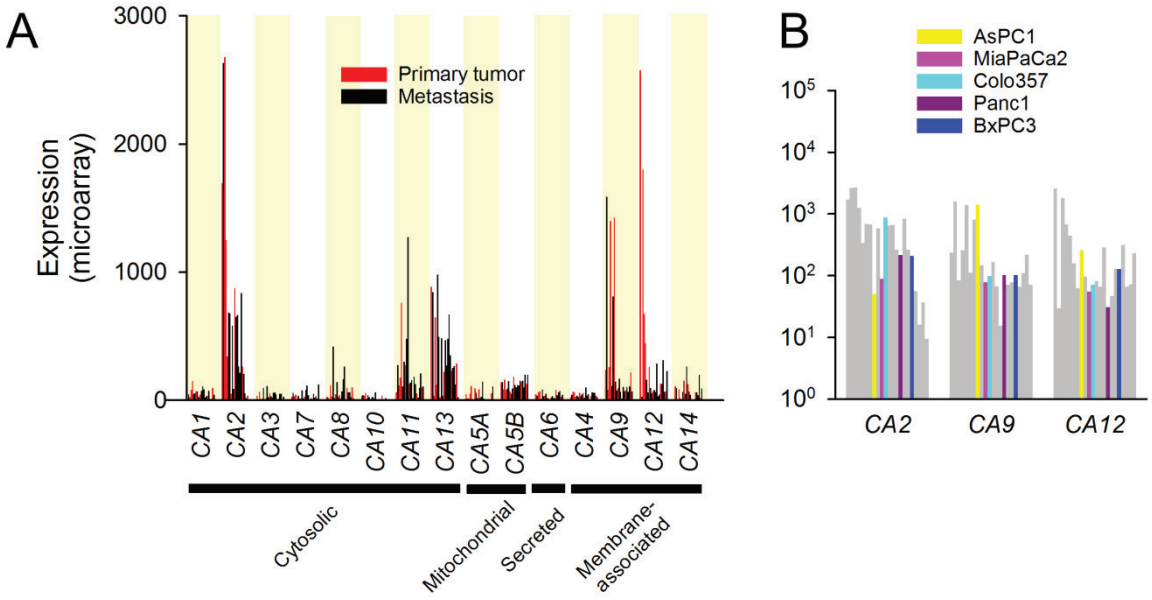


Figure 6.2.1.1 Gene expression of carbonic anhydrase isoforms in pancreatic ductal adenocarcinoma (PDAC) cell lines. ***(A)*** *mRNA microarray data of the expression of genes coding for carbonic anhydrase isoforms in 22 PDAC cell lines (BioGPS dataset: E-GEOD-216544). The PDAC cell lines were derived from primary tumours (red) or metastases (black). Gene expression was categorised according to histological localisation of the encoded protein (cytosolic, mitochondrial matrix, secreted and plasma membrane-associated).* ***(B)*** *Expression data for CA2, CA9 and CA12 replotted on a logarithmic scale highlighting the cells used in the present study (AsPC1, MiaPaCa2, Colo357, PANC1 and BxPC3).*

6.2.2 Immunoreactivity for carbonic anhydrase isoforms in PDAC cells

Introduction. The mRNA expression levels presented in **Fig 6.2.1.1** suggest that CAII is the most prominent cytosolic isoform in PDAC cells, whereas CAIX and CAXII may represent the most common extracellular membrane associated CA isoforms. As protein level may not be proportional to mRNA expression, the protein levels of carbonic anhydrases were assessed by immunoblotting in the 5 cell lines highlighted in

Fig 6.2.1.1 B (AsPC1, MiaPaCa2, Colo357, PANC1 and BxPC3). The Capan1 PDAC cell line not encompassed in the microarray dataset was included in the analysis of CA protein levels. Hypoxic signalling has been found to upregulate the expression of the membrane associated CAIX and CAXII. Due to the tight hypoxic regulation of CAIX, it has been used as a marker of hypoxia.

Methods. Cells monolayers were grown in 6 cm petri dishes and treated for 48 h with either DMSO (normoxia, control), 2% O_2 hypoxia or 1 mM DMOG to chemically induce hypoxic signalling (described in **section 3.6**) (68). Hypoxic conditions were attained upon incubation in a hypoxic chamber (New Brunswick) controlling the O_2 levels by infusion of nitrogen gas. Whole cell lysates of confluent monolayers were prepared in RIPA buffer. Protein was separated by SDS polyacrylamide gel electrophoresis at 55 µg total protein per lane prior to western blotting.

Results. The cytosolic isoform, CAII, was expressed in AsPC1 cells (**Fig 6.2.2.1**) confirming the microarray result (**Fig 6.2.1.1**). The protein level was attained during incubation in hypoxia and DMOG (**Fig 6.2.2.1**). Capan1 cells showed low levels of CAII in normoxia and CAII up-regulation under hypoxia but DMOG incubation was not sufficient to attain a CAII up-regulation similar to that found under hypoxia in Capan1 cells. CAII was not detected in BxPC3, Colo357, MiaPaCa2 or PANC1 cell lines. The protein levels of CAII thus showed no correlation with mRNA expression. Although mRNA levels of *CA2* were expressed in all five tested cell lines (AsPC1, MiaPaCa2, Colo357, PANC-1 and BxPC3) mRNA levels were lowest in AsPC1 cells which exhibited the highest amounts of protein expression (**Fig 6.2.1.1** and **6.2.2.1**).

The protein level of the exofacial membrane-associated carbonic anhydrase isozyme CAIX was assessed in PDAC cells. Colo357 cells showed high normoxic and hypoxic CAIX levels. Upon immunoblotting, CAIX gives rise to two bands of ~54 and ~58 kDa (244). CAIX was expressed under normoxic conditions in AsPC1 and Colo357 cells (photographic exposure of 15 s) but incubation in hypoxia or DMOG resulted in highly up-regulated CAIX levels in both cell lines. DMOG up-regulated CAIX to a level similar to that found in hypoxic incubation in both AsPC1 and Colo357 cells. BxPC3 and Capan1 cells showed absence of CAIX in normoxia, but exhibited high levels of CAIX after incubation in both hypoxia and DMOG. DMOG up-regulated CAIX protein levels to a higher extent than those under hypoxia in BxPC3 cells and to a lower extent than those under hypoxia in Capan1 cells. CAIX levels were undetectable in the MiaPaCa2 and PANC1 cell lines; therefore CAIX should not be used as a hypoxic marker within these PDAC cell lines.

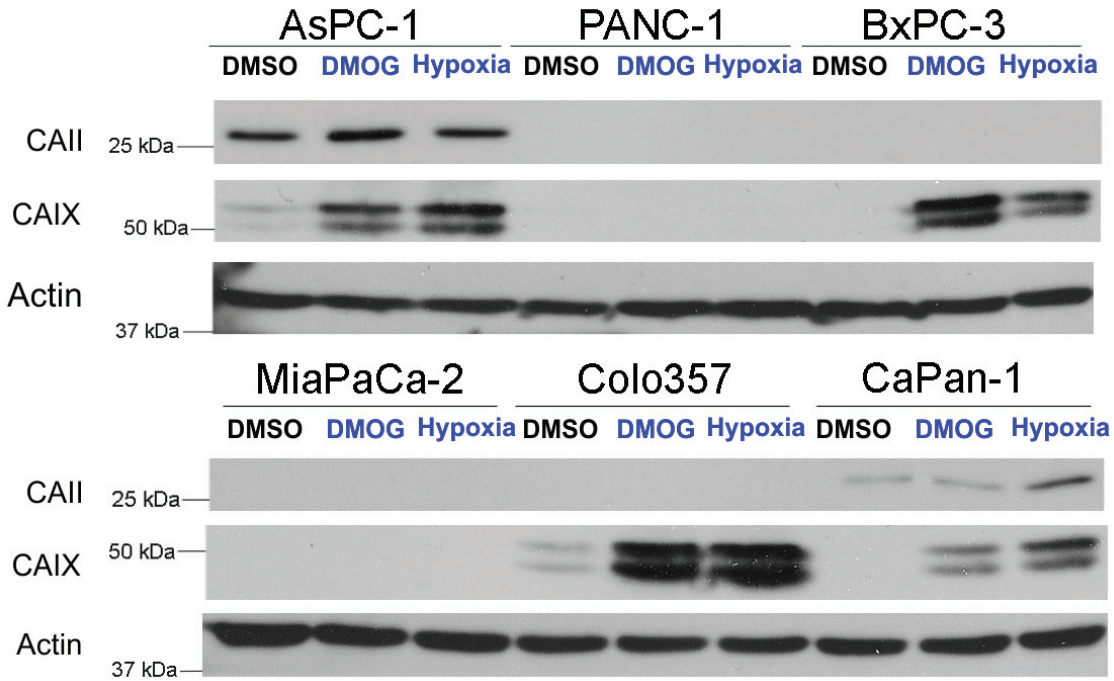


Figure 6.2.2.1 Protein levels of carbonic anhydrase (CA) isozymes in pancreatic ductal adenocarcinoma (PDAC) cell lines. *Western blots showing protein levels of the cytosolic CAII isoform which exhibited the highest mRNA expression among the cytosolic CAs in PDAC cell lines and the exofacial membrane-associated carbonic anhydrases CAIX. Protein levels were assessed in lysates of monolayers grown under normoxic control conditions (DMSO), chemically-induced hypoxia in 1 mM DMOG (48h) or 2% O_2 hypoxia (48 h). Actin was applied as a loading control. N = 3.*

6.2.3 Activity of intracellular carbonic anhydrase isoforms in PDAC cells

Introduction. Carbonic anhydrases (CAs) can differ in the subcellular localisation of their active site (cytosolic or extracellular), and can thus affect CO_2 and HCO_3^- levels differently in different subcellular compartments. The intracellular CA activity can be derived from cytosolic isoforms or membrane-associated isoforms with active sites facing the cytosol (245). Intracellular CA activity may therefore be important for rapid CO_2 and HCO_3^- equilibration, and could possess further importance in cancerous tissue upholding an increased metabolism. This would increase the need for intracellular CO_2- and HCO_3^--mediated buffering, and facilitation of H^+ venting in actively-respiring and excessively growing cancer cells. Pancreatic cancer patients with a high expression of the cytosolic CAII isoform show an increased survival compared to patients with a low CAII expression (242) and recent evidence suggests that low intracellular CA activity protects cancer cells from undesirable pH_i changes induced by fluctuating levels of CO_2, which can occur upon intermittent (acute) hypoxia due to irregular blood flow through the tumour (41). This type of hypoxia develops in areas of limited capillary perfusion. It is transient and differs from the chronic hypoxia that develops upon cancer cell growth past the O_2 diffusion-limit. Under such circumstances of repetitive transient changes in CO_2 levels, high intracellular CA levels lead to changes in pH_i that affect cellular growth through inhibition of the mTORC pathway (246).

Methods. Cells were pretreated with DMSO (control, normoxia) or 1mM DMOG for 48 h to chemically induce hypoxic signalling. Cells were loaded with cSNARF1 for 5

min to allow pH_i measurements upon confocal imaging and then superfused at 37°C with Hepes normal Tyrode buffer (CO_2/HCO_3^--free, pH 7.4) in IBIDI chambers to promote instantaneous change in superfusate solution. The change in pH_i which occurred upon a rapid switching to superfusion to 5% CO_2/22 mM HCO_3^- was used to measure the CO_2 hydration rate (**Fig 6.2.3.1** and **6.2.3.2**).

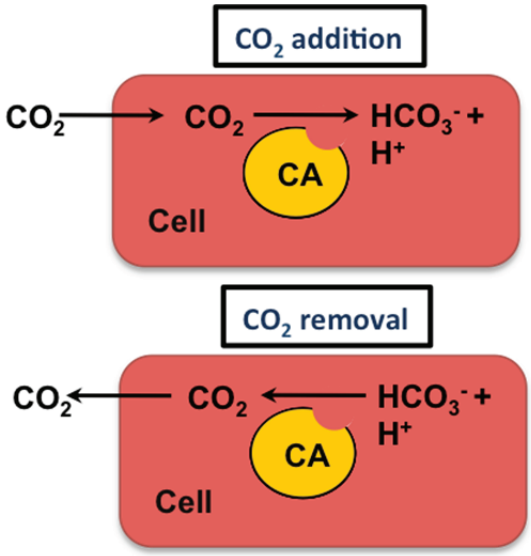


Figure 6.2.3.1 Principles of measuring intracellular carbonic anhydrase activity upon CO_2 addition and removal. *Upon changing the superfusate of cells bathed in Hepes-buffered (CO_2/HCO_3^--free) superfusate to CO_2-buffered superfusate, CO_2 will enter cells. This will present CO_2 to CA_i as a substrate and elicit the catalysis of CO_2 hydration. Measuring the rise in H^+ ion concentration using intracellular pH indicators can indicate the rate of the reaction. The intracellular carbonic anhydrase-catalysed reaction can then be normalised to the spontaneous rate, which can be measured upon chemical inhibition of CA activity.*

The spontaneous rate of CO_2 hydration was measured from the rate of pH_i change evoked by a similar protocol performed in the presence of the broad-spectrum cell-permeable CA inhibitor acetazolamide (ATZ) (211). A pulse of 40 mM NH_4Cl (in Hepes-buffered Tyrode pH 7.4) that elicited a rapid intracellular alkalinisation upon NH_3 entry and equilibration with NH_4^+ confirmed the rapid solution exchange (i.e. to exclude the possibility that slow pH changes are due to slow solution exchange). All solutions were prepared isosmotically at 300 mOsm/kg (see **Section 3.7.1**).

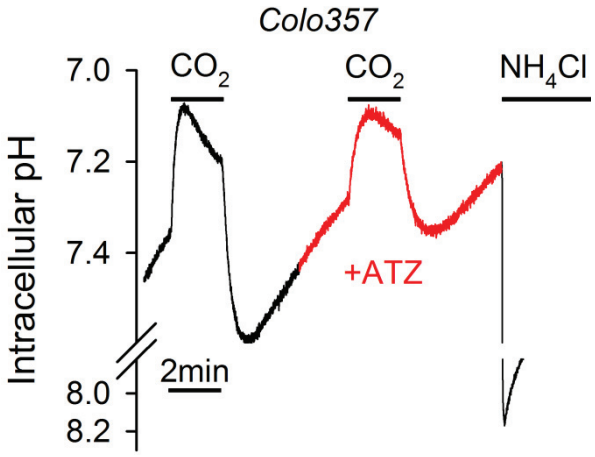


Figure 6.2.3.2 Protocol for measuring intracellular carbonic anhydrase (CA) activity in situ in intact cells. *Intracellular pH was reported via confocal imaging of cSNARF1 fluorescence in pancreatic ductal adenocarcinoma cell monolayers. The rate of CO_2 hydration was measured upon rapid change in superfusion from Hepes-buffered (CO_2/HCO_3^--free) superfusate to 5% CO_2/ 22mM HCO_3^- solution (indicated by CO_2 bars). CA catalytic activity was inferred from the rate of CO_2 hydration relative to the spontaneous CO_2 hydration rate measured in the presence of the broad-spectrum CA inhibitor acetazolamide (ATZ) (red trace). Rapid superfusion change was attained by superfusion in an IBIDI 30 µl chamber. Addition of NH_4Cl serves as a control to assure that the rate of superfusate change exceeds the rate of CA-catalysed CO_2 hydration.*

Results. Intracellular CA (CA_i) activity differed among the PDAC cell lines in the order: AsPC1 > PANC1 > Colo357 > BxPC3 > MiaPaCa2 (**Fig 6.2.3.3**). The CA catalysed CO_2 hydration was 10-fold faster than the spontaneous reaction. The cytosolic CAII protein levels detected in AsPC1 cells (**Fig 6.2.2.1**) was putatively responsible for the observed CA_i activity. PANC1 cells showed intermediate levels of CA_i activity, despite the absence of CAII protein levels. The CA_i activity in PDAC cells may be caused by the presence of other cytosolic CA proteins, such as CAXI and CAXIII detected in PDAC cell lines (**Fig 6.2.1.1**). The CA_i activity was low in Colo357 and BxPC3, cells and negligible in MiaPaCa2 cells. To test if hypoxia affects CA_i activity, cells were treated with DMOG to chemically induce hypoxic responses. MiaPaCa2 cells showed a significant increase in CA_i activity whereas no significant change was observed in the remaining cell lines.

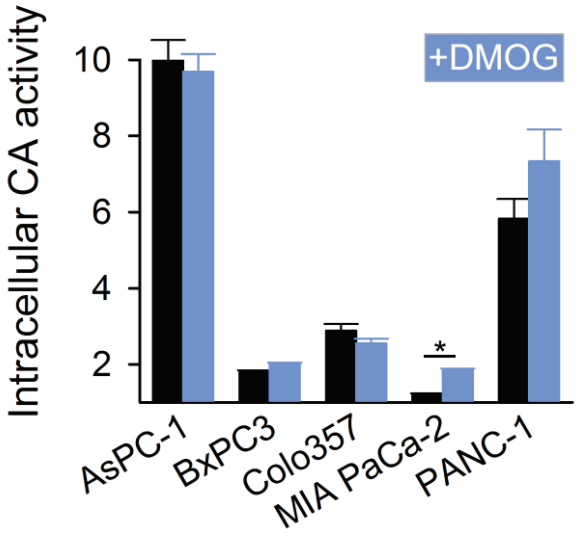


Figure 6.2.3.3 Measurement of intracellular carbonic anhydrase activity in situ. *Intracellular carbonic anhydrase activity was measured based on pH_i changes that occurred upon changing from Hepes-buffered superfusate (pH 7.4) to 5% CO_2/22 mM HCO_3^--buffered medium, eliciting intracellular CO_2 hydration (see **Fig 6.2.3.2**). The fold increase in CO_2 hydration compared to the spontaneous reaction measured in the presence of 100 µM acetazolamide was quantified in*

paired experiments. Cells were pre-treated for 48h with DMSO (control) or 1mM DMOG to chemically stabilise hypoxic signalling. N = 3 (67 – 148 cells).

6.2.4 Activity of exofacial carbonic anhydrase isoforms in PDAC monolayers

Introduction. Membrane-bound carbonic anhydrases (CAs) with an exofacially-located active site, such as CAIX and CAXII, have been associated with poor prognosis and hypoxia in many cancers. Exofacial CA (CA_e)-catalysed hydration of CO_2 may facilitate the venting of CO_2 from actively respiring cells. In addition, it provides substrate for sodium bicarbonate cotransporters and thus facilitates H^+ venting from cells. Exofacial CAs have been found to facilitate the diffusion of acids across the extracellular space of tissue growths, and thus assist pH_i regulation in cells particularly in hypoxic regions of a tissue structure, where diffusion is restricted (229).

Methods. The CA_e catalytical activity was measured in membrane regions of PDAC cells loaded with the H^+-sensitive pH fluorophore fluorescein-conjugated wheat germ agglutinin (WGA) for 10 s. WGA binds to the extracellular cell membrane, allowing local pH measurements based on fluorescein fluorescence. Monolayers were superfused with 5% CO_2/11mM HCO_3^- buffer (pH 7.2) at 37°C in IBIDI chambers to allow instantaneous change of superfusate. Note that a modestly acidic superfusate (pH 7.2, instead of pH 7.4) was used because the dye has a pK_a close to 6.5, and thus only shows a limited resolving power at pH 7.4. The CA_e-catalysed reaction was triggered by change to 30 mM NH_4Cl containing superfusate. The rapid cellular NH_3 entry evokes a local NH_4^+ deprotonation at the extracellular surface of the cell membrane via the reaction $NH_4^+ \rightarrow NH_3 + H^+$. This reaction is transient until a new

equilibrium is established (**Fig 6.2.4.1**). The H^+ ions released at the cell surface are a substrate for the CA_e-catalysed reaction and thus gauges the activity of CA_e. The experimental protocol for measuring CA_e-catalysed pH_e transients is shown in **figure 6.2.4.2**.

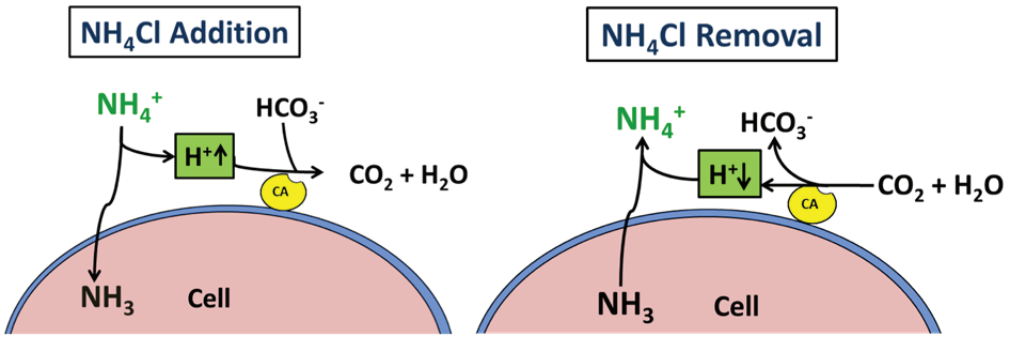


Figure 6.2.4.1 Mechanism of exofacial carbonic anhydrase activity measurements via the ammonium prepulse method. *Exofacial membrane-tethered CAs catalyse the reversible reaction of CO_2 hydration into H^+ and HCO_3^-. The addition of NH_4Cl to cells induces a local release of H^+ ions due to the diffusion of uncharged NH_3 across the cell membrane. The entry of NH_3 disturbs the NH_3 - NH_4^+ equilibrium on the cell surface and drives the reaction $NH_4^+ \rightarrow NH_3 + H^+$. The local rise in H^+ concentration gauges the CA activity, since H^+ ions are a substrate for CAs. A high CA activity will accelerate H^+ removal (via reaction with HCO_3^-) and thus dampen the observed pH_e response that can be measured with the H^+-sensitive fluorophore fluorescein coupled to wheat germ agglutinin, which binds to the extracellular cell membrane.*

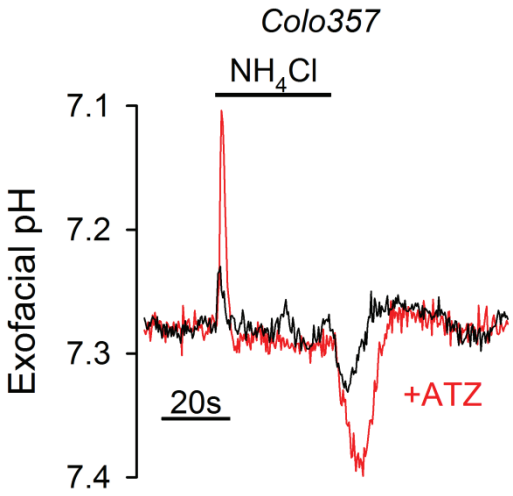


Figure 6.2.4.2 Protocol for measuring exofacial carbonic anhydrase activity in situ. *Extracellular surface membrane pH_e was reported using the proton-sensing fluorophore fluorescein coupled to wheat germ agglutinin, which bound to the extracellular cell membrane. Cells were superfused with low bicarbonate buffered solution (5% CO_2/11 mM HCO_3^-)*

Results. Under normoxic conditions, CA_e activity in PDAC cell lines decreased in the order: Colo357 > MiaPaCa2 > BxPC3 > AsPC1 > PANC1 and was negligible in PANC1 cells (**Fig 6.2.4.3**). The high normoxic CA_e activity in Colo357 is in agreement with the detection of CAIX protein in normoxia (**Fig 6.2.2.1**). Preincubation of cells with 1 mM DMOG for 48 h prior to the experiment, to chemically stimulate hypoxic signalling, led to an increase in CA_e activity in Colo357, BxPC3 and AsPC1 cells and a decrease in CA_e activity in MiaPaCa2 cells (**Fig 6.2.4.3**). The increase in CA_e activity in Colo357, BxPC3 and AsPC1 cells is likely attributed to the increase in CAIX protein levels that occurred after 48 h preincubation with 1mM DMOG observed in **figure 6.2.2.1**. Preincubation of PANC1 cells with 1 mM DMOG for 48 h had no effect on CA_e (**Fig 6.2.4.3**). Although the normoxic CA_e activity (**Fig 6.2.4.3**) did not directly correlate with CAIX protein levels (**Fig 6.2.2.1**), the increase in CAIX protein levels in DMOG-treated Colo357, BxPC3 and

AsPC1 cells (**Fig 6.2.2.1**) amounted to an increase in CA_e activity after 48 h preincubation with 1 mM DMOG, despite to differing levels (**Fig 6.2.4.3**).

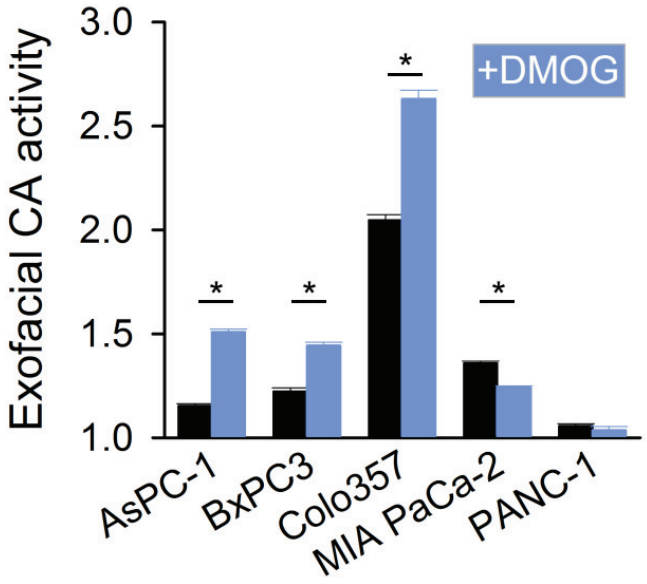


Figure 6.2.4.3 Measurement of exofacial carbonic anhydrase (CA_e) activity in situ. *The exofacial CA activity (CA_e) measured based on surface membrane H^+-changes upon NH_4Cl addition experiments. Measurements are expressed as fold increase in CA_e-catalysed CO_2 hydration rate, normalised to the spontaneous reaction. CA_e activity was measured in cells treated for 48 h with DMSO (control) or 1mM DMOG (chemically induced hypoxic signalling). Bars represent mean ± SEM of membrane regions from > 50 cells. N =3.*

6.2.5 Activity of exofacial carbonic anhydrase isoforms in Colo357 spheroids

Introduction. In cell monolayers, the measurement of CA_e activity is restricted to the extracellular volume in contact with the cell surface onto which WGA-fluorescein is tethered. Upon increasing distance from the surface membrane, the

catalytic effect of CA_e activity declines. In tissue structures, the cellular mass can occupy more than half of the volume (84). This will create an extracellular environment of limited diffusivity, within which membrane-tethered CA_e provides catalytic activity. In order to recapitulate the features of restricted diffusion and measure the CA_e activity in the enclosed extracellular compartment in which exofacial CAs function, the CA_e activity was measured in spheroids. Colo357 spheroids were chosen for three-dimensional spheroid growth due to their high CA_e activity in monolayers.

Methods. Spheroids were formed via the hanging drop method, using 400 Colo357 cells per drop (See **Section 3.3**). CA_e activity was measured in the extracellular compartment of spheroids using the ammonium prepulse method (**Fig 6.2.4.1**). Extracellular changes in pH were reported by superfusing the spheroid extracellular space with solution containing membrane-impermeant fluorescein sulfonic acid (**Section 3.9.2**). The fluorescein sulfonic acid thus reports pH in the extracellular compartment of spheroids. Superfusates were buffered with 5% CO_2/11 mM HCO_3^- producing a pH of 7.2 (instead of pH 7.4) because fluorescein has an apparent pK_a close to 6.5, and would have weaker resolving power at the physiological extracellular pH of 7.4. The CA catalysed reaction was stimulated by addition or removal of 30 mM NH_4Cl. Similarly to the ammonium prepulse in monolayers, addition of NH_4^+ to monolayers will lead to a release of H^+ ions in the extracellular space. The size of ensuing pH_e transients provides a measure of CO_2/HCO_3^- buffering and the degree to which CA_e catalyses this.

Results. Extracellular fluorescein sulfonic acid (FS_e) fluorescence was measured and averaged in 10 concentric regions of interest (**Fig 6.2.5.1 A**, insert). The CA_e-

catalysed reaction was measured upon NH_4Cl addition and normalised to the spontaneous reaction under CA inhibition using 100 µM ATZ. Inhibition of carbonic anhydrases by ATZ led to larger pH_e transients in comparison to control conditions (CA active). This confirmed CA_e catalytical activity in the extracellular compartment of spheroids. With increasing depth, the effect of CA_e inhibition on pH_e transients became more pronounced, indicating that equilibration of the CO_2/HCO_3^- buffering system became increasingly dependent on enzymatic activity (**Fig 6.2.5.1 A**, red trace), compared to that in the outermost region (**Fig 6.2.5.1 A**, black trace). The average CA_e-catalysed reaction throughout the spheroid was accelerated 1.58 ± 0.11 times compared to the spontaneous rate of the reaction (**Fig 6.2.5.1 B**). This corresponds to a $k_h = 0.28\ s^{-1}$ ($1.58 \times 0.18\ s^{-1}$ (246)) which was smaller than the k_h measured in Colo357 monolayers.

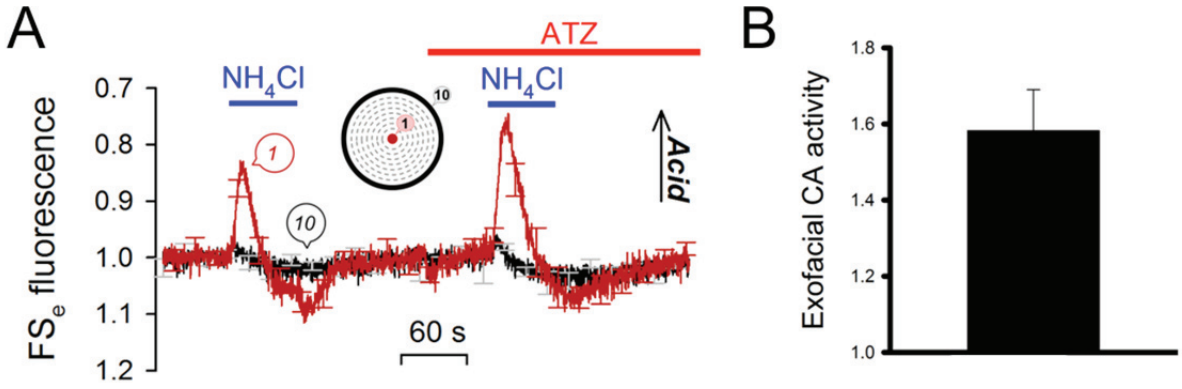


Figure 6.2.5.1 Exofacial carbonic anhydrase (CA_e) activity in spheroids. (A) *Spheroids were superfused with 5% CO_2/11 mM HCO_3^-. The CA_e-catalysed reaction was evoked upon the release of its H^+ substrate by changing superfusion to a 30 mM NH_4Cl-containing solution (blue bars). Extracellular fluorescein sulfonic acid (FS_e) fluorescence was used to indicate the release of acid upon NH_4Cl addition (pH_e). The CA_e-catalysed reaction was normalised to the*

spontaneous reaction measured in the presence of 100 µM of the broad-spectrum CA inhibitor acetazolamide (ATZ; red bar). The CA_e activity was measured in 10 concentric rings of $1/10^{th}$ of the spheroid radius, throughout the spheroid (indicated in insert). The change in FS_e fluorescence is shown in the first and innermost region of the spheroid (red trace) and the outermost 10th spheroid layer (black trace). ***(B)*** *CA_e catalytical activity measured by the ammonium prepulse method in spheroids was expressed as fold increase of CA_e catalysis, compared to the spontaneous rate (ATZ). N = 3 (average of 10 spheroids).*

6.2.6 Diffusive tortuosity imposed by extracellular space in Colo357 spheroids

Introduction. In water, HCO_3^- ions and CO_2 diffuse rapidly, with diffusion coefficients of 1800 and 2500 $\mu m^2/s$, respectively (87). In tissue, however, the presence of cells can impede diffusion (87). To assess the diffusivity of CO_2 and HCO_3^- ions in tissue growths, the relative proportion of intracellular and extracellular volume was estimated. Such a ratio can be used to estimate the hindrance to diffusion exerted by the tissue structure.

Methods. The ratio of the intracellular vs. extracellular space of spheroids was measured in Colo357 spheroids grown to a radius of ~110 ± 5 µm as described in **section 3.3**. The intra- vs. extracellular ratio was estimated by assessing the degree to which diffusion of fluorescein sulfonic acid (FS) was reduced by spheroid cell mass as compared to its diffusion in water. The relation of FS diffusion in spheroids vs. water expresses the tortuosity of the spheroid imposed by cells, and can thus estimate the ratio of intra- and extracellular volume. As FS is membrane-impermeant, it will diffuse only through the extracellular compartment of the spheroids. Spheroids were

superfused in Hepes buffer (pH 7.4) and rapidly switched to superfusate containing 30 μM FS. FS fluorescence was measured and average in 10 concentric regions throughout the spheroid. The diffusion coefficient of FS in spheroids was estimated from time delays at half-maximal fluorescence upon best-fitting to the experimental data as previously described. The best-fits (**Fig 6.2.6.1 A,** light grey) of the fluorescence in the outermost region (**Fig 6.2.6.1 A,** black) and inner-most region (**Fig 6.2.6.1 A,** red) were used to calculate the FS diffusion coefficient in spheroids.

Results. Addition of FS to Colo357 spheroids resulted in a delay in half-maximal fluorescence of several seconds in the core (**Fig 6.2.6.1 A)**. The FS diffusion coefficient in Colo357 spheroids was estimated to be 192 ± 13 $\mu m^2/s$. Since the diffusion coefficient of FS in water at 37°C is 621 $\mu m^2/s$ (87), the spheroids imposed a ~70% reduction of diffusivity. This implies that ~70% of the Colo357 spheroid mass was composed of cell mass, thus leaving ~30% to the extracellular space. These tortuosity measurements therefore suggest that the majority of the spheroid volume is attributable to the intracellular compartment.

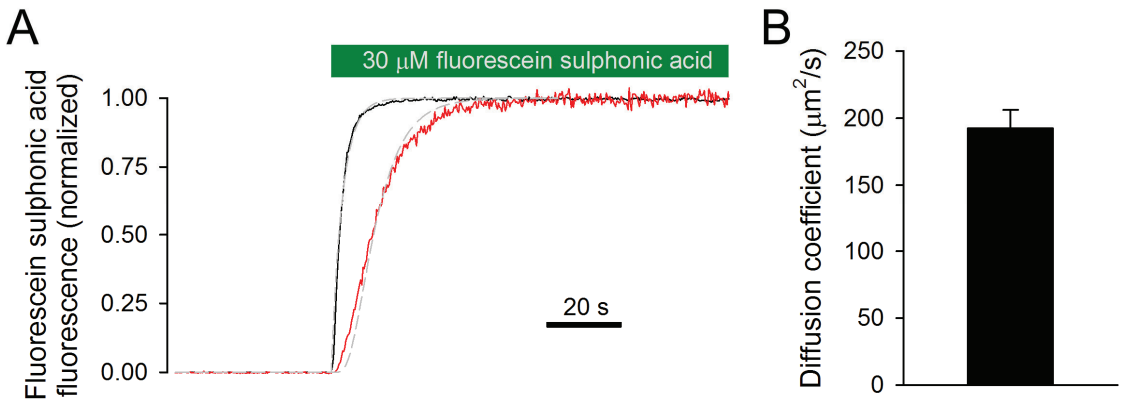


Figure 6.2.6.1 Measurement of the diffusive tortuosity imposed by the extracellular space in Colo357 spheroids. ***(A)*** *Colo357 spheroids of 110 ± 5 µM were superfused with Hepes buffered superfusate (pH 7.4, 37℃) and subjected to 30 µM fluorescein sulfonic acid (FS; green bar). FS fluorescence was normalised to absence (0) and maximal fluorescence (1.00). The fluorescence was measured in the innermost region (red, radius =11 µm) and outermost region of the spheroid (black, width = 11 µm). The modelled best fit to the curve is indicated in light grey.* ***(B)*** *The FS diffusion coefficient in Colo357 spheroids measured upon FS addition to spheroids. The diffusion coefficient was lowered by ca. 70% relative to its diffusion coefficient of 621 µm²/s in water. N = 9.*

6.2.7 CO_2 diffusion across Colo357 spheroids

Introduction. Due to the membrane-permeable gaseous nature of CO_2, it can diffuse through both intracellular and extracellular compartments. As described previously (**Chapter 5**), the equilibration of CO_2 and HCO_3^- is important for the H^+ ion buffering in cells. However, as CO_2 is a metabolic acid produced upon aerobic respiration, it must be vented from tissues. In order to determine the diffusivity of CO_2 across tissue, Colo357 spheroids showing both intracellular and exofacial CA activity

(**Fig 6.2.3.3** and **Fig 6.2.5.1**) were subjected to pulses of CO_2 pulse as previously described (**Fig 6.2.3.1**).

Methods. Colo357 spheroids were grown as previously described (**section 3.3**) and loaded with cSNARF1 to allow measurement of pH_i. Spheroids were superfused in Hepes-buffered (CO_2/HCO_3^- free) superfusate that was rapidly changed to 5% CO_2/22 mM HCO_3^- buffered superfusate. The progress of CO_2 diffusion was reported by changes in pH_i upon CO_2 hydration and measured in 10 concentric regions of the size of $1/10^{th}$ of the spheroid radius. The spontaneous rate of CO_2 hydration was inferred from the pH_i change upon CO_2 hydration under CA inhibition by ATZ. To ensure that the superfusion exchange was not the rate-limiting step in the observed reaction, a pulse of 20 mM NH_4Cl was added at the end of each experiment.

Results. The addition of CO_2 to spheroids led to a rapid decrease in pH_i in the periphery of the spheroids, explained by the intracellular hydration of CO_2 without an accompanied influx of HCO_3^- (**Fig 6.2.7.1 A**). The pH_i response was delayed in the core of the spheroid. Upon CO_2 removal from spheroids, the pH_i alkalinised, showing a faster alkalinisation in the periphery than in the core (**Fig 6.2.7.1 B**). Upon CA inhibition by 100 µM ATZ, CO_2 hydration was slower in the periphery, but showed a faster diffusion to the core (reduced time delay) of the spheroid upon CO_2 removal (**Fig 6.2.7.1 C, D, F**). The slower pH_i response in the periphery in the presence of ATZ compared to drug free conditions can be attributed to CA activity (**Fig 6.2.7.1 C, D**). Upon CO_2 removal, the presence of ATZ led to a significant decrease in the delay time of the pH_i response from the core to the periphery (**Fig 6.2.7.1 F**). This indicates that the apparent diffusion of CO_2 is higher in the absence of CA activity. This observation

can be explained in terms of the intracellular CA-catalysed reaction, which tends to trap diffusing CO_2 gas in the form of membrane-impermeant HCO_3^- ions in the cytoplasm. Of note, the observed delay times related to CO_2 diffusion remained below 4 s in both the presence and absence of CA activity (**Fig 6.2.7.1 F**). This result argues for a fast diffusion of CO_2 in Colo357 spheroids. The rapid alkalinisation of the spheroid periphery upon NH_4Cl addition exceeds the rate of pH_i response upon CO_2 addition, indicating that the rate of superfusate change was not the rate-limiting factor in the measurements.

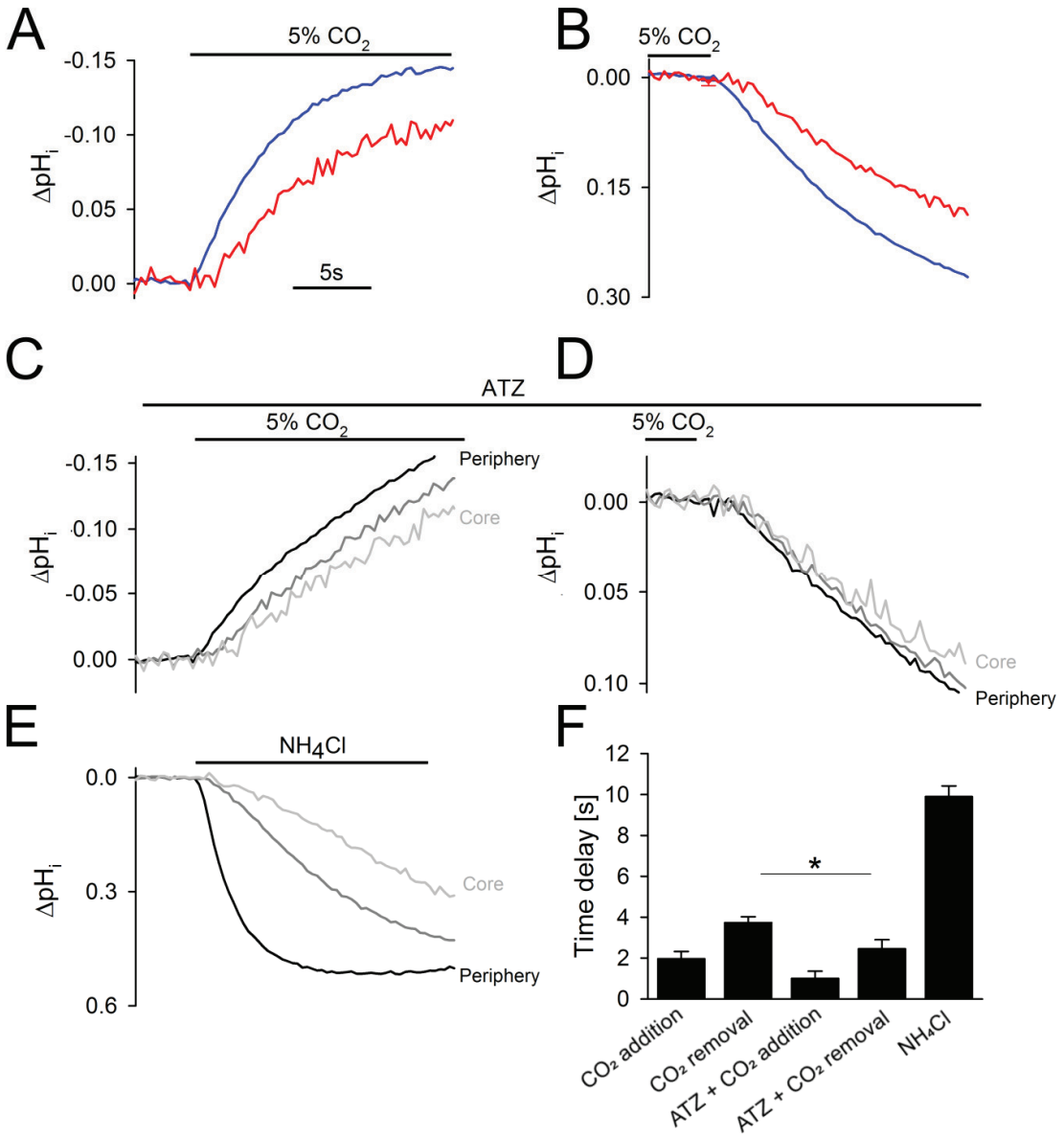


Figure 6.2.7.1 The effect of carbonic anhydrases (CAs) on CO_2 permeation across Colo357 spheroid tissue. *Colo357 spheroids were loaded with cSNARF1 and intracellular pH was measured in 10 concentric regions of the spheroid. Spheroids were superfused in Hepes buffer (pH 7.4). CO_2 diffusion was elicited by switching to and from superfusion with 5% CO_2/22 mM HCO_3^- (indicated above graph).* ***(A)*** *Diffusion of CO_2 into the spheroid upon CO_2 addition. CO_2 diffusion was reported by the Δ pH_i in the central and peripheral region of the spheroid.* ***(B)*** *Diffusion of CO_2 out of the spheroid upon CO_2 removal, reported by the Δ pH_i in the central and peripheral spheroid regions.* ***(C)*** *ΔpH_i CO_2 addition in the presence of the CA inhibitor*

acetazolamide (ATZ). ***(D)*** *ΔpH_i CO_2 removal in the presence of the CA inhibitor ATZ.* ***(E)*** *ΔpH_i upon addition of NH_4Cl as a control to ensure that the rate of superfusion change exceeds the CO_2 hydration rate observed.* ***(F)*** *The time delay of CO_2 diffusion from the spheroid periphery to spheroid (measured in A – D).*

6.2.8 Proton uncaging in spheroids

Introduction. In order to assess if the rates of extracellular HCO_3^- and CO_2 diffusion measured were sufficient to facilitate H^+ removal from spheroids, the proton-uncaging compound NVA was used to inject H^+ ions into the central region of Colo357 spheroids. The extracellular pH response was measured using the membrane-impermeable pH sensitive fluorescein sulfonic acid (FS).

Methods. Colo357 spheroids were grown as described in **section 3.3** and superfused in 5% CO_2/22 mM HCO_3^- buffer containing 30 µM FS. Extracellular pH changes were reported by the change in extracellular fluorescein sulfonic acid fluorescence (FS_e). The FS_e fluorescence was averaged in 10 concentric regions throughout each spheroid (**Fig 6.2.8.2 i**, insert). H^+ ions were photolytically injected into the central region of the spheroid upon uncaging via NVA, as described in **Section 3.11**. The FS_e fluorescence was converted to H^+ ion concentration based on a pH calibration curve (see **Fig 3.9.2.1**). In order to confirm that the 405 nm laser flashes used for NVA uncaging had no photobleaching effect on the FS fluorescence, 405 nm photolysis was performed in 30 µM FS-containing superfusate in the absence of NVA (**Fig 6.2.8.1**) showing no change in FS fluorescence during 405 nm flashes.

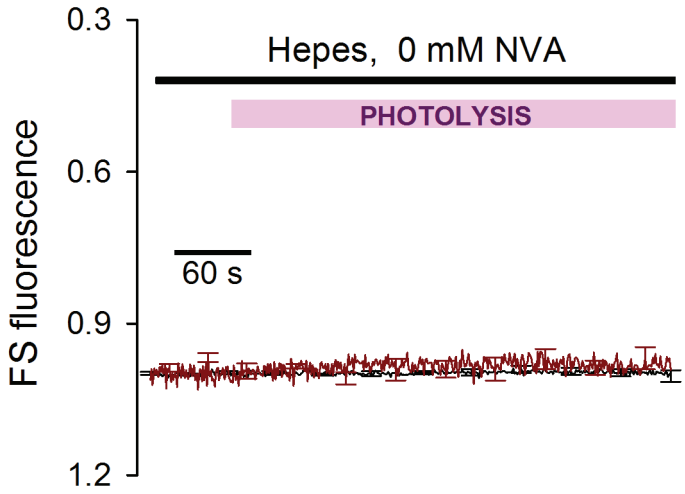


Figure 6.2.8.1 Effect of photolytic 405 nm flashes on the fluorescence of fluorescein sulfonic acid (FS). *Fluorescence of FS upon 100% 405 nm laser intensity (photolysis) in the absence of the photolytic H^+-uncaging agent 6-nitroveratraldehyde (NVA). The absence of change in FS fluorescence upon photolysis (pink bar) indicates that FS fluorescence was not bleached by the 405 nm laser.*

Results. The continuous injection of 20.6 ± 1.2 mM H^+ ions per min into the central region of spheroids led to an accumulation of acid which then spread through the four innermost regions of the spheroid ~60 µm from the periphery (**Fig 6.2.8.2 A, C**). The acid injection rate was estimated as described previously (**Section 3.12.4**). The H^+ uncaging rate was similar to the endogenous lactic acid production of PDAC cells (230, 231). The photolytic H^+-uncaging of NVA simultaneously induces intra- and extracellular H^+ ion accumulation and thus simulates metabolic acidosis. This H^+ ion accumulation caused a decrease of ~1 pH unit in the central region of the spheroid. In order to investigate the role of CA in CO_2 and HCO_3^--mediated extracellular H^+ venting, CA were inhibited with 100 µM ATZ. CA inhibition led to a small increase in H^+ ion build-up in the core region (**Fig 6.2.8.2, B, C**). This suggests that CA activity facilitates

the buffering of photolytically injected H^+ ions. It is possible that increased diffusional distances in larger spheroids would unveil a more substantial role of CAs.

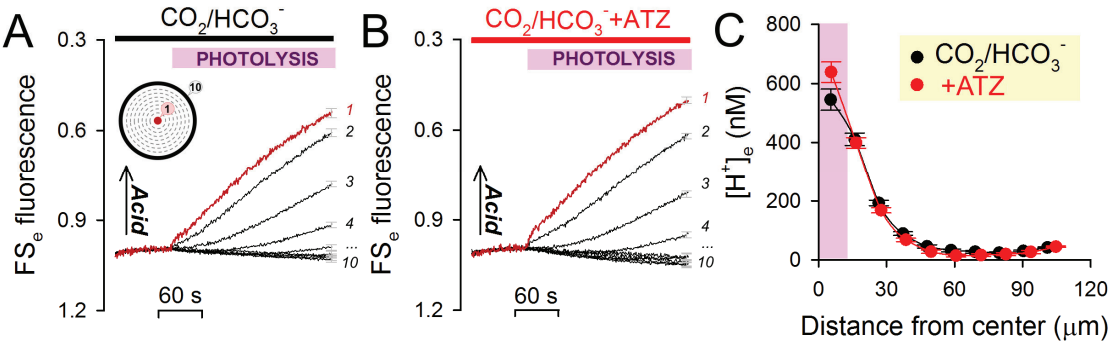


Figure 6.2.8.2 The effect of carbonic anhydrases (CAs) on extracellular H^+ venting during photolytic uncaging in spheroids. ***(A)*** *Change in extracellular fluorescein sulfonic acid fluorescence (FS_e) observed in spheroid regions upon constant H^+-uncaging in the central region of the spheroid (red trace; red insert indicates location). Acid injection is indicated by pink bar (photolysis). Uncaging was performed in 5% CO_2/22 mM HCO_3^- buffer (pH 7.4). The time course of change in extracellular pH_e upon H^+-injection is presented for the 10 regions of the spheroid (see insert).* ***(B)*** *Photolysis experiment as presented in (A), performed in the presence of the CA inhibitor acetazolamide (ATZ; 100 μM).* ***(C)*** *The H^+ ion concentration calculated based on the FS calibration curve (Fig* ***3.9.2.1****) expressed as a function of distance from the spheroid core (region 1).*

6.3 Summary of findings

- CAII was expressed in AspC1 and Capan1 cells.
- CAIX was expressed in normoxia in AsPC1 and Colo357 cells and upregulated in hypoxia in AsPC1, BxPC3, Capan1 and Colo357 cells.
- Intracellular CA activity in PDAC cell lines ranked in the order:

  AsPC1 > PANC1 > Colo357 > BxPC3 > MiaPaCa2
- Exofacial CA activity in PDAC monolayers ranked in the order:

  Colo357 > MiaPaCa2 > BxPC3 > AsPC1 > PANC1 (negligible)
- Colo357 spheroids showed exofacial CA activity.
- Extracellular diffusivity was 70% reduced in Colo357 spheroids.
- CO_2 diffusion was fast in Colo357 spheroids.
- CA activity facilitates extracellular H^+ venting in spheroids upon long diffusion distances (ca 100 μm).

7 METABOLIC ALTRUISM AND REMOTE HCO_3^- TRANSPORT

Objective: To evaluate the role of gap junctions in the transport of HCO_3^- anions across the syncytial intracellular volume of PDAC spheroids.

7.1 Background

The metabolic waste products produced by tumour cells confer an energetic burden on the tumour cells (84, 92). The long cell-to-capillary distances arising in PDAC tumours implies that tumour cells situated in hypoxic areas are dependent on the less-efficient glycolysis for the production of ATP (43, 45). Due to the long diffusion distances to nearby capillaries, the hypoxic cells not only experience the scarcest nutrient resources, but also the longest path for removing their acidic waste products (88). To facilitate the removal of the slow-diffusing H^+ ions, cells may take up HCO_3^- ions through sodium bicarbonate cotransporters (NBCs) (247). The CA-catalysed reaction of HCO_3^- anions with H^+ ions produce CO_2 (89, 247). Since CO_2 is cell permeable and readily diffuse across tissue, whereas H^+ ions do not, HCO_3^- uptake through NBCs may facilitate the removal of intracellular H^+ ions (87, 247). NBC cotransporters are a family of ten genes encoding for transmembrane proteins that co-transport Na^{+} ions and HCO_3^- anions into cells under varying stoichiometry (247) and because this process is a secondary active process, it requires ATP expenditure (247). As pancreatic cancer cell glycolysis accompanied by full hydrolysis of the ATP generated can produce 8 - 22 mmol H^+ ions per min per litre of tumour mass, the removal of H^+ ions may impose a significant burden on hypoxic cells (230, 231). The formation of a syncytium between cells via gap junctional coupling could provide

hypoxic cells with HCO_3^- anions remotely transported from normoxic and nutrient rich cells. This chapter aims to elucidate whether or not normoxic cells exert metabolic altruism by feeding hypoxic cells with HCO_3^- anions through gap junctional coupling.

7.2 Results

7.2.1 PDAC cells lines express various levels of connexin coding genes

Introduction. In order to assess gap junctional coupling between PDAC cells, mRNA expression of genes encoding the connexin protein isoforms was compiled. These connexin isoforms constitute the transmembrane subunits of the hexameric gap junction hemi-channels that could form an alternative HCO_3^- trafficking route in PDAC cells.

Methods. A previously published dataset assessing the mRNA expression in 22 PDAC cell lines was investigated for the expression of connexin isoforms (BioGPS dataset: E-GEOD-21654) (243). The PDAC cell lines analysed were derived from either primary tumours or metastases. All genes encoding connexin isoforms, except those encoding Cx23, Cx35 and Cx30.2, were assessed in the microarray analysis. The genes and corresponding proteins analysed were: *GJA1* (Cx43), *GJB2* (Cx26), *GJC1* (Cx45), *GJB3* (Cx31), *GJA9* (Cx36), *GJB5* (Cx31.1), *GJA5* (Cx40), *GJB6* (Cx30), *GJD2* (Cx36), *GJA3* (Cx46), *GJB1* (Cx32), *GJD3* (Cx31.9), *GJA8* (CX50), *GJA10* (Cx62), *GJA4* (Cx37), *GJC2* (Cx47), *GJB4* (Cx30.3) and *GJD4* (Cx40.1).

Results. mRNA expression of the 18 connexin coding genes was compiled and categorised according to the mean expression level among all 22 PDAC cell lines (**Fig**

7.2.1.1 A). The histological origin of each cell line is indicated by black (primary tumour) or red (metastasis) bars. The most highly expressed genes were *GJA1* (Cx43), *GJB* (Cx26) and *GJC1* (Cx45). These genes were therefore selected for further assessment.

Three PDAC cell types, BxPC3, Colo357 and MiaPaCa2, each of which exhibited different levels of expression of mRNA encoding for Cx43, Cx26 and Cx45 were selected for analysis. **Fig 7.2.1.1 B** shows mRNA levels encoding for Cx43, Cx26 and Cx45 in BxPC3, Colo357 and MiaPaCa2 cells. Both BxPC3 and MiaPaCa2 cells are derived from primary tumour (184, 186), whereas Colo357 cells are derived from a lymph node metastasis (175) (see **Sections 3.1.2, 3.1.5** and **3.1.4**, respectively). The BxPC3 cell line showed high levels of *GJA1* and *GJB2* mRNA encoding Cx43 and Cx26, respectively, and low levels of *GJC1* mRNA encoding Cx45. MiaPaCa2 cells expressed low levels of *GJA1* (Cx43), intermediate levels of *GJB2* (Cx26) and high levels of *GJC1* (Cx45). Colo357 cells expressed high levels of *GJA1* (Cx43) and *GJC1* (Cx45) and intermediate levels of *GJB2* mRNA (Cx26).

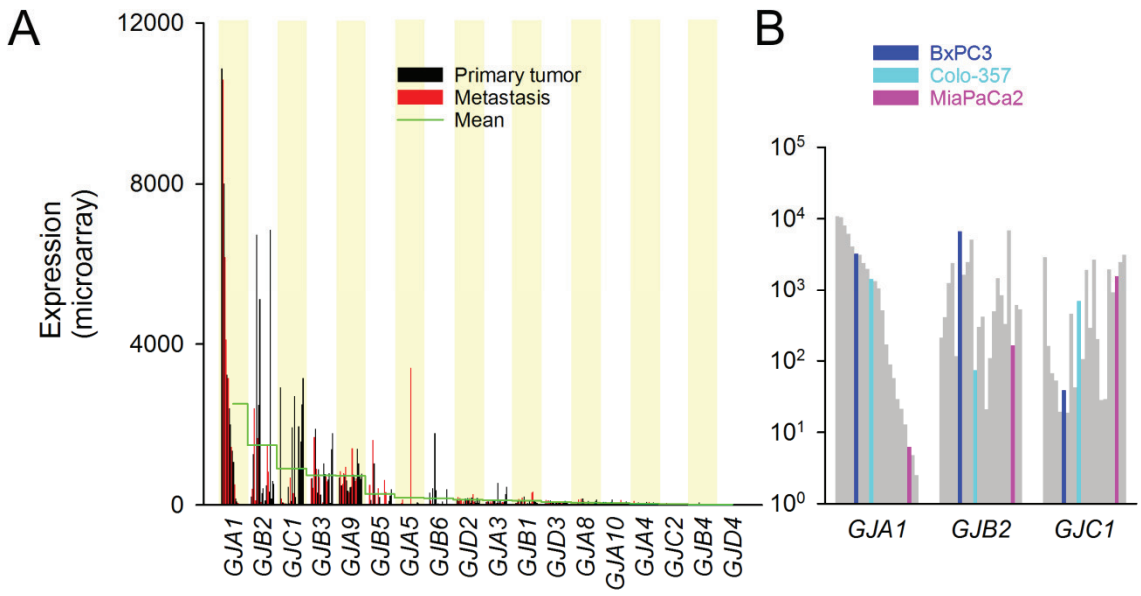


Figure 7.2.1.1 mRNA expression of gap junction-encoding genes in pancreatic ductal adenocarcinoma (PDAC) cell lines. (A) *Previously published microarray data analysed for the mRNA expression of genes encoding gap junction proteins in 22 PDAC cell lines (BioGPS database; E-GEOD-21654 dataset). The origin of the cell line is indicated in black (primary tumour) and red (metastasis). The green line indicates the mean mRNA expression of the 22 PDAC cell lines. Genes are ranked from high to low mean expression.* ***(B)*** *The connexin encoding mRNA expression of GJA1, GJB2 and GJC1 (the most prominent in PDAC) highlighting their expression levels in BxPC3, Colo357 and MiaPaCa2 cells. The data are identical to (A) and replotted on a logarithmic scale.*

7.2.2 PDAC cells show various levels of connexin proteins

Introduction. Since mRNA expression does not necessarily correlate with protein levels, the protein levels of Cx26 (*GJB2*), Cx45 (*GJC1*) and Cx43 (*GJA1)* were determined in BxPC3, Colo357 and MiaPaCa-2 cells. Protein expression was assessed in

cells that were cultured under normoxic conditions (DMSO, control), chemically-induced hypoxic signalling (DMOG) or in a hypoxic atmosphere (2% O_2).

Methods. Levels of Cx43, Cx45 and Cx26 proteins were assessed by immunoblotting upon 10% SDS-PAGE. Lysates of BxPC3, Colo357 and MiaPaCa2 cells were formed in RIPA buffer and loaded at 55 μg/well. Cells were grown for 24 h under normoxic conditions. Thereafter, cells were subjected to a 48 h incubation with 0.1% DMSO (control, normoxia), 1 mM DMOG or grown in a hypoxic atmosphere. DMOG chemically stabilises hypoxic signalling even in the presence of atmospheric oxygen levels by inhibiting 2-oxoglutarate dependent dioxygenase enzymes (68). Hypoxic conditions were attained by incubating cells in a hypoxic chamber containing 2% O_2.

Results. As seen in **figure 7.2.2.1**, all cells analysed exhibit presence of connexin proteins under both normoxic and hypoxic conditions. Colo357 cells showed the most prominent protein levels of Cx43 during normoxia (DMSO) and chemically-induced hypoxic signalling (DMOG) but showed reduced Cx43 levels under hypoxia (**Fig 7.2.2.1,** top panel). This is consistent with the high levels of mRNA expression of *GJA1* found in Colo357 cells (**Fig 7.2.1.1 B**). Colo357 cells showed no detectable presence of Cx45 or Cx26 (**Fig 7.2.2.1**) despite intermediate mRNA expression of *GJB2* (coding for Cx26) and high mRNA expression of *GJC1* (coding for Cx45) (**Fig 7.2.1.1 B**).

BxPC3 cells expressed Cx43 under normoxic conditions (DMSO), albeit at lower levels compared than those of Colo357 cells (**Fig 7.2.2.1,** top panel). These results are in contrast to the mRNA expression data, which showed that the highest *GJA1* mRNA levels were in BxPC3 cells (**Fig 7.2.1.1 B**). The Cx43 levels in BxPC3 cells were up-regulated by either DMOG or hypoxia, suggesting a positive regulation by hypoxic

signalling in this cell type (**Fig 7.2.2.1)**. An rVista database (https://rvista.dcode.org/) analysis of the human *GJA1* gene revealed the presence of a HIF-1α binding site (RCGTG motif; rVista code: AHRHIF_q6) situated 94 - 98 bases downstream of the start codon, which could explain the Cx43 upregulation in the presence of DMOG and hypoxia. A sequence alignment of the human and Mus musculus *GJA1* gene showed conservation of this HIF-1α binding site. No Cx45 and Cx26 protein was detected in BxPC3 cells. This is in contrast to the high expression of *GJB2* (Cx26) mRNA and the *GJC1* (Cx45) mRNA detected in these cells (**Fig 7.2.1.1 B**).

MiaPaCa2 cells showed protein levels of Cx45 in the presence of normoxia (DMSO), DMOG and hypoxia (**Fig 7.2.2.1)**. This is in accordance with the high *GJC1* mRNA expression found in MiaPaCa2 cells (**Fig 7.2.1.1 B**). However, Cx43 and Cx26 were not detected at protein level (**Fig 7.2.2.1)**, despite the detection of low and intermediate levels of *GJA1* and *GJB2* mRNA, respectively (**Fig 7.2.1.1 B**).

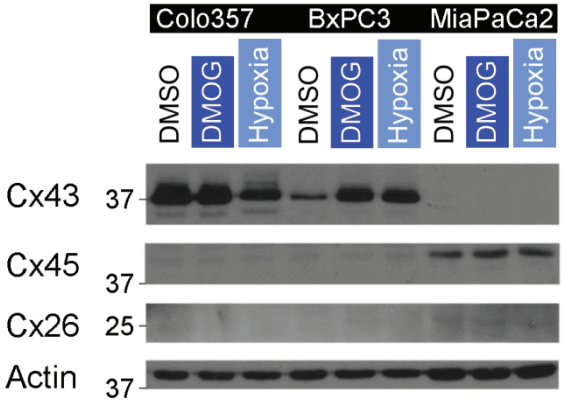


Figure 7.2.2.1 Protein levels of connexin (Cx) isoforms in pancreatic ductal adenocarcinoma (PDAC) cells. *Western blots showing the protein levels of Cx43 (GJA1), Cx45 (GJC1) and Cx26 (GJB2) in Colo357, BxPC3 and MiaPaCa2 cells. Cells were incubated for 48 h under normoxia (DMSO, control), chemically-induced hypoxic signalling (1mM DMOG) or hypoxia (2% O_2). Actin was used as a loading control. N = 4.*

7.2.3 Gap junctional permeability correlates with Cx43 levels in PDAC cells

Introduction. Gap junctional coupling is attained via the formation of gap junction channels between cells (205). The gap junction channel is formed when two hemi-channels couple together to form a channel between two adjoining cells (248). Each connexin hemi-channel (a connexon) consists of six connexin subunits (248). Gap junctions allow the cell-to-cell passive diffusion of small molecules (<1 kDa) down a concentration gradient (205, 248), but the hemi-channel must be situated in the cell membrane in order to form functional gap junctions between to cells (248). As the connexin protein levels shown in **figure 7.2.2.1** were derived from whole cell lysates, they do not reveal subcellular localisation. In order to assess if the connexin protein levels found in **figure 7.2.2.1** formed functional gap junctions, the cell-to-cell connectivity was probed upon fluorescent recovery after photobleaching (FRAP) in confluent PDAC monolayers. The amount of connexin found in a cell type is likely to correlate with connectivity, in case of a subcellular localisation to the plasma membrane. However, different connexin isoform expression may also be reflected in the cell-to-cell permeability. A quantification of cell-to-cell coupling would allow the identification of patterns of correlation between gap junctional permeability, connexin protein levels and the isoform expression found in **figure 7.2.2.1**.

Methods. The FRAP protocol was performed as described in **section 3.10**. PDAC monolayers were grown to confluency to allow the formation of cell contacts. The monolayers were passively loaded with calcein-AM. The cell-to-cell permeability of fluorescent calcein ($P_{junc,calcein}$) was used as a measure of gap junctional cell-to-cell

connectivity. Calcein possesses a molecular weight of 0.622 kDa and is thus capable of permeating gap junctions (205). Excess calcein-AM was removed upon washes with Hepes-buffered culture medium (DMEM, pH 7.4) prior to the experiment to avoid fluorophore loading during the photobleaching experiment.

A calcein-loaded cell in the monolayer was subjected to photobleaching until the cellular calcein fluorescence was reduced to 50%. The photobleaching was performed with a 488 nm laser at 100% intensity. The area of bleaching was confined to a small area in the centre of the bleached cell, to prevent co-bleaching of adjacent cells upon irradiating their protrusions. The fluorescence of the bleached and neighbouring cells was measured and normalised to remote, uncoupled cells in the monolayer. The fluorescence measurement in the bleached cell was fitted to a mono-exponential function in order to determine the time constant for the calcein fluorescence recovery (permeability). The cellular calcein permeability, $P_{junc,calcein}$ was determined as described in **Section 3.12.1**.

In order to knockdown Cx43, Colo357 cells were stably transfected with one of two shRNAs targeting the gene product of *GJA1* encoding Cx43 (see **Section 3.5**). As a control, Colo357 cells were stably transfected with unspecific scrambled shRNA. Stable shRNA transfection can be used for constant suppression of the mRNA translation upon degradation of the mRNA targeted. Thus it can lead to reduced protein levels of the target gene product. For western blots, cells were grown as described in **section 3.3** and western blot against Cx43 was performed as described in **section 3.6**. The Cx43 western blot band intensity was quantified using ImageJ software and normalised to the band intensity of the corresponding actin loading control. Transfected Colo357

cells used for FRAP experiments were grown for 4 days and subjected to FRAP as described in **section 3.10** and quantified as described in **section 3.12.1**. The eGFP fluorescence of transfected cells constituted less than 10% of the calcein fluorescence and did not interfere with FRAP recordings (**Fig 7.2.3.2 B**).

Results. The cellular calcein permeability is shown in **Figure 7.2.3.1 B** together with the time course of a FRAP experiment performed in Colo357 cells (**Fig 7.2.3.1 A**). The fluorescent image of the Colo357 monolayer subjected to FRAP is shown in conjunction with the corresponding time course insert. The monolayer shows a bleached (less fluorescent) cell surrounded by neighbouring coupled cells. As indicated by the time course, the intracellular fluorescence was reduced to 50% of the initial fluorescence (purple area). The time course shows the calcein fluorescence of a photobleached cell (red trace) and its neighbouring cells (black trace), normalised to the fluorescence of remote uncoupled cells. The photo-bleaching causes the photolysis of calcein and thus a decrease in the calcein concentration. The concentration difference between syncytially coupled cells drives the calcein permeability through gap junctions. This cell-to-cell calcein permeability from neighbour-cells into the bleached cells continues until a new calcein concentration equilibrium is established within the connected cell cluster. Immediately after the photobleaching of the central Colo357 cell is stopped, the calcein fluorescence increases in the bleached cell. Concomitantly, the fluorescence in the surrounding neighbour-cells decreases. This indicates permeation of calcein from the neighbouring cells into the bleached cell. The fluorescence level of the bleached and neighbouring cells approaches a similar

fluorescence level indicating the establishment of a novel calcein equilibrium among coupled cells.

The bar chart in **figure 7.2.3.1 B** shows the mean cellular calcein permeability constants measured from FRAP experiments. Among the PDAC cell lines, Colo357 cells showed the highest calcein permeability. BxPC3 cells grown under normoxic conditions showed a lower permeability to calcein than did BxPC3 cells preincubated for 48 h with 1 mM DMOG prior to the experiment to induce hypoxic signalling. MiaPaCa2 cells showed no permeability to calcein suggesting that these cells do not form functional gap junctions. This is in contrast to the protein levels of Cx45 detected in this cell line (**Fig 7.2.2.1**). The gap junctional coupling measured via FRAP in Colo357, BxPC3 and MiaPaCa2 cells (**Fig 7.2.3.1 B**) correlated directly with the cellular Cx43 protein levels measured in those cells (**Fig 7.2.2.1**), suggesting that this connexin isoform is important for establishing gap junctional coupling in PDAC cells. Gap junctional coupling was significantly inhibited in the presence of the gap junctional inhibitor carbenoxolone (CBX; 100 µM) shown in grey bars in **figure 7.2.3.1 B**. Similarly, permeability to calcein was negligible upon CBX treatment of DMOG incubated BxPC3 cells.

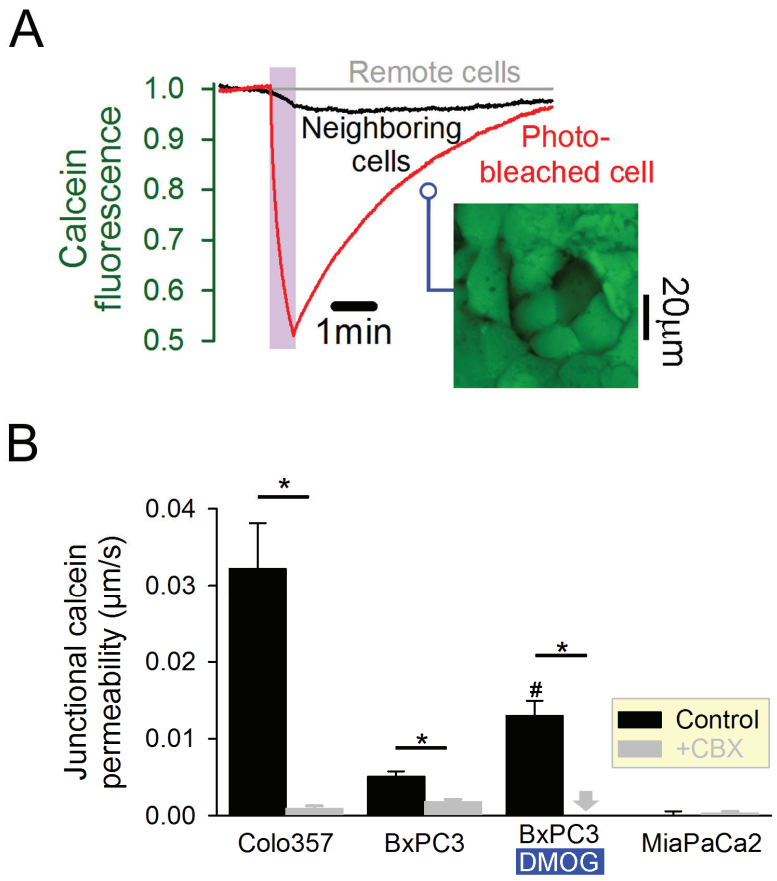


Figure 7.2.3.1 Gap junctional permeability to calcein (0.622 kDa) in pancreatic ductal adenocarcinoma PDAC cells. *Gap junctional permeability to calcein was assessed by fluorescence recovery after photbleaching (FRAP). (**A**) Time course of the calcein fluorescence in the photobleached Colo357 cell (red), neighbouring calcein donor cells (black) and remote uncoupled cells to which the fluorescence recordings were normalised. The calcein-loaded Colo357 monolayer subjected to photobleaching is inserted within the time course. The calcein photobleaching upon 100% 488 nm laser is indicated by the purple area.(**B**) Bar chart showing the cellular permeability to calcein quantified from FRAP recordings. Grey bars represent measurements performed in the presence of the broad-spectrum gap junction inhibitor carbenoxolone (CBX; 100µM). BxPC3 cells treated with 1mM DMOG for 48 h were included to assess the hypoxic response of Cx43 upregulation (**Fig 7.2.2.1**) Bars represent average ± SEM of 10-15 monolayers. P-values <0.01 are represented by * for control vs. CBX and by # for wild type vs. DMOG.*

In order to test whether the cellular calcein permeability observed in **figure 7.2.3.1** was attributable to the Cx43 protein found in **figure 7.2.2.1**, the gene product of *GJA1* was knocked down in Colo357 cells using shRNA as described in **Section 3.5** (**Fig 7.2.3.2**). Colo357 cells transfected with scrambled shRNA retained similar protein level of Cx43 (**Fig 7.2.3.2 A)**. Upon transfection with shRNA #1 against *GJA1,* the Cx43 protein level was reduced by 70±11%. The shRNA #2 against *GJA1* knockdown of Cx43, making shRNA #2 less efficient compared transfection with shRNA #1 (**Fig 7.2.3.2 A**). The protein level of Cx43 correlated directly with the junctional calcein permeability measured by FRAP, showing the highest connectivity in scrambled control cells and reduced connectivity in shRNA-transfected cells (**Fig 7.2.3.2 B** and **C**). In accordance with Cx43 protein reduction (**Fig 7.2.3.2 A**), the permeability to calcein decreased significantly by > 90% in shRNA #1 transfected cells and 70% in shRNA #2 transfected cells compared to scrambled control. These results suggest that the gap junctional connectivity of Colo357 cells is determined by the Cx43 protein level.

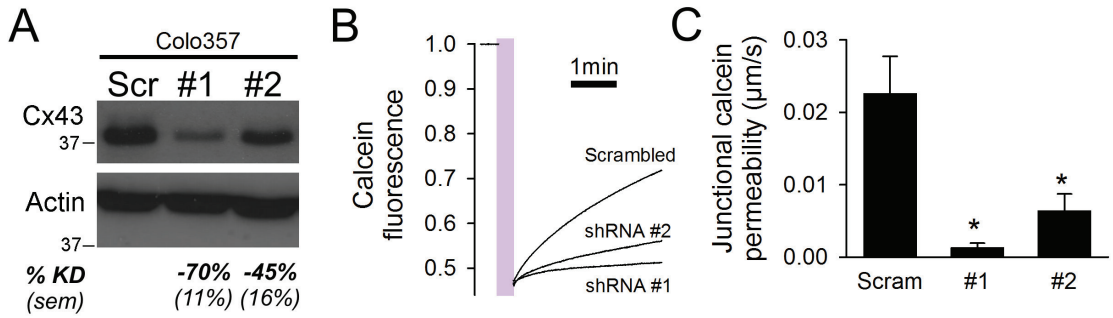


Figure 7.2.3.2 The effect of shRNA-mediated GJA1 (Cx43) knockdown of gap junctional coupling in Colo357 cells. (A) *Western blot showing Cx43 protein levels (gene product of GJA1) in Colo357 cells subjected to stable adenoviral transfection of unspecific scrambled*

(Scr) shRNA or one of two different shRNAs targeting GJA1 mRNA (#1 or #2). The Cx43 band intensity was quantified densitometrically for shRNA knockdowns and compared to scrambled control. The Cx43 band intensities were normalised to the actin loading control. The mean shRNA band intensity is indicated ± SEM below the blot. N=3. ***(B)*** *Time course of fluorescence recovery after photo-bleaching experiment using calcein as the fluorophore. Representative traces of fluorescence recovery after photo-bleaching (indicated in purple) is shown for Colo357 cells stably transfected with scrambled shRNA or shRNA #1 or #2 directed against GJA1 mRNA.* ***(C)*** *Quantification of gap junctional calcein permeability in Colo357 cells stably transfected with scrambled shRNA (Scram) or shRNA #1 or #2 directed against GJA1 mRNA. Bars represent average ± SEM of 11, 8 and 9 experiments.*

7.2.4 PDAC cells show protein levels of the Na^+-HCO_3^- cotransporter NBCe1

Introduction. In order to elucidate whether PDAC cells had the ability to take up HCO_3^-, the cells were assessed for the protein level of the electrogenic Na^+-$2HCO_3^-$ cotransporter NBCe1. NBCe1 is normally expressed in the ductal cells of the pancreas where it functions by transporting HCO_3^- anions from the interstitial space into the pancreatic ductal cells (249). NBCe1 is a candidate protein for HCO_3^- transport in PDAC cells.

Methods. PDAC cells were grown for 48h in the presence of 1mM DMSO (normoxia, control), 1mM DMOG for the chemically induction of hypoxic signalling or grown in a hypoxic atmosphere of 2% O_2. Cells were lysed in RIPA buffer and 55µg total protein were loaded in each lane. Proteins were separated via 10% SDS-PAGE and transferred to a PVDF membrane prior to protein detection.

Results. All six cell lines showed detection of NBCe1 protein levels (**Fig 7.2.4.1)** in normoxia (DMSO), chemically stimulated hypoxic signalling (DMOG) and under hypoxic incubation. The marker of hypoxic gene regulation, CAIX, was upregulated during incubation in DMOG and hypoxia in AsPC1, BxPC3 and Colo357 cell. MiaPaCa2 and PANC1 cells that do not express CAIX were incubated in identical conditions to the CAIX expressing cell lines. AsPC1 and Capan-1 cells showed low levels of NBCe1. Furthermore, incubation in DMOG and hypoxia led to a mild downregulation of NBCe1 in AsPC1 cells. In BxPC3, Colo357, MiaPaCa2 and PANC1 cells, NBCe1 was expressed at high levels in normoxia and did not change upon incubation in DMOG or hypoxia.

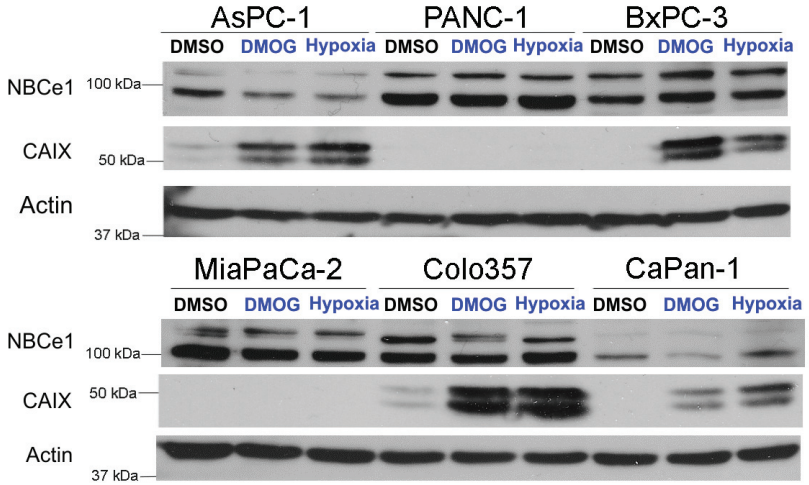


Figure 7.2.4.1 Immunoblot of the protein levels of Na^+/HCO_3^- cotransporter NBCe1 in six pancreatic ductal adenocarcinoma (PDAC) cell lines. *NBCe1 protein levels were analysed after incubation for 48h in normoxia (DMSO, control), chemically-stimulated hypoxia (1mM DMOG) or 2% O_2 atmosphere (hypoxia). The detection of the CAIX protein serves as an indicator of hypoxic gene regulation. MiaPaCa2 and PANC1 cells that did not exhibit CAIX protein, were incubated under circumstances identical to the remaining cell lines. The positions of protein marker bands are indicated in kDa on the left side of the blots. Actin was used as a loading control. N = 3.*

7.2.5 Measuring Na^+-HCO_3^- cotransport activity in Colo357 cells

Introduction. All six PDAC cell lines tested showed detectable levels of NBCe1 (**Fig 7.2.4.1**). NBCe1 must be situated in the plasma membrane in order to exert its function. NBC activity was tested for upon subjection to an acid load induced upon NH_4Cl removal in Colo357 cells.

Methods. Colo357 monolayers were grown and superfused in LabTek plates at a rate of 4 ml per min. Intracellular pH was measured using cSNARF1. The cells were subjected to ammonium prepulse solution manoeuvre which deposits an intracellular acidification. The transmembrane H^+ flux was determined from the pH_i recovery from such acid load. **Figure 7.2.5.1 A** shows an exemplar trace of the pH_i changes measured in a Colo357 monolayer in the presence (left) and absence (right) of 5% CO_2/22mM HCO_3^-. The HCO_3^- dependent flux was determined upon comparison of pH_i in the presence and absence of CO_2/HCO_3^-.

Results. As seen in **figure 7.2.5.1 A**, addition of NH_4Cl led to an intracellular alkalinisation in Colo357 cells. Upon removal of the NH_4Cl, the pH_i rapidly acidified due to the efflux of the membrane permeable NH_3. Subsequently, the pH_i recovers towards the cellular resting pH_i. The pH recovery was faster in the presence of 5% CO_2/22mM HCO_3^- compared to CO_2/HCO_3^- free conditions. The transmembrane H^+ flux was highest at low pH_i decreased when approaching neutral or slightly alkaline pH_i (**Fig 7.2.5.1 A – B**). The presence of the HCO_3^- transport inhibitor acid 4,4'diisothiocyano-2,2'-

stilbenedisulfonic acid (DIDS; 150 µM) inhibited the HCO_3^--mediated H^+ flux Colo357 cells (**Fig 7.2.5.1 A – B**).

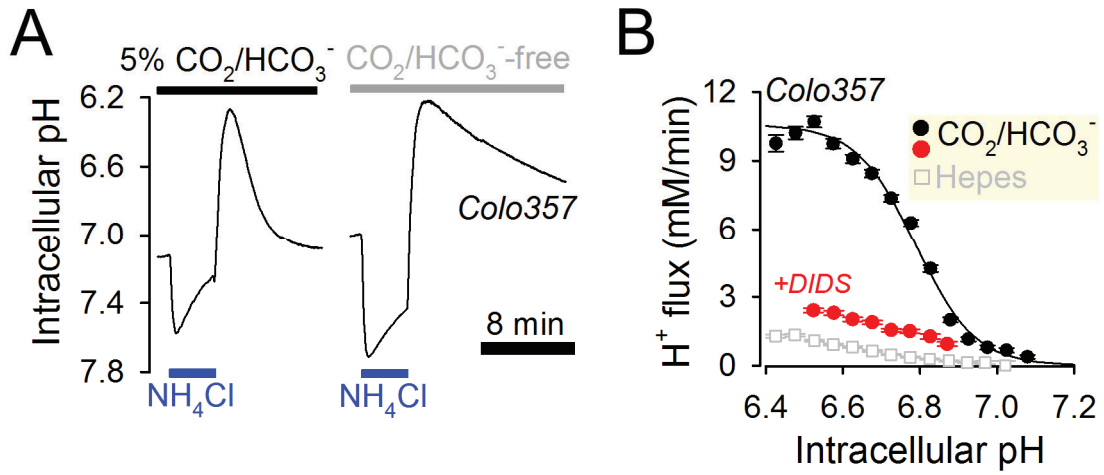


Figure 7.2.5.1 Measurement of HCO_3^--mediated H^+ flux in Colo357 cells. (A) *Signature time-course of a Colo357 cell subjected to an NH_4Cl prepulse in the presence (left) and absence (right) of 5% CO_2/22mM HCO_3^- . The cellular H^+ flux was determined from the recovery of the intracellular pH (pH_i) under the acid load induced by NH_4Cl removal. The HCO_3^-- independent element of the H^+ flux was established based on the pH_i recovery after acid load in the absence of HCO_3^-.* ***(B)*** *pH_i dependence of H^+ flux in Colo357 cells. Experiment was performed in the presence of 5% CO_2/22mM HCO_3^-, in Hepes buffer (CO_2/HCO_3^- free) or in the presence of 150 µM 4,4'diisothiocyano-2,2'-stilbenedisulfonic acid (DIDS) acting as a broad-spectrum inhibitor of HCO_3^- transport. Measurements represent mean ± SEM of 5 experiments.*

7.2.6 HCO_3^- facilitates intracellular H^+ removal in Colo357 spheroid tissue structures

Introduction. Cellular influx of HCO_3^- anions can facilitate the removal of acid in PDAC cells as shown in **figure 7.2.5.1**. In order to assess whether HCO_3^- can titrate intracellular H^+ ions in cells situated in a tissue structure, H^+ ions were uncaged in the centre of Colo357 spheroids with radii of ~100 µm in the presence or absence of CO_2/HCO_3^-.

Methods. Colo357 spheroids were superfused at 4 ml per min in CO_2/HCO_3^- free buffer (Hepes) or buffer containing 5% CO_2/22mM HCO_3^+. H^+ ions were uncaged every 0.73 s using 0.5 mM NVA. The H^+ ions were uncaged in a restricted region of $1/10^{th}$ of the spheroid radius and pH_i measured in the equatorial plane of the spheroid using cSNARF1. The rate of H^+-injection was calculated to be 20.6±1.2 mM/min as described in **Section 3.12.4** to obtain a similar injection rate to that of endogenous lactic acid production rates observed in PDAC cells (230, 231).

Results. Injection of H^+ ions into the centre of Colo357 spheroids led to a rapid central acidification in the absence of CO_2/HCO_3^- (**Fig 7.2.6.1 A**). The intracellular acidification then spread to nearby regions within the spheroid. Under these experimental conditions, HCO_3^- facilitated acid extrusion was absent and cellular acid extrusion low (**Fig 7.2.5.1**), allowing the acid to accumulate intracellularly at the spheroid core. The presence of CO_2/HCO_3^- greatly facilitated the removal of injected acid and led to a 50% reduction in the acid retention compared to CO_2/HCO_3^- free conditions (**Fig 7.2.6.1 B**).

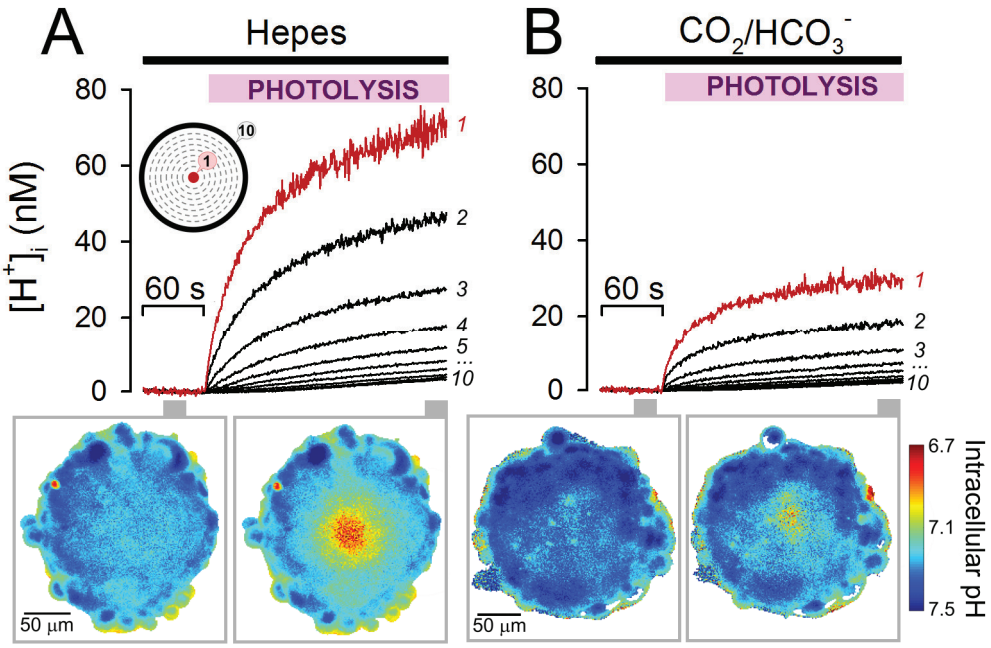


Figure 7.2.6.1 Colo357 spheroid pH_i regulation in the presence and absence of CO_2/HCO_3^-. ***(A)*** *Time course showing the intracellular H^+ concentration in 10 concentric regions of Colo357 spheroids (see insert) following photolytic H^+-uncaging with 0.5 mM NVA in the central region (red). The experiment was performed in the absence of CO_2/HCO_3^- (Hepes buffer). Time course represents mean ± SEM of 22 spheroids). Insert below the graph shows a representative pH_i prior and subsequent to 4 min of photolytic H^+-uncaging.* ***(B)*** *Time course of the intracellular H^+ concentration in 10 concentric regions of Colo357 spheroids in the presence of 5% CO_2/22 mM HCO_3^-. H^+ ions were photolytically uncaged using 0.5 mM NVA. Inserts below the graph show pH_i heat-map of a representative spheroid. The presence of 5% CO_2/22 mM HCO_3 reduces the intracellular accumulation of acid upon H^+-uncaging in comparison to that occurring under CO_2/HCO_3^- free conditions (A).*

In order to assess the cytoplasmic H^+ accumulation throughout the spheroid after the H^+-uncaging presented in **figure 7.2.6.1**, a radial profile of the intracellular H^+ concentration ($[H^+]_i$) was plotted (**Fig 7.2.6.2**). The data presented in **figure 7.2.6.2** show the $\Delta[H^+]_i$ after 4 min of uncaging, when the pH_i had approached a new steady state (see **Fig 7.2.6.1**). At this time-point, the intracellular H^+ accumulation throughout the spheroid was ~2.5 times lower in than the presence of CO_2/HCO_3^- compared to CO_2-free conditions in Hepes (**Fig 7.2.6.2**).

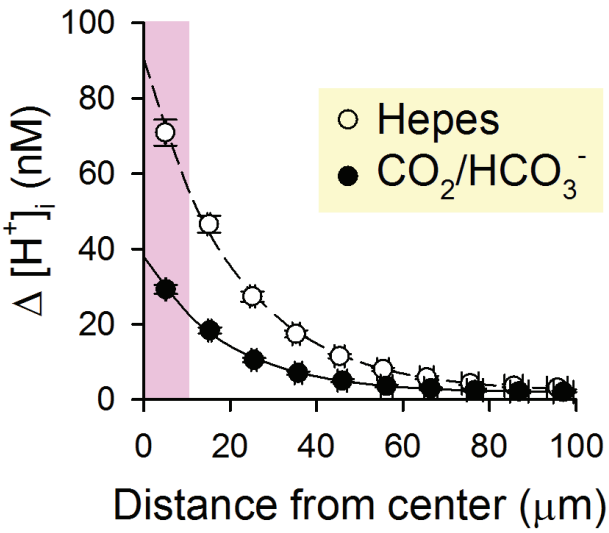


Figure 7.2.6.2 Radial measurements of cytoplasmic H^+ concentration at 4 min of H^+-uncaging. *Measurements were performed in the presence (solid) or absence (open, Hepes) of CO_2/HCO_3^- and expressed as distance from spheroid centre. The pink shaded region indicates the region of photolytic H^+-uncaging. The data are derived from figure 7.2.6.1.*

The reduced cytoplasmic H^+ retention observed in **figure 7.2.5.1 B** cannot solely be attributed to the increased buffering capacity (22 mM HCO_3^-) as this would be depleted after ~1 min of uncaging releasing ~21 mM H^+ ions. Therefore, flux of HCO_3^- must maintain adequate CO_2/HCO_3^- buffering. **Figure 7.2.6.3** shows the calculated time course of the continuous titration of H^+ ions onto imported HCO_3^- anions (β_c) and the fraction of H^+ ions titrated onto intrinsic buffers (β_i) (see **Section 3.12.4**). As seen from the figure, a substantial fraction of the uncaged H^+ ions are titrated by imported HCO_3^- ions.

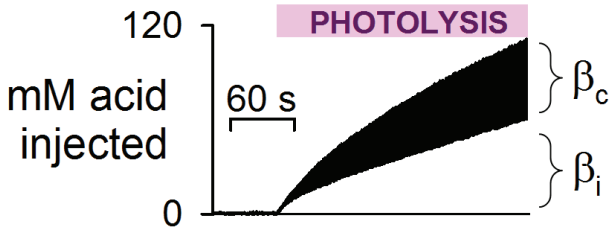


Figure 7.2.6.3 H^+ titration onto carbonic and intrinsic buffers during photolytic H^+-uncaging.
Time course showing the calculated concentration of uncaged H^+ ions titrated onto intrinsic cellular buffers β_i and onto the CO_2/HCO_3^- buffer system β_c. The data are derived from ***figure 7.2.6.1*** *and calculated as explained in* ***Section 3.12.4****.*

7.2.7 Cx43 channels facilitate HCO_3^- mediated venting of H^+ ions in Colo357 spheroids

Introduction. The extracellular diffusion of HCO_3^- is hindered by the tortuosity of the extracellular space (**section 6.2.6**). The NBCe1 mediated uptake of HCO_3^- may therefore become rate-limited by the extracellular HCO_3^- diffusion to hypoxic cells situated at long distances from capillaries. Non-carbonic intrinsic mobile H^+ buffers such as phosphates and dipeptides could vent H^+ ions away from hypoxic cells via gap junctions. In order to test whether intrinsic buffers present in the hypoxic cancer cells are sufficient to vent the photolytically uncaged H^+ ions away from the uncaged region, the photolytic H^+-uncaging was performed in CO_2/HCO_3^--free, Hepes buffered superfusates in the presence and absence of the gap junction inhibitor carbenoxolone (CBX). In the absence of CO_2/HCO_3^-, only intrinsic mobile buffers can mediate H^+ ion diffusion. In addition, the cellular capability of acid extrusion is considerably deactivated in the absence of CO_2/HCO_3^- (**Fig 7.2.5.1**).

Methods. cSNARF1-loaded Colo357 spheroids were subjected to photolytic H^+-uncaging in the central region of the spheroid using 0.5 mM NVA as described above. In order to test the capacity of intrinsic buffers to vent uncaged H^+ ions from the hypoxic core cells via gap junctions (**Fig 7.2.7.1**), the photolytic H^+-uncaging was performed in Hepes buffer in the presence or absence of 100 µM CBX to block gap junctions. The data for CBX-free conditions were identical to the data presented in **figure 7.2.6.1**. In order to test whether gap junctional transport of HCO_3^- ions could facilitate the cytoplasmic H^+ venting from the uncaged region (**Fig 7.2.7.2**), the

experiment was repeated in the presence of 22mM HCO_3^- and 5% CO_2. To test the role of Cx43 in gap junctional HCO_3^- transport (**Fig 7.2.7.3**), the experiment was performed in spheroids formed from Colo357 spheroids stably transfected with either unspecific scrambled shRNA (control) or shRNA directed against *GJA1* encoding the Cx43 protein. The experiment was performed in solution buffered with 22mM HCO_3^- and 5% CO_2.

Results. The presence of the gap junction inhibitor CBX did not change the time course of H^+ uncaged in the spheroids (**Fig 7.2.7.1 A**). Similarly, the radial intracellular H^+ distribution in the spheroid did not change in the presence of CBX (**Fig 7.2.7.1 B**). These results indicate that the intrinsic buffers were not present at sufficient levels to meaningfully facilitate the transport of H^+ ions away from the region of uncaging. Some regions experienced a small but significant increase in acidity in the presence of CBX, but without altering the H^+ gradient from the core to the periphery (**Fig 7.2.7.1 B**).

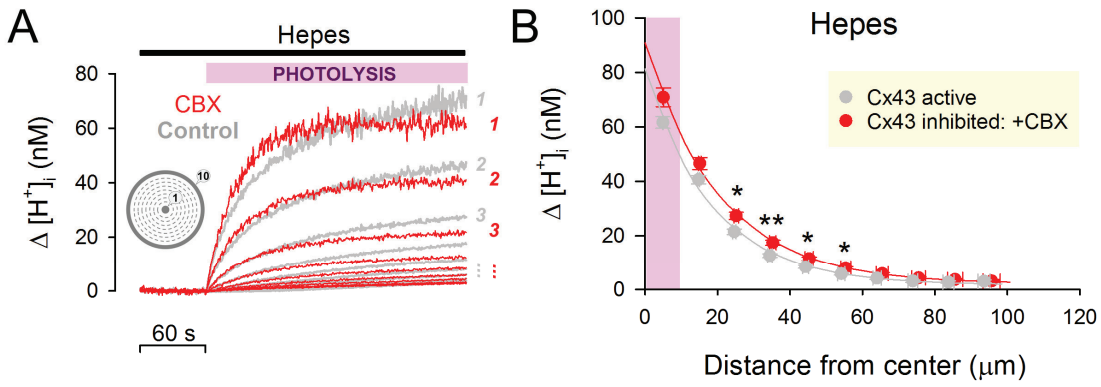


Figure 7.2.7.1 Intrinsic buffer-facilitated transport of H^+ ions through gap junctions. (A) *Time course of intracellular H^+ ion concentration in 10 consecutive regions of Colo357 spheroids subjected to central H^+-uncaging. Acid was uncaged in the central region of spheroids (region 1 in insert) using 0.5 mM NVA in the absence (control, grey) or presence of*

the gap junction inhibitor carbenoxolone (CBX; 100 µM, red) in order to test the ability of non-carbonic intrinsic buffers to transport H^+ ions through gap junctions. ***(B)*** *Radial intracellular pH (pH_i) distribution of spheroids subjected to photolytic H^+-uncaging in Hepes buffer (CO_2 /HCO_3^- free) in the absence (Cx43 active) or presence of 100 µM CBX (Cx43 inhibited). The data presented for control conditions are identical to those presented in* ***figure 7.2.6.1 A****.*

Since intrinsic buffers do not appear to facilitate the gap junctional transport of $H^{'+}$ ions from uncaged areas, junctional transport of HCO_3^- ions was assessed. Due to the extracellular tortuosity (**Section 6.2.6**), syncytial trans-cellular transport of HCO_3^- ions may be favourable in remote tissue areas. As seen in **figure 7.2.7.2 A**, the presence of CBX led to a ~2-fold increase in the H^+ retention in the central regions of the spheroid and a markedly increased cytoplasmic H^+ retention in the regions adjacent to the uncaging area (**Fig 7.2.7.2 B**). These results indicated that gap junctional communication was essential for the capacity of HCO_3^- ions to titrate H^+ ions uncaged in the spheroid core.

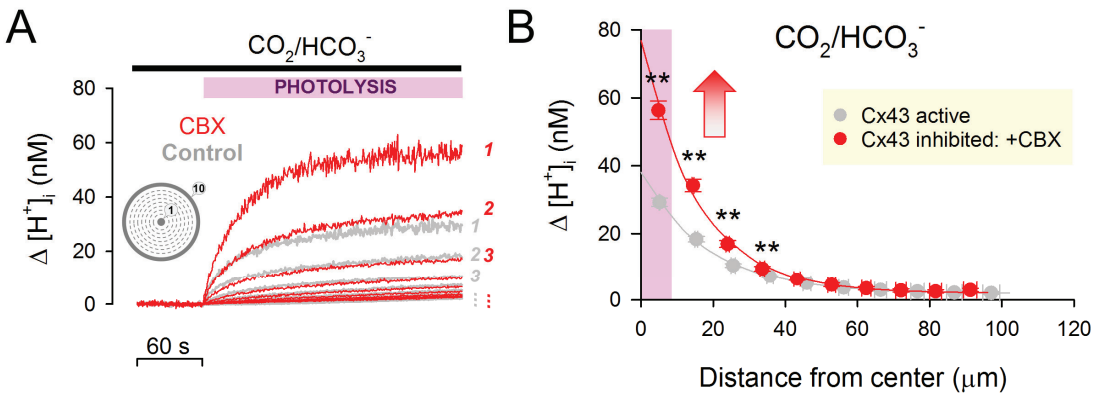


Figure 7.2.7.2 HCO_3^- transport through gap junctions in Colo357 spheroids. ***(A)*** *Time-course of the intracellular change in H^+ concentration ($[H^+]_i$) in the 10 regions of Colo357 spheroids.*

H^+ ions were uncaged in the central region (region 1) of the spheroid indicated by the purple bar. Intracellular pH was measured using cSNARF1 between each pulse of photolytic uncaging. The experiment was performed in the absence (grey) or presence (red) of the gap junction inhibitor carbenoxolone (CBX; 100 μM). ***(B)*** *The radial increase in H^+ concentration measured as a function of distance from the centre of the spheroid. The purple region indicates the region of photolytic H^+-uncaging. The red arrow indicates a significant increase in the cytoplasmic H^+ retention in the central spheroid regions in the presence of CBX. Statistical tests were performed using ANOVA in conjunction with post hoc Bonferroni correction (** signifies $P<0.01$).*

To test if Cx43 channels were responsible for the gap junctional transport of HCO_3^- in Colo357 spheroids, H^+-uncaging was performed in spheroids formed from Cx43 knockdown cells showing a ca 70% reduction in Cx43 protein levels. As seen in **figure 7.2.7.3 A**, a reduction in the Cx43 protein level (see western blot insert) led to an increase in the cytoplasmic H^+ retention in the central regions of the spheroids when compared to the scrambled controls. The knockdown of Cx43 caused a significant increase in the intracellular H^+ concentration in the two innermost regions of the spheroid (**Fig 7.2.7.3 B**). These results indicated that Cx43 was responsible for the transmission of HCO_3^- to the spheroid core, where HCO_3^- anions contribute to the titration of H^+ ions.

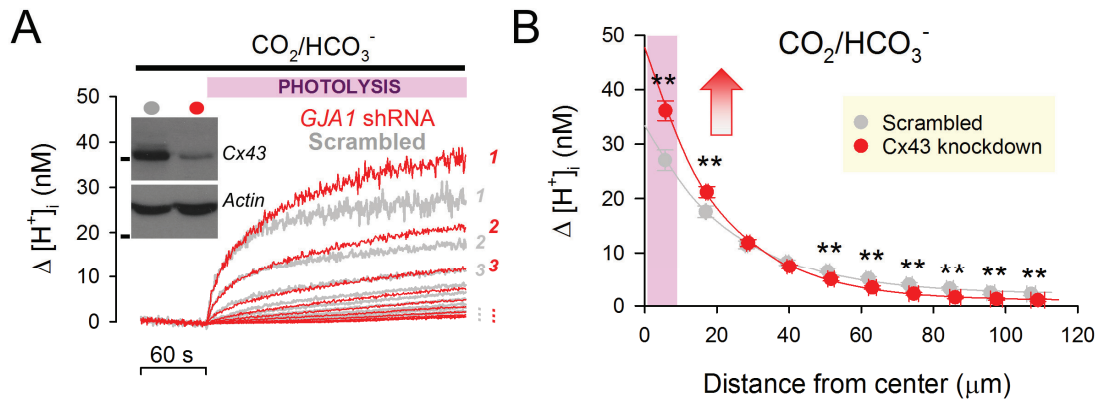


Figure 7.2.7.3 HCO_3^- transport through Cx43 channels in Colo357 spheroids. ***(A)*** *Time-course of the change in cytoplasmic H^+ concentration in 10 regions of Colo357 spheroids formed from cells stably transfected with either scrambled shRNA (grey) or shRNA directed against GJA1, the gene encoding the Cx43 protein. H^+ ions were photolytically uncaged in the centre of the spheroid using 0.5 mM NVA. Photolytic H^+-uncaging was alternated with measurements of intracellular pH using cSNARF1. The insert shows a western blot of the Cx43 protein level in Colo357 cells transfected with scrambled shRNA (grey, left) or shRNA against GJA1 (red, right).* ***(B)*** *The increase in cytoplasmic H^+ concentration measured radially throughout the scrambled and GJA1-knockdown spheroids. The red arrow indicates a significant increase in cytoplasmic H^+ retention in the spheroid core due to a reduced gap junctional flux of HCO_3^- anions. Data represent mean ± SEM of 25 scrambled and 25 GJA1 knockdown spheroids. Statistics represent ANOVA in conjunction with post hoc Bonferroni correction (** signifies P<0.01).*

The results presented in **figure 7.2.7.1 – 7.2.7.3** suggested that gap junctional coupling formed by Cx43 channels are important for venting H^+ ions from the hypoxic core of Colo357 spheroids in the presence of CO_2/HCO_3^- (**Fig 7.2.7.4**). The spheroid

periphery is likely to be the site of HCO_3^- import into the cytosolic compartment due to direct contact of the peripheral normoxic cells with the HCO_3^- buffered solution.

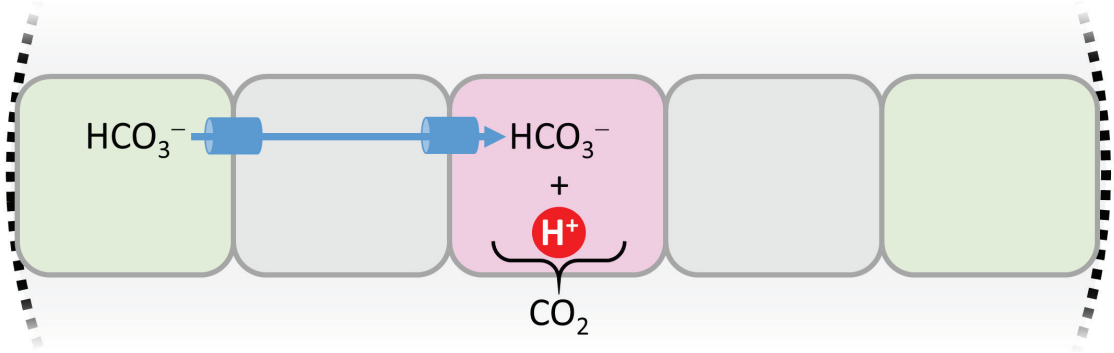


Figure 7.2.7.4 Model representation of the gap junctional transport of HCO_3^-. *HCO_3^- is taken up by cells in the spheroid periphery that are in direct contact with the HCO_3^- containing buffer. HCO_3^- anions are transported to the spheroid core through the intracellular syncytium formed by connexin 43 channels. In the spheroid core, the HCO_3^- anion reacts with the H^+ ion to form CO_2 which can permeate across tissue.*

7.2.8 Inferring the location of HCO_3^- uptake in Colo357 spheroids

Introduction. In order for HCO_3^- ions to be transported through gap junctions, they must be imported into the cytoplasmic compartment via NBC mediated transmembrane transport (247). The normoxic spheroid rim is thermodynamically the most favourable location for HCO_3^- uptake since the cells are subjected to the shortest HCO_3^- diffusional distances and the most alkaline pH_e activating HCO_3^- transport (250). In order to infer the infer the location of HCO_3^- uptake in Colo357 spheroids, the sensitivity to DIDS was assessed in the absence (**Fig 7.2.8.1**) and presence (**Fig 7.2.8.2**) of gap junctional coupling.

Methods. Photolytic H^+-uncaging was performed in the central spheroid region (section 3.11). Gap junctional coupling was inhibited with CBX or by shRNA mediated knockdown of *GJA1* in order to block the syncytial transport of HCO_3^- anions (**Fig 7.2.8.1**). HCO_3^- transport was blocked with 150 µM DIDS, which has previously been shown to inhibit HCO_3^- transport in monolayers (250). Photolytic H^+-uncaging experiments performed in spheroids with functional gap junctional coupling (**Fig 7.2.8.2**) i.e. wild type Colo357 spheroids or scrambled shRNA-transfected Colo357 spheroids.

Results. When gap junctional coupling is absent, the hypoxic cells in the spheroid core rely on NBC mediated HCO_3^- transport during H^+-uncaging. However, as seen in **figure 7.2.8.1 Ai**, the inhibition of HCO_3^- transporters with DIDS did not affect the radial intracellular H^+ profile in spheroids where gap junctional coupling was

inhibited with CBX. These results support the hypothesis that HCO_3^- transporters such as NBCe1 situated in the hypoxic core are not capable of providing a sufficient HCO_3^- uptake to titrate the H^+ ions uncaged in the spheroid core. In order to confirm that the acid uncaged in the spheroid core was titrated by HCO_3^-, the carbonic anhydrases were inhibited using 100 µM ATZ (**Fig 7.2.8.1 Aii**). Carbonic anhydrase activity contributes to the carbonic buffer system by facilitating the reversible reaction between H^+ and HCO_3^- to form CO_2. Carbonic anhydrase inhibition led to a significant increase in the cytoplasmic H^+ retention in the spheroid core (**Fig 7.2.8.1 Aii**) confirming that the carbonic buffer was responsible for the H^+ titration in the spheroid core. Upon shRNA mediated knockdown of *GJA1* (Cx43), DIDS had no effect (**Fig 7.2.8.1 Aiii**), confirming the results of chemical inhibition of gap junctional coupling with CBX (**Fig 7.2.8.1 Ai**).

In summary, the inhibition of the secondary active HCO_3^- transport had no effect on the H^+ venting in the hypoxic regions of Colo357 spheroids when gap junctional coupling was absent (**Fig 7.2.8.1 B**) despite potent inhibition in monolayer culture (**Fig 7.2.5.1**). The Na^+-HCO_3^- cotransporters such as NBCe1 (**Fig 7.2.4.1**) are thus inefficient in regulating pH_i in the hypoxic core. The extracellular acidosis may contribute to the inhibition of the Na^+-HCO_3^- cotransporters (250).

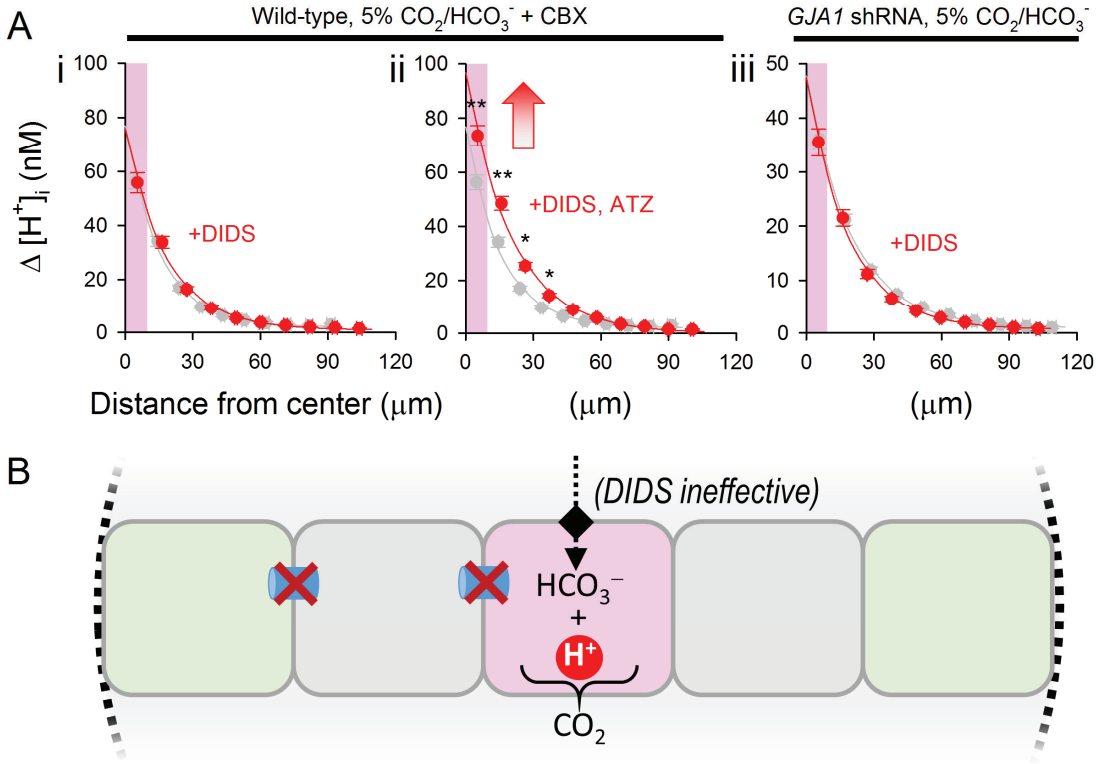


Figure 7.2.8.1 Spheroid HCO_3^- transport in the absence of gap junctions. ***(A)*** *Radial profile of intracellular H^+ concentration after 4 min of H^+-uncaging in connexin inhibited spheroids. Data in grey are identical to the data presented in* ***figure 7.2.7.2*** *and* ***7.2.7.3****.* ***(i)*** *Blocking Na^+-HCO_3^- cotransport with 150 μM DIDS has no effect on cytoplasmic H^+ retention when gap junctional coupling is inhibited with 100 μM CBX. Data represent mean ± SEM of 27 DIDS treated Colo357 wild type spheroids.* ***(ii)*** *Significant increase (red arrow) in cytoplasmic H^+ retention when 150 μM DIDS is combined with 100 μM ATZ to inhibit carbonic anhydrase activity. Data represent mean ± SEM of 39 spheroids.* ***(iii)*** *Untreated (grey) or 150 μM DIDS treated spheroids formed from GJA1 knockdown Colo357 cells. Data represent mean ± SEM of 13 spheroids. Statistics performed with using ANOVA in conjunction with post hoc Bonferroni correction (* and ** signifies P<0.05 and P<0.01 respectively).* ***(B)*** *Model of presented results showing the ineffectiveness of DIDS on cytoplasmic H^+ retention in the hypoxic core region of uncoupled spheroids. This indicates that the cellular HCO_3^- import via NBCs is ineffective in the hypoxic regions.*

The results above indicated that cells in the hypoxic spheroid core do not take up HCO_3^- ions through DIDS sensitive Na^+-HCO_3^- cotransporters such as NBCe1. Alternatively, in the presence of gap junctional coupling, hypoxic cells could receive HCO_3^- from cells in the spheroid rim where Na^+-HCO_3^- cotransport is thermodynamically most favourable. If the uncaged H^+ ions in the hypoxic core were titrated by HCO_3^- ions supplied from normoxic cells via gap junctions, the hypoxic core would show sensitivity towards DIDS, but only in the presence of gap junctions. As hypothesised, in the presence of gap junctional coupling, inhibition by DIDS led to a significant increase in the cytoplasmic H^+ retention (**Fig 7.2.8.2 Ai**). The cytoplasmic H^+ retention was increased even further upon co-inhibition of carbonic anhydrases with ATZ which reduces carbonic buffering kinetics (**Fig 7.2.8.2 Aii**). DIDS had a similar effect on cytoplasmic H^+ retention in scrambled shRNA Colo357 spheroids (**Fig 7.2.8.2 Aiii**). The DIDS sensitivity of connexin-coupled spheroids, but not of uncoupled spheroids, suggest that the Na^+-HCO_3^- cotransport functions in the normoxic spheroid rim (**Fig 7.2.8.2 B**). The normoxic cells thus demonstrate metabolic altruism by providing actively-sequestered HCO_3^- to hypoxic tumour cells in the spheroid core by a passive remote transport of HCO_3^- anions via Cx43 channels.

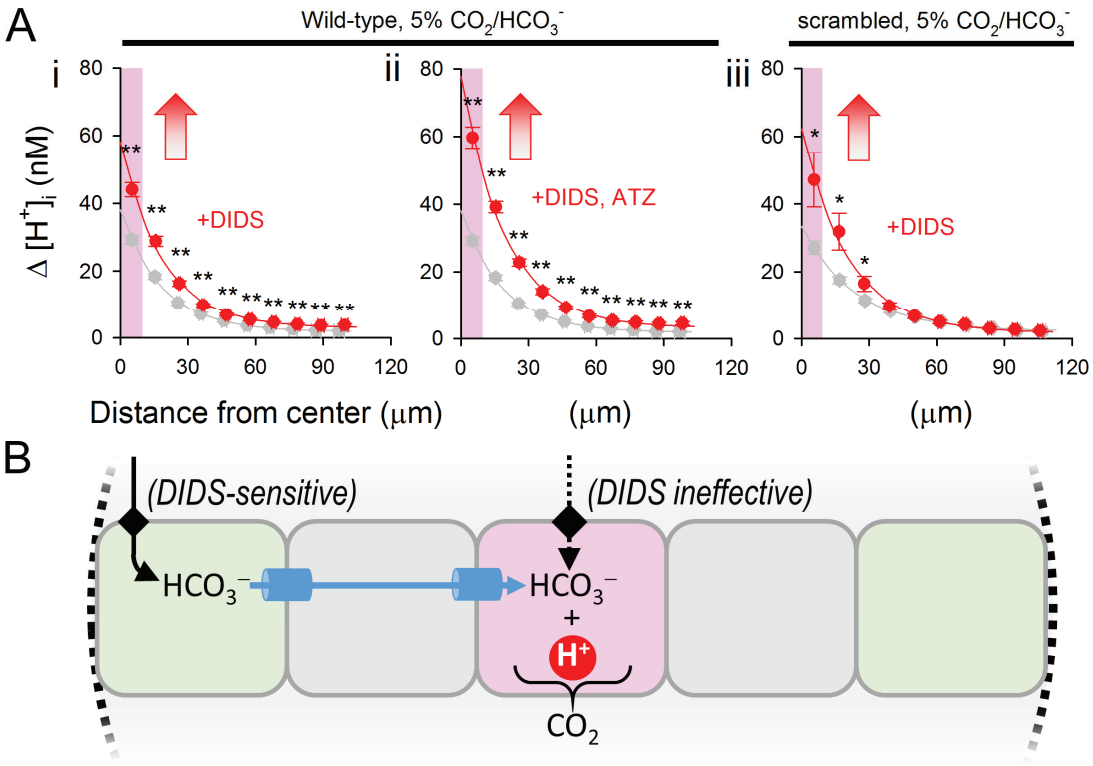


Figure 7.2.8.2 Inferring the location of HCO_3^- uptake in Colo357 spheroids. ***(A)*** *Radial profile of intracellular H^+ concentration after 4 min of H^+-uncaging in gap junction coupled Colo357 spheroids. Data in grey are identical to the data presented in in* ***figure 7.2.7.2*** *and* ***7.2.7.3****.* ***(i)*** *Inhibition of Na^+-HCO_3^- cotransport with 150 μM DIDS increases the cytoplasmic H^+ retention in wild type spheroids. Data represents mean ± SEM of 19 spheroids.* ***(ii)*** *Coinhibition of Na^+-HCO_3^- cotransport with 150 μM DIDS and carbonic anhydrase activity with 100 μM ATZ leads to a further increase in the cytoplasmic H^+ retention in connexin coupled wild type Colo357 spheroids. Data represents mean ± SEM of 29 spheroids.* ***(iii)*** *DIDS treatment increases the cytoplasmic H^+ retention in scrambled shRNA Colo357 control spheroids. Data represents mean ± SEM of 14 spheroids. Data represent mean ± SEM of 13 spheroids. Statistical analysis performed using ANOVA in conjunction with post hoc Bonferroni correction (** signifies P<0.01).* ***(B)*** *Model of DIDS sensitive and DIDS ineffective areas of the gap junction coupled spheroid. Inhibition of Na^+-HCO_3^- cotransport with DIDS only increases the cytoplasmic H^+ retention in the spheroid core when gap junctional coupling is functional.*

These results show that HCO_3^- is taken up by cells in the spheroid periphery and thereafter transmitted to the hypoxic core via gap junctions.

7.3 Summary of findings

- Gap junctional permeability (**Fig 7.2.3.1** and **7.2.3.2**) correlates with Cx43 protein levels (**Fig 7.2.2.1**) and ranked in the order of:

  Colo357 > BxPC3 DMOG > BxPC3 normoxia >> MiaPaCa2 (negligible)

- Na^+-HCO_3^- cotransport is an important mechanism for acid extrusion in PDAC, as demonstrated functionally in Colo357 cells (**Fig 7.2.5.1**).
- Carbonic buffer (CO_2/HCO_3^-) greatly facilitates cytoplasmic H^+ venting from the hypoxic core of Colo357 spheroids (**Fig 7.2.6.1**).
- HCO_3^- ions are transmitted through gap junctions from the spheroid rim to the hypoxic core down a concentration gradient maintained by core-acidosis (**Fig 8.2.8.2**).
- Normoxic cells in the spheroid rim demonstrate metabolic altruism by donating actively imported HCO_3^- ions to hypoxic cells via gap junctions (**Fig 8.2.8.2**).

8 LACTATE HANDLING PATHWAYS

Objective: To investigate the pathways available to PDAC cells for venting lactate anions.

The Pentra 400 lactate and glucose measurements presented in **Section 8.2.7** were kindly performed by Vicky Ball (University of Oxford) whereas cell work and other measurements were performed by me.

8.1 Background

The Warburg effect (aerobic glycolysis) observed in pancreatic cancer leads to a constitutive production of lactate even under normoxic conditions (42). In hypoxic areas, the Pasteur effect (anaerobic glycolysis) implies the glucose is exclusively fermented into lactate (54). In order for cells to proliferate, the pH_i must be tightly regulated to a slightly alkaline pH (89, 92, 251, 252). In order to grown and survive, the tumour cells thus need to match the rate of lactate production with the rate of lactate venting from the lactate producing tumour cell to the blood vessel (84, 89, 92). However, the conventional lactate efflux mechanism via MCTs is counteracted by the low extracellular pH (84). Due to the constitutive production of lactate, hypoxic tumour areas create an acidic extracellular microenvironment (52, 88). The canonical route for transmembrane lactate transport occurs through MCT transporters (103). However, the MCT-facilitated lactate efflux is counteracted by the low extracellular pH of tumours due to its cotransport with H^+ ions (84, 88). Due to this phenomenon, the

lactate efflux is inhibited by the low extracellular pH – a tumour hallmark (42, 43, 88). The presence of gap junctional coupling via connexin channels could offer an alternative route for venting lactate (253). These connexin channels create a high-conductance rout for the discharge of small molecules down a concentration gradient (248). As these channels are thermodynamically insensitive to a low extracellular pH (254), they may offer an alternative route to the compromised MCTs. Lactate transport via gap junctions have not yet been considered as gap junctions have been widely considered to be tumour suppressors (205, 255, 256) and downregulated in some cancers (257). However, many studies suggest that connexins play a role in late stage cancer (258-262). This chapter thus seeks to elucidate other pathways facilitating the transport of lactate in tumours.

8.2 Results

8.2.1 PDAC cell lines express monocarboxylate transporters

Introduction. The canonical MCT-mediated lactate transport involves the cotransport of lactate anions with H^+ ions in a 1:1 stoichiometry (103). The human genome contains four MCT isoforms, MCT1 and MCT4 being the most commonly expressed (103). The MCT1 protein encoded by the *SLC16A1* gene is widely expressed in human cells where it assists the cellular influx and efflux of lactate and other monocarboxylates, such as pyruvate (103, 263). Unlike MCT1, the MCT4 protein encoded by the *SLC16A3* gene is upregulated by hypoxia via HIF-1α and associated with a glycolytic pancreatic cancer phenotype (72, 102). MCT 4 is mainly considered to

be responsible for lactate efflux in cancer cells, as it has a lower affinity for pyruvate than MCT1 (263, 264) (263, 264). In contrast, the MCT1 mediated lactate efflux is dependent on intra- and extracellular concentrations of both pyruvate and lactate (264-266), which are governed by the cellular metabolism and oxygen availability (85).

Methods. PDAC cell lines (**Fig 8.2.1.1**) or Colo357 cells stably transfected with either scrambled shRNA or shRNA #1 or #2 directed against *GJA1* (Cx43) (**Fig 8.2.1.2**) were grown for three days and treated for 48 h in normoxia in the presence of 0.1% DMSO (control), 1mM DMOG to stimulate hypoxic signalling as previously described (**Section 3.6**) or in 2% O_2 hypoxia. Cells were lysed in RIPA buffer and proteins were separated via 10% SDS-PAGE and identified by western blot, using 55 µg total protein was loaded in each lane.

Results. Immunoblotting identified MCT1 protein in all six PDAC cell lines analysed (**Fig 8.2.1.1 A**). In AsPC1 cells, hypoxia and DMOG caused a decrease in MCT1 protein levels in comparison to normoxia. This was not observed in the other five PDAC cell lines. The presence of MCT1 in all cell lines is in accordance with MCT1 being the constitutively expressed MCT isoform responsible for lactate transport.

MCT4 protein levels were also observed in all six cell lines albeit at a low level in Capan1 cells (**Fig 8.2.1.1 B**). Hypoxia led to an upregulation of MCT4 in all cell lines except in Capan1. Similarly, induction of hypoxic signalling with DMOG and hypoxia led to an increase in MCT4 protein levels in all cells except Capan1. However, in PANC1 and MiaPaCa2 cells, the DMOG induced MCT4 upregulation was low compared to the upregulation observed in hypoxia. The MCT4 expression did not directly correlate with the cellular reliance on glycolysis (**Fig 4.3.2**) as previously reported (72).

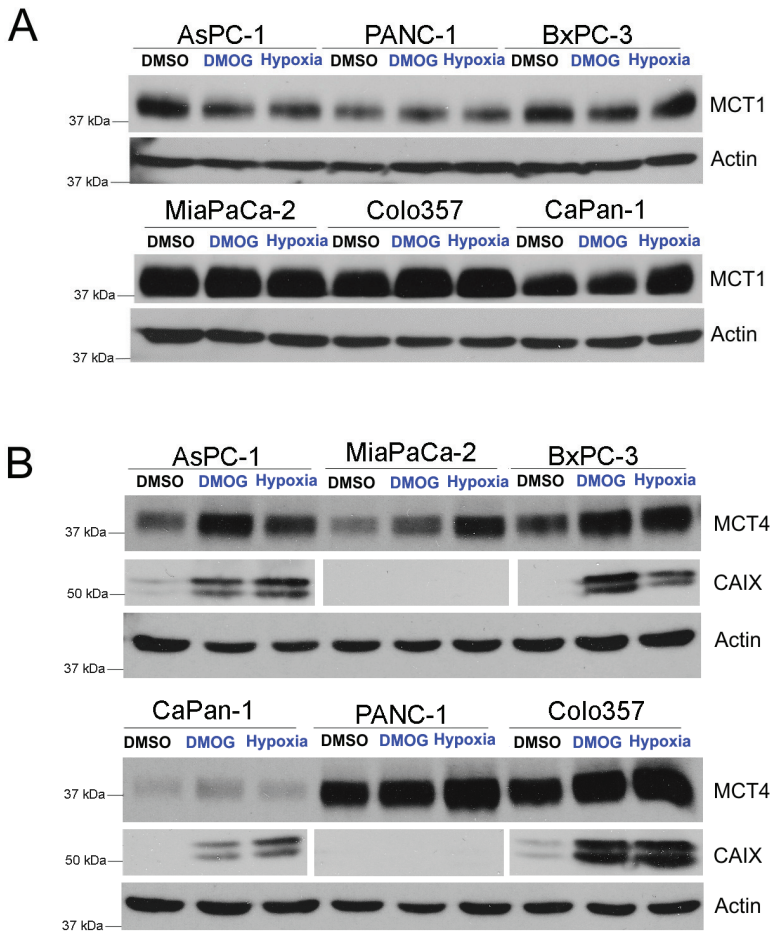


Figure 8.2.1.1 Expression of monocarboxylate transporters 1 and 4 in pancreatic ductal adenocarcinoma (PDAC) cell lines. *Immunoblots showing the presence of the monocarboxylate transporters MCT1* ***(A)*** *and MCT 4* ***(B)*** *in PDAC cell lines. Cells were grown for 48 h in normoxic conditions (DMSO), 1mM DMOG to induce hypoxic signalling in the presence of normal oxygen levels or in 2% O_2 hypoxia. The upregulation of CAIX under conditions of DMOG or hypoxia serves as an indicator of hypoxic cell signalling. CAIX blots are identical to the full blots presented in figure 6.2.2.1. PANC1 and MiaPaCa2, cells that did not express CAIX, were incubated in a hypoxic chamber (or similar DMOG treatment) together with the remaining cell lines expressing CAIX and thus experienced similar conditions. N = 3.*

The shRNA knockdown of Cx43 could result in global changes of gene expression. In order to assure that the shRNA mediated knockdown of Cx43 had no

effect on other lactate venting proteins, the MCT1 and MCT4 protein levels were tested using western blot. **Figure 8.2.1.2** shows the protein levels of the lactate transporters MCT1 and MCT4 in wild type Colo357 cells, scramble transfected Colo357 cells or Colo357 cells transfected with shRNA #1 or #2 against *GJA1* (Cx43). The protein levels of both MCT1 (**Fig 8.2.1.2 A**) and MCT4 (**Fig 8.2.1.2 B**) were unaltered in shRNA-transfected Colo357 cells compared to normal cells. No differences in MCT1 and MCT4 levels were observed between scrambled shRNA-transfected cells and cells transfected with shRNA #1 or #2 against *GJA1* (Cx43). These results suggest that stable transfection of shRNA against Cx43 does not alter MCT-facilitated transport.

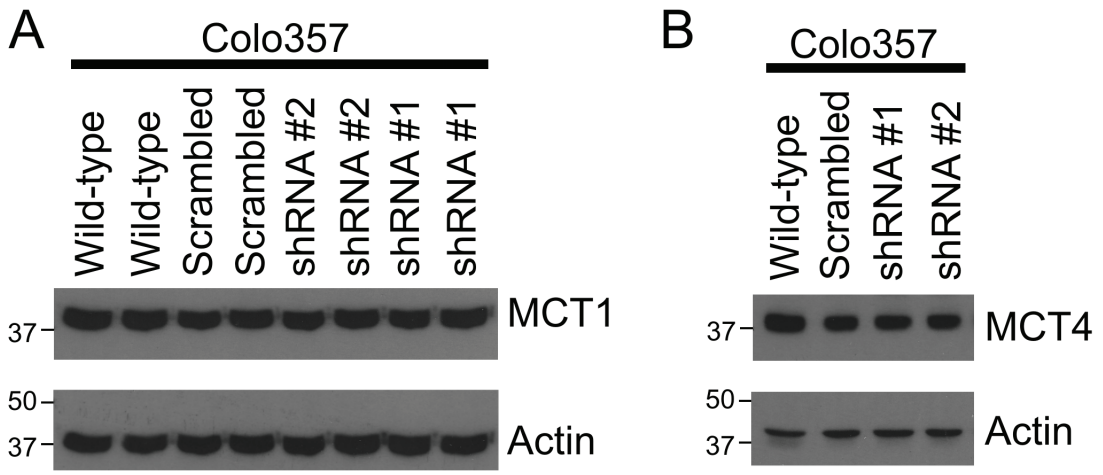


Figure 8.2.1.2 Monocarboxylate transporters (MCT) levels in Colo357 cells stably transfected with shRNA against GJA1 (Cx43). (A) *Western blot showing the MCT1 levels in wild-type Colo357 cells or Colo357 cells stably transfected with scrambled shRNA or shRNA#1 or #2 against GJA1 (Cx43).* ***(B)*** *MCT4 levels in wild type Colo357 cells or stably transfected Colo357 cells as in (A). No changes in MCT1 and MCT4 levels were observed upon stable shRNA transfection in Colo357 cells (compared to wild type cells). Actin was used as a loading control. Protein marker bands are indicated in kDa on the left side of the blots. N = 3.*

8.2.2 H^+ diffusion in PDAC monolayers

Introduction. Lactate could diffuse through an intracellular route through gap junctions upon entering the intracellular compartment through MCTs. As the lactate anion is co-transported with a H^+ ion through MCT, intracellular diffusion and permeation of both lactate anions and H^+ ions must be considered. Intracellular diffusion of lactate has previously been measured to 1000 $\mu m^2/s$ by NMR (100), but the gap junctional lactate permeability remains to be determined. The diffusion of protons in the cytoplasm can vary between cells depending on the amount of fixed intracellular buffers and the availability of small diffusible H^+-binding molecules (H^+ buffers). H^+ buffers less than 1kDa in size are predicted to permeate gap junctions and could thus shuttle H^+ ions syncytially. Since small molecules permeate gap junctions by passive diffusion, the ratio of junctional permeability and cytoplasmic diffusivity should yield a constant. The cytoplasmic diffusivity of H^+ and the cell-to-cell H^+ ion permeability can be measured by assessing pH_i upon photolytic H^+-injection into cells. No analogous method exists for eliciting a selective intracellular rise in the lactate concentration. However, by knowing the intracellular diffusivity of lactate measured previously, its gap junctional permeability can be inferred from the ratio of H^+ permeability and diffusivity as the diffusivity ratio of H^+ to lactate will be proportional to the permeability ratio, since both ions are very small compared to the gap junctional lumen. In order to establish an estimate of both H^+ ions and lactate anions through tissue, the intracellular H^+ diffusivity and cell-to-cell H^+ permeability was measured in PDAC monolayers.

Methods. Monolayers of BxPC3, Colo357 and MiaPaCa2 cells were grown in IBIDI chambers. Cells were placed in Hepes buffered culture medium to exclude H^+ buffering by the open CO_2 buffer system which would otherwise allow H^+ ions to bypass the junctional route. H^+-injection was performed upon photolysis of NVA upon flashes of 405 nm light. The NVA compound was used due to its reduced cytotoxicity compared to the previously used photolytic H^+ donor NBA (**Fig 3.11.1 C**). Protonation and deprotonation of gap junction permeable mobile H^+ buffers (267) were measured using the pH_i indicator cSNARF1.

Results. Due to the high reactivity of H^+ ions, their diffusion is dependent on intracellular mobile buffers that chaperone the H^+ diffusion through the intracellular compartment (schematically represented in **figure 8.2.2.1 A**). As seen from the fluorescent image inserted in **figure 8.2.2.1 B**, the injection of acid into one end of a cell led to the diffusional spread of acid throughout the cell. By measuring the pH spatially in regions throughout the cell, the diffusion of H^+ buffers can be inferred form pH. The time course presented in **figure 8.2.2.1 B** shows the rise in H^+ concentration measured in the three regions indicated by red, black and grey arrows on the fluorescent image insert. The rise in H^+ concentration had the steepest rate increase in the region closest to the source of injection and decreased rates upon increasing distance from the H^+-injection source. The H^+ diffusion measurements were quantified as described in **section 3.12.2**. The quantification of the cytoplasmic H^+ diffusivity revealed similar H^+ diffusion coefficients (D_H) in BxPC3, MiaPaCa2 and Colo357 cells. The intracellular H^+ diffusion coefficient in PDAC cells was ~200 $\mu m^2/s$. Thus the rate

intracellular H^+ diffusion was approximately five times slower than that of the intracellular lactate diffusion previously measured (100).

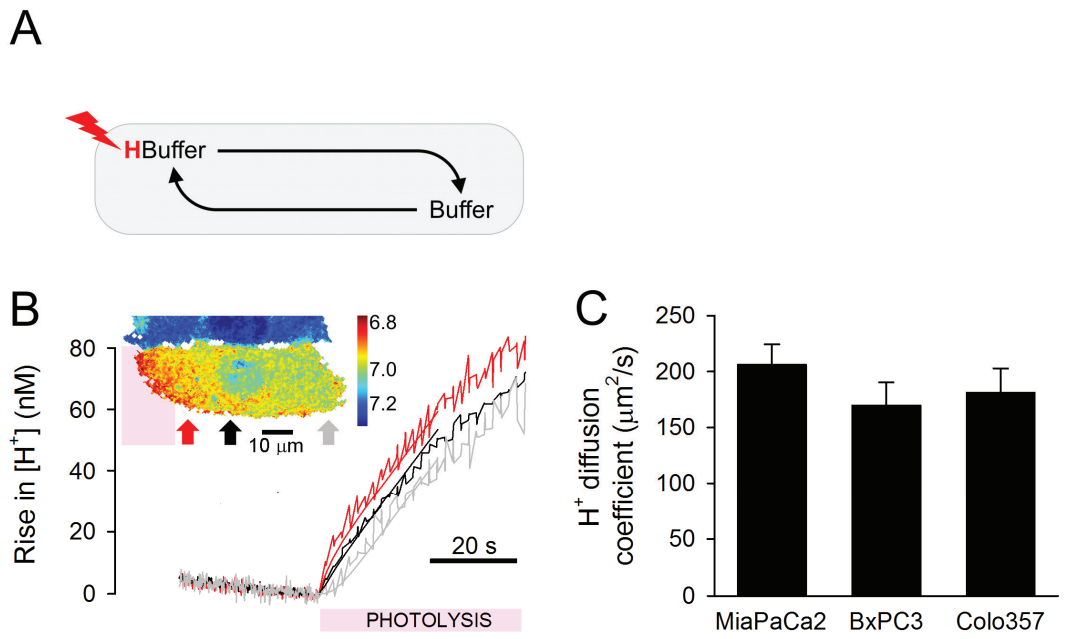


Figure 8.2.2.1 Measuring the intracellular H^+ diffusion coefficient in pancreatic ductal adenocarcinoma (PDAC) cells. ***(A)*** *Schematic representation of intracellular H^+ diffusion. Due to the high reactivity of the H^+ ion, its diffusion is dependent on the reaction with mobile buffers that chaperone its diffusion through the cytoplasm. In areas of lower H^+ concentration, the equilibrium of H^+-bound and H^+-free buffer will drive the dissociation of the buffer and the H^+ ion, giving rise to a local increase in H^+ concentration. Such a change in H^+ concentration was measured with the intracellular pH indicator cSNARF1.* ***(B)*** *The spatial H^+ diffusion measured throughout the cytoplasm of a Colo357 cell. The insert shows a Colo357 cell subjected to 405 nm photolytic H^+-uncaging (pink shaded area) in the presence of 1mM NVA. Red, black and grey arrows indicate the regions wherein the rise in $[H^+]_i$ was measured as shown in the time course. Red black and grey lines represent best-fits to the regional increase in intracellular H^+ concentration.* ***(C)*** *Bar plot showing the intracellular H^+ diffusion coefficients in PDAC cells determined upon intracellular H^+-injection as shown in (B). Bars represent mean ± SEM of 12, 15 and 10 experiments respectively.*

In order to assess the ability of mobile H^+ buffers to permeate gap junctions, the cell-to-cell permeation of H^+ ions was reported using cSNARF1 upon injection of H^+ using 0.5 mM NVA. H^+ ions were uncaged in a central cell in a confluent monolayer and the permeation of H^+ ions was then assessed in the adjacent cells (**Fig 8.2.2.2 B**). In accordance with the calcein permeability measurements (**Fig 7.2.3.1**), the H^+ ion permeability, $P_{junc,H}$, was highest in Colo357, intermediate in BxPC3 cells and negligible in MiaPaCa2 cells (**Fig 8.2.2.2 C**). BxPC3 cells incubated in DMOG showed a significant increase in their permeability to H^+ ions (**Fig 8.2.2.2 C**). This is in accordance with previous results showing upregulated Cx43 protein levels and increased calcein permeability upon DMOG incubation (**Fig 7.2.2.1** and **Fig 7.2.3.1** respectively). The gap junction blocker CBX significantly reduced the H^+ ion permeability in all cells with the exception of the low levels observed in MiaPaCa2 cells. Knockdown of *GJA1* mRNA (Cx43) by shRNA #1 led to a significant reduction in H^+ permeability compared to the scrambled shRNA control. Despite a reduction in junctional calcein permeability (**Fig 7.2.3.2 C**), shRNA #2 against *GJA1* mRNA did not lead to a significant reduction in the gap junctional H^+ permeability (**Fig 8.2.2.2 C**). The measured ratio of H^+ ion permeability and diffusion $P_{junc,H}/D_H$ is ~0.001 (~0.2/~200). Therefore, by approximating $P_{junc,lactate}/D_{lactate}$ using the measured $P_{junc,H}/D_H$ ratio of 0.001 and an intracellular lactate diffusivity (D_{lac}) of 1000 $\mu m^2/s$, the cell-to-cell lactate permeability, $P_{junc,lactate}$ was predicted to be in the order of ~1 μm/s in Colo357 cells as well as in hypoxic BxPC3 cells.

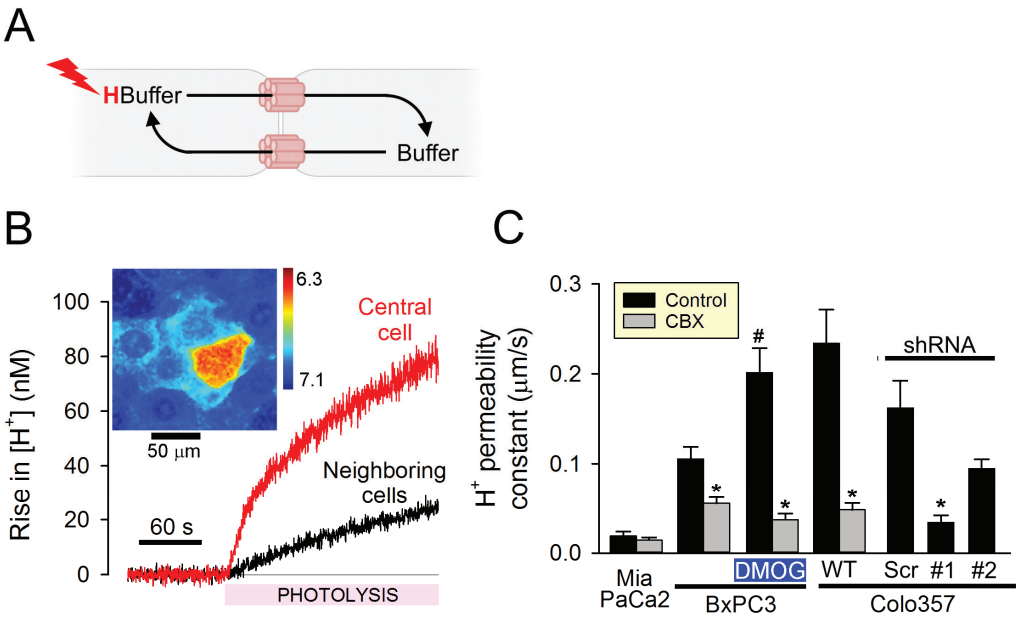


Figure 8.2.2.2 The effect of shRNA-mediated GJA1 (Cx43) knockdown on gap junctional coupling in Colo357 cells. ***(A)*** *Western blot showing Cx43 protein levels (gene product of GJA1) in Colo357 cells subjected to stable adenoviral transfection of unspecific scrambled (Scr) shRNA or one of two different shRNAs targeting GJA1 mRNA (#1 or #2). The Cx43 band intensity was quantified densitometrically for shRNA knockdowns and compared to the scrambled control. The Cx43 band intensities were normalised to the actin loading control. The mean shRNA band intensity is indicated ± SEM below the blot. N=3.* ***(B)*** *Time course of fluorescence recovery after photo-bleaching (FRAP) experiment using calcein as the fluorophore. Representative traces of fluorescence recovery after photo-bleaching (indicated in purple) are shown for Colo357 cells stably transfected with scrambled shRNA or shRNA #1 or #2 directed against GJA1 mRNA.* ***(C)*** *Quantification of gap junctional calcein permeability in Colo357 cells stably transfected with scrambled shRNA (Scram) or shRNA #1 or #2 directed against GJA1 mRNA. Bars represent average ± SEM of 11, 8 and 9 experiments, respectively.*

8.2.3 Junctional lactate diffusion in PDAC monolayers

Introduction. The measurements of intracellular H^+ diffusion presented in **Section 8.2.2** indicate that protons diffuse approximately five times slower than do lactate anions. Since the ratio of intracellular diffusion and cell-to-cell permeability is expected to be constant, lactate anions are also expected to permeate gap junctions faster than protons. However, this assumption is based on a previously published value for intracellular lactate anion diffusion (100). In order to confirm whether lactate anions do permeate gap junctions faster than the buffered H^+ ions in PDAC cells, confluent PDAC monolayers were subjected to an extracellular gradient of 40 mM lactate leading to a syncytial gradient of intracellular lactate. The relative proportion of lactate anions and H^+ ions permeating the gap junctions was inferred from the pH_i signature driven by the standing lactate gradient.

Methods. Colo357 monolayers were subjected to an extracellular gradient of lactate upon superfusion with a double barrelled micropipette (268). The double barrel of the micropipette simultaneously superfused the monolayers with (left) and without (right) 40 mM NaLactate in Hepes-buffered solution (pH 7.4). The presence of the lactate drives MCT-facilitated entry of lactate anions and H^+ ions in a 1:1 ratio leading to an acidification of the cells in the lactate-containing micro-stream. This acidification continues until an equilibrium of extracellular and intracellular lactic acid is reached ($[H^+]_e \times [lactate]_e = [H^+]_i \times [lactate]_i$). Intracellular lactate anions and H^+ ions can dissipate syncytially in the presence of gap junctional coupling. Since the permeation of lactate anions and H^+ ions through gap junctions is passive and occurs

independently, the ratio of lactate or H^+ permeability depends on their respective permeability constants. In the case that lactate permeates gap junctions faster than do H^+ ions, the reduction in $[lactate]_i$ would result in additional MCT-facilitated lactic acid entry into the cells situated in the lactate containing micro-stream (according to $[H^+]_e \times [lactate]_e = [H^+]_i \times [lactate]_i$). This would in turn lead to a further increase in the acid load of these cells and result in a steeper pH_i gradient between the two micro-streams.

Results. Colo357 monolayers subjected to a micro-stream containing 40 mM lactate developed an intracellular acidification (**Fig 8.2.3.1 A, i-iiii**). The intracellular acidification upon exposure to extracellular lactate is a result of cotransport of transmembrane H^+ ion and lactate anion cotransport through MCTs (**Fig 8.2.3.1 B**). The pH_i gradient was measured laterally between the lactate containing (left) and lactate free micro-stream. This pH_i gradient was larger in the presence of gap junctional coupling compared to that under the inhibition with 100 μM CBX (**Fig 8.2.3.1 C**). This indicates that the lactate and H^+ ion permeation through gap junctions does not follow a 1:1 stoichiometry and suggest that lactate permeates gap junctions faster than H^+ ions in CO_2/HCO_3^--free conditions. The basis of this inference are intracellular [lactate] dynamics; if lactate is allowed to dissipate rapidly between coupled cells, its lateral gradient will be shallower. This allows more lactate entry at the lactate-exposed end, producing a larger pH_i change that is reported as a steeper pH_i gradient. If, on the other hand, H^+ ions diffused faster between cells, the pH_i gradient would become more dissipated. In order to confirm that Cx43 was responsible for the gap junctional transmission of lactate anions and H^+ ions, the experiment was performed in Colo357 monolayers stably transfected with scrambled control shRNA or shRNA #1 directed

against *GJA1* (Cx43). GJA1 knockdown by shRNA #1 led to a decrease in the micro-stream gradient (**Fig 8.2.3.1 D**) similar to the reduction seen in the presence of CBX (**Fig 8.2.3.1 C**). The increased pH_i gradient observed in scrambled shRNA compared to shRNA #1 transfected cells suggests that the gap junctional permeation of lactate anions is mediated by Cx43. Overall, these results confirm, that lactate permeates gap junctions faster than do buffered H^+ ions.

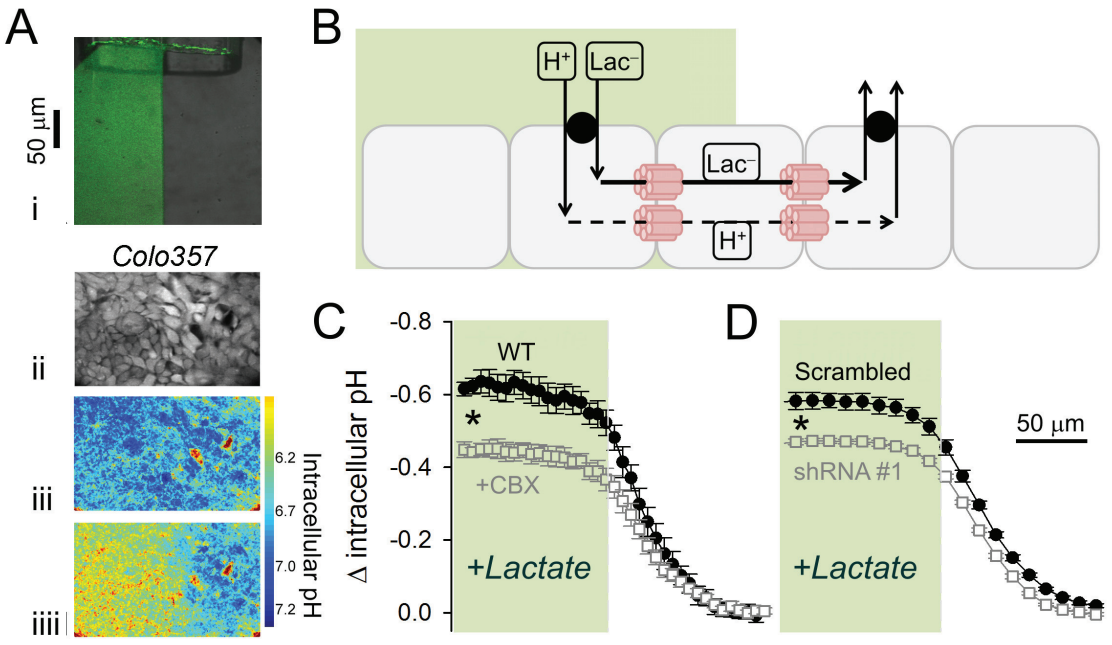


Figure 8.2.3.1 Lactate anions permeate Cx43 gap junctions faster than do H^+ in Colo357 monolayers. *Colo357 monolayers were exposed to an extracellular gradient of 40 mM lactate upon dual micro-superfusion with a double-barrelled micropipette. This serves to establish an intracellular gradient of lactic acid within a syncytially coupled monolayer.* ***(Ai)*** *The integrity of the inter-stream boundary visualised by the presence of 30 µM fluorescein in the left micro-stream.* ***(Aii)*** *Intracellular cSNARF1 fluorescence used for pH_i measurements in the Colo357 monolayer.* ***(Aiii-Aiiii)*** *Heatmap of intracellular pH (pH_i) prior to (Aiii) and after exposure to 40 mM lactate in the left micro-stream (Aiiii).* ***(B)*** *Model of lactate and H^+ transport in the*

presence of an extracellular standing gradient of lactate. Extracellular lactate present in the left micro-stream is co-transported into the Colo357 cell with H^+ ions in a 1:1 ratio. In the presence of gap junctional coupling, lactate permeates faster through gap junctions than do H^+ ions. This leads to an increased monocarboxylate transporter (MCT)-mediated transport of lactic acid in the lactate micro-stream, increasing the pH_i gradient between the micro-streams. ***(C)*** *The change in pH_i (compared to resting pH_i) after exposure to 40 mM lactate (left barrel) for 2 min. The pH_i was measured throughout the two micro-streams in wild type (WT) Colo357 monolayers and in monolayers treated with 100 µM carbenoxolone (CBX) to inhibit gap junctional coupling. Measurements represent mean ± SEM of 7 (WT) and 10 (CBX) monolayers.* ***(D)*** *pH_i measurements in shRNA# 1 transfected Colo357 cells compared to scrambled control transfected Colo357 cells subjected to 40mM lactate (left barrel) for 2 min. Measurements represent mean ± SEM of 5 (N=5 scrambled, 5 shRNA#1). Statistics performed using ANOVA (* represents $p < 0.05$) to compare between wild type and CBX and between scrambled and shRNA#1.*

8.2.4 Measuring MCT activity in PDAC monolayers

Introduction. Glycolytic cells have two routes for discharging lactate produced by metabolism: Syncytially through the cytoplasm via gap junctions or via transport into the extracellular compartment mediated by MCTs in the plasma membrane. The relative traffic through the gap junctional- and MCT-facilitated routes depend on the relative lactate permeability through gap junctions and MCTs, $P_{junc,lactate}$ and $P_{mct,lac}$ respectively. The gap junctional permeability in Colo357 cells was estimated in **Sections 8.2.2** and **8.2.3**. In order to appreciate both possible routes for lactate the cellular lactate permeability through MCT, $P_{mct,lac}$, was assessed first. Since the

functional activity of MCTs is dependent on plasma membrane localisation, the MCT1 and MCT4 protein levels detected from whole cell lysates (**Fig 8.2.1.1**) may not reflect the transporter activity. By subjecting cells to a uniform and rapid switch of superfusion to a lactate containing superfusate, the MCT activity was determined. Uniform lactate superfusion eliminates the cell-to-cell lactate gradient, thereby abolishing gap junctional fluxes of lactate.

Methods. Colo357 monolayers were grown for 48 h in normoxia or 1mM DMOG to chemically stabilise the hypoxic upregulation of MCT4 as presented in **figure 8.2.1.1 B**. Cells were superfused in IBIDI chambers to allow quick superfusate change. The monolayers were superfused with 5% CO_2/22mM HCO_3^- buffered solution and then exposed transiently (minutes) to 40 mM NaLactate. The NaLactate was isosmotically replaced with NaCl in the solution to avoid changes in osmolarity. The transport of lactate anions through MCTs is accompanied by H^+ ions in a 1:1 stoichiometry. The H^+-linked lactate cotransport was estimated from the pH_i response using confocal microscopy of cells loaded with cSNARF1. All experiments were followed by a pulse of 30 mM NH_4Cl to ensure that the rate of superfusate change and thus substrate delivery was not the rate-limiting step in the measurements of MCT activity. Addition of 30 mM NH_4Cl gives rise to a rapid alkalinisation of the cell upon diffusion of NH_3 across the cell membrane ($NH_3 + H^+ \rightarrow NH_4^+$). Due to the low intracellular CA activity found in Colo357 cells, kinetics of the CO_2/HCO_3^- reaction were applied to the calculation of MCT flux as described previously (246). $P_{mct,lac}$ was calculated based on the H^+ flux (and thus lactate flux) through MCTs via the equation $J_{mct} = P_{mct,lac} \times [lactate]_e \times \rho$, where ρ is the ratio of surface area/volume. $J_{mct,lac}$ was

determined as the product of cellular buffering capacity and the rate of change in pH_i. The surface area to volume ratio, ρ, is the reciprocal of the height of the monolayer, 1/6.0 μm^{-1}. The monolayer height was estimated from the surface area of the cell determined from the x-y plane upon confocal microscopy (592±34 μm^2) and cell volume was determined by flow cytometry (3570 μm^3).

Results. The pH_i response in Colo357 monolayers upon addition and removal of extracellular lactate is shown in **figure 8.2.4.1 A**. This shows an acidification upon lactate addition and alkalinisation upon lactate removal. This response is consistent with MCT-facilitated cotransport of an H^+ ion together with the lactate anion. The change in cellular pH_i was faster upon addition of ammonium (NH_4Cl) compared to the pH_i change observed upon addition or removal of lactate. The faster pH_i response upon addition of ammonium confirms that the observed fluxes of lactate through MCT transporters were not rate-limited by the lactate delivery upon superfusate change.

To compare the rate of change in pH_i, the ΔpH_i was plotted on one set of axes (**Fig 8.2.4.1 A**). The insert shows that the ΔpH_i upon ammonium addition greatly exceeded the MCT-mediated pH_i response upon lactate addition indicating that the speed of solution change was not rate limiting for the lactate-evoked response. The MCT flux (J_{mct}) was derived from the product of the buffering capacity (**Fig 5.3.1**) and pH_i change. Furthermore, the insert shows that the magnitude of lactate fluxes upon lactate entering (on) and leaving (off) cells were similar.

Lactate permeability mediated by MCT did not change between incubation in normoxia (DMSO) or chemically induced hypoxic signalling (DMOG). This indicates that

the increased MCT4 levels observed upon incubation in DMOG (**Fig 8.2.1.1 B**) were not sufficient to significantly increase the cellular permeability towards lactate. Presence of the gap junctional inhibitor CBX led to an inhibition of the lactate permeability ($P_{mct,lac}$). These results suggested that CBX exerted an off-target effect by inhibiting the MCT-mediated lactate transport. The MCT-mediated lactate permeability, $P_{mct,lac}$ was ~0.3 µm/s both in normoxia (DMSO) and chemically induced hypoxic signalling (DMOG). This is considerably smaller than the gap junctional lactate permeability of ~1 µm/s. These results thus indicated that lactate may permeate gap junctions faster than it permeates MCTs in Colo357 cells.

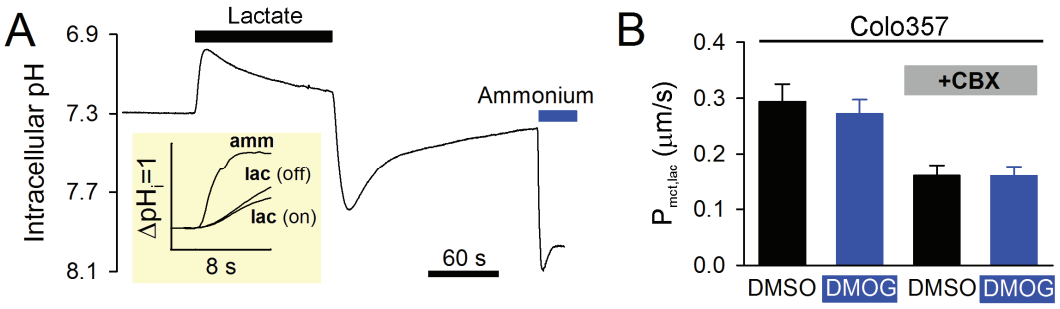


Figure 8.2.4.1 Measuring the cellular monocarboxylate transporter (MCT) activity in Colo357 monolayers. (A) *The intracellular pH (pH_i) measured upon addition and removal of 40 mM lactate (black bar) in 5% CO_2/22 mM HCO_3^- buffered superfusate. The pH_i was inferred from confocal microscopy of cSNARF1-loaded Colo357 monolayers superfused in IBIDI chambers. To ensure that the rate of lactate MCT substrate delivery exceeded the lactate fluxes, a 30 mM ammonium pulse was added after each experiment (blue bar). The insert (shaded yellow) shows the pH_i change upon addition (on) and removal (off) of lactate and upon addition of 30 mM NH_4Cl (amm). The Δ pH_i change upon addition of NH_4Cl exceeded that which occurred upon lactate addition or removal, indicating that MCT activity is not rate-limited by*

delivery of its substrate lactate. ***(B)*** *Cellular MCT-mediated lactate permeability in cells incubated in DMSO (control, normoxia) or 1mM DMOG for 48 h. The lactate permeability was measured experimentally, as shown in (A). Presence of the gap junctional inhibitor carbenoxolone (CBX; 100 µM, grey bar) showed an off-target effect and partially inhibited* $P_{mct,lac}$. *(N= 20, 19, 20, 19).*

8.2.5 Junctional versus MCT-mediated transport of lactate in Colo357 spheroids

Introduction. The results presented in **Sections 8.2.2 – 8.2.4** indicate that lactate may permeate gap junctions faster than its transport by MCTs, and that a substantial amount of lactate traffic may therefore occur syncytially via the gap junctional route. Experiments performed in monolayers do not resemble the complex structure of a tissue. In relation to pH_i, the immediate contact of cells with a large superfusate volume exposes cells to a direct reservoir wherein the cells can deposit their acidic metabolic waste products, CO_2 and lactic acid. In cancerous tissue cells often grow over 100 µm away from blood vessels. Therefore, cells are not always in direct contact with blood supply. Therefore, cells situated in a tissue often experience a significant barrier to diffusion. This is especially true in hypoxic areas developing 100 µm – 150 µm away from blood vessels. In these hypoxic areas cells rely on the glycolytic production of lactate. The specific route of lactate traffic through a multicellular tissue structure was thus examined. Monolayer experiments (**Sections 8.2.2 – 8.2.4**) indicated that gap junctional lactate permeability was more than three-fold higher than MCT permeability in Colo357 cells. These results indicated that the

syncytial route of lactate venting could be the predominant mode of lactate venting through a tissue structure. In order to test whether lactate was predominantly transported syncytially via gap junctions or extracellularly via MCTs, multicellular Colo357 spheroids were subjected to lactate pulses. Although lactate sensors do exist (269), they are incapable of indicating whether lactate transport is mediated by gap junctions or MCT. However, since MCT transport is proton linked whereas gap junctional transport is not, the lactate transport through MCTs and gap junctions give rise to distinct pH_i responses that can distinguished with pH_i reporter dyes such as cSNARF1. Since MCT transport of lactate is accompanied by the transport of protons in a 1:1 ratio, the lactate flux through MCT can be monitored via the presence of H^+ (pH_i). In contrast, the transport of lactate and H^+ ions through gap junctions is uncoupled and the two molecules are transported separately (as described in **Sections 8.2.2** and **8.2.3**). Upon subjecting Colo357 spheroids to pulses of lactate, the relative contribution of gap junctional and MCT-mediated lactate transport can be inferred from the pH_i.

Methods. Colo357 spheroids were grown to a radius of ~110 μm and loaded with cSNARF1 in order to measure pH_i. cSNARF1 fluorescence was measured in the equatorial plane of a spheroid using confocal microscopy. Spheroids were subjected to superfusion with 5% CO_2/22 mM HCO_3^- and then rapidly shifted to a buffer containing 40 mM NaLactate (substituted with equimolar amounts of NaCl). Lactate-evoked pH_i changes occurred upon MCT-facilitated cotransport of a lactate anion and H^+ ion. Within the intracellular compartment, H^+ ions and lactate anions can diffuse independently from cell-to-cell in the presence of gap junctions.

Results. Colo357 spheroids imaged through the equatorial plane, exhibited a pH_i gradient from the core to the periphery with increasing alkalinity towards the periphery (**Fig 8.2.5.1 A**). The lower pH_i in the core indicates the development of a mildly hypoxic environment. The radial diffusion of lactate was investigated spatio-temporally through the spheroid equatorial plane upon addition and removal of 40 mM lactate (**Fig 8.2.5.1 B**). The pH_i response in the core (red) and periphery (black) is shown in **Fig 8.2.5.1 B**. In the periphery, the lactate addition led to a monophasic acidification upon lactate addition and an alkalinisation upon lactate removal. The monophasic pH_i response of peripheral cells is in accordance with canonical MCT-mediated co-transport of lactate and H^+ ions in 1:1 stoichiometry. The cells in the spheroid periphery were directly subjected to the lactate containing superfusate solution, so there was no diffusional barrier to lactate in those cells.

Upon increasing depth into the spheroid, the increased extracellular tortuosity exerted by the presence of cells may rate-limit the MCT-mediated lactate flux. This may result in cell-to-cell gap junctional fluxes of lactate that do not follow a 1:1 stoichiometry of H^+ ions and lactate anions. As seen in **Section 6.2.6** the tortuosity exerted by the presence of cells can reduce the extracellular diffusion by ~70%. In the spheroid core (**Fig 8.2.5.1 B**, red trace), the addition of lactate led to a biphasic pH_i response consisting of a rapid alkalinisation followed by a slower acidification. The rapid alkalinisation observed in the spheroid upon lactate addition suggests that lactate anions diffuse rapidly via gap junctions to the spheroid core where the lactate anions alkalinises cells. In order to enter the intracellular compartment and thus allow gap junctional traffic, the lactate anions must be taken up by MCTs in the periphery.

This is consistent with the pH_i response seen in the periphery. The rapid core alkalinisation could be a result of the rapid gap junctional permeability of the lactate anions and the slow diffusion of H^+ ions (**Fig 8.2.5.1 C**). The subsequent acidification observed in the core upon lactate addition could be a result of slower cell-to-cell diffusion of H^+ ions and a slow extracellular lactic acid diffusion limiting MCT-mediated transport into the cells in the core. Thus, the biphasic pH_i response observed upon addition and removal of lactate indicates that a fraction of the lactate transport to cells in the core was derived from cell-to-cell transport via gap junctions.

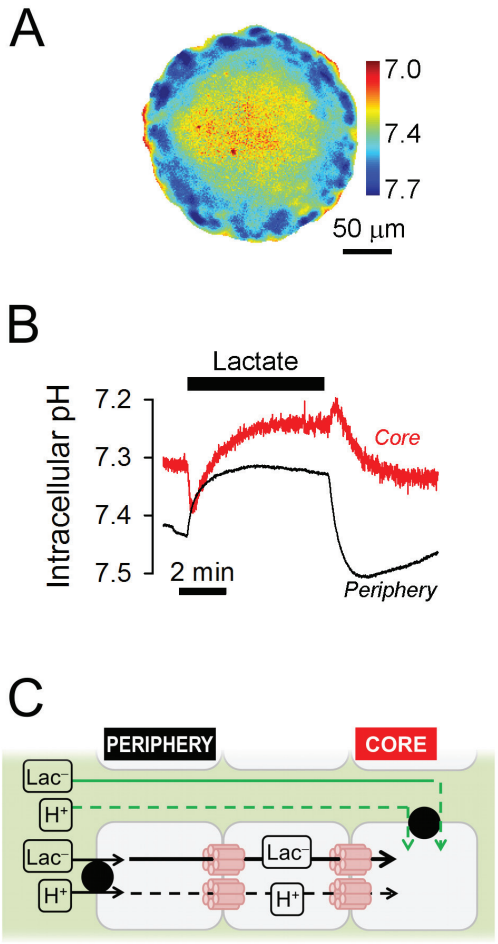


Figure 8.2.5.1 Lactic acid diffusion in Colo357 spheroids. ***(A)*** *Heatmap of intracellular pH (pH_i) through the equatorial plane of a Colo357 spheroid.* ***(B)*** *pH_i time course in the peripheral (black) and central (red) region of a spheroid exposed to a pulse of 40 mM NaLactate (black bar) superfused in 5% CO_2/22 mM HCO_3^- (pH 7.4). In peripheral cells (black trace), the pH_i response to lactate was unidirectional, indicating H^+-coupled MCT transport. In contrast, the pH_i response in the spheroid core (red trace) was bi-directional indicating rapid gap junctional transmission of lactate anions that was uncoupled from slower gap junctional transmission of H^+ ions (see* ***Section 7.5 – 7.6)*** ***(C)*** *Model of bimodal transport of lactic acid in spheroid. In the periphery, lactate was co-transported into cells with H^+ ions via monocarboxylate (MCT) transporters (black circle) in a 1:1 stoichiometry. Once inside cells, rapid syncytial lactate diffusion and slower H^+ diffusion led to a rapid alkalinisation and a subsequent acidification of the spheroid core since gap junctional transport was faster than MCT mediated transport here.*

To confirm that the biphasic pH_i response observed in the spheroid core was caused by gap junctional transport of lactate, gap junctional coupling was inhibited with CBX at a concentration of 100 µM, which has previously been shown to inhibit gap junctional coupling (270) (seen also **figure 7.2.3.1** and **8.2.2.2 C**). In Colo357 spheroids, gap junctional coupling was inhibited upon superfusion with 100 µM CBX for 20 min to assure sufficient inhibition of gap junctional coupling throughout the Colo357 spheroids. The presence of CBX ablated the transient biphasic pH_i response in the spheroid core in paired experiments of lactate addition and removal (**Fig 8.2.5.2**). This indicates that a substantial proportion of lactate is transported through gap junctions. Of note, upon gap junctional inhibition with 100 µM CBX, the rate of change of pH_i in the periphery decreased, indicating a partial inhibition of MCT as an off-target effect of CBX (See also **figure 8.2.4.1 B**).

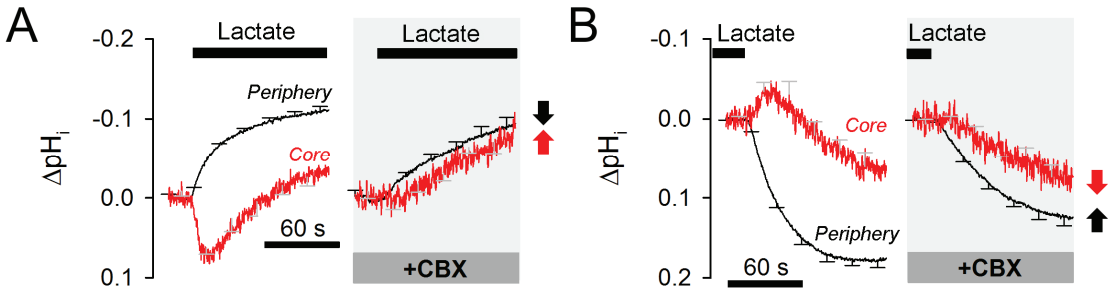


Figure 8.2.5.2 Lactate-induced biphasic response of intracellular pH (pH_i) in the spheroid core is inhibited by the gap junctional blocker carbenoxolone (CBX). ***(A)*** *Addition of 40 mM lactate (black bar) led to a monophasic acidification in the periphery, whereas the spheroid core experienced a biphasic pH_i response consisting of a rapid alkalinisation followed by a subsequent acidification. The biphasic pH_i response in the core was reverted upon inhibition of gap junctional coupling via 100 µM CBX suggesting that the biphasic response is caused by a*

rapid translocation of the weak basic lactate anion to the core and a slower translocation of the heavily-buffered H^+ ion. ***(B)*** *The removal of lactate from spheroids mirrored the pH_i response observed upon lactate addition (A). Removal of lactate led to a rapid acidification in the spheroid core followed by an alkalinisation. The biphasic pH_i response in the core generated by lactate removal was inhibited by the gap junctional blocker, CBX. The slower rate of pH_i change in the spheroid periphery and core upon inhibition of gap junctional coupling with CBX is likely attributable to its off-target effect of inhibiting MCT.*

Fluxes of lactate through MCTs and gap junctions (J_{mct} and J_{junc}) can be quantified based the rate of pH_i change observed in a spheroid. In the presence of the gap junctional blocker CBX, the rate of pH_i change, dpH_i/dt_{cbx}, is proportional to $-J_{mct}$ as the influx of lactate leads to a reduction in pH_i. This calculation was corrected for the limited off-target MCT inhibitory effect of CBX (See **figure 8.2.4.1 B**). In control spheroids where gap junctional coupling was active, the dpH/dt_{con} could be expressed as $J_{junc} - J_{mct}$. This can estimate the fraction of lactate that is transported through gap junctions using the following equation:

$$\frac{J_{junc}}{J_{junc} + J_{mct}} = \frac{dpH/dt_{con} - dpH/dt_{cbx}}{dpH/dt_{con} - 2 \times dpH/dt_{cbx}}$$

Based on the data presented in **figure 8.2.5.2**, the proportion of lactate transported through gap junctions was calculated to be 77±3%, indicating that only a minor fraction of lactate is transported through MCTs in Colo357 spheroids. It should

be noted, however, that the lactate transported through gap junctions needs to enter the intracellular compartment through MCTs in the cells of the spheroid periphery.

The biphasic pH_i response observed in the spheroid core upon lactate pulses suggests that lactate transport through MCTs at longer diffusion distances becomes rate-limited by the diffusion of its lactate and H^+ ion substrates. The translocation of lactic acid from the extracellular to the intracellular compartment is dependent on MCT activity. In the spheroid periphery, where cells are in direct contact with the surrounding lactate-containing superfusate, no diffusion distance exists between an MCT transporter and its substrate. As the spheroid core is approached, however, MCT activity depends on the extracellular diffusion of H^+ ions and lactate anions. Due to their high reactivity H^+ ions are prone to bind fixed buffers such as proteins situated in the cell membrane (97). The binding to fixed buffers in the extracellular space slows down its diffusion. At greater diffusion distances, MCT activity is therefore likely to be rate-limited by the availability of substrates, due to the low extracellular diffusion of H^+ ions. To test if the slow extracellular H^+ diffusion was the rate-limiting step for MCT-mediated transport of lactic acid in the spheroid core, spheroids were subjected to lactate pulses in the presence of increased amounts of mobile extracellular buffer. Higher levels of mobile extracellular H^+ buffer was used to overcome the effect of H^+ ions binding to the fixed buffers situated on cell membranes. The mobile membrane-impermeant H^+ buffer Hepes was used to manipulate extracellular mobile H^+ buffering capacity. The physiological CO_2/HCO_3^- buffer was substituted with either 20 mM Hepes (high mobile H^+ buffering) or 1 mM Hepes (low mobile H^+ buffering). The presence of 20 mM Hepes was thus expected to facilitate extracellular H^+ ion diffusion by reducing

the proportion of H^+ binding to fixed buffers, which would increase MCT transport. Conversely, a low concentration of mobile buffering with 1 mM Hepes was expected to reduce the rate of H^+ diffusion, and thus decrease MCT-mediated transport.

Under low levels of extracellular mobile H^+ buffering (1 mM Hepes), the biphasic pH_i response in the core suggested that lactate was transported through gap junctions to the spheroid core (**Fig 8.2.5.3**). Thus, low levels of extracellular mobile buffering limited MCT transport in the core, which was similar to the response previously observed in the presence of 5% CO_2/22 mM HCO_3^- (**Fig 8.2.5.1 B** and **8.2.5.2**). When the extracellular mobile H^+ buffering was increased with 20 mM Hepes, the biphasic response in the core was abolished and replaced with a monophasic pH_i response, which follows the MCT-facilitated cotransport of lactate and H^+ ions. These results suggest that the rate of extracellular H^+ diffusion is a rate-limiting step for the MCT-facilitated lactate transport in the spheroid core.

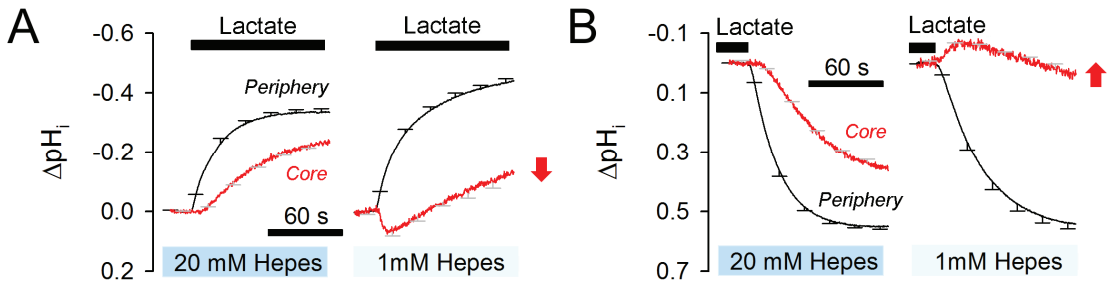


Figure 8.2.5.3 The effect of mobile extracellular H^+ buffering on lactate traffic in spheroids. ***(A)*** *In conditions of low extracellular mobile H^+ buffering (1 mM Hepes) the addition of lactate led to a biphasic response in intracellular pH (pH_i^+) in the spheroid core, which is an indication of gap junctional lactate traffic. When extracellular mobile H^+ buffering was increased (20 mM Hepes), the pH_i response in the core was monophasic, showing an acidification in both the*

periphery and the core in response to lactate addition. This response suggests that lactate is transported through MCTs and not through gap junctions in the presence of high extracellular mobile H^+ buffering. ***(B)*** *The pH_i response upon removal of lactate was symmetrical to that which occurred during lactate addition. In the presence of low extracellular mobile buffering, the lactate was transported through gap junctions, as evidenced by the biphasic pH_i response in the spheroid core. Conversely, in the presence of high mobile buffering, the pH_i response was reversed to a monophasic response indicating MCT transport. This emphasises that H^+ diffusion is the rate-limiting step for MCT transport of lactate in the spheroid core. The extent of mobile extracellular H^+ buffering thus determines the route of lactate traffic in spheroids.*

To test if gap junctional lactate transport in spheroids was established by Cx43 channels, lactate pulses were performed on spheroids formed by Colo357 cells that had been stably transfected with shRNA #1 against *GJA1* (Cx43). As a control, spheroids were grown from Colo357 cells stably transfected with unspecific scrambled shRNA. Spheroids generated from scramble-transfected Colo357 cells showed a biphasic pH_i response in the core in the presence of low extracellular mobile H^+ buffer (1 mM Hepes; **Fig 8.2.5.4**). This response is similar to that observed in wild type Colo357 spheroids in 1 mM Hepes (**Fig 8.2.5.3**). In spheroids grown from shRNA-induced knockdown of Cx43 (shRNA #1), the biphasic pH_i response in the core was markedly reduced in response to both lactate addition and removal (**Fig 8.2.5.4 A** and **B**). These results indicate that gap junctional lactate transport in Colo357 spheroids is mediated by Cx43 channels.

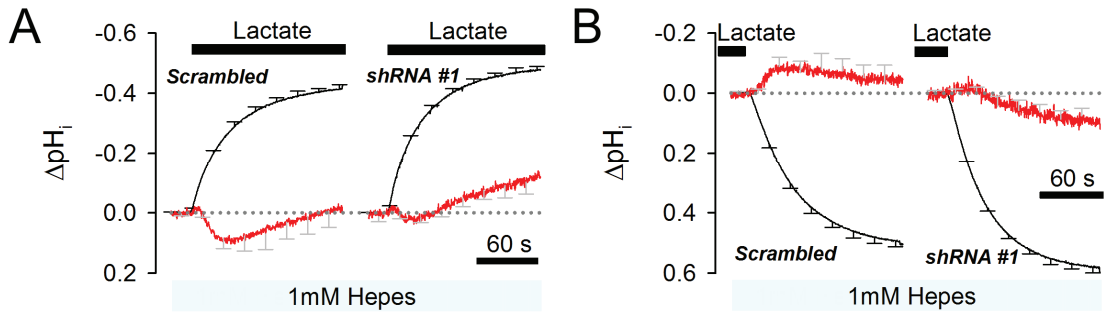


Figure 8.2.5.4 The effect of connexin 43 (Cx43) on syncytial lactate traffic in Colo357 spheroids. ***(A)*** *The response in intracellular pH (pH_i) measured in relation to the addition of 40 mM lactate in Colo357 cells transfected with a scrambled shRNA construct (scrambled) or shRNA #1 targeting GJA1 (Cx43).* ***(B)*** *The pH_i response measured in relation to the removal of 40 mM lactate. The experiment was performed in the presence of low extracellular H^+ buffering (1 mM Hepes). Scramble-transfected Colo357 cells exhibited a biphasic pH_i response in the core in accordance with gap junctional lactate transport. Upon down-regulation of Cx43 caused by shRNA #1, the biphasic response was abolished, indicating a shift towards MCT-facilitated lactate transport. These results suggest that Cx43 is responsible for the gap junctional transport of lactate in Colo357 cells. N = 3.*

Lactic acid generated by anaerobic glucose metabolism and ATP hydrolysis imposes an obstacle for the continued growth and survival of hypoxic cancer cells. To survive and maintain an alkaline pH_i permissive for proliferation, the hypoxic cancer cells must vent the acid generated from metabolism at a rate similar to that of its generation. Since the exofacial carbonic anhydrase CAIX has been shown to be upregulated in hypoxic areas in many cancers, CAs may play a role in the facilitation of lactic acid diffusion. Colo357 spheroids possessing both intra- and extracellular CA

activity (**Figs 6.2.3.3** and **6.4.3.3**) were assessed for the CA facilitated diffusion of lactic acid.

To assess whether CAs could play a role in facilitating the diffusion of lactic acid through a spheroid structure, spheroids were subjected to a lactate pulse in the presence of the CA inhibitor ATZ (100 µM). As seen in **Fig 8.2.5.5**, CA inhibition with ATZ led to an increased alkalinisation in the spheroid core upon the addition of lactate (**Fig 8.2.5.5 A**). Furthermore, the core acidification observed after the initial alkalinisation was slower in comparison to untreated control conditions. Accordingly, the presence of ATZ led to a mirror image of this response upon lactate removal (**Fig 8.2.5.5 B**), suggesting that CA inhibition reduces the extracellular lactate diffusion to the core of the spheroid and consequently increases the gap-junctionally-mediated lactate traffic.

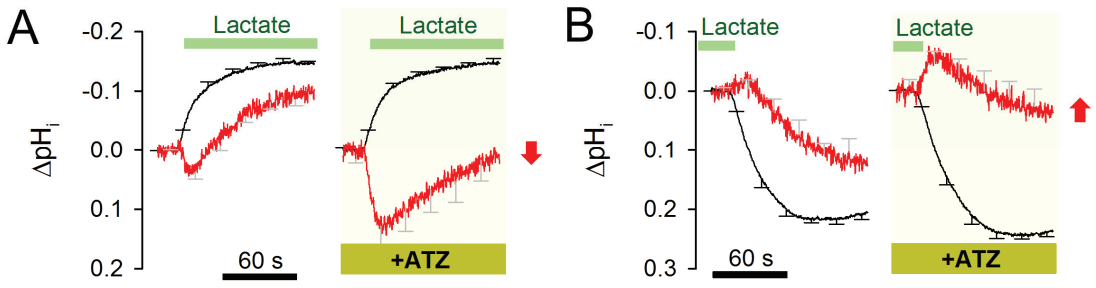


Figure 8.2.5.5 Facilitation of lactic acid diffusion by carbonic anhydrases (CAs). (A) *The pH_i response upon addition of 40 mM lactate to Colo357 spheroids superfused in 5% CO_2/22 mM HCO_3^- to allow the CA catalysed reaction. The ΔpH_i was measured in the periphery (black) and core (red) of the spheroids. Paired experiments were performed in the absence (left panel) or presence (right panel) of the CA inhibitor ATZ (100 µM).* ***(B)*** *The pH_i response as in (A) in response to removal of lactate.*

8.2.6 Endogenously produced lactate alkalinises the rim of Colo357 spheroids

Introduction. The cellular resting pH is determined by the in- and outward fluxes of acids and bases. In Colo357 monolayers, the resting pH was measured to 7.126±0.0075 (mean ± SEM, N = 250 cells). In syncytially coupled cells, the flux of chemically basic lactate ions produced by glycolytic metabolism may lead to an alkalinisation of recipient cells. The radial pH_i was therefore studied in lactate producing (glucose) or lactate deficient (galactose) Colo357 spheroids.

Methods. In order to test whether lactate produced endogenously could affect the cellular pH of gap junctionally coupled cells, Colo357 spheroids were grown in medium containing either glucose or galactose. Whereas glucose can feed both oxidative and glycolytic metabolism, galactose can only be respired oxidatively since no net ATP is generated from the glycolytic metabolism of galactose (229). Therefore, galactose containing medium does not lead to the endogenous production of lactate from glycolysis. Spheroids were grown from Colo357 cells for 3 days. Spheroids reached a radius of 110 µm. The spheroids were placed in medium containing either glucose or galactose for 3h. The pH_i was inferred from cSNARF1 fluorescence through the equatorial plane of the spheroid using confocal microscopy.

The effect of gap junctional coupling on radial pH_i of the spheroid was furthermore assess in glucose containing medium in the presence of 100 µM CBX in order to inhibit syncytial coupling through gap junctions.

In order to test whether endogenously produced lactate could affect pH_i via its transport through Cx43, spheroids were formed from Colo357 cells stably transfected with scrambled shRNA or shRNA #1 targeting *GJA1* (Cx43). The spheroids were incubated in glucose containing medium to allow production of lactate.

The spheroid pH_i measurements were performed under superfusion with physiological 5% CO_2/22 mM HCO_3^- buffered solution containing 11 mM of either glucose or galactose. The pH_i was assessed in nine concentric regions throughout the spheroid in order to assess whether gap junctional transport of lactate could affect the pH_i gradient from the core to the periphery.

Results. Colo357 spheroids grown in glucose containing medium showed a resting pH_i in the peripheral cells of ~0.3 pH units above the resting pH measured in Colo357 monolayers. When the lactate production was blocked by incubation in galactose, the alkalinity of the cells in the periphery was reduced (**Fig 8.2.6.1 B**). Therefore the alkaline pH_i of the cells in the spheroid periphery is a product of endogenous lactate production. Similarly, the downregulation of Cx43 led to a decreased alkalinisation of the spheroid periphery, indicating that Cx43 channels were responsible for the traffic of lactate (**Fig 8.2.6.1 C**). The chemical inhibition of gap junctional coupling with 100 μM CBX for 3 h also led to a reduction in peripheral alkalinisation. Incubation with CBX was accompanied by an additional acidification in the core. This is likely to be a side effect of the partial inhibitory effect of CBX on MCTs, possibly reducing the rate of lactic acid efflux from glycolytic cells.

In summary, these results suggest that endogenously produced lactate from the hypoxic spheroid core is transported through gap junctions to the periphery, where it alkalinises cells. This syncytial lactate transport is mediated by Cx43. The pH_i response arises from the uncoupled diffusion of fast lactate anions and slow H^+ ions through gap junctions.

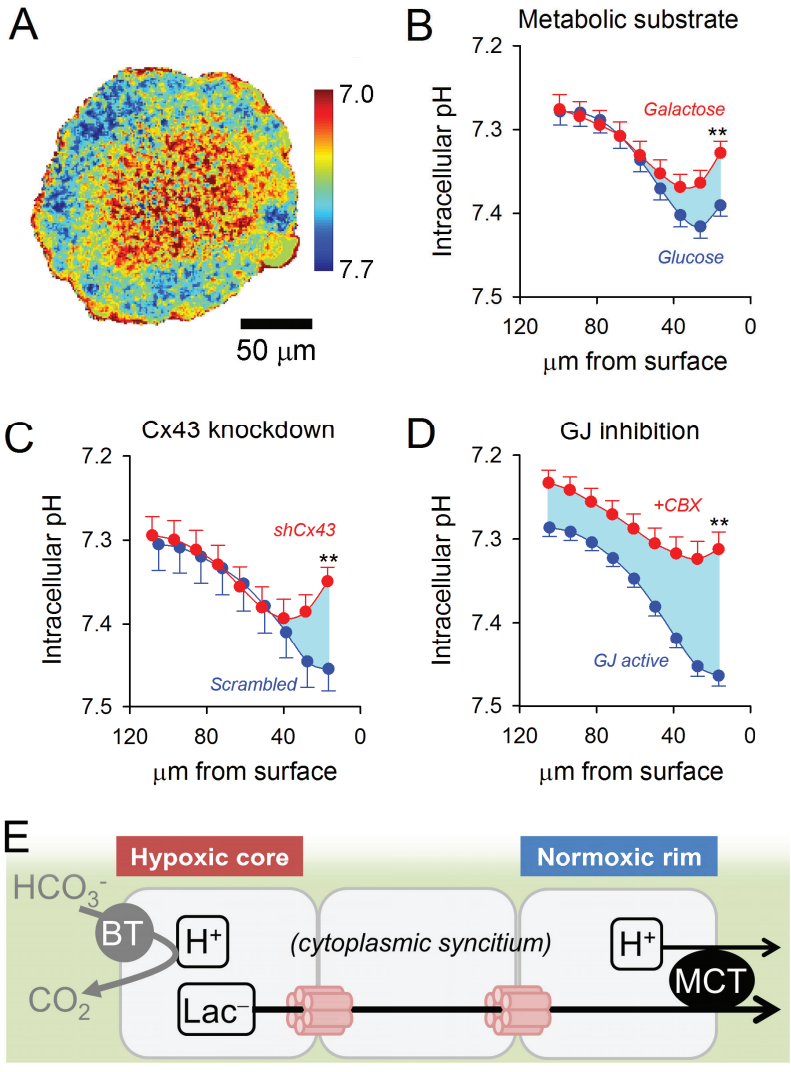


Figure 8.2.6.1 Lactate alkalinises the spheroid periphery upon transport from the hypoxic core via gap junctions. ***(A)*** *Heatmap showing the resting pH_i imaged through the equatorial*

plane of a Colo357 spheroid incubated in glucose. The spheroid periphery shows a higher degree of alkalinisation compared to the spheroid core. ***(B)*** *The pH_i of spheroids measured radially in nine regions of the spheroid. Spheroids incubated in glucose show an alkalinisation of the spheroid periphery. This alkalinisation is reduced upon incubation in galactose to inhibit the formation of lactate. N = 12 glucose and 8 galactose* ***(C)*** *Knockdown of Cx43 with shRNA #1 reduces the peripheral alkalinisation compared to scrambled shRNA controls. N = 12 scrambled, 14 shRNA #1.* ***(D)*** *Inhibition of gap junctional coupling with 100 µM CBX (3 h) reduces the peripheral alkalinisation of Colo357 spheroids. CBX also leads to an acidification of the spheroid core likely due to an off-target inhibition of MCTs.* ***(E)*** *Model of the gap junctional transport of lactate. Lactate produced in the hypoxic core is transported to the periphery where it alkalinises cells. Lactate is transported into the extracellular space via MCTs in the peripheral cells. H^+ ions in the hypoxic core are titrated by HCO_3^- taken up by bicarbonate transporters (BT).*

8.2.7 Cx43 knockdown increases lactic acid retention in Colo357 spheroids.

Introduction. Hypoxic cells situated far from blood supply are likely to be situated in an acidic extracellular environment. This imposes a barrier to MCT transport of lactate, since the permeation of lactate through MCT depends on the relative distribution of intracellular and extracellular lactate and H^+ ions ($[H^+]_I \times [lactate]_i = [H^+]_e \times [lactate]_e$). The extracellular acidity in hypoxic areas thus counteracts the transmembrane lactic acid transport in cells with the highest requirements of lactic acid export. The formation of an intracellular syncytium between hypoxic and normoxic cells close to a blood vessel could thus provide access of lactic acid into

normoxic cells. Since the extracellular acidity is expected to be reduced in normoxic compared to hypoxic areas, the conditions are more favourable to MCT-facilitated lactate transport. This will thus present hypoxic cells with a passive transport route for the lactic acid generated by metabolism. It is thus possible that a reduction of gap junctional coupling would lead to enhanced intracellular lactate retention in cells subjected to long diffusion distances. In order to test this, the steady-state intracellular lactate levels were analysed in Colo357 spheroids and monolayers.

Methods. Intracellular lactate retention was measured upon measurement of lactate in intracellular and extracellular fluid. Aliquots of the intracellular fraction was used for the measurement of osmolarity, protein and glucose concentration in order to determine the intracellular lactate concentration (**Fig 8.2.7.1 A**). The procedure and calculations are specified in **section 3.13**. In order to test the intracellular lactate retention in circumstances of minimal diffusion distance to the surrounding medium, cells were grown in monolayers. Under such circumstances, the cells are in direct contact with the culture medium and the intracellular lactate is thus not subjected to an extracellular diffusion barrier. On the contrary, cells situated in the core of spheroids are subjected to longer diffusion distances to the surrounding medium. Monolayers were grown for 96 h prior to measurements. Spheroids were grown to different sized upon incubation in spinner flasks for 36 to 120 h under constant rotation (**Section 3.3, Fig 8.2.7.1 A**). In order to assess the role of gap junctions in lactate retention, measurements were made in monolayers and spheroids generated from wild type Colo357 cells, Colo357 cells stably transfected with scrambled shRNA, or shRNA #1 or #2 against *GJA1* (Cx43).

Results. In order to assure that shRNA transfection did not affect the endogenous production of lactate, Colo357 monolayers were assessed for intracellular lactate. As seen in **figure 8.2.7.1 B**, all shRNA transfectant Colo357 cell lines showed similar levels of lactate as wild type cells when grown in glucose. These results indicate that the rate of glycolysis is comparable among the cell lines. The measured lactate concentrations were derived from glycolysis, as wild type Colo357 cells grown in galactose (blocking glycolytic metabolism) showed absence of intracellular lactate (**Fig 8.2.7.1 B**, first column).

The intracellular lactate retention could increase upon increasing the diffusion distance in spheroids. The lactate retention was thus assessed in Colo357 monolayers that doesn't experience a diffusion distance and compared the measurements to Colo357 spheroids grown to different sizes (**Fig 8.2.7.1 C**). Monolayers and spheroids of ~75 µm showed similar lactate retention levels, indicating that spheroids up to this size are fully capable of venting endogenously produced lactate. In larger spheroids (>250 µm) the lactate retention significantly increased (**Fig 8.2.7.1 C**). This indicates that increased diffusion distances are a barrier to lactate traffic.

In order to test whether the lactate venting properties seen in spheroids of ~75 µm (**Fig 8.2.7.1 C**) was associated with gap junctional coupling, spheroids of similar size were grown from shRNA#1 Colo357 cells showing reduced levels of Cx43 (**Fig 7.2.3.2 A**). As seen in **figure 8.2.7.1 D**, Cx43 knockdown spheroids grown for 3 days to ~75 µm showed a significant increase in the lactate retention compared to scrambled control. These results were not attributable to changes in glycolysis or MCT expression as seen

in figure **8.2.7.1 B** and **figure 8.2.1.2** respectively. Cx43 knockdown spheroids grown for 5 days did not show an increased lactate retention compared to scrambled controls (**Fig 8.2.7.1 D**). This may however be a consequence of a higher growth rate observed in scrambled spheroids (**Fig 8.2.7.1 D**, lower panel). This increased growth rate may be a result of improved lactate venting.

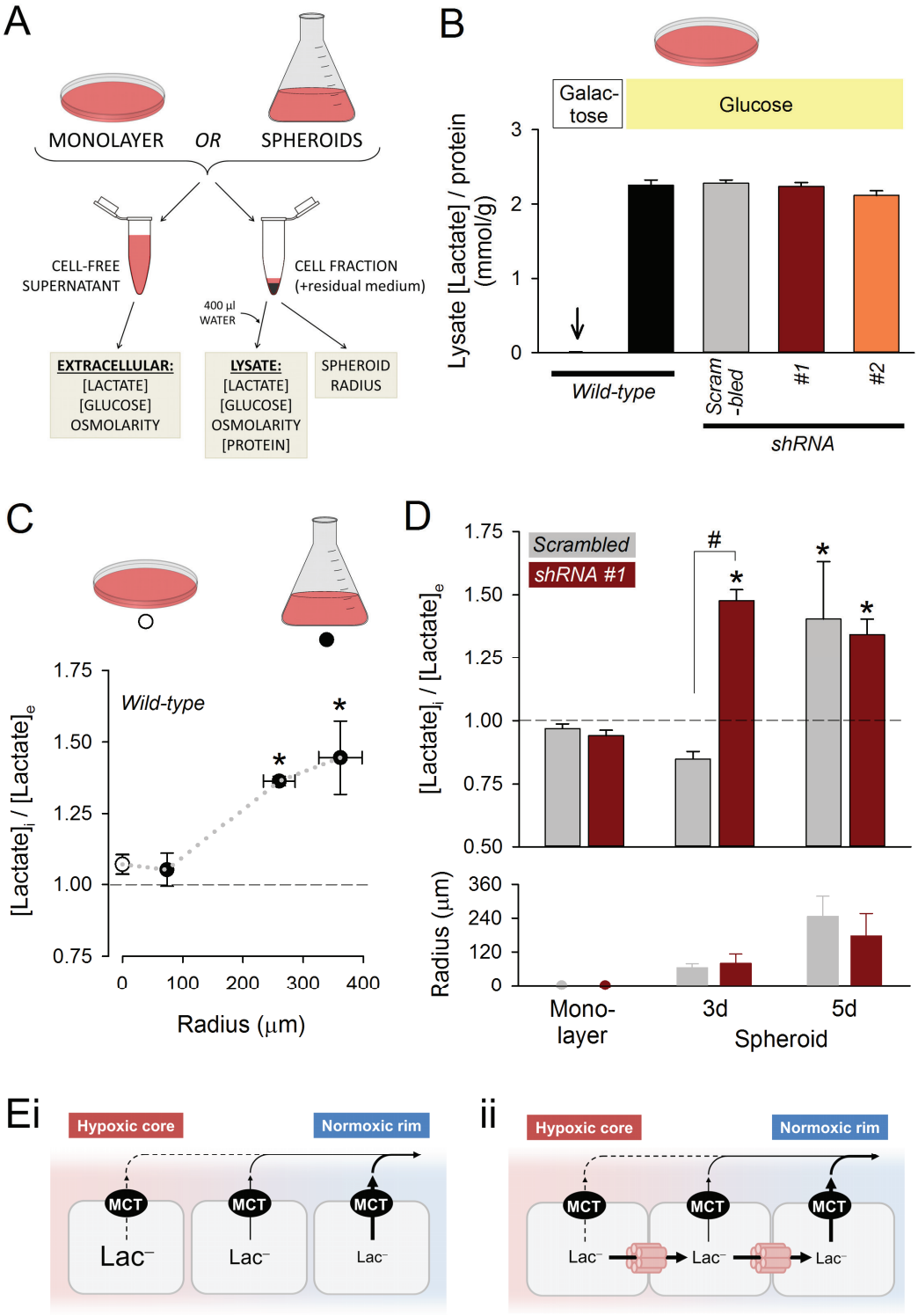


Figure 8.2.7.1 Biochemical determination of intracellular lactate retention. (A) *Schematic representation of the protocol. Monolayers and spheroids were grown from Colo357 cells of either wild type, scrambled shRNA, shRNA #1 against GJA1 (Cx43) or shRNA #2 against GJA1*

(Cx43). Extracellular medium was collected and centrifuged to remove cells and spheroids. Spheroids were collected and lysed in 400 µl H_2O and cell debris removed upon centrifugation. The extracellular supernatant was analysed for osmolarity, lactate and glucose concentrations. The intracellular lysate was assessed for osmolarity, lactate, glucose and protein concentrations. From each spheroid batch, 30 – 120 spheroids were collected for measurement of size. ***(B)*** *The ratio of intracellular lactate / protein in lysates from monolayers of the four cell types grown in the presence of glucose. Incubation in glucose containing medium allows for the glycolytic production of lactate. To inhibit glycolytic production of lactate, wild type Colo357 cells were grown in galactose. Bars represent mean ± SEM of six lysates.* ***(C)*** *The intracellular lactate retention in Colo357 monolayers and spheroids expressed as a function of measured radius. Intracellular lactate retention was measured as the ratio of intracellular and extracellular lactate concentrations. Measurements were made in wild type Colo357 monolayers (open circle, radius = 0, N=6) or spheroids of different size (four lysates from over 1000 spheroids in each condition). Measurements represent mean ± SEM. A statistically significant increase in lactate retention compared to monolayers was denoted with * (unpaired t-test, $p<0.05$).* ***(D)*** *Lactate retention in stable shRNA Colo357 transfectants. The lower panel shows the radius and time points of the samples shown in the upper panel. The upper panel shows the lactate retention measurements (the ratio of intra- and extracellular lactate concentrations) in scrambled-transfected Colo357 samples and shRNA #1-transfected samples. Statistical analysis was performed using unpaired t-test. Significant difference between scrambled and shRNA #1 samples drawn from identical time points is denoted with # ($p<0.05$). Statistically significant difference between lactate retention in spheroids compared to monolayers is denoted with * ($p<0.05$).* ***(E)*** *Model representing the lactate transport routes from hypoxic to normoxic areas of a spheroid. (i) Without gap junctional coupling, lactate is transported through MCT into the extracellular space. The low pH_e of hypoxic areas impose a barrier to MCT-facilitated lactate extrusion. (ii) In the presence of gap junctions, the intracellular syncytium allows lactate to diffuse to normoxic cells, where MCT-facilitated*

lactate extrusion is favoured. The presence of gap junctions thus decreases the lactate retention by facilitating its extrusion through MCT in normoxic areas.

8.2.8 Knockdown of *GJA1* (Cx43) renders Colo357 cells less able to expand in the proliferating rim of spheroids

Introduction. As determined in **section 8.2.5 – 8.2.7**, gap junctional coupling formed by Cx43 proteins provide Colo357 cells with a transport route for lactate. The basic lactate anion produced in glycolytic cells in the spheroid core can thus alkalinise normoxic cells in the spheroid periphery upon traffic through gap junctions (**Fig 8.2.6.1**). Such alkalinisation of the cells in the spheroid periphery renders the cells with a pH_i conductive for proliferation (90). It is thus possible that cells expressing high levels of Cx43 protein would acquire a growth advantage and be more efficient in colonising the proliferating periphery of spheroids in comparison to cells expressing low levels of Cx43 protein. In order to test this, wild-type Colo357 cells expressing high levels of Cx43 protein were co-cultured with shRNA-induced Cx43 knockdown cells.

Methods. Spheroids were formed from co-culturing wild-type Colo357 cells with Colo357 cells stably transfected with shRNA #1 against *GJA1*, shRNA #2 against *GJA1*. Spheroids were formed from 400 cells consisting of wild-type and shRNA-transfected cells in a 1:1 ratio. The spheroids co-cultures were grown for 3 days prior to confocal imaging through the equatorial plane. Transmission images were acquired in order to determine the spatial location of wild-type cells. eGFP fluorescence was used for determination of transfectants. Fluorescent images of eGFP fluorescence

were acquired with a 488 nm laser and a 3 µm pinhole. Spheroid fluorescence was quantified in in 10 consecutive regions and normalised to the mean fluorescence throughout the spheroid.

Results. The spheroid co-culture competition assay revealed a segregation of the non-fluorescent Cx43 expressing wild type Colo357 cells to the proliferating spheroid periphery, whereas the fluorescent Cx43 knockdowns (shRNA #1) were preferentially found in the spheroid core (**Fig 8.2.8.1 A**). The wild type cells preferentially occupied the periphery, and formed a crescent around the core of fluorescent Cx43 knockdown cells. The Colo357 cells stably transfected with shRNA #1 showed a 70% reduction in Cx43 protein levels (see **figure 7.2.3.2 A**). The results shown in **figure 8.2.8.1 A** indicate that cells expressing high levels of Cx43 are more successful in colonising the proliferating periphery of spheroids whereas cells expressing low levels of Cx43 (shRNA #1) are referred to the spheroid core. These cells are thus placed further away from the culture medium providing nutrients and oxygen. In order to further investigate the role of Cx43 in the ability of cells to colonise the proliferating spheroid periphery, co-cultures were made from shRNA #2 transfected cells showing a 45% knockdown of Cx43 (**Fig 8.2.8.1 B**). As in **figure 8.2.8.1 A**, the reduced level of Cx43 in shRNA #2 knockdown co-cultures led to a segregation of cells based on the Cx43 protein levels. The co-cultures showed clustering of eGFP positive cells to the spheroid core whereas eGFP negative wild type cells occupied the spheroid periphery.

As a control for the effect of Cx43 in the co-culture experiment, co-cultures of wild type and scrambled shRNA-transfected Colo357 cells were made (**Fig 8.2.8.1 C**). These co-culture spheroids showed a random allocation of fluorescent scrambled shRNA-transfectants and non-fluorescent wild type cells. This indicates that none of the two phenotypes showed a significant advantage in colonising the proliferating spheroid periphery.

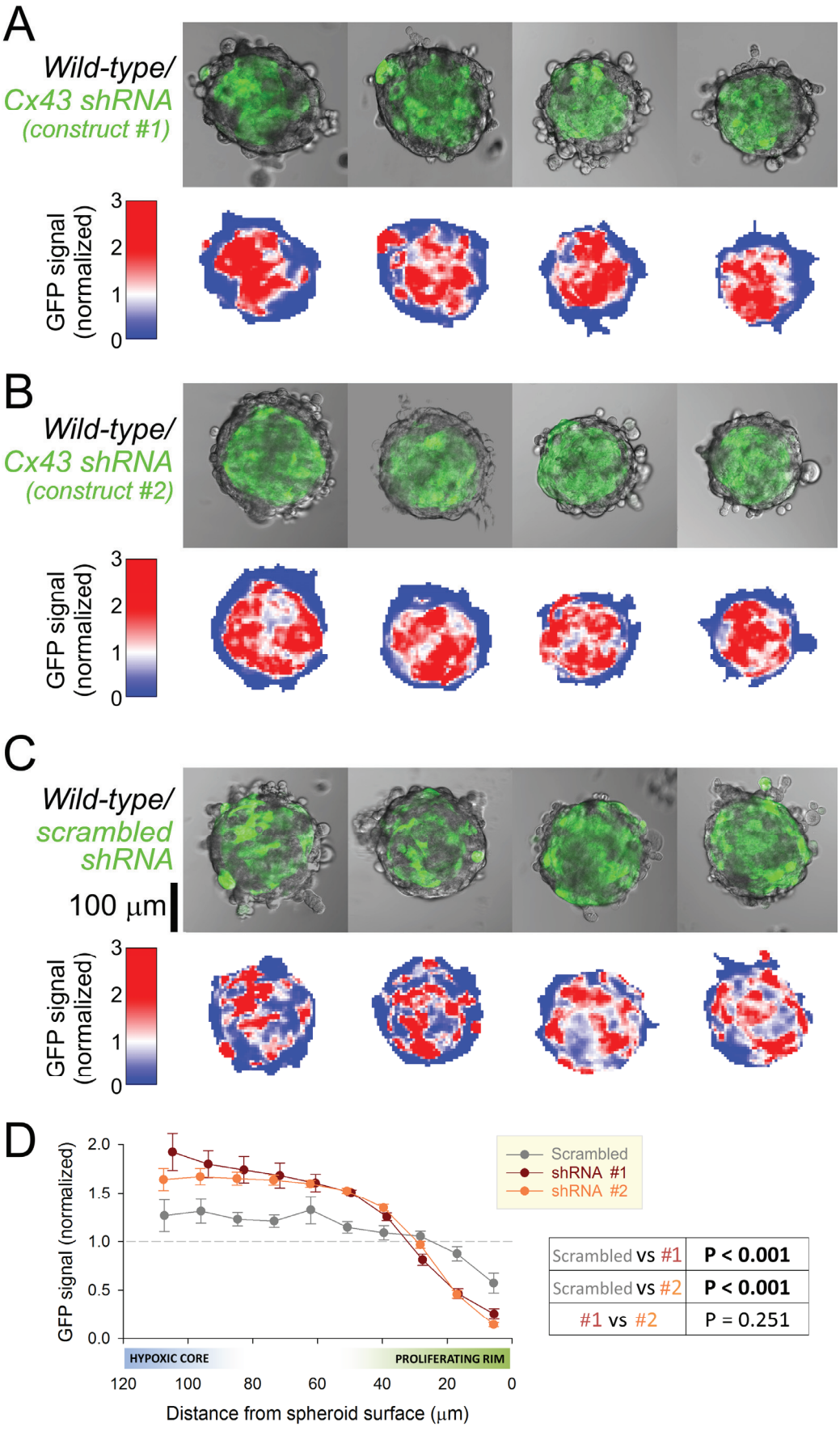

A
Wild-type/
Cx43 shRNA
(construct #1)
GFP signal
(normalized)
3
2
1
0
B
Wild-type/
Cx43 shRNA
(construct #2)
GFP signal
(normalized)
3
2
1
0
C
Wild-type/
scrambled
shRNA
100 μm
GFP signal
(normalized)
3
2
1
0
D
GFP signal (normalized)
2.0
1.5
1.0
0.5
0.0
Scrambled
shRNA #1
shRNA #2
HYPOXIC CORE
PROLIFERATING RIM
120
100
80
60
40
20
0
Distance from spheroid surface (μm)
Scrambled vs #1
P < 0.001
Scrambled vs #2
P < 0.001
#1 vs #2
P = 0.251

Figure 8.2.8.1 Co-culturing of wild-type and GJA1 knockdown Colo357 cells in spheroids. ***(A)*** *Spheroid co-culture of non-fluorescent wild-type and green eGFP fluorescent shRNA #1 transfected Colo357 cells showing a 70% Cx43 knockdown (as seen in figure 7.4.2 A). Wild type and Cx43 knockdown cells were seeded in a 1:1 ratio. Upper panel shows the superimposition of eGFP fluorescence and transmission image acquired in the equatorial plane of the spheroid. The corresponding fluorescence normalised to the mean spheroid fluorescence is shown in the lower panel. Red coloured pixels represent above mean fluorescence whereas blue coloured pixels represent below mean fluorescence. Fluorescence signal acquisition was performed with a 3 µm pinhole. Cx43 knockdown cells segregate to the spheroid core whereas Cx43 expressing wild-type cells occupy the proliferating periphery of the spheroid.* ***(B)*** *Spheroid co-culture consisting of wild-type and shRNA #2 transfected Colo357 cells showing a 45% knockdown of Cx43 (see figure 7.4.2 A). The two cell types were mixed in a 1:1 ratio. The Cx43 knockdown cells show a similar spatial segregation as observed in (a).* ***(B)*** *Control experiment showing co-culture spheroids composed of wild-type and unspecific scrambled shRNA-transfected Colo357 cells seeded in a 1:1 ratio. Wild type and scrambled shRNA-transfected cells show a random spatial allocation with no clear segregation.* ***(D)*** *Quantification of the eGFP signal normalised to the mean fluorescent signal of the spheroid. The eGFP signal is plotted as a function of distance from the surface of the spheroid. The plot represents mean ± SEM of 13, 22 and 11 spheroids (shRNA#1, shRNA#2 and scrambled respectively. Statistical analysis (ANOVA) is shown in the table.*

8.3 Summary of findings

- Gap junctional coupling facilitates lactate transport across Colo357 spheroids.
- In hypoxic regions of tumour growths, lactate permeates Cx43 gap junctions faster than the canonical MCT dependent mechanism in Colo357 spheroids.
- Endogenously produced lactate transported via gap junctions alkalinises recipient cells and creates an environment conductive for growth herein.
- Cx43 expressing cells are better at colonising the proliferating rim of spheroids compared to Cx43 knockdown cells.

9 IN VIVO INVESTIGATION OF CX43 IN ORTHOTOPIC XENOGRAFT MOUSE MODELS

Objective: To assess the protein localisation of Cx43 in vivo in orthotopic PDAC tumour xenografts and their metastases and compare to the distribution of markers of chronic acidosis (LAMP2 staining).

The data presented in this chapter was performed during a secondment to Professor Frauke Alves' laboratory as described in **section 3.14** and is thus not solely my own work.

9.1 Background

The tumour microenvironment changes when tumour cells grow away from blood vessels supplying nutrients and oxygen (40). This may create hypoxic niches in areas distant from blood vessels. Due to the high reactivity of the H^+ ion, its diffusion is slow (84). This slow H^+ diffusion leads to areas of extracellular acidosis upon long diffusion distances to the nearest blood vessel. In areas of high extracellular H^+ ion concentration, MCT-meditated lactate efflux from cells is inhibited (84). Under such circumstances lactate may be transported through gap junctions that are not affected by changes in pH_e. The role of gap junction coupling in cancer has been overlooked due to the consensus that connexins are downregulated in cancer (205). Furthermore, studies performed in monolayers under uniform superfusion leads to a collapse of cell-to-cell gradient which is a prerequisite for the conductance of net current through gap junctions. Similarly, when cell lines are cultured in monolayers in direct contact with

the culture medium, the cell-to-cell gradients are disrupted. Therefore there is no survival advantage of upregulating gap junctions in cell monolayers. The micro-environmental changes in tumours such as development of hypoxia and acidosis are likely to create micro-environmental selection pressures (**section 2.10**) (42, 52, 271). This section serves to investigate the immunoreactivity of Cx43 in vivo.

9.2 Results

9.2.1 Xenografts of MiaPaCa2 cells

Introduction. Some PDAC cell lines such as MiaPaCa2 do not express Cx43 when grown in monolayer culture *in vitro (Fig 7.2.2.1)*. When grown in monolayers, cells are in direct contact with the culture medium. Due to the direct contact with the culture medium, the cells do not experience diffusional restrictions on the solutes that are transported in and out of the cells. Therefore, cells grown in monolayer culture are not likely to experience a cell-to-cell lactate gradient. Thus, they are not presented with the circumstances under which the Cx43 expression may confer an advantage to cells via its facilitation of lactate transport. For Cx43 to confer an advantage to cells, lactate transport through MCT should be rate-limited in areas of the tumour. This may be the case *in vivo* in tumour tissue. In 3-dimensional tissue structure where lactate diffusion may be restricted, Cx43 expression may thus become evident. In order to test whether Cx43 expression would be upregulated in MiaPaCa2 cells grown in a tissue structure, MiaPaCa2 xenografts were analysed for their expression of Cx43. In order

for the connexin 43 protein to form functional gap junctions *in vivo*, the protein must assemble into channels in the plasma membrane. Therefore, the presence of Cx43 staining at the cell-to-cell borders was investigated.

Methods. MiaPaCa2 cells were orthotopically implanted into male NMRI $fox^{nu/nu}$ mice. Sections of the primary tumour as well as areas invading the mouse pancreas, duodenum mucosa and the muscularis externa of the stomach were analysed for Cx43 levels. Sections of metastatic lesions in the lungs were included in the analysis. Human EGFR staining was used in order to distinguish the human xenografted MiaPaCa2 cells from the endogenous mouse tissue. The Cx43 and EGFR staining was performed on adjacent sections of the tumour. Image J software was used for computational generation of overlay images of Cx43 and EGFR staining. Histological landmarks in adjacent sections were traced and used for the registration of image pairs between the tissue sections. Red AEC staining of antibodies against EGFR or Cx43 was identified computationally by colour filtering. In overlay images, EGFR-positive pixels indicating the presence of human MiaPaCa2 cells were assigned a blue colour whereas Cx43-positive pixels were assigned a red colour. Purple areas indicate areas of Cx43 and EGFR colocalisation.

Cx43 positive areas of lung metastases and duodenum invasion were assessed for the presence of membrane associated Cx43 staining. The Cx43 expression was assessed in tissue expressing low levels of Cx43 (lung metastasis, **Fig 9.2.1.2 A**) and strong Cx43 staining (tumour invading the duodenum, **Fig 9.2.1.2 B**). These areas were

chosen in order to determine whether differences in Cx43 protein levels fostered discrepancies in Cx43 protein localisation *in vivo*.

Results. Primary tumours derived from MiaPaCa2 xenografts showed no visible levels of Cx43 staining (**Fig 9.2.1.1 A**). The cells of the primary tumour mass consisted of human MiaPaCa2 cells as indicated by the EGFR staining. This is represented by the blue colour in the overlay image (**Fig 9.2.1.1 A**, right column). The lack of Cx43 protein levels in the primary tumour is in accordance with the lack of Cx43 protein in MiaPaCa2 cells grown in monolayers as assessed by western blot (**Fig 7.2.2.1**). The majority of metastatic lung lesions induced by the MiaPaCa2 xenografts showed negative or low Cx43 immunoreactivity, although a subset of metastasis were positive for Cx43 staining. Tissue sections of Cx43 negative and positive lung metastases are shown in **figure 9.2.1.1 B** and **figure 9.2.1.1 C** respectively. Cx43 immunoreactivity was profoundly increased in areas of the primary tumour invading adjacent mouse tissue. Clusters of MiaPaCa2 cells invading the mouse pancreas showed high Cx43 immunoreactivity (**Fig 9.2.1.1 D**). The Cx43 immunoreactivity in these invading areas is in marked contrast to the absence of Cx43 immunoreactivity observed in the primary tumour mass (**Fig 9.2.1.1 A**). Areas of MiaPaCa2 tumour invasion into the duodenal mucosa also showed extensive Cx43 expression (**Fig 9.2.1.1 E**). Assessment of MiaPaCa2 tumour invasion into the stomach muscularis revealed widespread EGFR-positive areas showing high levels of Cx43 immunoreactivity (**Fig 9.2.1.1 F**). These results reveal a remarkable upregulation of Cx43 protein in all of the assessed areas of tumour invasion, despite absence of Cx43 immunoreactivity within the primary tumour

mass. This could indicate a role of Cx43 in areas of tumour invasion of MiaPaCa2 xenografts.

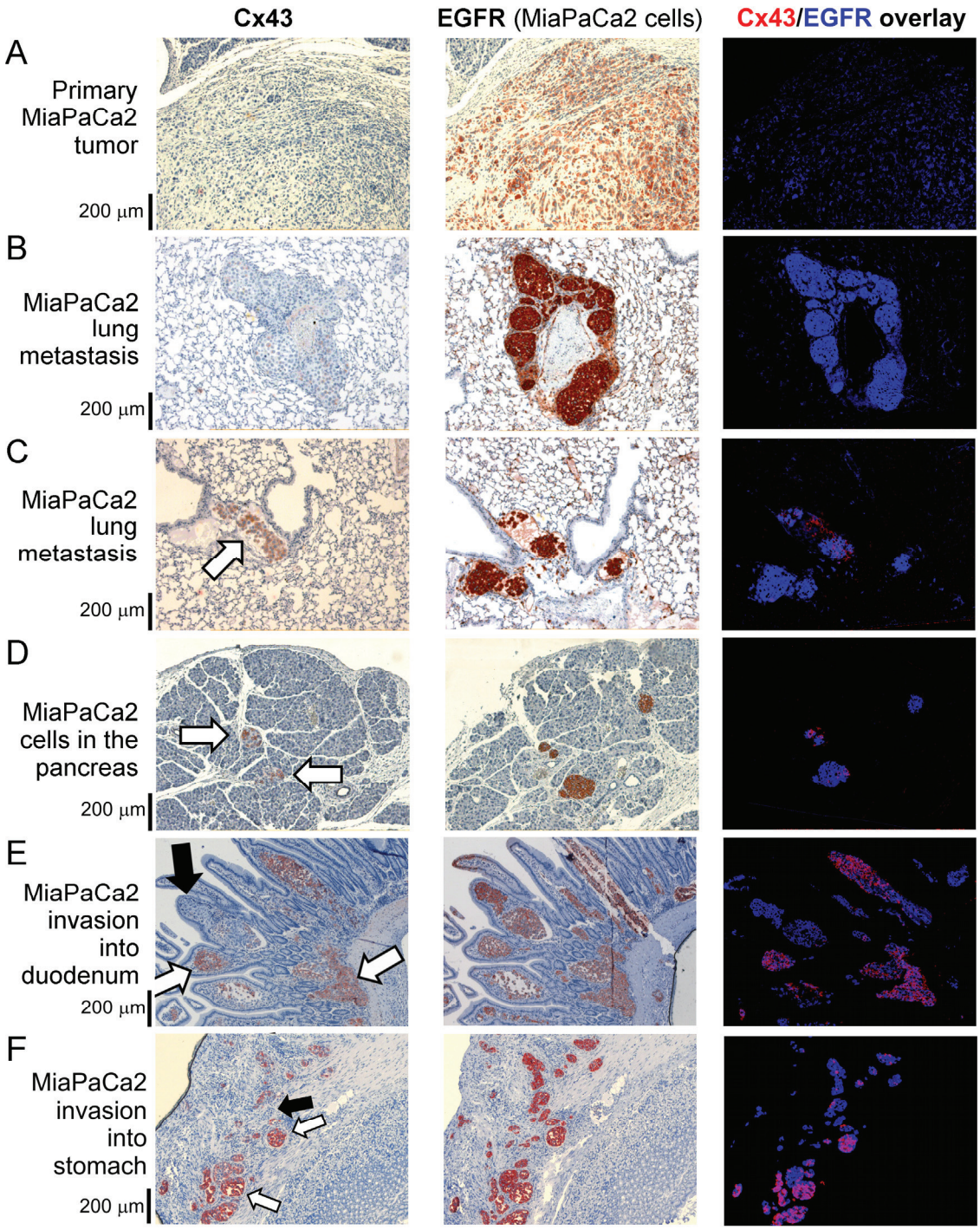


Figure 9.2.1.1 Immunohistochemical investigation of connexin 43 (Cx43) in orthotopic MiaPaCa2 xenografts. *Connexin 43 (Cx43) and human epidermal growth factor receptor (EGFR) were immunohistochemically analysed in adjacent sections of MiaPaCa2 xenograft. Immunohistochemical analysis was performed on sections including the MiaPaCa2 primary tumour, sites of invasion into pancreas, duodenum and stomach as well as metastasis to the lungs. Cx43 immunoreactivity is presented in the left column. Human EGFR receptor staining (central column) serves as a marker of human cells. Computated overlay images of Cx43 (red) and EGFR staining (blue) is shown in the right column. The computated overlay images serves to visualise the Cx43 staining present in areas of human MiaPaCa2 cells marked by EGFR staining (blue). Overlay images (right column) were generated upon registration of image pairs of Cx43 and EGFR staining and filtered by colour in adjacent tumour sections using Image J software.* ***(A)*** *Sections of the primary MiaPaCa2 tumour. The primary tumour mass shows absence of Cx43 staining (left column). Red AEC staining of EGFR presented in the central column probes MiaPaCa2 cells situated in the H&E stained mouse pancreas visible in top left corner of the image. Overlay image (right column) shows the absence of red Cx43 signal and presence of EGFR staining in the primary tumour mass represented by blue colour.* ***(B)*** *Cx43 negative MiaPaCa2 lung metastasis identified by EGFR staining (central column). Overlay image presented in the right column shows the MiaPaCa2 lung metastasis (blue colour) negative for Cx43 staining (red colour).* ***(C)*** *Lung metastasis showing Cx43 staining (left column, white arrow) within the EGFR-positive MiaPaCa2 cells (central column).* ***(D)*** *Cx43 positive regions of MiaPaCa2 tumour invasion into the mouse pancreas. The areas of MiaPaCa2 staining were visualised by red AEC stained EGFR regions within the H&E stained mouse pancreas (central column). The Cx43 stained areas are represented by white arrows (left column) and red colour in the overlay image (right column).* ***(E)*** *Cx43 positive areas of tumour invasion into the duodenum. Sections of the mouse duodenum were infiltrated by Cx43 positive MiaPaCa2 tumour cells (white arrows, left column). The colocalisation of Cx43 and MiaPaCa2 cells is shown by overlap with EGFR staining (central and right column). Some EGFR positive*

areas did not show Cx43 staining as shown by black arrow in left column and overlay images in right column ***(F)*** *Cx43 positive tumour invasion (white arrows) into the stomach muscularis. The Cx43 staining was confined to MiaPaCa2 cells as shown in overlay images (right column). Some EGFR positive areas are Cx43 negative as shown by black arrows and blue areas of overlay images.*

In metastatic MiaPaCa2 lesions in the lung showing low levels of Cx43 staining, the staining was concentrated along the cell-to-cell border (**Fig 9.2.1.2 A**). These results suggest that even sparse levels of Cx43 can localise to the cell membrane where they may form functional gap junctions. In areas of tumour invasion into the duodenum where Cx43 expression is high, the Cx43 expression appeared most concentrated along the cell-to-cell borders, indicated with black arrows (**Fig 9.2.1.2 B**). Such membrane associated Cx43 structures are likely to be assembled into functional gap junctions. The presence of Cx43 staining in the tumour cell cytoplasm may be a result of constitutive Cx43 production and a resulting accumulation of Cx43 protein in the golgi apparatus. These results suggest that the amount of Cx43 protein level within cells does not affect its localisation to the cell membrane.

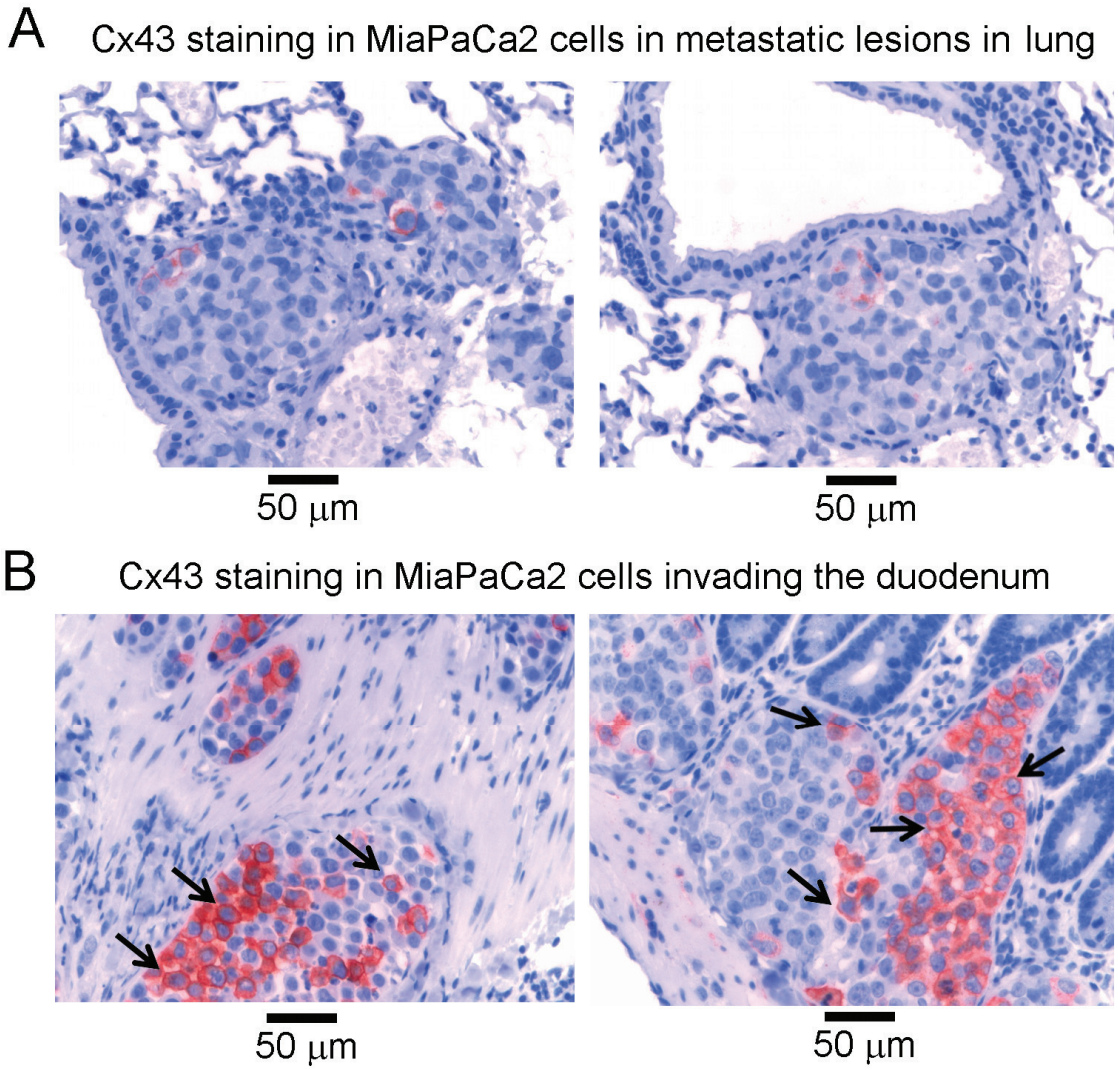


Figure 9.2.1.2 Observation of membrane associated Cx43 immunoreactivity in MiaPaCa2 invasion and metastasis. ***(A)*** *Low Cx43 staining in MiaPaCa2 lung metastases from two different animals. The most intense Cx43 staining appears along the cell-to-cell borders.* ***(B)*** *High levels of Cx43 staining observed in areas of tumour invasion into the duodenum. The Cx43 staining is high throughout the cells but appears most concentrated along cell-to-cell borders (black arrows) where they may form functional gap junctions.*

9.2.2 Xenografts of PANC1 cells

Introduction. To test whether the Cx43 staining patterns observed in MiaPaCa2 xenografts were specific for that individual cell line or whether it could be recapitulated in xenografts from another PDAC cell line, xenografts of a different PDAC cell line, PANC1, were grown and analysed.

Methods. Orthotopic PANC1 xenografts were generated in male NMRI $fox^{nu/nu}$ mice. Adjacent tumour sections were analysed for Cx43 and EGFR staining. Tumour sections of the primary PANC1 tumour mass and areas of PANC1 invasion into the pancreas were analysed. Western blots of PANC1 monolayer lysates were performed in order to determine the Cx43 protein levels of PANC1 cells grown in monolayer culture.

Results. PANC1 cells grown in monolayer culture showed low levels of Cx43 protein (**Fig 9.2.2.1 A**). In comparison, MiaPaCa2 cells showed no Cx43 protein level when grown in monolayer culture (**Fig 7.2.2.1**). As in monolayers, orthotopic PANC1 primary tumour xenografts showed low levels of Cx43 (**Fig 9.2.2.1 B**). The area of the primary tumour invading the mouse pancreas showed elevated levels of Cx43 staining (**Fig 9.2.2.1 C**). These results indicate that the upregulation of Cx43 protein levels in invasive areas are not confined to the MiaPaCa2 cell line. The results presented in **figure 9.2.2.1** thus provide further evidence for a role of Cx43 in invasive areas of PDAC tumours.

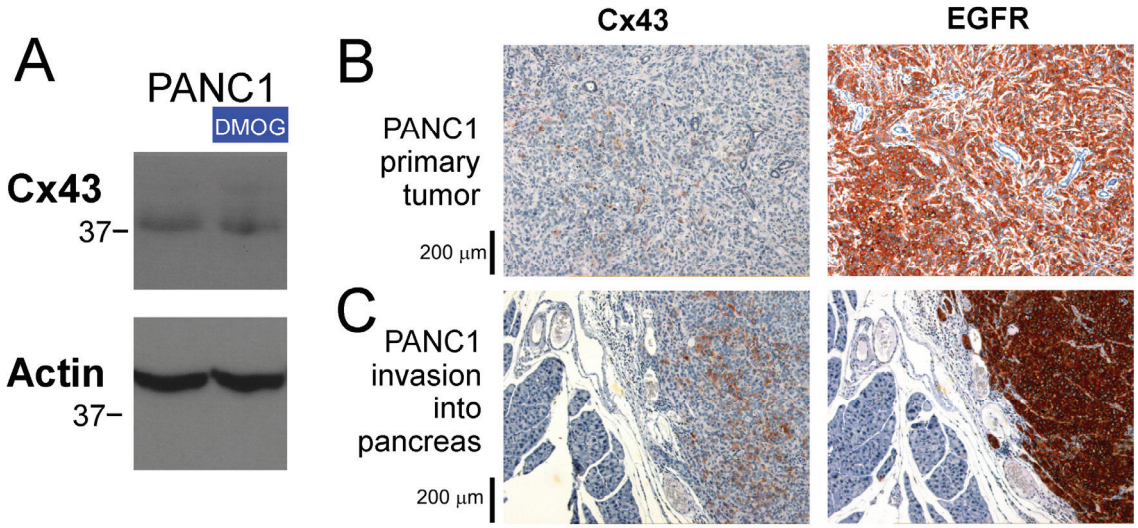


Figure 9.2.2.1 Cx43 immunoreactivity in PANC1 cells grown in monolayer culture and orthotopic xenografts. ***(A)*** *Western blot showing the detection of low levels of Cx43 protein in PANC1 cells grown in monolayer culture in normoxia (left column) and chemically induced hypoxic signalling (1 mM DMOG). Protein marker bands are indicated in kDa on the left side of the blots. Actin was used as a loading control.* ***(B)*** *Adjacent sections of a primary PANC1 primary tumour stained for Cx43 and EGFR. Low levels of Cx43 staining are present in PANC1 cells of the primary tumours.* ***(C)*** *Areas of PANC1 invasion into the mouse pancreas reveals an increase in Cx43 staining along the invasive border of the primary tumour.*

9.2.3 Evidence for chronic acidosis in MiaPaCa2 metastasis and invasive areas

Introduction. Gap junctional transport of lactate may be preferential in tumour areas where MCT-facilitated lactate transport is inhibited by a low extracellular pH (84). Such areas may develop in under-perfused regions of the tumour. Due to the 1:1 ratio of lactate and H^+ ions, high extracellular H^+ ion concentration (low pH_e) is

expected to limit the MCT-mediated lactate efflux from cells. This may create an environment where gap junctional lactate transport is beneficial to the tumour cells. Plasma membrane associated lysososomal-associated membrane protein-2 (LAMP2) has recently been identified as a marker of chronic extracellular acidosis (108). Therefore the membrane association of LAMP2 was assessed in areas of tumour invasion where Cx43 immunoreactivity was shown to be high (**Fig 9.2.1.1 E - F**).

In order to gather further information on the extent of Cx43 expression and chronic extracellular acidosis in the invading regions of MiaPaCa2 xenografts, the proportions of Cx43 and LAMP2 positive regions within EGFR-positive invading areas were quantified.

Methods. Tissue sections of primary MiaPaCa2 tumour xenografts and areas of invasion into the mouse duodenum and stomach muscularis were stained for LAMP2. The subcellular localisation was assessed in all tissue sections in order to identify membrane associated LAMP2. Clusters of MiaPaCa2 cells invading the pancreas or gut of the mouse were chosen for the analysis. 13 tissue sections from four mice were included in the Cx43 staining. 17 tissue sections from four mice were investigated for LAMP2. Adjacent tissue sections were stained with EGFR in order to distinguish human MiaPaCa2 cells from mouse tissue. Invading clusters of MiaPaCa2 cells were identified by positive EGFR staining in adjacent sections and scored positive or negative for Cx43 or LAMP2 immunoreactivity. For the analysis of Cx43, 547 EGFR-positive MiaPaCa2 cell clusters were analysed whereas 117 MiaPaCa2 cell clusters were included in the analysis of LAMP2 staining.

Results. Tissue sections of the primary MiaPaCa2 tumour revealed a diffuse staining of LAMP2 (**Fig 9.2.3.1 Ai and ii**). The primary tumours did not show a clear allocation of LAMP2 staining to the cell membrane. These results suggest that the MiaPaCa2 cells were not subjected to chronic extracellular acidosis. However, MiaPaCa2 cells invading the mouse mucosa of the duodenum revealed a subset of cells with plasma membrane associated LAMP2 staining (**Fig 9.2.3.1 Bi**, black arrows). Likewise, MiaPaCa2 cells invading the stomach muscularis showed a subset of cells with plasma membrane associated LAMP2 staining (**Fig 9.2.3.1 Bi**, black arrows). These results suggest that invasive areas experience a degree of chronic extracellular acidosis as revealed by the allocation of LAMP2 to the plasma membrane.

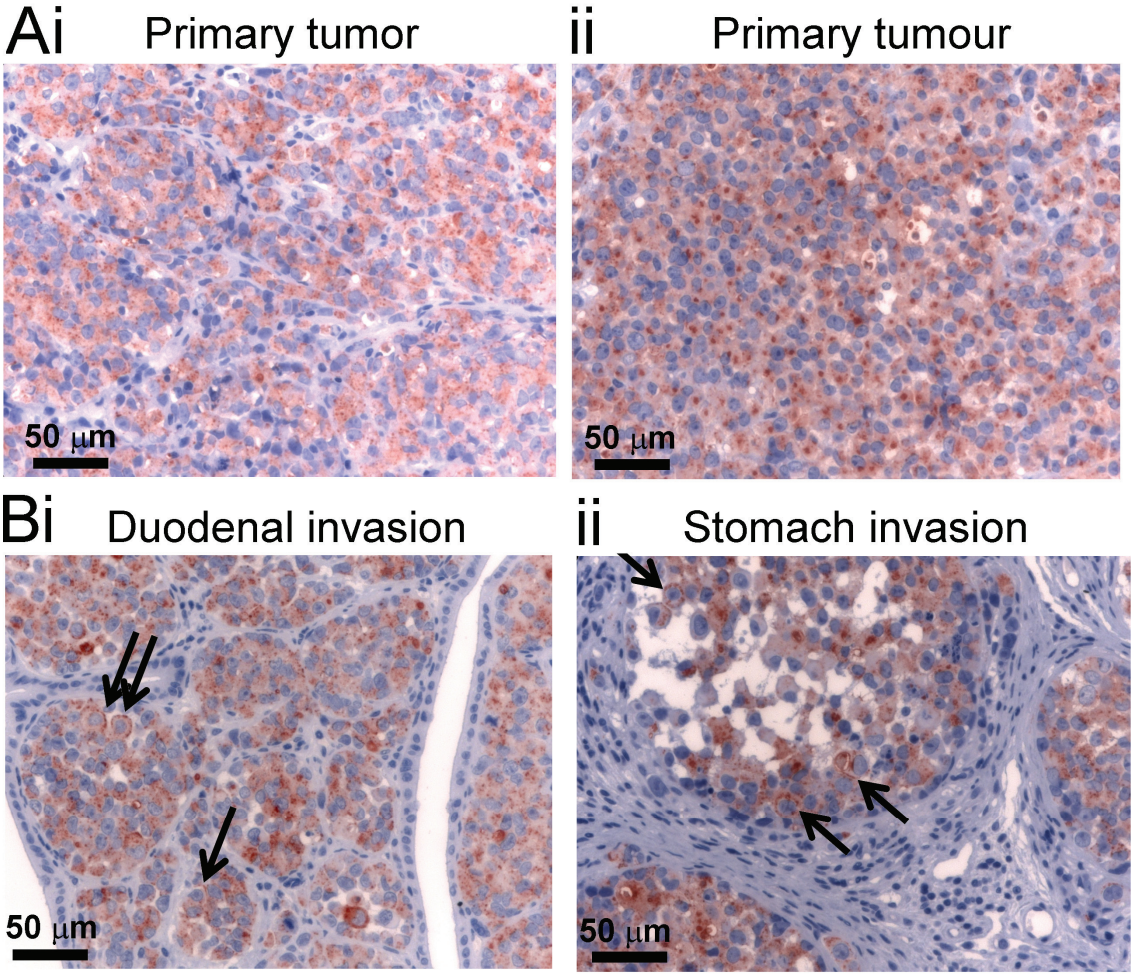
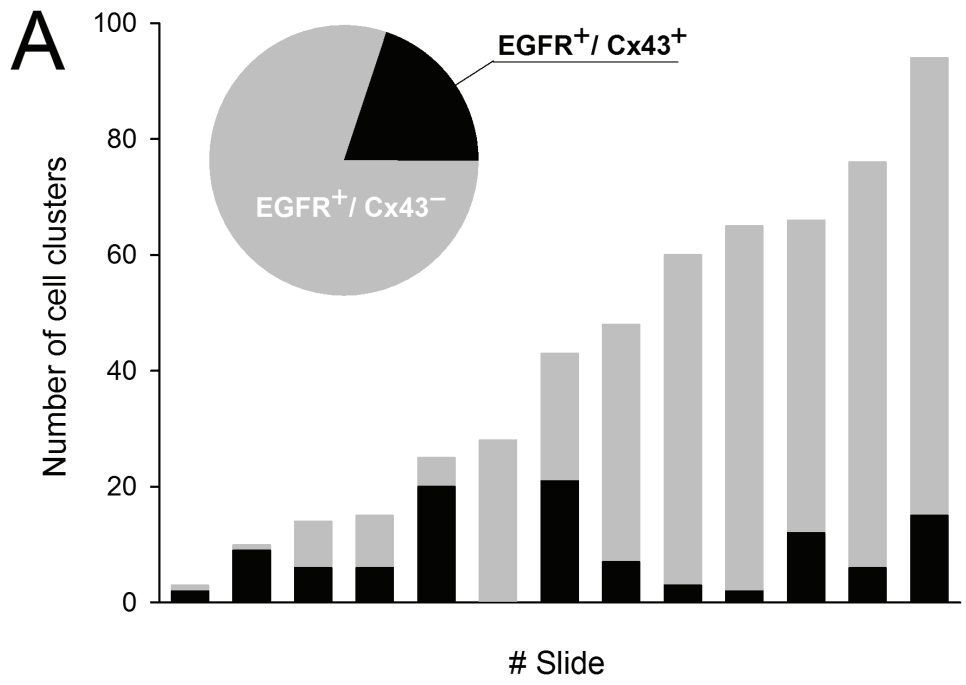


Figure 9.2.3.1 Immunoreactivity of lysosomal associated membrane protein-2 (LAMP2) in primary tumour mass and invasive areas of orthotopic MiaPaCa2 xenografts. ***(A)*** *LAMP2 staining in two sections (i and ii) of primary MiaPaCa2 tumour xenografts. The Cx43 staining appear diffuse throughout the cytoplasm with no clear segregation to the cell borders.* ***(B)*** *LAMP2 staining relocates to the cell borders in a subset of MiaPaCa2 cell invasions into the mucosa of the duodenum (i) and the stomach muscularis (ii). Concentration of LAMP2 along the cell border marks chronic extracellular acidosis.*

The analysis of the 547 MiaPaCa-2 cell clusters stained for Cx43 revealed that Cx43 protein was present in 20% of all clusters (**Fig 9.2.3.2 A**). All except one section analysed included some degree of Cx43-positive/EGFR-positive clusters. The regions containing Cx43 staining showed a homogeneous staining pattern between cells. This would argue that the cell derived from one progenitor clone from which the cluster is generated upon clonal expansion. This suggests that Cx43 expression could confer a selective advantage in invasive areas.

Quantitative analysis of LAMP2 staining revealed that 39% of the EGFR-positive MiaPaCa2 cell clusters contained cells with LAMP2 immunoreactivity at or in the proximity of the plasma membrane (**Fig 9.2.3.2 B**). These results suggest that a substantial proportion of the invading front of the xenografted MiaPaCa2 tumours experience chronic extracellular acidosis.



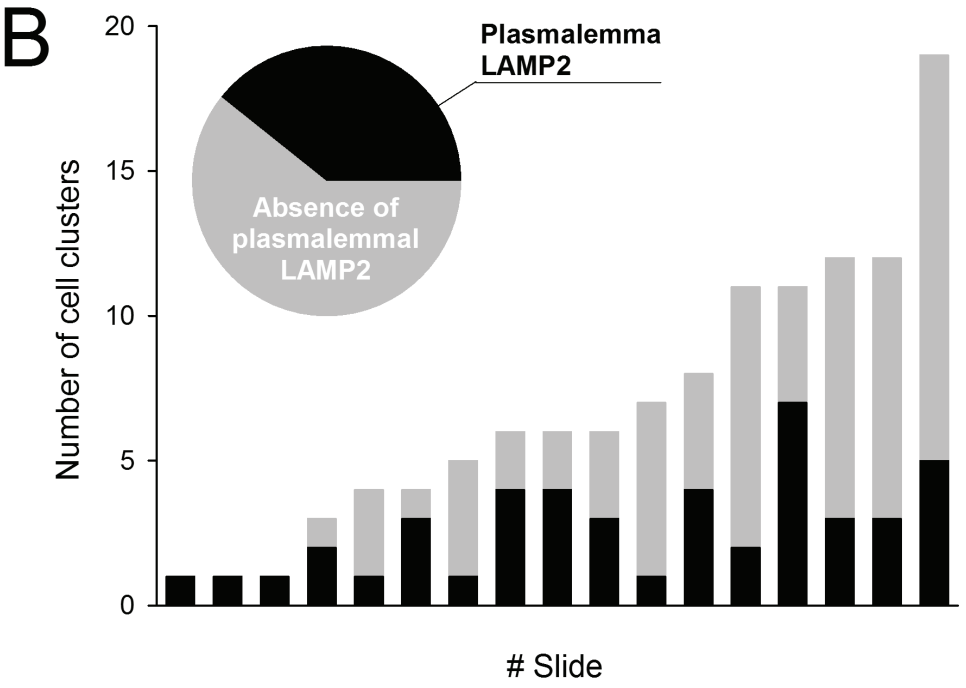


Figure 9.2.3.2 Analysis of Cx43 and LAMP2 immunoreactivity in MiaPaCa2 cell clusters invading the pancreas or gut. (A) *Cx43 staining analysed in areas of tumour invasion into the pancreas or gut. The analysis was based on 13 tissue sections derived from four mice*

containing orthotopically implanted MiaPaCa2 xenografts. Human EGFR staining was used as a marker of the human MiaPaCa2 cells. Bars represent tissue sections and circle diagram shows total proportion of $EGFR^+$ / $Cx43^+$ and $EGFR^+$ / $Cx43^-$ stained tumour clusters. Of the 547 EGFR-positive tumour regions, 20% showed high levels of Cx43 staining. ***(B)*** *Subcellular LAMP2 staining analysis in areas of tumour invasion into the pancreas or gut. The analysis was based on 17 tissue sections (represented by each bar) derived from four mice. The tumours were derived from orthotopically implanted MiaPaCa2 cells and identified by EGFR staining. Of the 117 EGFR-positive regions of tumour invasion, LAMP2 staining was found at or in proximity of the plasma membrane in 39%. Plasma membrane associated LAMP2 serves as a marker of extracellular acidosis.*

9.3 Summary of findings

- Cx43 is upregulated at the invasive front compared to the primary tumour mass in MiaPaCa2 (**Fig 9.2.1.1**) and PANC1 xenografts (**Fig 9.2.2.1**).
- Cx43 immunoreactivity was detected in 20% of the MiaPaCa2 clusters invading the gut or pancreas (**Fig 9.2.3.2 A**).
- Cx43 staining was identified along the cell borders in invasive and metastatic areas of MiaPaCa2 xenografts (**Fig 9.2.1.2**).
- LAMP2 immunoreactivity at the plasma membrane was detected in 39% of MiaPaCa2 clusters in invading the pancreas or gut (**Fig 9.2.3.1, Fig 9.2.3.2 B**), indicating chronic extracellular acidosis in these areas.

10 GENERAL DISCUSSION

10.1 Metabolic profiling of cancer cells

Metabolism is an integral part of pH_i homeostasis due to its acidic by-products CO_2 and lactic acid. Whereas extracellular pH_e is often 6.9 - 7.0 and in some cases 6.0 in tumours (89), the pH_i is strictly regulated to a slightly alkaline pH_i of 7.0 - 7.4, which promotes proliferation and cell cycle progression (90, 91, 105). As the intracellular H^+-buffering moieties are finite, the cells must restore the weak basic form of the buffer in order to prevent their saturation (250). Despite a reduced blood flow to pancreatic tumours, the delivery of glucose to pancreatic cancer tissue is ~3 mmol $\times$ L^{-1} $\times$ min^{-1} (45). With abundant delivery of glucose, PDAC cell glycolysis along with full hydrolysis of the ATP generated can produce H^+ ions at 8 – 22 mmol per min per litre of tumour tissue, which can reduce the cytoplasmic pH by one pH-unit within a few minutes (230, 231). A constant production of acid from metabolism thus imposes a profound challenge for PDAC cells.

Some PDAC cell lines have been shown to rely on glutamine for their growth (76). **Figure 4.3.1** shows the cell viability of PDAC cell lines in the absence of carbohydrate metabolism. The carbohydrate-independent cell viability ranged from 10% of that in glucose in Colo357 cells to ~40% of that in glucose in PANC1 cells (**Fig 4.3.1**). These data suggest that glucose is the primary substrate utilised for cell viability in the six PDAC cell lines tested.

Pancreatic cancer cells commonly up-regulate glycolysis for their production of ATP even in the presence of oxygen, a metabolic shift termed the Warburg effect (42). Despite the inefficiency of ATP production via glycolysis, it protects the cells against hypoxia, which is prevalent in pancreatic tumours (42, 43) As a consequence of the Warburg effect, PDAC cells increase their production of metabolic lactate (231). Upon replacing glucose with galactose, cellular reliance on oxidative phosphorylation was assessed. Incubating cells in galactose-containing medium serves as a measure of their reliance on oxidative phosphorylation for cell viability, as the metabolism of galactose via glycolysis does not produce any ATP (217, 224-226) (**Fig 4.3.2**). These results suggest a profound reliance on glycolysis for cell viability in all tested cell lines, with cell viabilities ranging from ~40% in AsPC1 cells to 70% in Colo357 cells (**Fig 4.3.2**).

Lactate can be a substrate for oxidative phosphorylation in normoxic PDAC cells upon conversion to pyruvate by LDH-B (75). Normoxic cancer cells can thus consume lactate generated by hypoxic cancer cells. Oxidative phosphorylation of the physiological L-enantiomer of lactate was compared to the oxidative phosphorylation of galactose, which does not yield ATP via glycolysis (**Fig 4.3.3**). L-lactate was able to stimulate cell viability to a level similar to that of galactose in all cell lines except in Colo357 cells, which experienced a 33% reduction in cell viability in L-lactate (**Fig 4.3.3 G**). This could be due to a lower expression of LDH-B in Colo357 cells, but this was not assessed in this study.

10.2 H^+ Buffering capacity of PDAC cell lines

Intracellular H^+ buffers act as a dynamic but finite storage for H^+ ions, allowing the cell to attain its normal functions under fluctuating H^+ generation. The intracellular buffers consist of CO_2/HCO_3^- and intrinsic buffers, such as histidine dipeptides and inorganic phosphate (203). Whereas the intrinsic buffers are cell impermeable, CO_2 (the product of HCO_3^- titration with H^+) can rapidly cross tissue; therefore, CO_2/HCO_3^- is an open buffer system. The intrinsic buffering capacities of PDAC cells were measured experimentally (**Fig 5.3.1**) and determined to be ~10 – 20 mM within a pH_i of 7.0 – 7.4 (intrinsic buffering capacity measurements in Colo357 cells were experimentally restricted to pH_i of ~6.4 - 7.2). As pancreatic cancer cells can produce up to 22 mmol H^+ ions per min per litre of tumour tissue (230, 231), the buffering capacity provided by intrinsic buffers is limited. Calculations of the buffering capacity provided by CO_2/HCO_3^- allowed an estimation of the total cellular buffering capacity (**Fig 5.3.1,** light grey). The total cellular buffering capacity was in the range of ~20 – 65 mM within a pH_i of 7.0 – 7.4. These buffers can thus be saturated within minutes if their chemically basic form is not restored via acid extrusion or import of HCO_3^-. The results presented in **figure 5.3.1**, suggest that the intrinsic buffers are responsible for the majority of H^+ buffering at acidic pH_i, whereas the carbonic CO_2/HCO_3^- buffer is dominant at a more alkaline pH_i.

10.3 CO_2/HCO_3^- handling by carbonic anhydrases in PDAC cell lines

Whereas upregulation of the exofacial carbonic anhydrase IX and XII is hypoxia-induced and often associated with poor prognosis in other cancers (238-241), downregulation of the intracellular CA II correlates with poor PDAC prognosis (242). The tested PDAC cell lines showed some degree of intracellular CA activity (**Fig 6.2.3.3**), with AsPC1 cells showing the highest intracellular CA activity in accordance with the high protein levels of CAII in these cells (**Fig 6.2.2.1**). Colo357 cells exhibited the highest exofacial CA activity, which was further induced by chemically stimulating hypoxic signalling caused by DMOG. Despite a 2 – 2.5-fold acceleration of CO_2 hydration in Colo357 cells grown in monolayers (**Fig 6.2.4.3**), the exofacial CA activity in Colo357 spheroids was only accelerated 1.58-fold (**Fig 6.2.5.1**). The tortuosity of the spheroid reduced the diffusion of fluorescein sulfonic acid by 70%, compared to its diffusion in water (**Fig 6.2.6.1**)(87). These results suggest that the diffusion of membrane-impermeable substances in the extracellular compartment is restricted. The delivery of substrate to cellular transporters could be rate-limited by slow extracellular diffusion. Indeed, inhibition of CAs led to a marked increase in core alkalinisation upon subjection to a 40 mM lactate pulse (**Fig 8.2.5.5**). Inhibition of CAs thus increases the gap junctional transport of lactate relative to MCT-facilitated transport, indicating that CAs facilitate the extracellular diffusion of lactic acid in PDAC.

10.4 Metabolic altruism and remote HCO_3^- transport

As the intracellular H^+ buffering moieties are finite, cancer cells must employ mechanisms to restore the chemically-basic form of the buffers (92). This must be done to prevent the saturation of the intrinsic and carbonic CO_2/HCO_3^- buffer systems by constant acid generation from metabolism (250). The secondary-active uptake of HCO_3^- is an important mechanism for restoring intracellular HCO_3^- levels and regulating pH_i (247). Na^+-HCO_3^- cotransporters such as NBCe1 can mediate such cellular HCO_3^- uptake (247, 249). HCO_3^- regulates pH_i by titrating H^+ ions upon the formation of CO_2. Because CO_2 permeates tissue rapidly, CO_2/HCO_3^- buffer is well-suited for pH_i regulation (87, 250). Furthermore, since pancreatic ductal cells function in bicarbonate secretion into the pancreatic duct, these cells normally express NBCe1 in the basolateral membrane (113, 249). In turn, bicarbonate transporters have pH_i-regulating roles in cancers and can be induced by tumour hypoxia (272).

Analysis of H^+ fluxes in Colo357 cells showed that the majority of acid extrusion is HCO_3^- dependent (**Fig 7.2.5.1**). This is in line with the high NBCe1 protein levels observed (**Fig 7.2.4.1**) and the HCO_3^--secreting function of normal pancreatic duct cells (113, 249). A disadvantage of secondary-active NBC-mediated HCO_3^- transport is that it requires ATP, which could be a significant burden on substrate-limited hypoxic cells situated in an acidic environment (247). In the presence of gap junctions that allow the permission of small molecules (<1kDa), however, HCO_3^- ions could be transferred from normoxic cells (spending the ATP on the HCO_3^- import) to hypoxic cancer cells (248). Such remote transport would thus only require energy for the normoxic cells importing

the HCO_3^- (247). Different connexin isoforms are present in PDAC cell lines (**Fig 7.2.1.1 and 7.2.2.1**), but the cell-to-cell permeability to calcein (0.6 kDa) (**Figs 7.2.3.1 and 7.2.3.2**) correlated with the protein level of Cx43 (**Fig 7.2.2.1**).

The results presented in **figure 7.2.8.2** show that the hypoxic core of Colo357 spheroids can sequester HCO_3^- ions from normoxic (peripheral) cells via passive diffusion through Cx43 gap junctions. Since some pancreatic cancers are coupled by gap junctions (273, 274), the gap junctional flux of HCO_3^- may be a significant means of regulating pH_i in hypoxic cells, thereby decoupling these cells from the energy expenditure required for HCO_3^- import (247, 275). Connexin coupling from normoxic to hypoxic areas may provide hypoxic cells with a survival advantage by providing a pH_i regulatory mechanism that does not require ATP consumption in the hypoxic cell. The normoxic cell may in turn benefit from such coupling by receiving lactate anions, (**Fig 8.2.6.1**), which can be utilised as a substrate for oxidative phosphorylation (**Fig 4.3.3**). Furthermore, endogenously-produced lactate anions transmitted through gap junctions can alkalinise normoxic cells, rendering their pH_i favourable for proliferation (**Fig 8.2.6.1**) (90).

It is important to note that the remote HCO_3^- transport via gap junctions relies on secondary-active NBC-mediated transport in the normoxic cell, as the HCO_3^- anions must be transported across the plasma membrane to enter the cytoplasmic compartment (**Fig 7.2.8.2**). Gap junctional coupling thus allows hypoxically-stressed cells to transfer the energetic burden of HCO_3^- transport onto normoxic cells, (**Fig 8.2.8.2**) where HCO_3^- uptake is a smaller energetic burden due to the availability of HCO_3^-, glucose and oxygen. The normoxic cells display a metabolic altruistic behaviour

by committing to secondary-active transport of HCO_3^- for the purpose of regulating pH_i in distant hypoxic cells. In addition to the conventional primary or secondary active transport mechanisms, these results argue for a novel category of "remote transport" where protein expression in one cell serves regulatory purposes in a different cell.

Remote HCO_3^- transport through gap junctions was discovered by employing a novel method for interrogating pH_i regulation in three-dimensional spheroid growths. H^+ ions were photolytically uncaged into the central region of spheroids, to imitate constant metabolic acid generation from hypoxic tissue. This was accomplished using NVA, which is less toxic than the previously used NBA, and fully dissociates upon photolytic conversion to 6-nitroveratric acid (**Fig 3.11.1 C** and **D**). This method provides a constant H^+ source within the concentration range measured in pancreatic cancer cells (8 – 22 mmol × min^{-1} × L^{-1} (230, 231)) and thus investigates the cellular response to physiological metabolic acid challenges. Upon activation of cellular pH_i-regulating mechanisms during the constant H^+-uncaging protocol, the pH_i approached a new steady state (**Fig 7.2.6.1**), likely resembling the pH_i-regulating processes in tumour tissue. This method thus represents a more physiological method for disturbing pH_i, compared to the previously-used ammonium prepulse method (250). The ammonium prepulse method induces a very acidic level uniformly in all cells, whereupon the dynamic pH_i response can be assessed. Since all cells are acidified, however, the cell-to-cell H^+ gradients necessary for junctional transport are absent; therefore, this method is not suitable for measuring transport through gap junctions. Whereas the ammonium prepulse presents cells with an instantaneous acid load, the H^+-uncaging protocol induces constant pH_i disturbances within the physiological range.

Furthermore, in contrast to the ammonium prepulse method, photolytic H^+-uncaging also acidifies the extracellular compartment, which resembles the metabolic acidification of pH_i and pH_e in tumours.

The remote transport of HCO_3^- ions could be favourable to hypoxic cells situated in areas where the extracellular delivery of HCO_3^- anions to NBC transporters is hindered. The tortuosity of the extracellular space of Colo357 spheroids reduced extracellular diffusion by 70%, which could be a barrier to extracellular HCO_3^- diffusion, thus restricting NBC-mediated uptake in hypoxic cancer cells (**Fig 6.2.6.1**). Furthermore, the inhibition of HCO_3^- transporters by low pH_e may provide an additional barrier to HCO_3^- uptake in hypoxic areas where pH_e is likely to be acidic.

10.5 Lactate handling pathways

PDAC cells have been shown to benefit from elevated levels of glycolysis (75). However, such elevated glycolysis is associated with a 1:1 production of lactate and H^+ ions, when the ATP formed via glycolysis is fully hydrolysed (84). This lactic acid must be vented from the cells (84). Lactate and H^+ ions can be co-transported out of cells via MCTs (**Fig 8.2.4.1**) such as MCT1 and MCT4 which are expressed in PDAC cells (**Fig 8.2.1.1**). The passive cotransport of lactate and H^+ ions via MCTs is dependent on the transmembrane pH and lactate gradients. Since the pH_e is often lower than the alkaline pH_i (105-110), MCT transport may be especially hindered in poorly-perfused hypoxic areas of the tumours. The high cell-to-cell coupling (**Fig 7.2.3.1**) provides an additional route for lactate in coupled PDAC cells. The proportion of lactate

transported via MCT and gap junctions was assessed based on pH_i responses to the addition of lactate (**Figs 8.2.5.1 – 8.2.5.5**). The transport route was inferred from the difference in pH_i response between MCTs and gap junctions. Whereas lactate is cotransported through MCTs with a H^+ ion, lactate transport through gap junctions is faster than and independent from H^+ transport (**Fig 8.2.3.1**). The results presented in **figure 8.2.5.2** show that 77±3% of all lactate ions transmitted to the spheroid core were transported through gap junctions. This MCT-independent flux of lactate anions via gap junctions is unlikely to result in a net electric current, since Cx43 channels (present in Colo357 spheroids) are permeant to small monovalent ions such as Cl^- and K^+ (276). The Cl^- and K^+ ion concentrations are present at up to 100 mM in cancer cells, and syncytial flux of these ions could thus counteract the electric current of lactate transport (277). The syncytial cellular networks via gap junctional coupling reduces the retention of lactate in spheroid growths (**Fig 8.2.7.1**), indicating a functional role of the gap junctions in venting lactate from hypoxic tissue. A syncytial Cx43-coupled cellular network allows the lactate anions to dissipate through the cytoplasmic compartment, thereby circumventing MCT transport in hypoxic areas, where this route is thermodynamically hindered by a low pH_e. Connexin channels may thus facilitate the transport of lactate anions from hypoxic cells to normoxic cells situated in the spheroid periphery or near blood vessels, where MCT transport is favourable due to a higher pH_e. Upon passive gap junctional lactate transport from hypoxic areas of production in the spheroid core to the normoxic areas of the spheroid periphery, the pH_i of the spheroid periphery is rendered more alkaline, thus promoting growth (**Fig 8.2.6.1**). This change in pH_i comes at no energetic cost from secondary active transporters in the

peripheral cells. In normoxic cells, the lactate donated by hypoxic cells may provide a substrate for oxidative phosphorylation (**Fig 4.3.3**). Gap junction-coupled cells may thus exhibit a metabolic symbiosis between normoxic and hypoxic cells. In hypoxic cells, the gap junctional coupling provides a pathway for extruding lactate down its concentration gradient, upheld by the O_2 gradient. In addition, the hypoxic cells benefit from gap junctional coupling by receiving HCO_3^- from normoxic donor cells (**Fig 7.2.8.2**). Conversely, the lactate received by the normoxic cells can be utilised as a substrate for oxidative phosphorylation and thereby render the pH_i suitable for growth.

10.6 *In vivo* investigation of Cx43 and LAMP2 in orthotopic xenografts

Connexins have in general been considered to be tumour suppressors, due to their frequent down-regulation in primary tumours (205). Some evidence, however, suggests that connexin expression could have the opposite effect in the later tumour stages of invasion and metastasis (205, 259, 278-280). When orthotopically implanted in nude mouse pancreas, MiaPaCa2 cells did not express Cx43 in the primary tumour (**Fig 9.2.1.1 A**). This is in line with the absence of Cx43 protein levels in MiaPaCa2 cells *in vitro* (**Fig 7.2.2.1**) and the general notion that Cx43 is downregulated in primary tumours (205). Interestingly, however, Cx43 immunoreactivity *in vivo* was markedly increased in a subpopulation of xenograft areas that were invading the host pancreas (**Fig 9.2.1.1 D**), duodenum mucosa (**Fig 9.2.1.1 E**), stomach muscularis (**Fig 9.2.1.1 F**) and some metastases (**Fig 9.2.1.1 C**). These results are in line with evidence of a role of

Cx43 at later tumour stages (205). The membrane location of Cx43 immunoreactivity in MiaPaCa2 lung metastases and duodenal invasions suggest that Cx43 forms functional channels *in vivo* (**Fig 9.2.1.2**). Furthermore, the pattern of Cx43 up-regulation in invasive areas was not restricted to the MiaPaCa2 cell line, as orthotopic xenografts of PANC1 cells also showed an upregulation of Cx43 in invasive areas *in vivo* in addition to expressing lower levels in the primary tumour and *in vitro* (**Fig 9.2.2.1**). Plasma membrane or near-membranous localisation of the lysosomal protein LAMP2 is an indicator of chronic extracellular acidosis (108). Areas with prevalent chronic extracellular acidosis are likely to show inhibited MCT-facilitated lactate extrusion. Whereas the primary tumours showed cytosolic localisation of LAMP2 (**Fig 9.2.3.1 A**), areas of invasion into the stomach and duodenum showed aggregation of LAMP2 at the cell-to-cell borders, indicating that these areas were subjected to chronic acidosis. In the invading xenograft clusters, membranous LAMP2 staining was found in 39% of cases. Analysis of Cx43 staining revealed that 20% of invading clusters were positive for Cx43 (**Fig 9.2.3.2**), indicating that chronic extracellular acidosis is common in invading areas where Cx43 channels may have a function in lactate transport to circumvent MCT-mediated lactate extrusion. Furthermore, the Cx43 channels could facilitate HCO_3^- to cells situated in an acidic environment. These results support the idea that Cx43 channels may play a role in the later stages of cancer, such as invasion and metastasis, where extracellular acidosis may become prevalent. In such areas, the need for an alternative lactate venting route may be met by Cx43 up-regulation. Increased expression of Cx43 has previously been found in lymph node metastases of breast cancer (278), as well as in the increasing metastatic adhesion of cancer cells to

lung epithelium (259). Moreover, downregulation of Cx43 has been shown to suppress invasion and metastasis in rat hepatocellular carcinoma cells (279). Cx43 has also been shown to enhance tumour cell emigration through vascular endothelium (280, 281). These results suggest a role for Cx43 in malignant tumours, although some breast cancer metastasis models show reduced metastasis upon Cx43 up-regulation. The results presented in this study suggest that Cx43 channels confer a selective advantage over MCTs in areas of acidic pH_e. Since cancer cells may benefit from Cx43 channels by allowing the dissipation of lactate and HCO_3^- down their respective concentration gradients, Cx43 expression may plausibly confer an advantage in colonising new areas. Co-culturing Cx43-expressing wild type cells with *GJA1*-knockdown cells shown in **figure 8.2.8.1** showed that Cx43-expressing cells preferentially segregate in the proliferating rim of spheroids. These results support the hypothesis that Cx43 expression is advantageous. The advantage of lactate and HCO_3^- transport through Cx43 channels may explain the Cx43 upregulation found by others in some pancreatic tumours Bandea (3.5 fold, $P=10^{-9}$), Buchholz (1.6 fold, P=0.02) and Segara (4.1 fold, P= 0.001) (281-283) .

10.7 Future directions

The findings presented in this thesis reveal non-canonical pathways for acid-handling in PDAC, which hitherto have not been investigated for therapeutic potential. Since pH is critically important for survival, manipulating these aforementioned PDAC pathways could alter the disease trajectory. This would form the basis of future work.

11 REFERENCES

1. Kleeff J, Korc M, Apte M, La Vecchia C, Johnson CD, Biankin AV, et al. Pancreatic cancer. Nature reviews Disease primers. 2016;2:16022.

2. Siegel RL, Miller KD, Jemal A. Cancer statistics, 2016. CA: a cancer journal for clinicians. 2016;66(1):7-30.

3. Malvezzi M, Bertuccio P, Rosso T, Rota M, Levi F, La Vecchia C, et al. European cancer mortality predictions for the year 2015: does lung cancer have the highest death rate in EU women? Annals of oncology : official journal of the European Society for Medical Oncology. 2015;26(4):779-86.

4. Stathis A, Moore MJ. Advanced pancreatic carcinoma: current treatment and future challenges. Nature reviews Clinical oncology. 2010;7(3):163-72.

5. Storz P. Acinar cell plasticity and development of pancreatic ductal adenocarcinoma. Nature reviews Gastroenterology & hepatology. 2017;14(5):296-304.

6. Kopp JL, von Figura G, Mayes E, Liu FF, Dubois CL, Morris JPt, et al. Identification of Sox9-dependent acinar-to-ductal reprogramming as the principal mechanism for initiation of pancreatic ductal adenocarcinoma. Cancer cell. 2012;22(6):737-50.

7. Liou GY, Doppler H, Necela B, Edenfield B, Zhang L, Dawson DW, et al. Mutant KRAS-induced expression of ICAM-1 in pancreatic acinar cells causes attraction of macrophages to expedite the formation of precancerous lesions. Cancer Discov. 2015;5(1):52-63.

8. Rahib L, Smith BD, Aizenberg R, Rosenzweig AB, Fleshman JM, Matrisian LM. Projecting cancer incidence and deaths to 2030: the unexpected burden of thyroid, liver, and pancreas cancers in the United States. Cancer research. 2014;74(11):2913-21.

9. Raimondi S, Maisonneuve P, Lowenfels AB. Epidemiology of pancreatic cancer: an overview. Nature reviews Gastroenterology & hepatology. 2009;6(12):699-708.

10. Parkin DM. 2. Tobacco-attributable cancer burden in the UK in 2010. British journal of cancer. 2011;105 Suppl 2:S6-S13.

11. Ezzati M, Henley SJ, Lopez AD, Thun MJ. Role of smoking in global and regional cancer epidemiology: current patterns and data needs. International journal of cancer. 2005;116(6):963-71.

12. Boffetta P, Aagnes B, Weiderpass E, Andersen A. Smokeless tobacco use and risk of cancer of the pancreas and other organs. International journal of cancer. 2005;114(6):992-5.

13. Tramacere I, Scotti L, Jenab M, Bagnardi V, Bellocco R, Rota M, et al. Alcohol drinking and pancreatic cancer risk: a meta-analysis of the dose-risk relation. International journal of cancer. 2010;126(6):1474-86.

14. Lucenteforte E, La Vecchia C, Silverman D, Petersen GM, Bracci PM, Ji BT, et al. Alcohol consumption and pancreatic cancer: a pooled analysis in the International Pancreatic Cancer Case-Control Consortium (PanC4). Annals of oncology : official journal of the European Society for Medical Oncology. 2012;23(2):374-82.

15. Calton BA, Stolzenberg-Solomon RZ, Moore SC, Schatzkin A, Schairer C, Albanes D, et al. A prospective study of physical activity and the risk of pancreatic cancer among women (United States). BMC cancer. 2008;8:63.

16. Behrens G, Jochem C, Schmid D, Keimling M, Ricci C, Leitzmann MF. Physical activity and risk of pancreatic cancer: a systematic review and meta-analysis. European journal of epidemiology. 2015;30(4):279-98.

17. Genkinger JM, Kitahara CM, Bernstein L, Berrington de Gonzalez A, Brotzman M, Elena JW, et al. Central adiposity, obesity during early adulthood, and pancreatic cancer mortality in a pooled analysis of cohort studies. Annals of oncology : official journal of the European Society for Medical Oncology. 2015;26(11):2257-66.

18. Berrington de Gonzalez A, Spencer EA, Bueno-de-Mesquita HB, Roddam A, Stolzenberg-Solomon R, Halkjaer J, et al. Anthropometry, physical activity, and the risk of pancreatic cancer in the European prospective investigation into cancer and nutrition. Cancer epidemiology, biomarkers & prevention : a publication of the American Association for Cancer Research, cosponsored by the American Society of Preventive Oncology. 2006;15(5):879-85.

19. Stevens RJ, Roddam AW, Spencer EA, Pirie KL, Reeves GK, Green J, et al. Factors associated with incident and fatal pancreatic cancer in a cohort of middle-aged women. International journal of cancer. 2009;124(10):2400-5.

20. Wang F, Herrington M, Larsson J, Permert J. The relationship between diabetes and pancreatic cancer. Molecular cancer. 2003;2:4.

21. Permert J, Adrian TE, Jacobsson P, Jorfelt L, Fruin AB, Larsson J. Is profound peripheral insulin resistance in patients with pancreatic cancer caused by a tumor-associated factor? American journal of surgery. 1993;165(1):61-6; discussion 6-7.

22. Everhart J, Wright D. Diabetes mellitus as a risk factor for pancreatic cancer. A meta-analysis. JAMA. 1995;273(20):1605-9.

23. Waddell N, Pajic M, Patch AM, Chang DK, Kassahn KS, Bailey P, et al. Whole genomes redefine the mutational landscape of pancreatic cancer. Nature. 2015;518(7540):495-501.

24. Jonckheere N, Skrypek N, Van Seuningen I. Mucins and pancreatic cancer. Cancers. 2010;2(4):1794-812.

25. Basturk O, Hong SM, Wood LD, Adsay NV, Albores-Saavedra J, Biankin AV, et al. A Revised Classification System and Recommendations From the Baltimore Consensus Meeting for Neoplastic Precursor Lesions in the Pancreas. Am J Surg Pathol. 2015;39(12):1730-41.

26. Bardeesy N, DePinho RA. Pancreatic cancer biology and genetics. Nature reviews Cancer. 2002;2(12):897-909.

27. Hruban RH, Goggins M, Parsons J, Kern SE. Progression model for pancreatic cancer. Clinical cancer research : an official journal of the American Association for Cancer Research. 2000;6(8):2969-72.

28. Yachida S, Jones S, Bozic I, Antal T, Leary R, Fu B, et al. Distant metastasis occurs late during the genetic evolution of pancreatic cancer. Nature. 2010;467(7319):1114-7.

29. Makohon-Moore A, Iacobuzio-Donahue CA. Pancreatic cancer biology and genetics from an evolutionary perspective. Nature reviews Cancer. 2016;16(9):553-65.

30. Rozenblum E, Schutte M, Goggins M, Hahn SA, Panzer S, Zahurak M, et al. Tumor-suppressive pathways in pancreatic carcinoma. Cancer research. 1997;57(9):1731-4.

31. Chiorean EG, Coveler AL. Pancreatic cancer: optimizing treatment options, new, and emerging targeted therapies. Drug Des Devel Ther. 2015;9:3529-45.

32. Biankin AV, Waddell N, Kassahn KS, Gingras MC, Muthuswamy LB, Johns AL, et al. Pancreatic cancer genomes reveal aberrations in axon guidance pathway genes. Nature. 2012;491(7424):399-405.

33. Jones S, Zhang X, Parsons DW, Lin JC, Leary RJ, Angenendt P, et al. Core signaling pathways in human pancreatic cancers revealed by global genomic analyses. Science. 2008;321(5897):1801-6.

34. Hingorani SR, Petricoin EF, Maitra A, Rajapakse V, King C, Jacobetz MA, et al. Preinvasive and invasive ductal pancreatic cancer and its early detection in the mouse. Cancer cell. 2003;4(6):437-50.

35. Hingorani SR, Wang L, Multani AS, Combs C, Deramaudt TB, Hruban RH, et al. Trp53R172H and KrasG12D cooperate to promote chromosomal instability and widely metastatic pancreatic ductal adenocarcinoma in mice. Cancer cell. 2005;7(5):469-83.

36. Aguirre AJ, Bardeesy N, Sinha M, Lopez L, Tuveson DA, Horner J, et al. Activated Kras and Ink4a/Arf deficiency cooperate to produce metastatic pancreatic ductal adenocarcinoma. Genes & development. 2003;17(24):3112-26.

37. Izeradjene K, Combs C, Best M, Gopinathan A, Wagner A, Grady WM, et al. Kras(G12D) and Smad4/Dpc4 haploinsufficiency cooperate to induce mucinous cystic neoplasms and invasive adenocarcinoma of the pancreas. Cancer cell. 2007;11(3):229-43.

38. Bond-Smith G, Banga N, Hammond TM, Imber CJ. Pancreatic adenocarcinoma. Bmj. 2012;344:e2476.

39. Wolfgang CL, Herman JM, Laheru DA, Klein AP, Erdek MA, Fishman EK, et al. Recent progress in pancreatic cancer. CA: a cancer journal for clinicians. 2013;63(5):318-48.

40. Vaupel P, Kallinowski F, Okunieff P. Blood flow, oxygen and nutrient supply, and metabolic microenvironment of human tumors: a review. Cancer research. 1989;49(23):6449-65.

41. Vaupel P, Mayer A. Hypoxia in cancer: significance and impact on clinical outcome. Cancer metastasis reviews. 2007;26(2):225-39.

42. Gatenby RA, Gillies RJ. Why do cancers have high aerobic glycolysis? Nature reviews Cancer. 2004;4(11):891-9.

43. Koong AC, Mehta VK, Le QT, Fisher GA, Terris DJ, Brown JM, et al. Pancreatic tumors show high levels of hypoxia. International journal of radiation oncology, biology, physics. 2000;48(4):919-22.

44. Vaupel P, Hockel M, Mayer A. Detection and characterization of tumor hypoxia using pO2 histography. Antioxidants & redox signaling. 2007;9(8):1221-35.

45. Komar G, Kauhanen S, Liukko K, Seppanen M, Kajander S, Ovaska J, et al. Decreased blood flow with increased metabolic activity: a novel sign of pancreatic tumor aggressiveness.

Clinical cancer research : an official journal of the American Association for Cancer Research. 2009;15(17):5511-7.

46. DuFort CC, DelGiorno KE, Carlson MA, Osgood RJ, Zhao C, Huang Z, et al. Interstitial Pressure in Pancreatic Ductal Adenocarcinoma Is Dominated by a Gel-Fluid Phase. Biophysical journal. 2016;110(9):2106-19.

47. Provenzano PP, Cuevas C, Chang AE, Goel VK, Von Hoff DD, Hingorani SR. Enzymatic targeting of the stroma ablates physical barriers to treatment of pancreatic ductal adenocarcinoma. Cancer cell. 2012;21(3):418-29.

48. Cohen R, Neuzillet C, Tijeras-Raballand A, Faivre S, de Gramont A, Raymond E. Targeting cancer cell metabolism in pancreatic adenocarcinoma. Oncotarget. 2015;6(19):16832-47.

49. Kitano M, Kudo M, Maekawa K, Suetomi Y, Sakamoto H, Fukuta N, et al. Dynamic imaging of pancreatic diseases by contrast enhanced coded phase inversion harmonic ultrasonography. Gut. 2004;53(6):854-9.

50. McKeown SR. Defining normoxia, physoxia and hypoxia in tumours-implications for treatment response. The British journal of radiology. 2014;87(1035):20130676.

51. Buchler P, Reber HA, Lavey RS, Tomlinson J, Buchler MW, Friess H, et al. Tumor hypoxia correlates with metastatic tumor growth of pancreatic cancer in an orthotopic murine model. J Surg Res. 2004;120(2):295-303.

52. Gatenby RA, Gillies RJ. A microenvironmental model of carcinogenesis. Nature reviews Cancer. 2008;8(1):56-61.

53. Verduzco D, Lloyd M, Xu L, Ibrahim-Hashim A, Balagurunathan Y, Gatenby RA, et al. Intermittent hypoxia selects for genotypes and phenotypes that increase survival, invasion, and therapy resistance. PloS one. 2015;10(3):e0120958.

54. Gatenby RA, Smallbone K, Maini PK, Rose F, Averill J, Nagle RB, et al. Cellular adaptations to hypoxia and acidosis during somatic evolution of breast cancer. British journal of cancer. 2007;97(5):646-53.

55. Gatenby RA, Gillies RJ. Glycolysis in cancer: a potential target for therapy. The international journal of biochemistry & cell biology. 2007;39(7-8):1358-66.

56. Fang JS, Gillies RD, Gatenby RA. Adaptation to hypoxia and acidosis in carcinogenesis and tumor progression. Seminars in cancer biology. 2008;18(5):330-7.

57. Spivak-Kroizman TR, Hostetter G, Posner R, Aziz M, Hu C, Demeure MJ, et al. Hypoxia triggers hedgehog-mediated tumor-stromal interactions in pancreatic cancer. Cancer research. 2013;73(11):3235-47.

58. Masamune A, Kikuta K, Watanabe T, Satoh K, Hirota M, Shimosegawa T. Hypoxia stimulates pancreatic stellate cells to induce fibrosis and angiogenesis in pancreatic cancer. Am J Physiol Gastrointest Liver Physiol. 2008;295(4):G709-17.

59. Hamada S, Masamune A, Takikawa T, Suzuki N, Kikuta K, Hirota M, et al. Pancreatic stellate cells enhance stem cell-like phenotypes in pancreatic cancer cells. Biochemical and biophysical research communications. 2012;421(2):349-54.

60. Erkan M, Michalski CW, Rieder S, Reiser-Erkan C, Abiatari I, Kolb A, et al. The activated stroma index is a novel and independent prognostic marker in pancreatic ductal adenocarcinoma. Clin Gastroenterol Hepatol. 2008;6(10):1155-61.

61. Xu Z, Vonlaufen A, Phillips PA, Fiala-Beer E, Zhang X, Yang L, et al. Role of pancreatic stellate cells in pancreatic cancer metastasis. The American journal of pathology. 2010;177(5):2585-96.

62. Liu H, Ma Q, Xu Q, Lei J, Li X, Wang Z, et al. Therapeutic potential of perineural invasion, hypoxia and desmoplasia in pancreatic cancer. Current pharmaceutical design. 2012;18(17):2395-403.

63. Semenza GL. Hypoxia-inducible factors: mediators of cancer progression and targets for cancer therapy. Trends in pharmacological sciences. 2012;33(4):207-14.

64. Jaakkola P, Mole DR, Tian YM, Wilson MI, Gielbert J, Gaskell SJ, et al. Targeting of HIF-alpha to the von Hippel-Lindau ubiquitylation complex by O2-regulated prolyl hydroxylation. Science. 2001;292(5516):468-72.

65. Maxwell PH, Wiesener MS, Chang GW, Clifford SC, Vaux EC, Cockman ME, et al. The tumour suppressor protein VHL targets hypoxia-inducible factors for oxygen-dependent proteolysis. Nature. 1999;399(6733):271-5.

66. Iwai K, Yamanaka K, Kamura T, Minato N, Conaway RC, Conaway JW, et al. Identification of the von Hippel-lindau tumor-suppressor protein as part of an active E3 ubiquitin ligase complex. Proceedings of the National Academy of Sciences of the United States of America. 1999;96(22):12436-41.

67. Semenza GL. Defining the role of hypoxia-inducible factor 1 in cancer biology and therapeutics. Oncogene. 2010;29(5):625-34.

68. Elvidge GP, Glenny L, Appelhoff RJ, Ratcliffe PJ, Ragoussis J, Gleadle JM. Concordant regulation of gene expression by hypoxia and 2-oxoglutarate-dependent dioxygenase inhibition: the role of HIF-1alpha, HIF-2alpha, and other pathways. The Journal of biological chemistry. 2006;281(22):15215-26.

69. Vander Heiden MG, Cantley LC, Thompson CB. Understanding the Warburg effect: the metabolic requirements of cell proliferation. Science. 2009;324(5930):1029-33.

70. Sun HC, Qiu ZJ, Liu J, Sun J, Jiang T, Huang KJ, et al. Expression of hypoxia-inducible factor-1 alpha and associated proteins in pancreatic ductal adenocarcinoma and their impact on prognosis. International journal of oncology. 2007;30(6):1359-67.

71. Mohammad GH, Olde Damink SW, Malago M, Dhar DK, Pereira SP. Pyruvate Kinase M2 and Lactate Dehydrogenase A Are Overexpressed in Pancreatic Cancer and Correlate with Poor Outcome. PloS one. 2016;11(3):e0151635.

72. Baek G, Tse YF, Hu Z, Cox D, Buboltz N, McCue P, et al. MCT4 defines a glycolytic subtype of pancreatic cancer with poor prognosis and unique metabolic dependencies. Cell reports. 2014;9(6):2233-49.

73. Juhasz M, Chen J, Lendeckel U, Kellner U, Kasper HU, Tulassay Z, et al. Expression of carbonic anhydrase IX in human pancreatic cancer. Alimentary Pharmacology and Therapeutics. 2003;18(8):837-46.

74. Ying H, Kimmelman AC, Lyssiotis CA, Hua S, Chu GC, Fletcher-Sananikone E, et al. Oncogenic Kras maintains pancreatic tumors through regulation of anabolic glucose metabolism. Cell. 2012;149(3):656-70.

75. Guillaumond F, Leca J, Olivares O, Lavaut MN, Vidal N, Berthezene P, et al. Strengthened glycolysis under hypoxia supports tumor symbiosis and hexosamine biosynthesis in pancreatic adenocarcinoma. Proceedings of the National Academy of Sciences of the United States of America. 2013;110(10):3919-24.

76. Son J, Lyssiotis CA, Ying H, Wang X, Hua S, Ligorio M, et al. Glutamine supports pancreatic cancer growth through a KRAS-regulated metabolic pathway. Nature. 2013;496(7443):101-5.

77. Commisso C, Davidson SM, Soydaner-Azeloglu RG, Parker SJ, Kamphorst JJ, Hackett S, et al. Macropinocytosis of protein is an amino acid supply route in Ras-transformed cells. Nature. 2013;497(7451):633-7.

78. Christofk HR, Vander Heiden MG, Harris MH, Ramanathan A, Gerszten RE, Wei R, et al. The M2 splice isoform of pyruvate kinase is important for cancer metabolism and tumour growth. Nature. 2008;452(7184):230-3.

79. Koppenol WH, Bounds PL, Dang CV. Otto Warburg's contributions to current concepts of cancer metabolism. Nature reviews Cancer. 2011;11(5):325-37.

80. Warburg O. On the origin of cancer cells. Science. 1956;123(3191):309-14.

81. Rodrigues TB, Serrao EM, Kennedy BW, Hu DE, Kettunen MI, Brindle KM. Magnetic resonance imaging of tumor glycolysis using hyperpolarized 13C-labeled glucose. Nature medicine. 2014;20(1):93-7.

82. Chen YJ, Mahieu NG, Huang X, Singh M, Crawford PA, Johnson SL, et al. Lactate metabolism is associated with mammalian mitochondria. Nature chemical biology. 2016;12(11):937-43.

83. Sonveaux P, Vegran F, Schroeder T, Wergin MC, Verrax J, Rabbani ZN, et al. Targeting lactate-fueled respiration selectively kills hypoxic tumor cells in mice. The Journal of clinical investigation. 2008;118(12):3930-42.

84. Swietach P, Vaughan-Jones RD, Harris AL, Hulikova A. The chemistry, physiology and pathology of pH in cancer. Philosophical transactions of the Royal Society of London Series B, Biological sciences. 2014;369(1638):20130099.

85. Feron O. Pyruvate into lactate and back: from the Warburg effect to symbiotic energy fuel exchange in cancer cells. Radiotherapy and oncology : journal of the European Society for Therapeutic Radiology and Oncology. 2009;92(3):329-33.

86. Koukourakis MI, Giatromanolaki A, Harris AL, Sivridis E. Comparison of metabolic pathways between cancer cells and stromal cells in colorectal carcinomas: a metabolic survival role for tumor-associated stroma. Cancer research. 2006;66(2):632-7.

87. Hulikova A, Swietach P. Rapid CO2 permeation across biological membranes: implications for CO2 venting from tissue. FASEB journal : official publication of the Federation of American Societies for Experimental Biology. 2014;28(7):2762-74.

88. Cruz-Monserrate Z, Roland CL, Deng D, Arumugam T, Moshnikova A, Andreev OA, et al. Targeting pancreatic ductal adenocarcinoma acidic microenvironment. Scientific reports. 2014;4:4410.

89. Swietach P, Vaughan-Jones RD, Harris AL. Regulation of tumor pH and the role of carbonic anhydrase 9. Cancer metastasis reviews. 2007;26(2):299-310.

90. Schonichen A, Webb BA, Jacobson MP, Barber DL. Considering protonation as a posttranslational modification regulating protein structure and function. Annual review of biophysics. 2013;42:289-314.

91. Stubbs M, Bhujwalla ZM, Tozer GM, Rodrigues LM, Maxwell RJ, Morgan R, et al. An assessment of 31P MRS as a method of measuring pH in rat tumours. NMR in biomedicine. 1992;5(6):351-9.

92. Parks SK, Chiche J, Pouyssegur J. pH control mechanisms of tumor survival and growth. Journal of cellular physiology. 2011;226(2):299-308.

93. Leem CH, Lagadic-Gossmann D, Vaughan-Jones RD. Characterization of intracellular pH regulation in the guinea-pig ventricular myocyte. The Journal of physiology. 1999;517 (Pt 1):159-80.

94. Fencl V, Leith DE. Stewart's quantitative acid-base chemistry: applications in biology and medicine. Respir Physiol. 1993;91(1):1-16.

95. Missner A, Pohl P. 110 years of the Meyer-Overton rule: predicting membrane permeability of gases and other small compounds. Chemphyschem. 2009;10(9-10):1405-14.

96. Jain RK. Transport of molecules in the tumor interstitium: a review. Cancer research. 1987;47(12):3039-51.

97. Junge W, McLaughlin S. The role of fixed and mobile buffers in the kinetics of proton movement. Biochimica et biophysica acta. 1987;890(1):1-5.

98. Swietach P, Wigfield S, Cobden P, Supuran CT, Harris AL, Vaughan-Jones RD. Tumor-associated carbonic anhydrase 9 spatially coordinates intracellular pH in three-dimensional multicellular growths. The Journal of biological chemistry. 2008;283(29):20473-83.

99. Hallerdei J, Scheibe RJ, Parkkila S, Waheed A, Sly WS, Gros G, et al. T tubules and surface membranes provide equally effective pathways of carbonic anhydrase-facilitated lactic acid transport in skeletal muscle. PloS one. 2010;5(12):e15137.

100. Schilling F, Duwel S, Kollisch U, Durst M, Schulte RF, Glaser SJ, et al. Diffusion of hyperpolarized (13) C-metabolites in tumor cell spheroids using real-time NMR spectroscopy. NMR in biomedicine. 2013;26(5):557-68.

101. Swietach P, Hulikova A, Vaughan-Jones RD, Harris AL. New insights into the physiological role of carbonic anhydrase IX in tumour pH regulation. Oncogene. 2010;29(50):6509-21.

102. Ullah MS, Davies AJ, Halestrap AP. The plasma membrane lactate transporter MCT4, but not MCT1, is up-regulated by hypoxia through a HIF-1alpha-dependent mechanism. The Journal of biological chemistry. 2006;281(14):9030-7.

103. Halestrap AP, Price NT. The proton-linked monocarboxylate transporter (MCT) family: structure, function and regulation. The Biochemical journal. 1999;343 Pt 2:281-99.

104. Le Floch R, Chiche J, Marchiq I, Naiken T, Ilc K, Murray CM, et al. CD147 subunit of lactate/H+ symporters MCT1 and hypoxia-inducible MCT4 is critical for energetics and growth of glycolytic tumors. Proceedings of the National Academy of Sciences of the United States of America. 2011;108(40):16663-8.

105. Vaupel P, Kallinowski F, Okunieff P. Blood flow, oxygen consumption and tissue oxygenation of human tumors. Advances in experimental medicine and biology. 1990;277:895-905.

106. Gillies RJ, Raghunand N, Karczmar GS, Bhujwalla ZM. MRI of the tumor microenvironment. Journal of magnetic resonance imaging : JMRI. 2002;16(4):430-50.

107. Ojugo AS, McSheehy PM, McIntyre DJ, McCoy C, Stubbs M, Leach MO, et al. Measurement of the extracellular pH of solid tumours in mice by magnetic resonance spectroscopy: a comparison of exogenous (19)F and (31)P probes. NMR in biomedicine. 1999;12(8):495-504.

108. Damaghi M, Tafreshi NK, Lloyd MC, Sprung R, Estrella V, Wojtkowiak JW, et al. Chronic acidosis in the tumour microenvironment selects for overexpression of LAMP2 in the plasma membrane. Nature communications. 2015;6:8752.

109. Gatenby RA, Gawlinski ET, Gmitro AF, Kaylor B, Gillies RJ. Acid-mediated tumor invasion: a multidisciplinary study. Cancer research. 2006;66(10):5216-23.

110. Tannock IF, Rotin D. Acid pH in tumors and its potential for therapeutic exploitation. Cancer research. 1989;49(16):4373-84.

111. Kennedy KM, Dewhirst MW. Tumor metabolism of lactate: the influence and therapeutic potential for MCT and CD147 regulation. Future oncology. 2010;6(1):127-48.

112. Estrella V, Chen T, Lloyd M, Wojtkowiak J, Cornnell HH, Ibrahim-Hashim A, et al. Acidity generated by the tumor microenvironment drives local invasion. Cancer research. 2013;73(5):1524-35.

113. Pedersen SF, Novak I, Alves F, Schwab A, Pardo LA. Alternating pH landscapes shape epithelial cancer initiation and progression: Focus on pancreatic cancer. Bioessays. 2017;39(6).

114. Hofmann C, Obermeier F, Artinger M, Hausmann M, Falk W, Schoelmerich J, et al. Cell-cell contacts prevent anoikis in primary human colonic epithelial cells. Gastroenterology. 2007;132(2):587-600.

115. Carroll DK, Carroll JS, Leong CO, Cheng F, Brown M, Mills AA, et al. p63 regulates an adhesion programme and cell survival in epithelial cells. Nature cell biology. 2006;8(6):551-61.

116. Derksen PW, Liu X, Saridin F, van der Gulden H, Zevenhoven J, Evers B, et al. Somatic inactivation of E-cadherin and p53 in mice leads to metastatic lobular mammary carcinoma through induction of anoikis resistance and angiogenesis. Cancer cell. 2006;10(5):437-49.

117. Eckert LB, Repasky GA, Ulku AS, McFall A, Zhou H, Sartor CI, et al. Involvement of Ras activation in human breast cancer cell signaling, invasion, and anoikis. Cancer research. 2004;64(13):4585-92.

118. Smallbone K, Gatenby RA, Gillies RJ, Maini PK, Gavaghan DJ. Metabolic changes during carcinogenesis: potential impact on invasiveness. Journal of theoretical biology. 2007;244(4):703-13.

119. Ding D, Moskowitz SI, Li R, Lee SB, Esteban M, Tomaselli K, et al. Acidosis induces necrosis and apoptosis of cultured hippocampal neurons. Exp Neurol. 2000;162(1):1-12.

120. Williams AC, Collard TJ, Paraskeva C. An acidic environment leads to p53 dependent induction of apoptosis in human adenoma and carcinoma cell lines: implications for clonal selection during colorectal carcinogenesis. Oncogene. 1999;18(21):3199-204.

121. Lloyd MC, Cunningham JJ, Bui MM, Gillies RJ, Brown JS, Gatenby RA. Darwinian dynamics of intratumoral heterogeneity: not solely random mutations but also variable environmental selection forces. Cancer research. 2016.

122. Epstein T, Xu L, Gillies RJ, Gatenby RA. Separation of metabolic supply and demand: aerobic glycolysis as a normal physiological response to fluctuating energetic demands in the membrane. Cancer & metabolism. 2014;2:7.

123. Rothberg JM, Bailey KM, Wojtkowiak JW, Ben-Nun Y, Bogyo M, Weber E, et al. Acid-mediated tumor proteolysis: contribution of cysteine cathepsins. Neoplasia. 2013;15(10):1125-37.

124. Bailey KM, Wojtkowiak JW, Cornnell HH, Ribeiro MC, Balagurunathan Y, Hashim AI, et al. Mechanisms of buffer therapy resistance. Neoplasia. 2014;16(4):354-64 e1-3.

125. Rofstad EK, Mathiesen B, Kindem K, Galappathi K. Acidic extracellular pH promotes experimental metastasis of human melanoma cells in athymic nude mice. Cancer research. 2006;66(13):6699-707.

126. Kato Y, Nakayama Y, Umeda M, Miyazaki K. Induction of 103-kDa gelatinase/type IV collagenase by acidic culture conditions in mouse metastatic melanoma cell lines. The Journal of biological chemistry. 1992;267(16):11424-30.

127. Ibrahim-Hashim A, Cornnell HH, Abrahams D, Lloyd M, Bui M, Gillies RJ, et al. Systemic buffers inhibit carcinogenesis in TRAMP mice. The Journal of urology. 2012;188(2):624-31.

128. Martin NK, Robey IF, Gaffney EA, Gillies RJ, Gatenby RA, Maini PK. Predicting the safety and efficacy of buffer therapy to raise tumour pHe: an integrative modelling study. British journal of cancer. 2012;106(7):1280-7.

129. Robey IF, Baggett BK, Kirkpatrick ND, Roe DJ, Dosescu J, Sloane BF, et al. Bicarbonate increases tumor pH and inhibits spontaneous metastases. Cancer research. 2009;69(6):2260-8.

130. Ibrahim Hashim A, Cornnell HH, Coelho Ribeiro Mde L, Abrahams D, Cunningham J, Lloyd M, et al. Reduction of metastasis using a non-volatile buffer. Clinical & experimental metastasis. 2011;28(8):841-9.

131. Ibrahim-Hashim A, Wojtkowiak JW, de Lourdes Coelho Ribeiro M, Estrella V, Bailey KM, Cornnell HH, et al. Free Base Lysine Increases Survival and Reduces Metastasis in Prostate Cancer Model. Journal of cancer science & therapy. 2011;Suppl 1(4).

132. Silva AS, Yunes JA, Gillies RJ, Gatenby RA. The potential role of systemic buffers in reducing intratumoral extracellular pH and acid-mediated invasion. Cancer research. 2009;69(6):2677-84.

133. Bockhorn M, Uzunoglu FG, Adham M, Imrie C, Milicevic M, Sandberg AA, et al. Borderline resectable pancreatic cancer: a consensus statement by the International Study Group of Pancreatic Surgery (ISGPS). Surgery. 2014;155(6):977-88.

134. Vincent A, Herman J, Schulick R, Hruban RH, Goggins M. Pancreatic cancer. Lancet. 2011;378(9791):607-20.

135. Maftouh M, Avan A, Sciarrillo R, Granchi C, Leon LG, Rani R, et al. Synergistic interaction of novel lactate dehydrogenase inhibitors with gemcitabine against pancreatic cancer cells in hypoxia. British journal of cancer. 2014;110(1):172-82.

136. Cheng ZX, Wang DW, Liu T, Liu WX, Xia WB, Xu J, et al. Effects of the HIF-1alpha and NF-kappaB loop on epithelial-mesenchymal transition and chemoresistance induced by hypoxia in pancreatic cancer cells. Oncology reports. 2014;31(4):1891-8.

137. Yokoi K, Fidler IJ. Hypoxia increases resistance of human pancreatic cancer cells to apoptosis induced by gemcitabine. Clinical cancer research : an official journal of the American Association for Cancer Research. 2004;10(7):2299-306.

138. Oettle H, Neuhaus P, Hochhaus A, Hartmann JT, Gellert K, Ridwelski K, et al. Adjuvant chemotherapy with gemcitabine and long-term outcomes among patients with resected pancreatic cancer: the CONKO-001 randomized trial. JAMA. 2013;310(14):1473-81.

139. Neoptolemos JP, Stocken DD, Bassi C, Ghaneh P, Cunningham D, Goldstein D, et al. Adjuvant chemotherapy with fluorouracil plus folinic acid vs gemcitabine following pancreatic cancer resection: a randomized controlled trial. JAMA. 2010;304(10):1073-81.

140. Neoptolemos JP, Stocken DD, Friess H, Bassi C, Dunn JA, Hickey H, et al. A randomized trial of chemoradiotherapy and chemotherapy after resection of pancreatic cancer. The New England journal of medicine. 2004;350(12):1200-10.

141. Diener MK, Fitzmaurice C, Schwarzer G, Seiler CM, Huttner FJ, Antes G, et al. Pylorus-preserving pancreaticoduodenectomy (pp Whipple) versus pancreaticoduodenectomy (classic Whipple) for surgical treatment of periampullary and pancreatic carcinoma. Cochrane Database Syst Rev. 2014(11):CD006053.

142. Fernandez-Cruz L, Orduna D, Cesar-Borges G, Lopez-Boado MA. Distal pancreatectomy: en-bloc splenectomy vs spleen-preserving pancreatectomy. HPB : the official journal of the International Hepato Pancreato Biliary Association. 2005;7(2):93-8.

143. Hartwig W, Gluth A, Hinz U, Bergmann F, Spronk PE, Hackert T, et al. Total pancreatectomy for primary pancreatic neoplasms: renaissance of an unpopular operation. Annals of surgery. 2015;261(3):537-46.

144. Esposito I, Kleeff J, Bergmann F, Reiser C, Herpel E, Friess H, et al. Most pancreatic cancer resections are R1 resections. Annals of surgical oncology. 2008;15(6):1651-60.

145. Tempero MA, Malafa MP, Behrman SW, Benson AB, 3rd, Casper ES, Chiorean EG, et al. Pancreatic adenocarcinoma, version 2.2014: featured updates to the NCCN guidelines. J Natl Compr Canc Netw. 2014;12(8):1083-93.

146. Burris HA, 3rd, Moore MJ, Andersen J, Green MR, Rothenberg ML, Modiano MR, et al. Improvements in survival and clinical benefit with gemcitabine as first-line therapy for patients with advanced pancreas cancer: a randomized trial. Journal of clinical oncology : official journal of the American Society of Clinical Oncology. 1997;15(6):2403-13.

147. Ferrone CR, Marchegiani G, Hong TS, Ryan DP, Deshpande V, McDonnell EI, et al. Radiological and surgical implications of neoadjuvant treatment with FOLFIRINOX for locally advanced and borderline resectable pancreatic cancer. Annals of surgery. 2015;261(1):12-7.

148. Gillen S, Schuster T, Meyer Zum Buschenfelde C, Friess H, Kleeff J. Preoperative/neoadjuvant therapy in pancreatic cancer: a systematic review and meta-analysis of response and resection percentages. PLoS Med. 2010;7(4):e1000267.

149. Apps MG, Choi EH, Wheate NJ. The state-of-play and future of platinum drugs. Endocr Relat Cancer. 2015;22(4):R219-33.

150. Sultana A, Smith CT, Cunningham D, Starling N, Neoptolemos JP, Ghaneh P. Meta-analyses of chemotherapy for locally advanced and metastatic pancreatic cancer. Journal of

clinical oncology : official journal of the American Society of Clinical Oncology. 2007;25(18):2607-15.

151. Von Hoff DD, Ervin T, Arena FP, Chiorean EG, Infante J, Moore M, et al. Increased survival in pancreatic cancer with nab-paclitaxel plus gemcitabine. The New England journal of medicine. 2013;369(18):1691-703.

152. Conroy T, Desseigne F, Ychou M, Bouche O, Guimbaud R, Becouarn Y, et al. FOLFIRINOX versus gemcitabine for metastatic pancreatic cancer. The New England journal of medicine. 2011;364(19):1817-25.

153. Moore MJ, Goldstein D, Hamm J, Figer A, Hecht JR, Gallinger S, et al. Erlotinib plus gemcitabine compared with gemcitabine alone in patients with advanced pancreatic cancer: a phase III trial of the National Cancer Institute of Canada Clinical Trials Group. Journal of clinical oncology : official journal of the American Society of Clinical Oncology. 2007;25(15):1960-6.

154. Ryan DP, Hong TS, Bardeesy N. Pancreatic adenocarcinoma. The New England journal of medicine. 2014;371(11):1039-49.

155. Collisson EA, Sadanandam A, Olson P, Gibb WJ, Truitt M, Gu S, et al. Subtypes of pancreatic ductal adenocarcinoma and their differing responses to therapy. Nature medicine. 2011;17(4):500-3.

156. Witkiewicz AK, McMillan EA, Balaji U, Baek G, Lin WC, Mansour J, et al. Whole-exome sequencing of pancreatic cancer defines genetic diversity and therapeutic targets. Nature communications. 2015;6:6744.

157. Bailey P, Chang DK, Nones K, Johns AL, Patch AM, Gingras MC, et al. Genomic analyses identify molecular subtypes of pancreatic cancer. Nature. 2016;531(7592):47-52.

158. Daemen A, Peterson D, Sahu N, McCord R, Du X, Liu B, et al. Metabolite profiling stratifies pancreatic ductal adenocarcinomas into subtypes with distinct sensitivities to

metabolic inhibitors. Proceedings of the National Academy of Sciences of the United States of America. 2015;112(32):E4410-7.

159. Moffitt RA, Marayati R, Flate EL, Volmar KE, Loeza SG, Hoadley KA, et al. Virtual microdissection identifies distinct tumor- and stroma-specific subtypes of pancreatic ductal adenocarcinoma. Nat Genet. 2015;47(10):1168-78.

160. Collisson EA, Trejo CL, Silva JM, Gu S, Korkola JE, Heiser LM, et al. A central role for RAF-->MEK-->ERK signaling in the genesis of pancreatic ductal adenocarcinoma. Cancer Discov. 2012;2(8):685-93.

161. Huang L, Holtzinger A, Jagan I, BeGora M, Lohse I, Ngai N, et al. Ductal pancreatic cancer modeling and drug screening using human pluripotent stem cell- and patient-derived tumor organoids. Nature medicine. 2015;21(11):1364-71.

162. Solimini NL, Luo J, Elledge SJ. Non-oncogene addiction and the stress phenotype of cancer cells. Cell. 2007;130(6):986-8.

163. Mikuriya K, Kuramitsu Y, Ryozawa S, Fujimoto M, Mori S, Oka M, et al. Expression of glycolytic enzymes is increased in pancreatic cancerous tissues as evidenced by proteomic profiling by two-dimensional electrophoresis and liquid chromatography-mass spectrometry/mass spectrometry. International journal of oncology. 2007;30(4):849-55.

164. Zhou W, Capello M, Fredolini C, Racanicchi L, Piemonti L, Liotta LA, et al. Proteomic analysis reveals Warburg effect and anomalous metabolism of glutamine in pancreatic cancer cells. Journal of proteome research. 2012;11(2):554-63.

165. Rong Y, Wu W, Ni X, Kuang T, Jin D, Wang D, et al. Lactate dehydrogenase A is overexpressed in pancreatic cancer and promotes the growth of pancreatic cancer cells. Tumour biology : the journal of the International Society for Oncodevelopmental Biology and Medicine. 2013;34(3):1523-30.

166. Yang W, Zheng Y, Xia Y, Ji H, Chen X, Guo F, et al. ERK1/2-dependent phosphorylation and nuclear translocation of PKM2 promotes the Warburg effect. Nature cell biology. 2012;14(12):1295-304.

167. Fantin VR, St-Pierre J, Leder P. Attenuation of LDH-A expression uncovers a link between glycolysis, mitochondrial physiology, and tumor maintenance. Cancer cell. 2006;9(6):425-34.

168. Kanno T, Sudo K, Maekawa M, Nishimura Y, Ukita M, Fukutake K. Lactate dehydrogenase M-subunit deficiency: a new type of hereditary exertional myopathy. Clinica chimica acta; international journal of clinical chemistry. 1988;173(1):89-98.

169. Baba M, Inoue M, Itoh K, Nishizawa Y. Blocking CD147 induces cell death in cancer cells through impairment of glycolytic energy metabolism. Biochemical and biophysical research communications. 2008;374(1):111-6.

170. Mathupala SP, Parajuli P, Sloan AE. Silencing of Monocarboxylate Transporters via Small Interfering Ribonucleic Acid Inhibits Glycolysis and Induces Cell Death in Malignant Glioma: An in Vitro Study. Neurosurgery. 2004:1410-9.

171. Bouzin C, Feron O. Targeting tumor stroma and exploiting mature tumor vasculature to improve anti-cancer drug delivery. Drug Resist Updat. 2007;10(3):109-20.

172. Heldin CH, Rubin K, Pietras K, Ostman A. High interstitial fluid pressure - an obstacle in cancer therapy. Nature reviews Cancer. 2004;4(10):806-13.

173. Hingorani SR, Harris WP, Beck JT, Berdov BA, Wagner SA, Pshevlotsky EM, et al. Phase Ib Study of PEGylated Recombinant Human Hyaluronidase and Gemcitabine in Patients with Advanced Pancreatic Cancer. Clinical cancer research : an official journal of the American Association for Cancer Research. 2016;22(12):2848-54.

174. Deer EL, Gonzalez-Hernandez J, Coursen JD, Shea JE, Ngatia J, Scaife CL, et al. Phenotype and genotype of pancreatic cancer cell lines. Pancreas. 2010;39(4):425-35.

175. Morgan RT, Woods LK, Moore GE, Quinn LA, McGavran L, Gordon SG. Human cell line (COLO 357) of metastatic pancreatic adenocarcinoma. International journal of cancer. 1980;25(5):591-8.

176. Sipos B, Moser S, Kalthoff H, Torok V, Lohr M, Kloppel G. A comprehensive characterization of pancreatic ductal carcinoma cell lines: towards the establishment of an in vitro research platform. Virchows Archiv : an international journal of pathology. 2003;442(5):444-52.

177. Karandish F, Mallik S. Biomarkers and Targeted Therapy in Pancreatic Cancer. Biomarkers in cancer. 2016;8(Suppl 1):27-35.

178. Kalthoff H, Schmiegel W, Roeder C, Kasche D, Schmidt A, Lauer G, et al. p53 and K-RAS alterations in pancreatic epithelial cell lesions. Oncogene. 1993;8(2):289-98.

179. Naumann M, Savitskaia N, Eilert C, Schramm A, Kalthoff H, Schmiegel W. Frequent codeletion of p16/MTS1 and p15/MTS2 and genetic alterations in p16/MTS1 in pancreatic tumors. Gastroenterology. 1996;110(4):1215-24.

180. Berrozpe G, Schaeffer J, Peinado MA, Real FX, Perucho M. Comparative analysis of mutations in the p53 and K-ras genes in pancreatic cancer. International journal of cancer. 1994;58(2):185-91.

181. Schutte M, Hruban RH, Hedrick L, Cho KR, Nadasdy GM, Weinstein CL, et al. DPC4 gene in various tumor types. Cancer research. 1996;56(11):2527-30.

182. Chen WH, Horoszewicz JS, Leong SS, Shimano T, Penetrante R, Sanders WH, et al. Human pancreatic adenocarcinoma: in vitro and in vivo morphology of a new tumor line established from ascites. In Vitro. 1982;18(1):24-34.

183. Hahn SA, Schutte M, Hoque AT, Moskaluk CA, da Costa LT, Rozenblum E, et al. DPC4, a candidate tumor suppressor gene at human chromosome 18q21.1. Science. 1996;271(5247):350-3.

184. Tan MH, Nowak NJ, Loor R, Ochi H, Sandberg AA, Lopez C, et al. Characterization of a new primary human pancreatic tumor line. Cancer Invest. 1986;4(1):15-23.

185. Kyriazis AP, Kyriazis AA, Scarpelli DG, Fogh J, Rao MS, Lepera R. Human pancreatic adenocarcinoma line Capan-1 in tissue culture and the nude mouse: morphologic, biologic, and biochemical characteristics. The American journal of pathology. 1982;106(2):250-60.

186. Yunis AA, Arimura GK, Russin DJ. Human pancreatic carcinoma (MIA PaCa-2) in continuous culture: sensitivity to asparaginase. International journal of cancer. 1977;19(1):128-35.

187. Lieber M, Mazzetta J, Nelson-Rees W, Kaplan M, Todaro G. Establishment of a continuous tumor-cell line (panc-1) from a human carcinoma of the exocrine pancreas. International journal of cancer. 1975;15(5):741-7.

188. Foty R. A simple hanging drop cell culture protocol for generation of 3D spheroids. J Vis Exp. 2011(51).

189. Gaunitz F, Heise K. HTS compatible assay for antioxidative agents using primary cultured hepatocytes. Assay and drug development technologies. 2003;1(3):469-77.

190. Perrot S, Dutertre-Catella H, Martin C, Warnet JM, Rat P. A new nondestructive cytometric assay based on resazurin metabolism and an organ culture model for the assessment of corneal viability. Cytometry Part A : the journal of the International Society for Analytical Cytology. 2003;55(1):7-14.

191. de Fries R, Mitsuhashi M. Quantification of mitogen induced human lymphocyte proliferation: comparison of alamarBlue assay to 3H-thymidine incorporation assay. Journal of clinical laboratory analysis. 1995;9(2):89-95.

192. Promega. CellTiter-Blue Cell Viability Assay Protocol Technical Bulletin TB317. 2016.

193. Mittal V. Improving the efficiency of RNA interference in mammals. Nat Rev Genet. 2004;5(5):355-65.

194. Dykxhoorn DM, Novina CD, Sharp PA. Killing the messenger: short RNAs that silence gene expression. Nat Rev Mol Cell Biol. 2003;4(6):457-67.

195. Graham FL, van der Eb AJ. A new technique for the assay of infectivity of human adenovirus 5 DNA. Virology. 1973;52(2):456-67.

196. Liu F, Korc M. Cdk4/6 inhibition induces epithelial-mesenchymal transition and enhances invasiveness in pancreatic cancer cells. Mol Cancer Ther. 2012;11(10):2138-48.

197. Swietach P, Vaughan-Jones RD. Novel method for measuring junctional proton permeation in isolated ventricular myocyte cell pairs. American journal of physiology Heart and circulatory physiology. 2004;287(5):H2352-63.

198. Wilhelm S. LSM 700 Operating Manual. Carl Zeiss MicroImaging GmbH. 2011.

199. Haugland RP. Molecular Probes™ Handbook. A Guide to Fluorescent Probes and Labeling Technologies. 11th Edition: ThermoFisher Scientific; 2010. p. 3-9.

200. Haugland RP. Molecular Probes™ Handbook. A Guide to Fluorescent Probes and Labeling Technologies. 11th Edition: ThermoFisher Scientific; 2010. p. 883-902.

201. Dubbin PN, Cody SH, Williams DA. Intracellular Ph Mapping with Snarf-1 and Confocal Microscopy .2. Ph Gradients within Single Cultured-Cells. Micron. 1993;24(6):581-6.

202. Buckler KJ, Vaughan-Jones RD. Application of a new pH-sensitive fluoroprobe (carboxy-SNARF-1) for intracellular pH measurement in small, isolated cells. Pflugers Archiv : European journal of physiology. 1990;417(2):234-9.

203. Vaughan-Jones RD, Peercy BE, Keener JP, Spitzer KW. Intrinsic H(+) ion mobility in the rabbit ventricular myocyte. The Journal of physiology. 2002;541(Pt 1):139-58.

204. Abbaci M, Barberi-Heyob M, Blondel W, Guillemin F, Didelon J. Advantages and limitations of commonly used methods to assay the molecular permeability of gap junctional intercellular communication. Biotechniques. 2008;45(1):33-52, 6-62.

205. Naus CC, Laird DW. Implications and challenges of connexin connections to cancer. Nature reviews Cancer. 2010;10(6):435-41.

206. Swietach P, Spitzer KW, Vaughan-Jones RD. pH-Dependence of extrinsic and intrinsic H(+)-ion mobility in the rat ventricular myocyte, investigated using flash photolysis of a caged-H(+) compound. Biophysical journal. 2007;92(2):641-53.

207. Smith G, Lynch DE, Byriel KA, Kennard CHL. The utility of 4-aminobenzoic acid in promotion of hydrogen bonding in crystallization processes: the structures of the cocrystals with halo and nitro substituted aromatic compounds, and the crystal structures of the adducts with 4-nitroaniline (1:1), 4-(4-nitrobenzyl)pyridine (1:2), and (4-nitrophenyl)acetic acid (1:1). J Chem Crystallogr. 1997;27(5):307-17.

208. Alves F, Contag S, Missbach M, Kaspareit J, Nebendahl K, Borchers U, et al. An orthotopic model of ductal adenocarcinoma of the pancreas in severe combined immunodeficient mice representing all steps of the metastatic cascade. Pancreas. 2001;23(3):227-35.

209. Fogh J, Orfeo T, Tiso J, Sharkey FE, Fogh JM, Daniels WP. Twenty-three new human tumor lines established in nude mice. Exp Cell Biol. 1980;48(3):229-39.

210. Saccomano M, Dullin C, Alves F, Napp J. Preclinical evaluation of near-infrared (NIR) fluorescently labeled Cetuximab as a potential tool for fluorescence-guided surgery. International journal of cancer. 2016;(in press).

211. Supuran CT. Carbonic anhydrases: novel therapeutic applications for inhibitors and activators. Nature reviews Drug discovery. 2008;7(2):168-81.

212. Bustamante E, Pedersen PL. High aerobic glycolysis of rat hepatoma cells in culture: role of mitochondrial hexokinase. Proceedings of the National Academy of Sciences of the United States of America. 1977;74(9):3735-9.

213. Graffman S, Bjork P, Ederoth P, Ihse I. Polarographic pO2 measurements of intra-abdominal adenocarcinoma in connection with intraoperative radiotherapy before and after change of oxygen concentration of anaesthetic gases. Acta oncologica. 2001;40(1):105-7.

214. Ewaschuk JB, Naylor JM, Zello GA. D-lactate in human and ruminant metabolism. J Nutr. 2005;135(7):1619-25.

215. Ewaschuk JB, Naylor JM, Zello GA. D-Lactate in human and ruminant metabolism. J Nutr. 2005;135(7):1619-25.

216. Allen SE, Holm JL. Lactate: physiology and clinical utility. J Vet Emerg Crit Car. 2008;18(2):123-32.

217. Reitzer LJ, Wice BM, Kennell D. Evidence that glutamine, not sugar, is the major energy source for cultured HeLa cells. The Journal of biological chemistry. 1979;254(8):2669-76.

218. Galluzzi L, Kepp O, Vander Heiden MG, Kroemer G. Metabolic targets for cancer therapy. Nature reviews Drug discovery. 2013;12(11):829-46.

219. Owen OE, Kalhan SC, Hanson RW. The key role of anaplerosis and cataplerosis for citric acid cycle function. The Journal of biological chemistry. 2002;277(34):30409-12.

220. Wick AN, Drury DR, Nakada HI, Wolfe JB. Localization of the primary metabolic block produced by 2-deoxyglucose. The Journal of biological chemistry. 1957;224(2):963-9.

221. Wood IS, Wang B, Lorente-Cebrian S, Trayhurn P. Hypoxia increases expression of selective facilitative glucose transporters (GLUT) and 2-deoxy-D-glucose uptake in human adipocytes. Biochemical and biophysical research communications. 2007;361(2):468-73.

222. Pelicano H, Martin DS, Xu RH, Huang P. Glycolysis inhibition for anticancer treatment. Oncogene. 2006;25(34):4633-46.

223. Chen W, Gueron M. The inhibition of bovine heart hexokinase by 2-deoxy-D-glucose-6-phosphate: characterization by 31P NMR and metabolic implications. Biochimie. 1992;74(9-10):867-73.

224. Rossignol R, Gilkerson R, Aggeler R, Yamagata K, Remington SJ, Capaldi RA. Energy substrate modulates mitochondrial structure and oxidative capacity in cancer cells. Cancer research. 2004;64(3):985-93.

225. Marroquin LD, Hynes J, Dykens JA, Jamieson JD, Will Y. Circumventing the Crabtree effect: replacing media glucose with galactose increases susceptibility of HepG2 cells to mitochondrial toxicants. Toxicological sciences : an official journal of the Society of Toxicology. 2007;97(2):539-47.

226. Aguer C, Gambarotta D, Mailloux RJ, Moffat C, Dent R, McPherson R, et al. Galactose enhances oxidative metabolism and reveals mitochondrial dysfunction in human primary muscle cells. PloS one. 2011;6(12):e28536.

227. Robinson BH, Petrova-Benedict R, Buncic JR, Wallace DC. Nonviability of cells with oxidative defects in galactose medium: a screening test for affected patient fibroblasts. Biochemical medicine and metabolic biology. 1992;48(2):122-6.

228. Gohil VM, Sheth SA, Nilsson R, Wojtovich AP, Lee JH, Perocchi F, et al. Nutrient-sensitized screening for drugs that shift energy metabolism from mitochondrial respiration to glycolysis. Nature biotechnology. 2010;28(3):249-55.

229. Swietach P, Patiar S, Supuran CT, Harris AL, Vaughan-Jones RD. The role of carbonic anhydrase 9 in regulating extracellular and intracellular ph in three-dimensional tumor cell growths. The Journal of biological chemistry. 2009;284(30):20299-310.

230. Cheng G, Zielonka J, McAllister D, Tsai S, Dwinell MB, Kalyanaraman B. Profiling and targeting of cellular bioenergetics: inhibition of pancreatic cancer cell proliferation. British journal of cancer. 2014;111(1):85-93.

231. Liu M, Quek LE, Sultani G, Turner N. Epithelial-mesenchymal transition induction is associated with augmented glucose uptake and lactate production in pancreatic ductal adenocarcinoma. Cancer & metabolism. 2016;4:19.

232. Boron WF. Regulation of intracellular pH. Adv Physiol Educ. 2004;28(1-4):160-79.

233. Swietach P, Vaughan-Jones RD. Relationship between intracellular pH and proton mobility in rat and guinea-pig ventricular myocytes. The Journal of physiology. 2005;566(Pt 3):793-806.

234. Swietach P, Camelliti P, Hulikova A, Kohl P, Vaughan-Jones RD. Spatial regulation of intracellular pH in multicellular strands of neonatal rat cardiomyocytes. Cardiovascular research. 2010;85(4):729-38.

235. Zaniboni M, Swietach P, Rossini A, Yamamoto T, Spitzer KW, Vaughan-Jones RD. Intracellular proton mobility and buffering power in cardiac ventricular myocytes from rat, rabbit, and guinea pig. American journal of physiology Heart and circulatory physiology. 2003;285(3):H1236-46.

236. Geers C, Gros G. Carbon dioxide transport and carbonic anhydrase in blood and muscle. Physiological reviews. 2000;80(2):681-715.

237. Wykoff CC, Beasley NJ, Watson PH, Turner KJ, Pastorek J, Sibtain A, et al. Hypoxia-inducible expression of tumor-associated carbonic anhydrases. Cancer research. 2000;60(24):7075-83.

238. Chien MH, Ying TH, Hsieh YH, Lin CH, Shih CH, Wei LH, et al. Tumor-associated carbonic anhydrase XII is linked to the growth of primary oral squamous cell carcinoma and its poor prognosis. Oral Oncol. 2012;48(5):417-23.

239. Giatromanolaki A, Koukourakis MI, Sivridis E, Pastorek J, Wykoff CC, Gatter KC, et al. Expression of hypoxia-inducible carbonic anhydrase-9 relates to angiogenic pathways and independently to poor outcome in non-small cell lung cancer. Cancer research. 2001;61(21):7992-8.

240. Chia SK, Wykoff CC, Watson PH, Han C, Leek RD, Pastorek J, et al. Prognostic significance of a novel hypoxia-regulated marker, carbonic anhydrase IX, in invasive breast

carcinoma. Journal of clinical oncology : official journal of the American Society of Clinical Oncology. 2001;19(16):3660-8.

241. Koukourakis MI, Giatromanolaki A, Sivridis E, Simopoulos K, Pastorek J, Wykoff CC, et al. Hypoxia-regulated carbonic anhydrase-9 (CA9) relates to poor vascularization and resistance of squamous cell head and neck cancer to chemoradiotherapy. Clinical cancer research : an official journal of the American Association for Cancer Research. 2001;7(11):3399-403.

242. Sheng W, Dong M, Zhou J, Li X, Dong Q. Down regulation of CAII is associated with tumor differentiation and poor prognosis in patients with pancreatic cancer. Journal of surgical oncology. 2013;107(5):536-43.

243. Maupin KA, Sinha A, Eugster E, Miller J, Ross J, Paulino V, et al. Glycogene expression alterations associated with pancreatic cancer epithelial-mesenchymal transition in complementary model systems. PloS one. 2010;5(9):e13002.

244. Pastorekova S, Parkkila S, Parkkila AK, Opavsky R, Zelnik V, Saarnio J, et al. Carbonic anhydrase IX, MN/CA IX: analysis of stomach complementary DNA sequence and expression in human and rat alimentary tracts. Gastroenterology. 1997;112(2):398-408.

245. Mahieu I, Hollande E, Carter N. Membrane targeting of carbonic anhydrase II (CAII) in human pancreatic ductal Capan 1 cells in culture. Biochem Soc Trans. 1994;22(4):438S.

246. Hulikova A, Aveyard N, Harris AL, Vaughan-Jones RD, Swietach P. Intracellular carbonic anhydrase activity sensitizes cancer cell pH signaling to dynamic changes in CO2 partial pressure. The Journal of biological chemistry. 2014;289(37):25418-30.

247. Romero MF, Chen AP, Parker MD, Boron WF. The SLC4 family of bicarbonate (HCO(3)(-)) transporters. Mol Aspects Med. 2013;34(2-3):159-82.

248. Aasen T, Mesnil M, Naus CC, Lampe PD, Laird DW. Gap junctions and cancer: communicating for 50 years. Nature reviews Cancer. 2016;16(12):775-88.

249. Lee MG, Ohana E, Park HW, Yang D, Muallem S. Molecular mechanism of pancreatic and salivary gland fluid and HCO3 secretion. Physiological reviews. 2012;92(1):39-74.

250. Hulikova A, Vaughan-Jones RD, Swietach P. Dual role of CO2/HCO3(-) buffer in the regulation of intracellular pH of three-dimensional tumor growths. The Journal of biological chemistry. 2011;286(16):13815-26.

251. Putney LK, Barber DL. Na-H exchange-dependent increase in intracellular pH times G2/M entry and transition. The Journal of biological chemistry. 2003;278(45):44645-9.

252. Schreiber R. Ca2+ signaling, intracellular pH and cell volume in cell proliferation. J Membr Biol. 2005;205(3):129-37.

253. Kumar NM, Gilula NB. The gap junction communication channel. Cell. 1996;84(3):381-8.

254. Hulikova A, Black N, Hsia LT, Wilding J, Bodmer WF, Swietach P. Stromal uptake and transmission of acid is a pathway for venting cancer cell-generated acid. Proceedings of the National Academy of Sciences of the United States of America. 2016;113(36):E5344-53.

255. McLachlan E, Shao Q, Wang HL, Langlois S, Laird DW. Connexins act as tumor suppressors in three-dimensional mammary cell organoids by regulating differentiation and angiogenesis. Cancer research. 2006;66(20):9886-94.

256. Mesnil M. Connexins and cancer. Biology of the cell / under the auspices of the European Cell Biology Organization. 2002;94(7-8):493-500.

257. Loewenstein WR, Kanno Y. Intercellular communication and the control of tissue growth: lack of communication between cancer cells. Nature. 1966;209(5029):1248-9.

258. Lin JH, Takano T, Cotrina ML, Arcuino G, Kang J, Liu S, et al. Connexin 43 enhances the adhesivity and mediates the invasion of malignant glioma cells. The Journal of neuroscience : the official journal of the Society for Neuroscience. 2002;22(11):4302-11.

259. Elzarrad MK, Haroon A, Willecke K, Dobrowolski R, Gillespie MN, Al-Mehdi AB. Connexin-43 upregulation in micrometastases and tumor vasculature and its role in tumor cell attachment to pulmonary endothelium. BMC medicine. 2008;6:20.

260. Ito A, Katoh F, Kataoka TR, Okada M, Tsubota N, Asada H, et al. A role for heterologous gap junctions between melanoma and endothelial cells in metastasis. The Journal of clinical investigation. 2000;105(9):1189-97.

261. el-Sabban ME, Pauli BU. Cytoplasmic dye transfer between metastatic tumor cells and vascular endothelium. The Journal of cell biology. 1991;115(5):1375-82.

262. Zhang A, Hitomi M, Bar-Shain N, Dalimov Z, Ellis L, Velpula KK, et al. Connexin 43 expression is associated with increased malignancy in prostate cancer cell lines and functions to promote migration. Oncotarget. 2015;6(13):11640-51.

263. Hong CS, Graham NA, Gu W, Espindola Camacho C, Mah V, Maresh EL, et al. MCT1 Modulates Cancer Cell Pyruvate Export and Growth of Tumors that Co-express MCT1 and MCT4. Cell reports. 2016;14(7):1590-601.

264. Dimmer KS, Friedrich B, Lang F, Deitmer JW, Broer S. The low-affinity monocarboxylate transporter MCT4 is adapted to the export of lactate in highly glycolytic cells. The Biochemical journal. 2000;350 Pt 1:219-27.

265. Broer S, Schneider HP, Broer A, Rahman B, Hamprecht B, Deitmer JW. Characterization of the monocarboxylate transporter 1 expressed in Xenopus laevis oocytes by changes in cytosolic pH. The Biochemical journal. 1998;333 (Pt 1):167-74.

266. Halestrap AP, Meredith D. The SLC16 gene family-from monocarboxylate transporters (MCTs) to aromatic amino acid transporters and beyond. Pflugers Archiv : European journal of physiology. 2004;447(5):619-28.

267. Swietach P, Rossini A, Spitzer KW, Vaughan-Jones RD. H+ ion activation and inactivation of the ventricular gap junction: a basis for spatial regulation of intracellular pH. Circulation research. 2007;100(7):1045-54.

268. Richards M, Lomas O, Jalink K, Ford KL, Vaughan-Jones RD, Lefkimmiatis K, et al. Intracellular tortuosity underlies slow cAMP diffusion in adult ventricular myocytes. Cardiovascular research. 2016.

269. San Martin A, Ceballo S, Ruminot I, Lerchundi R, Frommer WB, Barros LF. A genetically encoded FRET lactate sensor and its use to detect the Warburg effect in single cancer cells. PloS one. 2013;8(2):e57712.

270. Thompson RJ, Zhou N, MacVicar BA. Ischemia opens neuronal gap junction hemichannels. Science. 2006;312(5775):924-7.

271. Moellering RE, Black KC, Krishnamurty C, Baggett BK, Stafford P, Rain M, et al. Acid treatment of melanoma cells selects for invasive phenotypes. Clinical & experimental metastasis. 2008;25(4):411-25.

272. McIntyre A, Hulikova A, Ledaki I, Snell C, Singleton D, Steers G, et al. Disrupting Hypoxia-Induced Bicarbonate Transport Acidifies Tumor Cells and Suppresses Tumor Growth. Cancer research. 2016;76(13):3744-55.

273. McDonald OG, Li X, Saunders T, Tryggvadottir R, Mentch SJ, Warmoes MO, et al. Epigenomic reprogramming during pancreatic cancer progression links anabolic glucose metabolism to distant metastasis. Nat Genet. 2017;49(3):367-76.

274. Solan JL, Hingorani SR, Lampe PD. Changes in connexin43 expression and localization during pancreatic cancer progression. J Membr Biol. 2012;245(5-6):255-62.

275. DeBerardinis RJ, Chandel NS. Fundamentals of cancer metabolism. Sci Adv. 2016;2(5):e1600200.

276. Bukauskas FF, Bukauskiene A, Verselis VK. Conductance and permeability of the residual state of connexin43 gap junction channels. J Gen Physiol. 2002;119(2):171-85.

277. Ibsen KH, McKee RW. Inorganic ion concentrations in Ehrlich ascites carcinoma cells and fluid. Cancer research. 1967;27(9):1648-51.

278. Kanczuga-Koda L, Sulkowski S, Lenczewski A, Koda M, Wincewicz A, Baltaziak M, et al. Increased expression of connexins 26 and 43 in lymph node metastases of breast cancer. J Clin Pathol. 2006;59(4):429-33.

279. Ogawa K, Pitchakarn P, Suzuki S, Chewonarin T, Tang M, Takahashi S, et al. Silencing of connexin 43 suppresses invasion, migration and lung metastasis of rat hepatocellular carcinoma cells. Cancer science. 2012;103(5):860-7.

280. Pollmann MA, Shao Q, Laird DW, Sandig M. Connexin 43 mediated gap junctional communication enhances breast tumor cell diapedesis in culture. Breast Cancer Res. 2005;7(4):R522-34.

281. Gadaleta E, Cutts RJ, Kelly GP, Crnogorac-Jurcevic T, Kocher HM, Lemoine NR, et al. A global insight into a cancer transcriptional space using pancreatic data: importance, findings and flaws. Nucleic acids research. 2011;39(18):7900-7.

282. Faller BA, Burtness B. Treatment of pancreatic cancer with epidermal growth factor receptor-targeted therapy. Biologics : targets & therapy. 2009;3:419-28.

283. Oliveira-Cunha M, Newman WG, Siriwardena AK. Epidermal growth factor receptor in pancreatic cancer. Cancers. 2011;3(2):1513-26.

12 Appendices

OPEN

Oncogene (2017) **36,** 4538–4550

CC BY 4.0 **www.nature.com/onc**

ORIGINAL ARTICLE

Connexin-43 channels are a pathway for discharging lactate from glycolytic pancreatic ductal adenocarcinoma cells

TH Dovmark[1], M Saccomano[2], A Hulikova[1], F Alves[2,3,4] and P Swietach[1]

Glycolytic cancer cells produce large quantities of lactate that must be removed to sustain metabolism in the absence of oxidative phosphorylation. The only venting mechanism described to do this at an adequate rate is H^+-coupled lactate efflux on monocarboxylate transporters (MCTs). Outward MCT activity is, however, thermodynamically inhibited by extracellular acidity, a hallmark of solid tumours. This inhibition would feedback unfavourably on metabolism and growth, raising the possibility that other venting mechanisms become important in under-perfused tumours. We investigated connexin-assembled gap junctions as an alternative route for discharging lactate from pancreatic ductal adenocarcinoma (PDAC) cells. Diffusive coupling (calcein transmission) *in vitro* was strong between Colo357 cells, weaker yet hypoxia-inducible between BxPC3 cells, and very low between MiaPaCa2 cells. Coupling correlated with levels of connexin-43 (Cx43), a protein previously linked to late-stage disease. Evoked lactate dynamics, imaged in Colo357 spheroids using cytoplasmic pH as a read-out, indicated that lactate anions permeate gap junctions faster than highly-buffered H^+ ions. At steady-state, junctional transmission of lactate (a chemical base) from the spheroid core had an alkalinizing effect on the rim, producing therein a milieu conducive for growth. Metabolite assays demonstrated that Cx43 knockdown increased cytoplasmic lactate retention in Colo357 spheroids (diameter ~ 150 μm). MiaPaCa2 cells, which are Cx43 negative in monolayer culture, showed markedly increased Cx43 immunoreactivity at areas of invasion in orthotopic xenograft mouse models. These tissue areas were associated with chronic extracellular acidosis (as indicated by the marker LAMP2 near/at the plasmalemma), which can explain the advantage of junctional transmission over MCT *in vivo*. We propose that Cx43 channels are important conduits for dissipating lactate anions from glycolytic PDAC cells. Furthermore, lactate entry into the better-perfused recipient cells has a favourable alkalinizing effect and supplies substrate for oxidative phosphorylation. Cx43 is thus a novel target for influencing metabolite handling in junctionally-coupled tumours.

Oncogene (2017) **36,** 4538–4550; doi:10.1038/onc.2017.71; published online 3 April 2017

INTRODUCTION

Tumours produce large amounts of lactate,[1] which, in the absence of oxidative phosphorylation, is a waste product that must be removed. The best characterized venting mechanism involves monocarboxylate transporters (MCT) that translocate lactate and H^+ ions across the cell membrane.[2–5] However, solid tumours commonly develop a profoundly acidic extracellular microenvironment,[6–11] which thermodynamically hinders H^+-coupled lactate efflux. It is therefore unclear how MCTs could produce an adequate export of lactate anions under these circumstances. Alternative routes for discharging lactate may be necessary to support glycolytic cancer metabolism. Without a complete characterization of all lactate-handling pathways, full efficacy of therapies aimed at attenuating lactate removal[12] cannot be achieved.

An alternative route for venting lactate anions from poorly perfused cells may involve gap junctions assembled from connexin proteins.[13] These channels couple the cytoplasm of neighbouring cells into a syncytium and establish high-conductance pathways for the passage of small molecules. Since direct cell-to-cell junctional flux is thermodynamically insensitive to extracellular pH (pH_e),[14] it may compensate for reduced MCT activity in acidic microenvironments. As yet, this junctional route has not been considered as a means of handling cancer metabolites because of the widely held notion that gap junctions are not associated with cancer,[15] and act as tumour suppressors in at least some types of neoplastic disease.[16–18] However, several reports have produced evidence that connexins may, in fact, facilitate late-stage disease in certain cancers.[19–23]

Pancreatic ductal adenocarcinoma (PDAC) tumours, a highly invasive cancer, are characterized by profoundly under-perfused regions[24,25] which require efficient mechanisms for off-loading lactate into the nearest functional blood vessel. Genes coding for connexins are expressed in many PDAC cell lines,[26] and we hypothesize that gap junctions are important conduits for transmitting lactate across clusters of PDAC cells, towards regions that have the most favourable transmembrane gradient for MCT-assisted off-loading. We produce evidence that junctional transport of lactate benefits tumours dually by (i) offering a pH_e-insensitive route for discharging metabolic waste from glycolytic cells, and (ii) alkalizing recipient cells to levels that are generally conducive for proliferation.[27–29] Our findings propose a novel, lactate-handling role for Cx43 which may be particularly critical in acidotic regions of tumours.

[1]Department of Physiology, Anatomy and Genetics, Oxford University, Oxford, UK; [2]Max-Planck-Institute of Experimental Medicine, Goettingen, Germany; [3]Institute for Diagnostic and Interventional Radiology, University Medical Center Goettingen, Goettingen, Germany and [4]Department of Haematology and Medical Oncology, University Medical Center Goettingen, Goettingen, Germany. Correspondence: Dr P Swietach, Department of Physiology, Anatomy and Genetics, Oxford University, Parks Road, Oxford OX1 3PT, UK.
E-mail: pawel.swietach@dpag.ox.ac.uk
Received 9 September 2016; revised 27 January 2017; accepted 14 February 2017; published online 3 April 2017

RESULTS

PDAC cell lines differ in their gap junctional connectivity

The canonical pathway for removing lactate involves MCT proteins. Expression of MCT isoforms 1 and 4 was measured by immunoblotting in cell lines[30,31] established from primary PDAC tumours (MiaPaCa2, BxPC3, PANC1), ascites (AsPC1) and metastatic lesions (Colo357, Capan1) (Figure 1a). MCT1 was detected in all cell lines, and hypoxia-inducible MCT4 was strongly expressed in all except Capan1. A possible alternative to MCT-dependent venting is cell-to-cell lactate transmission via connexin channels. A published microarray dataset of 22 human PDAC cell lines established from either primary tumour or metastatic lesions[26] demonstrates expression of genes coding for connexins (Figure 1bi). Among these, the most prominently expressed genes code for Cx43, Cx26 and Cx45 (genes: *GJA1*, *GJB2* and *GJC1*). Colo357, BxPC3 and MiaPaCa2 were selected for further studies on

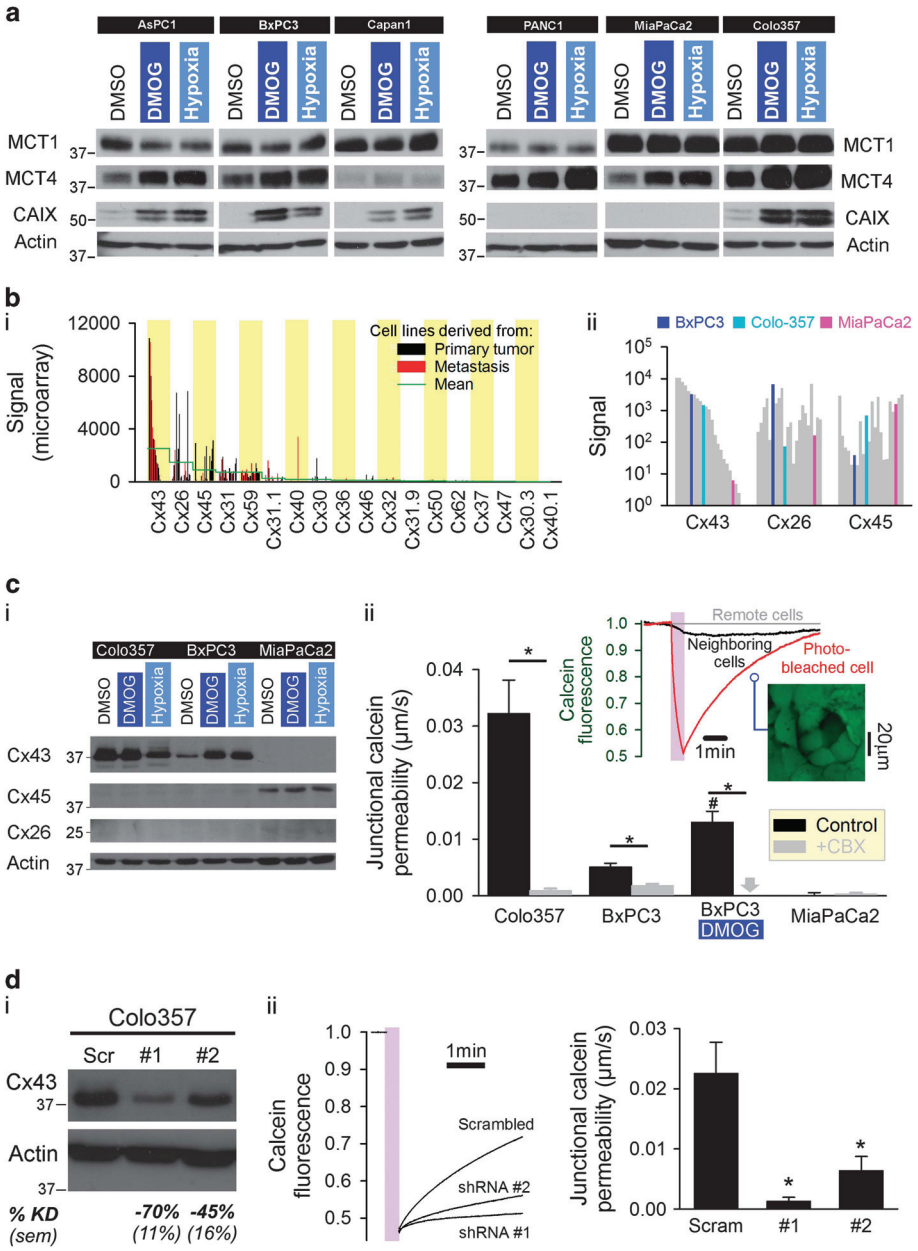


Figure 1. Gap junctional connectivity in PDAC cells. (**a**) Western blot (one of three repeats) for MCT1 and MCT4; CAIX induction is used as a marker of hypoxic signalling. (**b**(i)) Microarray data (BioGPS dataset E-GEOD-21654) for expression of connexin-coding genes in PDAC cell lines (see Supplementary Information for list; note that Cx23, Cx25 and Cx30.2 were not determined). (ii) Expression re-plotted on logarithmic scale, highlighting data for BxPC3, Colo357 and MiaPaCa2 cells. (**c**,i) Western blot (one of four repeats) for Cx43, Cx45 and Cx26 under normoxic conditions, after treatment with 1 mM dimethyloxalylglycine (DMOG), and incubation in 2% O_2 (hypoxia). (ii) Fluorescence recovery after photobleaching (FRAP) protocol for measuring junctional calcein permeability. Specimen trace for Colo357 monolayer. Carbenoxolone (CBX; 100 µM) inhibited coupling. Mean ± s.e.m. of 15 Colo357, 15 BxPC3 and 10 MiaPaCa2 cell clusters. Unpaired *t*-test $^{*}P < 0.01$ (control vs CBX), $^{\#}P < 0.01$ (DMOG vs normoxia). (**d**(i)) shRNA knockdown of Cx43 (*GJA1* gene) in Colo357 (lentiviral delivery) reduces Cx43 expression; two constructs (of four tested) with best knockdown efficiency are shown. Knockdown efficiency (% KD) determined densitometrically from the change in Cx43/actin ratio from three blots (mean ± s.e.m.). (ii) Cx43 knockdown reduces cell-to-cell coupling assayed by FRAP. Note that enhanced green fluorescent protein (eGFP) signal associated with lentivirally-infected cells, is negligible (< 10%) compared with calcein fluorescence and does not contribute to fluorescence recovery. Specimen time courses shown; histogram shows mean ± s.e.m. ($n = 11, 8, 9$); unpaired *t*-test $^{*}P < 0.01$.

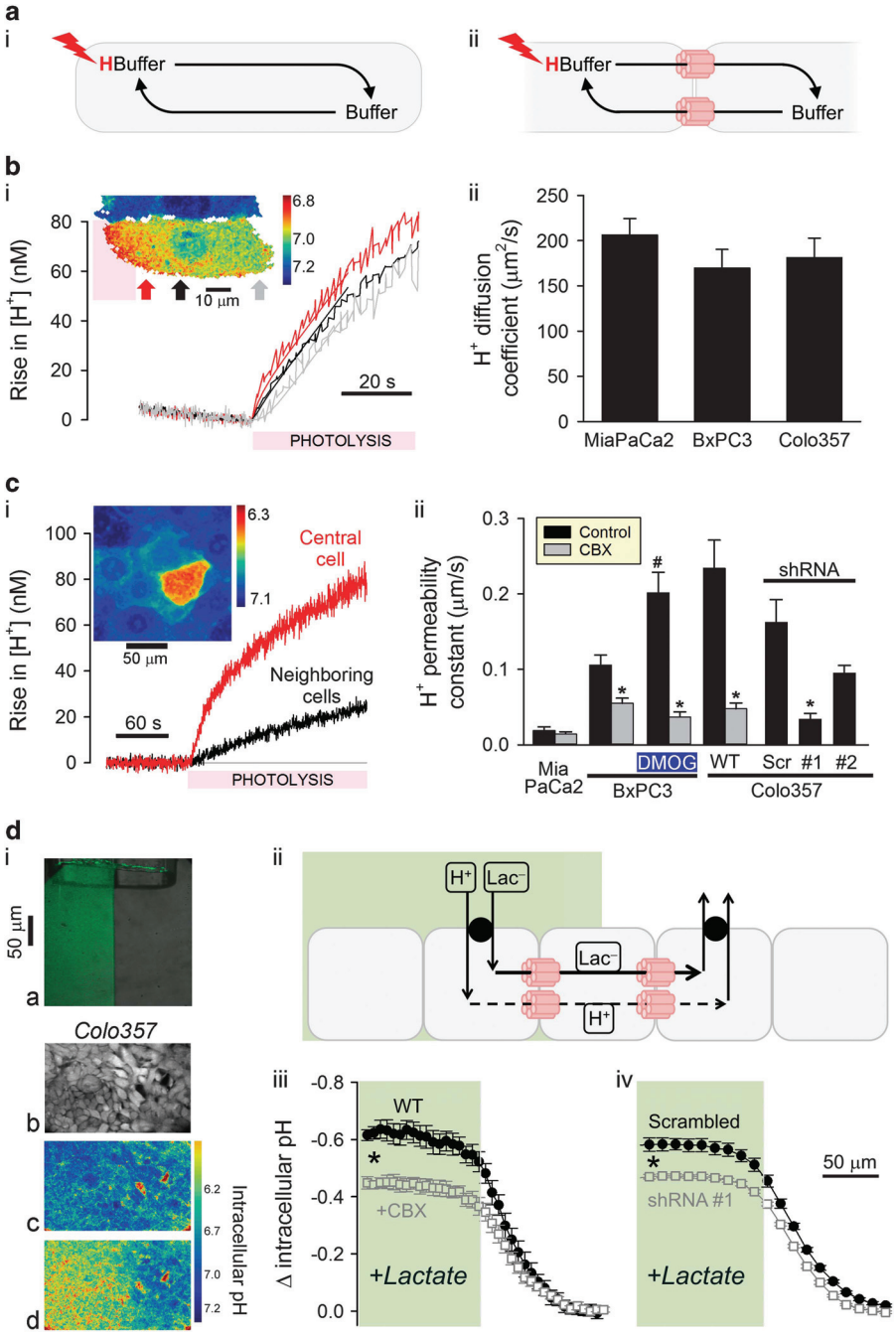


Figure 2. Junctional transmission of lactate and H^+ ions. (**a**(i)) A source of H^+ ions drives passive exchange of protonated and unprotonated buffers. Cytoplasmic H^+ diffusivity probes buffer mobility in a cell. (ii) Cell-to-cell H^+ permeability probes buffer transmission through gap junctions. (**b**(i)) Measuring H^+ diffusion in a Colo357 cell, superfused in Hepes-buffered solution containing 1 mM NVA, the caged H^+-compound. H^+-uncaging (shaded region) produces a H^+ microdomain that spreads diffusively in cytoplasm. Time courses of $[H^+]$ in three regions of interest (indicated by arrows) best-fitted with diffusion equation. (ii) Mean ± s.e.m. ($N = 12, 15, 10$). (**c**(i)) Measuring junctional H^+ permeability between Colo357 cells. H^+ ions were uncaged from 0.5 mM NVA in a central cell and time courses of $[H^+]$ in the central and neighboring cells derive junctional H^+ permeability. (ii) Mean ± s.e.m. ($N = 10, 11, 12, 10, 14, 12, 18, 10, 12, 14, 10$). Experiments repeated in presence of carbenoxolone (CBX; 100 µM) and on *GJA1* knockdown cells. Unpaired *t*-test $^*P < 0.01$ (effect of CBX), $^{\#}P < 0.02$ (effect of DMOG). (**d**(i-a)) Regional exposure of a monolayer to 40 mM lactate-containing Hepes-buffered solution using a double-barrelled micropipette. For illustrative purposes, one microstream was labelled with 30 µM fluorescein; (b) fluorescence of cSNARF1-loaded monolayer; (c) pH_i before and (d) during regional exposure to lactate. (ii) Rapid junctional lactate transmission dissipates syncytial $[lactate]_i$ gradient and permits further MCT-dependent H^+-lactate entry into cells under the lactate-containing microstream (shaded green). (iii) Steady-state intracellular pH across monolayer of wild-type Colo357 cells measured after 2 min of regional exposure to lactate, minus intracellular pH under resting conditions. Experiment repeated in presence of CBX (100 µM). Mean ± s.e.m. ($N = 7$ WT, 10 CBX). (iv) Measurements on Colo357 cells transduced with shRNA #1 (knockdown) or scrambled construct. Mean ± s.e.m. ($N = 5$ WT, 5 CBX). ANOVA $^*P < 0.05$ for effect of CBX and for the effect of knockdown.

the basis that these represent various combinations of *GJA1*, *GJB2* and *GJC1* expression (Figure 1bii).

At protein level, Cx43 was present in Colo357 and BxPC3 cells, but not in MiaPaCa2 cells *in vitro*. Cx45 was present in MiaPaCa2 only, whereas Cx26 was negligible in all three lines (Figure 1ci). Activation of hypoxic signalling (by incubation with DMOG or 2% O_2) raised Cx43 levels in BxPC3 cells (Figure 1c). To determine how connexin immunoreactivity relates to cell-to-cell coupling, junctional permeability to the fluorescent marker calcein ($P_{junc,calc}$) was measured from fluorescence recovery after photobleaching (FRAP; Figure 1cii). Calcein-loaded confluent monolayers were imaged and fluorescence in a central cell was bleached to 50% of initial intensity. Recovery of fluorescence due to calcein diffusion from neighbouring cells quantified $P_{junc,calc}$; this was highest in Colo357 monolayers, moderate in BxPC3 monolayers yet raised by hypoxic signalling, and very low in MiaPaca2 monolayers (Figure 1cii). Thus, cell-to-cell diffusive coupling correlated with Cx43 levels. Transmission was blocked by the gap junctional inhibitor carbenoxolone (CBX; 100 μM). To test that Cx43 is responsible for assembling the conduits for calcein, *GJA1* knockdown was performed in Colo357 cells transduced with shRNA constructs. Compared with the scrambled control, the shRNA construct with the greatest knockdown efficacy (construct #1) reduced Cx43 immunoreactivity by 70% (Figure 1di) and reduced $P_{junc,calc}$ by $>90\%$ (Figure 1dii), confirming Cx43 to be a major gap junction-forming protein. Construct #2 had lower knockdown efficiency (45%) and produced a smaller decrease in $P_{junc,calc}$ (70%). *GJA1* knockdown did not change the expression of MCT1 or MCT4 (Supplementary Figure S1), indicating that MCT-dependent lactate handling is unaffected by genetic ablation of junctional coupling.

Lactate anions permeate gap junctions faster than heavily buffered H^+ ions

Previous studies[32] have measured cytoplasmic lactate diffusivity (D_{lac}) in tumours to be ~1000 μm^2/s. In contrast, lactate permeability through gap junctions connecting cancer cells ($P_{junc,lac}$) is poorly characterized. Direct $P_{junc,lac}$ measurements would require a means of evoking a local rise of intracellular [lactate] ([lactate]$_i$), but such manoeuvres are not easily implemented. However, as small (≪1 kDa) ions permeate gap junctions by a diffusive process, a constant of proportionality can be used to convert diffusivity measurement into permeability constants (for example, D_{lac} into $P_{junc,lac}$). Conveniently, this proportionality constant can be determined by studying the dynamics of H^+-binding small molecules, commonly referred to as mobile buffers. Photolytic H^+-uncaging from the membrane-permeable donor 6-nitroveratraldehyde (NVA) drives the diffusive exchange of protonated for unprotonated mobile buffers,[33] which can be imaged using pH-sensitive cSNARF1 fluorescence to derive cytoplasmic H^+ diffusivity (D_H) and junctional H^+ permeability ($P_{junc,H}$) (Figure 2a). Among the cytoplasmic H^+-buffers, CO_2/HCO_3^- is unusual because CO_2 permeation across membranes can short-circuit the junctional route. Thus, to characterize only those H^+-buffers that exchange between cells via gap junctions, experiments were performed using CO_2/HCO_3^--free (Hepes-buffered) superfusates. D_H measurements were made on MiaPaCa2, BxPC3 and Colo357 cells (Figure 2bi). H^+-uncaging at one end of a cell produces a local cytoplasmic build-up of H^+ ions which then spreads diffusively. The cytoplasm of all three PDAC lines had comparable D_H (Figure 2bii). To measure $P_{junc,H}$, H^+ ions were released in a larger region of a cell at the middle of a confluent monolayer, and their spread into neighbouring cells was imaged (Figure 2ci). $P_{junc,H}$ was highest in Colo357 cells, moderate in BxPC3 cells (but increased by hypoxic signalling) and very low in MiaPaCa2 cells (Figure 2cii). CBX (100 μM) inhibited transmission in coupled wild-type cells, as did *GJA1* knockdown with shRNA #1, relative to Colo357 cells transduced with scrambled construct (Figure 2cii). Thus, by using the experimentally determined $P_{junc,H}/D_H$ ratio to approximate $P_{junc,lac}/D_{lac}$, $P_{junc,lac}$ was estimated to be ~1 μm/s in Colo357 and hypoxic BxPC3 monolayers.

To confirm that lactate anions penetrate gap junctions faster than highly-buffered H^+ ions, Colo357 monolayers were exposed to a standing gradient of extracellular [lactate] ([lactate]$_e$) maintained by a double-barrelled micropipette[34] (Figure 2di). MCT-dependent H^+-lactate entry into cells under the lactate-containing microstream is reported as an intracellular acidification; this produces a smooth longitudinal gradient of pH_i between cells exposed to the lactate-containing microstream and cells under the lactate-free microstream (Figure 2di). At steady-state, the size of this longitudinal gradient of pH_i depends on junctional fluxes of H^+ and lactate ions (Figure 2dii). If junctional transmission of lactate anions were faster than the highly-buffered H^+ ions, rapid syncytial dissipation of lactate would allow further lactate (and H^+) entry into cells under the lactate-containing microstream. As net MCT activity continues until equilibriation ($[H^+]_i \times [lactate]_i = [H^+]_e \times [lactate]_e$), a more dissipated syncytial [lactate]$_i$ gradient is predicted to evoke a steeper pH_i gradient. Indeed, the experimentally measured pH_i gradients were larger when gap junctions were open, compared to when they were blocked with CBX (100 μM; Figure 2diii) or ablated genetically by knockdown (shRNA #1; Figure 2div). Thus, unlike MCT which transports H^+ and lactate ions in strict 1:1 stoichiometry, junctional lactate permeability exceeds junctional H^+ permeability, at least in Colo357 monolayers under CO_2/HCO_3^--free conditions.

Gap junctions can transmit a substantial traffic of lactate in PDAC spheroids

A glycolytic cell may discharge lactate via gap junctions or by MCTs, depending on the magnitude of junctional lactate permeability ($P_{junc,lac}$) and lactate permeability via MCT ($P_{mct,lac}$). $P_{mct,lac}$ was measured in cSNARF1-loaded Colo357 monolayers exposed rapidly to lactate-containing solution. Uniform superfusion collapses any cell-to-cell gradients and thus eliminates net junctional flux. The experiment shown in Figure 3a, performed in CO_2/HCO_3^--containing buffer, derives the magnitude of MCT flux (J_{mct}) from the product of the rate of pH_i change and buffering capacity (intrinsic plus CO_2/HCO_3^--dependent buffering; Supplementary Figure S2). As intracellular carbonic anhydrase activity in Colo357 cells is low (Supplementary Figure S3), CO_2/HCO_3^- reaction kinetics were implemented in the calculation.[35] The relationship between J_{mct} and $P_{mct,lac}$ is given as $J_{mct} = P_{mct,lac} \times \rho \times [lactate]_e$, where ρ is the surface area/volume ratio. For a Colo357 monolayer, ρ is the reciprocal of monolayer height which was estimated from the cells' area in the *x*–*y* plane (592 ± 34 μm^2) and volume measured separately by flow cytometry (3570±69 μm^3). Thus, $P_{mct,lac}$ in Colo357 cells was 0.3 μm/s (Figure 3b), which is smaller than $P_{junc,lac}$ (~1 μm/s). For note, the junctional blocker CBX had a small, off-target inhibitory effect on $P_{mct,lac}$.

A direct comparison between junctional and MCT-mediated lactate transport can be made in spheroid tissue growths, where radial [lactate]$_i$ gradients are able to drive junctional fluxes. Although lactate sensors[36] can report [lactate]$_i$ dynamics, they are unable to distinguish whether lactate is transported by MCT or through gap junctions. The route taken by lactate can, however, be inferred from its pH_i-signature. Lactate entering a cell by MCT carries with it an H^+ ion, producing acidification; in contrast, junctionally transmitted lactate diffuses faster than heavily buffered H^+ ions, evoking the opposite (that is, alkalinizing) pH_i-response. Colo357 spheroids grown to a radius of ~110 μm develop modest core-hypoxia, and can be imaged confocally for pH_i across the equatorial plane (Figure 3ci). At the spheroid periphery, the 'lactate addition/removal' protocol evoked a pH_i

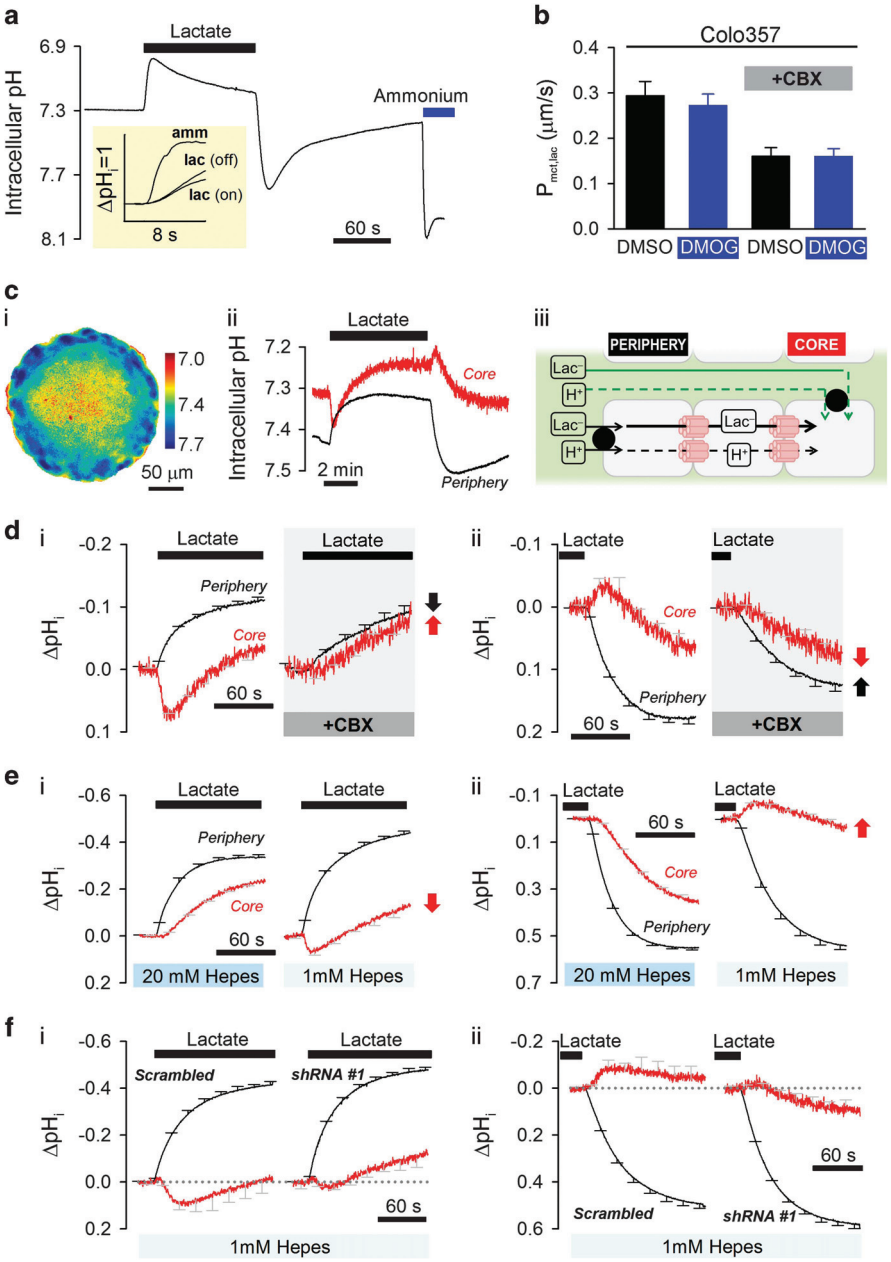


Figure 3. Intracellular lactate diffuses ahead of H^+ ions in Colo357 spheroids. (**a**) pH_i response in cSNARF1-loaded Colo357 monolayer to 40 mM lactate-containing solution (probes MCT activity) followed by 30 mM ammonium-containing solution (tests speed of solution change). Inset: lactate-evoked pH_i changes are not rate-limited by solution change. (**b**) Membrane lactate permeability ($P_{mct,lac}$) calculated from MCT activity. Gap junctional blocker CBX (100 μM) had partial inhibitory effect on $P_{mct,lac}$. Mean ± s.e.m. ($N = 20, 19, 20, 19$). (**c**,i) pH_i map through equatorial plane of cSNARF1-loaded Colo357 spheroid (radius 110 μm). (ii) pH_i dynamics in peripheral layer (11 μm-thick rim; black time course) and core (radius 11 μm; red time course). (iii) Two routes of lactate entry into cells at the spheroid core. (**d**) pH_i response, in presence of CO_2/HCO_3^-, to (i) adding and (ii) removing lactate. Biphasic response at core is blocked by CBX (100 μM; paired experiment). Mean ± s.e.m. ($N = 8$). (**e**) pH_i response, in absence of CO_2/HCO_3^-, to (i) adding and (ii) removing lactate; extracellular buffering was provided by 20 mM or 1 mM Hepes (paired experiments). Mean ± s.e.m ($N = 7$). MCT activity at the core is rate-limited by slow H^+ supply attained under a low (1 mM) [Hepes] buffering regime; this exposes a higher junctional component of lactate handling at the spheroid core. (**f**) Measurements in 1 mM Hepes performed on size matched spheroids grown from Colo357 cells transduced with shRNA #1 or scrambled construct. Unpaired measurements. Radius: 125.4 ±2.3 μm, 127.7 ± 2.4 μm. Mean ± s.e.m ($N = 5, 4$).

response that was similar to that recorded in monolayers (Figure 3cii). The direction of this pH_i change indicates that most lactate traffic in peripheral cells is carried by MCT. With depth, diffusion across the tortuous extracellular space becomes increasingly rate-limiting for MCT-mediated transport (tortuosity was estimated to reduce diffusivity by 70%; Supplementary Figure S4). Reduced MCT fluxes may unmask junctional transmission occurring across the larger, syncytial cytoplasmic volume. Indeed, the pH_i response to lactate addition/removal measured at the spheroid core was biphasic (Figure 3cii; further analysis in Figure 3d). This direction of the initial pH_i transients is thermodynamically inconsistent with MCT activity; instead, it indicates that a significant fraction of lactate traffic to and from the spheroid core is routed through gap junctions (Figure 3aiii). In support of the involvement of Cx43 channels, blocking gap junctions with CBX eliminated the initial pH_i transients (Figure 3d).

To further investigate the two routes for lactate handling at the core of spheroids, the balance between MCT and junctional fluxes was manipulated experimentally. In the absence of CO_2/HCO_3-buffer, MCT flux can be modulated by changing the concentration of Hepes, a membrane-impermeant buffer which carries H^+ ions towards and away from MCT proteins.[37] MCT activity in cells that are furthest away from the bulk superfusate will be most sensitive to a reduction in [Hepes], whereas cells at the spheroid rim (with good diffusive coupling) are the least sensitive. Superfusion with 20 mM Hepes provides a high level of mobile buffering that greatly facilitates extracellular H^+ diffusivity. Under this buffering regime, lactate addition evokes prompt intracellular acidification at the periphery and at the core, indicative of a major component of MCT-dependent entry throughout the spheroid. Reducing [Hepes] to 1 mM substantially weakens diffusive coupling, particularly with the spheroid core. In these low-buffer conditions, lactate addition evoked an intracellular alkalinization at the spheroid core (Figure 3ei) and lactate removal acidified the core (Figure 3eii), both of which are consistent with junctional transmission. Furthermore, these transient pH_i responses were ablated in *GJA1* knockdown spheroids (shRNA #1; Figure 3f). At the spheroid rim, where diffusion distances are short, pH_i responses were less sensitive to a reduction in [Hepes] (that is, MCT activity remained fast).

Junctional and MCT-mediated lactate fluxes (J_{junc}, J_{mct}) at the core of spheroids can be quantified from the rates of pH_i change (dpH_i/dt). In spheroids treated with CBX (to block J_{junc}), dpH_i/dt_{CBX} is proportional to $-J_{mct}$ (corrected for the partial inhibitory effect of CBX on MCT; Figure 3b). In junctionally coupled spheroids, dpH/dt_{con} reports $J_{junc} - J_{mct}$. Thus, the fraction of lactate traffic that is routed through gap junctions is:

$$\frac{J_{junc}}{J_{junc}+J_{mct}} = \frac{dpH/dt_{con} - dpH/dt_{CBX}}{dpH/dt_{con} - 2\times dpH/dt_{CBX}}.$$

This equation estimates that 77 ± 3% of lactate flux at the core of in Colo357 spheroids was carried junctionally. At the core of spheroids grown from Cx43-positive NHDF-Ad fibroblasts and HEK293.T kidney cells, the fraction of lactate carried junctionally was 50 ± 5% and 30 ± 4%, respectively (Supplementary Figure S5). Thus, gap junctions are an important route for transporting lactate in Cx43-expressing tissue growths.

Junctional discharge of lactate from hypoxic cells alkalinizes the normoxic rim of PDAC spheroids

Resting pH_i is set by the balance of all acid-base fluxes and is 7.126 ± 0.0075 (s.e.m.; $N = 250$ cells) in Colo357 monolayers. In 3D tissue growths, junctional flux of lactate (a chemical base) may exert an additional influence on the resting pH_i of recipient cells. This was studied in Colo357 spheroids (Figure 4a). In spheroids grown in glucose-containing media, resting pH_i in the outermost layer was ~0.3 pH units more alkaline than in monolayers (Figure 4b). Replacing glucose with galactose (to block lactate production[38]) reduced the degree of peripheral alkalinization (Figure 4b). Thus, the highly alkaline spheroid rim is related to metabolic lactate production. Spheroids grown from Cx43-knockdown cells (construct #1; Figure 1d) were less alkaline at the rim compared to control spheroids (scrambled construct), indicating that the junctional route carries the aforementioned alkalinizing flux (Figure 4c). In support of this, treatment of wild-type spheroids with CBX (100 μM; 3 h) blocked peripheral alkalinization (Figure 4d). CBX also acidified the spheroid core, which is likely due to the partial inhibitory effects of CBX on MCT activity (Figure 3b). In summary, the junctional spread of intracellular lactate from the spheroid core alkalinizes the outermost cells (Figure 4e). This effect is able to take place because the junctional flow of lactate is uncoupled from the flow of H^+ ions that are also produced by glycolytic metabolism (Figure 4e).

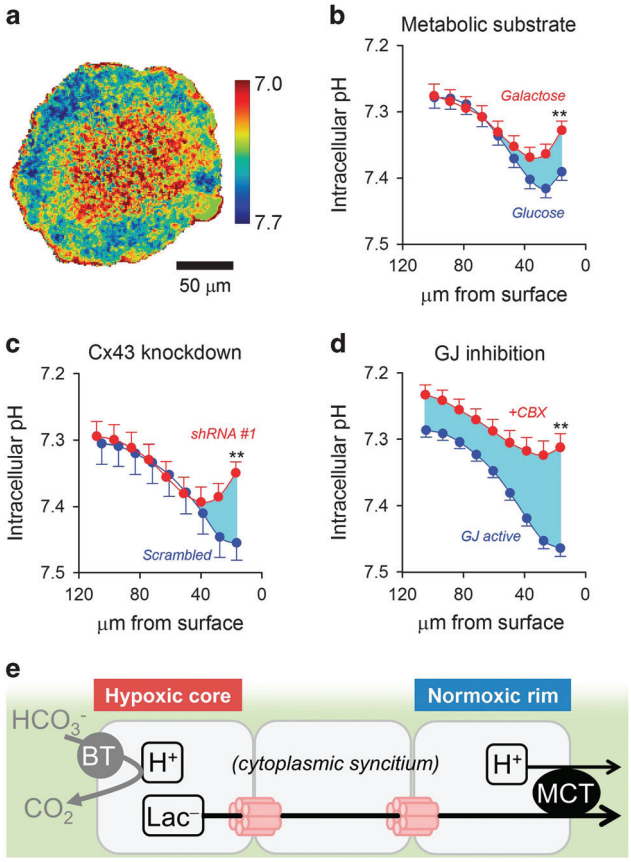


Figure 4. Junctional venting of lactate from the hypoxic core alkalinizes cells at the rim of Colo357 spheroids. (**a**) Steady-state pH_i across the equatorial plane of a Colo357 spheroid. (**b**) Radial pH_i gradient in Colo357 spheroids showing alkalinization at rim. Replacing glucose with galactose reduces degree of peripheral alkalinization. Unpaired *t*-test with Bonferroni correction, $^{**}P < 0.01$. Mean ± s.e.m. ($N = 12$ glucose, 8 galactose). (**c**) Peripheral alkalinization is smaller in Cx43-knockdown Colo357 spheroids (shRNA #1; Figure 1d) compared to scrambled controls. Mean ± s.e.m. ($N = 14$ shRNA #1, 12 scrambled). (**d**) CBX reduces peripheral alkalinization; the modest acidification at the core likely relates to the partial inhibitory off-target effect on MCT. Mean ± s.e.m. ($N = 11$ control, 8 CBX). (**e**) Mechanism by which junctional lactate transport alkalinizes recipient cells at the spheroid rim. Lactate and H^+ ions are co-produced by hypoxic metabolism. HCO_3^- (for example, taken-up by a bicarbonate transporter, BT) titrates cytoplasmic H^+ ions in hypoxic cells.

Junctional coupling reduces intracellular lactate retention in PDAC spheroids

Junctional transmission of metabolites would benefit under-perfused tissues by giving all cells access to regions with the most favourable transmembrane gradient for off-loading lactate by MCTs, which would normally be at the normoxic rim. Inactivation of junctional lactate flux is therefore expected to increase lactate retention in the intracellular compartment. This was tested by comparing steady-state lactate levels in intracellular fluids and in samples of medium. Colo357 cells were grown as monolayers (that is, minimal diffusion distances) or spheroids (structures with restricted diffusion). After a set period of growth, aliquots of media and cell lysates were prepared for measurements of [lactate], as well as of [glucose], osmolarity and protein that are required for calculating intracellular [lactate] ($[lactate]_i$), as explained in the Methods (Figure 5a). To test if transduction with shRNA constructs had affected lactate production, wild-type and genetically modified Colo357 monolayers were grown in glucose-

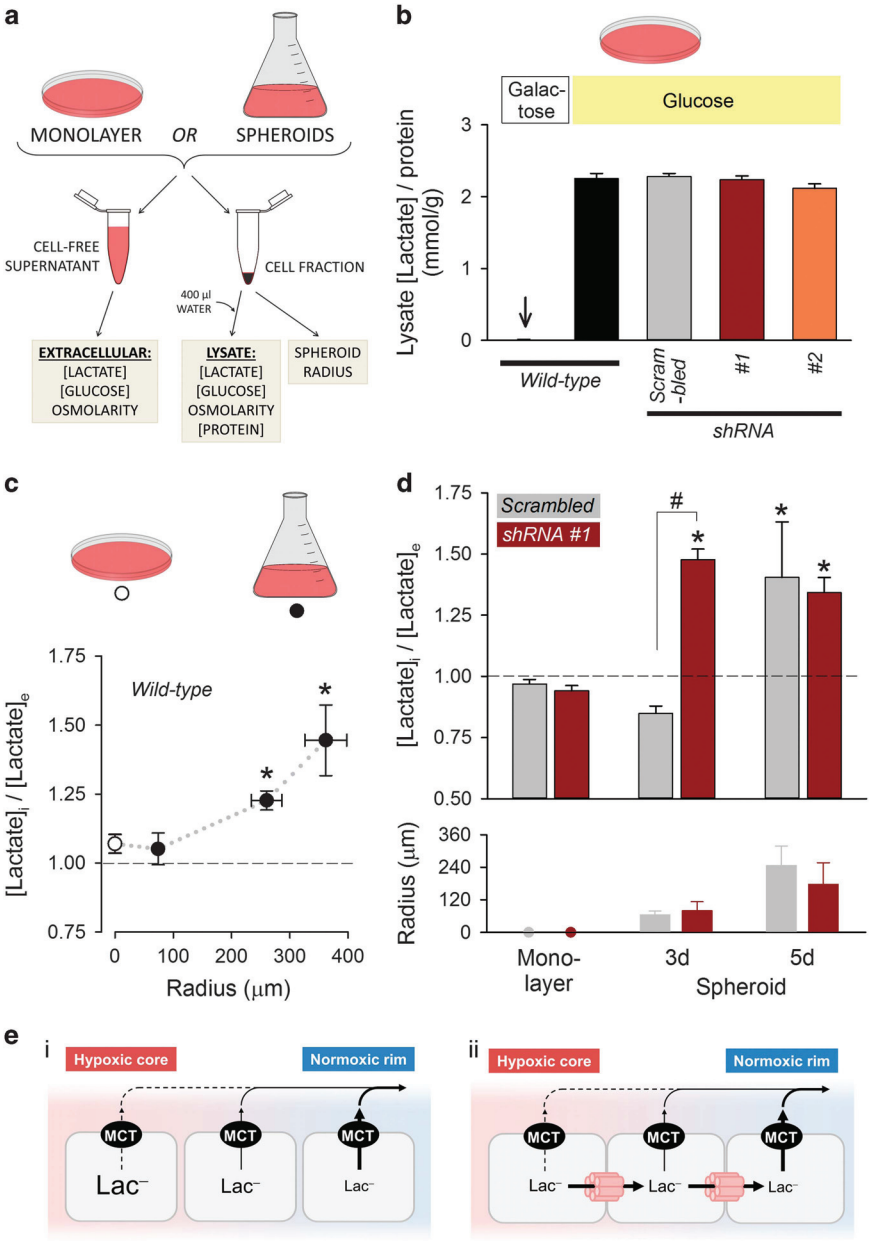


Figure 5. Intracellular lactate retention measured by biochemical assays. (**a**) Collection protocol: Colo357 cells were grown as monolayers for 96 h or as spheroids for 36–120 h. Between 30 and 100 spheroids were collected for measuring radius. Aliquots of medium and of cells were collected for biochemical assays; cells were lysed in 400 µl water and centrifuged to remove debris. (**b**) Lysates from monolayers grown in glucose- or galactose-containing medium were assayed for [lactate]/protein ratio. Lactate is produced only in the presence of glucose, and to comparable levels in wild-type and shRNA-transduced Colo357 cells (time-matched incubations). Mean ± s.e.m. (six lysates each). (**c**) $[lactate]_i/[lactate]_e$ ratio (a measure of intracellular lactate retention) in wild-type monolayers (six lysates) and spheroids as a function of radius (four batches each containing >1000 spheroids). Mean ± s.e.m. Unpaired *t*-test: * denotes significant increase in lactate retention relative to monolayer ($P < 0.05$). (**d**) Upper panel: intracellular lactate retention in Colo357 cells infected with scrambled construct or shRNA #1, grown as monolayers (six lysates each) or as spheroids for 3 or 5 days. Mean ± s.e.m. (four batches each containing >1000 spheroids). Unpaired *t*-test: * denotes significant increase in lactate retention relative to monolayer ($P < 0.05$). # denotes significant difference between scrambled and shRNA #1 for duration-matched experiments ($P < 0.01$). Lower panel: radius of spheroid, Mean ± s.d. (**e**) Schematic diagram illustrating the routes for venting lactate. (i) In the absence of junctional coupling, all lactate traffic is through MCTs. Efflux in hypoxic regions with poor diffusive coupling is curtailed by an unfavourable transmembrane gradient; this leads to intracellular lactate retention. (ii) With junctional coupling, lactate can dissipate between cells and access normoxic regions that have a more favourable transmembrane gradient for MCT-facilitated off-loading; this reduces intracellular lactate retention.

containing media. After 4 days of growth, the [lactate]/protein ratio in lysates of wild-type Colo357 cells and cells transduced with scrambled shRNA, shRNA #1 and #2 were comparable (Figure 5b). This result indicates that the genetic ablation of *GJA1* does not affect glycolytic rate in 2D culture. As confirmation that the source of lactate is glycolytic, wild-type cells incubated with galactose-containing media produced no detectable [lactate] (Figure 5b). The longer extracellular diffusion distances inside spheroids are expected to increase intracellular lactate retention, reported as the $[lactate]_i/[lactate]_e$ ratio. Wild-type spheroids as large as ~75 µm in radius were able to vent lactate as efficiently as monolayers (Figure 5c). However, intracellular lactate retention

increased in larger spheroids (Figure 5c). To test if the ability of ~75 μm spheroids to minimize lactate retention is related to junctional coupling, measurements were performed on *GJA1* knockdown spheroids (shRNA #1). Compared to scrambled controls (matched for growth period), lactate retention was substantially greater in knockdown spheroids (Figure 5d), an observation that cannot be explained by metabolic rate (Figure 5b) or MCT expression (Supplementary Figure S1). Lactate retention increased in larger spheroids, but junctionally coupled tissues were able to grow at a faster rate, which may relate to better lactate venting. The proposed mechanism for Cx43-facilitated lactate venting from tissues is illustrated in Figure 5e.

GJA1-knockdown Colo357 cells are less successful in colonizing the proliferating rim of spheroids

Gap junctions provide a route for dissipating lactate which benefits a syncitium of glycolytic cells (Figure 5e). In addition, junctional transmission of lactate alkalinizes recipient cells, producing a milieu chemistry that is conducive for growth (Figure 4e). Thus, cells with high Cx43 coupling are predicted to be more successful in areas of proliferation. Competition for space between Colo357 cells expressing various levels of Cx43 activity was tested in spheroid co-culture models; the more successful phenotype is expected to expand in the proliferating rim of spheroids. Spheroids were grown from a 1:1 mixture of Cx43-positive wild-type Colo357 cells and *GJA1*-knockdown Colo357 cells (shRNA #1 and #2, Figure 1d). The knockdown cells were identified by eGFP fluorescence. The upper panels in Figure 6a show transmission images superimposed with eGFP fluorescence measured across the equatorial plane of the co-culture spheroid. The lower panels analyse fluorescence relative to the mean signal across the imaging plane (above-average pixels shown as red and below-average pixels appearing blue). Wild-type/shRNA #1 spheroids showed a clear segregation of cells by Cx43 levels (Figure 6a): wild-type cells (Cx43-positive) were abundant in the proliferating rim, typically along a crescent; in contrast, *GJA1*-knockdown cells clustered at the core. A similar observation was made with wild-type/shRNA #2 spheroids (Figure 6b). As a control, co-culture of wild-type cells with cells expressing the scrambled construct produced a random pattern of fluorescent and non-fluorescent patches, indicating no clear advantage of either phenotype in populating the proliferating rim (Figure 6c). Fluorescence images were quantified further in Figure 6d as a function of distance from the spheroid surface. In summary, higher Cx43 activity is an advantage for Colo357 cells competing for space in the proliferating rim of spheroids.

Cx43 immunoreactivity is increased in invading PDAC cells *in vivo*

A number of PDAC lines, including MiaPaCa2, do not express Cx43 *in vitro* when grown as monolayers (Figures 1bii and ci). Under uniform culture conditions, monolayers are unable to benefit from junctional lactate flux, which may explain the redundancy of Cx43 function. Nonetheless, a lactate-venting role for gap junctions may become apparent *in vivo*. To test this, orthotopic xenografts were established from MiaPaCa2 cells in the proximal part of the pancreas of nude mice. Sections of primary tumour excised together with normal pancreatic tissue, duodenum and stomach, as well as sections of lung were stained for human Cx43 or human epidermal growth factor receptor (EGFR) as a human PDAC marker. To identify co-localization between Cx43 and EGFR immunoreactivity, image pairs were registered by matching histological landmarks, filtered by colour to identify positive staining and then overlaid. The EGFR-positive primary tumour showed no evidence for Cx43 immunoreactivity (Figure 7a; showing as blue on overlay), which phenocopies monolayer culture *in vitro*. In most cases of lung metastases, Cx43 staining was weak or absent (Figure 7b), but some examples of metastatic

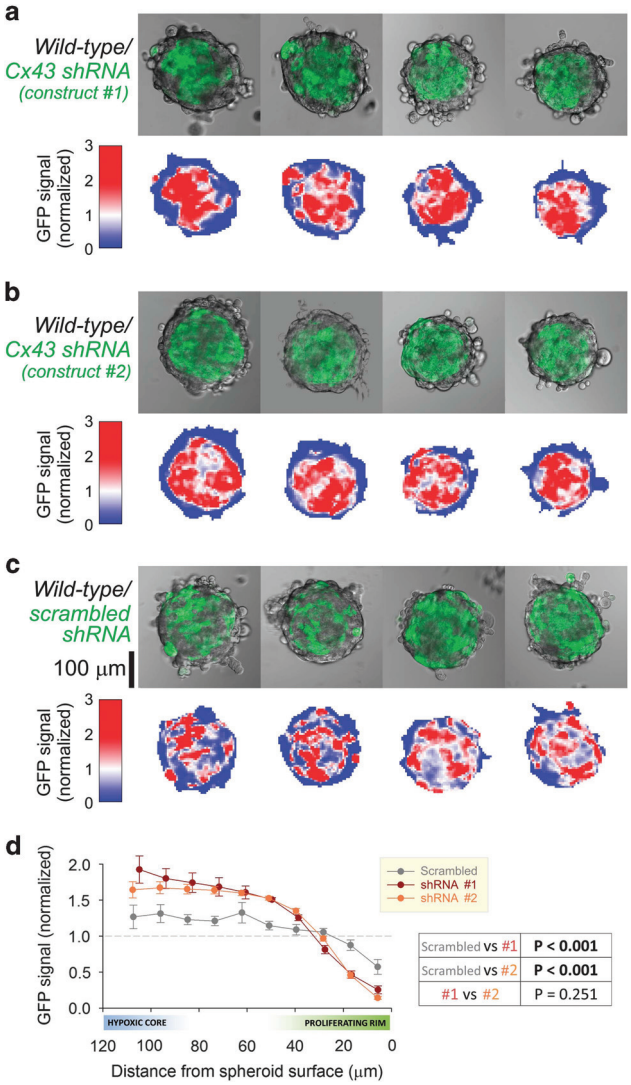


Figure 6. Spheroid co-cultures of Colo357 cells with different levels of Cx43. (**a**) Colo357 spheroid co-culture (1:1) of wild-type (non-fluorescent) cells mixed with eGFP-fluorescent *GJA1*-knockdown cells (shRNA construct #1). Upper panels: transmission image superimposed with fluorescence measured confocally across equatorial plane (pinhole = 3 μm). Lower panels: fluorescence maps normalized to mean signal (blue pixels indicate below-average fluorescence; red pixels indicate above-average fluorescence), showing segregation by level of Cx43. Cx43-positive wild-type cells are more abundant in the peripheral rim. (**b**) Experiment repeated with the same imaging settings with shRNA construct #2, confirming the result with construct #1. (**c**) Experiment repeated with the same imaging settings with scrambled construct. Scrambled and wild-type cells mixed randomly, without clear radial segregation. (**d**) Analysis of eGFP fluorescence, normalised to spheroid-wide signal, as a function of radial depth: cells with high Cx43 levels segregate preferentially in the proliferating rim. Mean ± s.e.m. ($N = 11$ scrambled, 13 shRNA #1, 22 shRNA #2). Table shows results of ANOVA.

lesions were Cx43 positive (Figure 7c). Markedly increased Cx43 immunoreactivity was observed in MiaPaCa2 cells invading host pancreatic tissue (Figure 7d), and also in clusters of MiaPaCa2 cells invading the duodenal mucosa (Figure 7e) and the stomach muscularis externa (Figure 7f; co-localization of Cx43 and EGFR staining indicated by purple pixels on overlay). Cx43 staining was concentrated at the surface membrane, where the protein is able

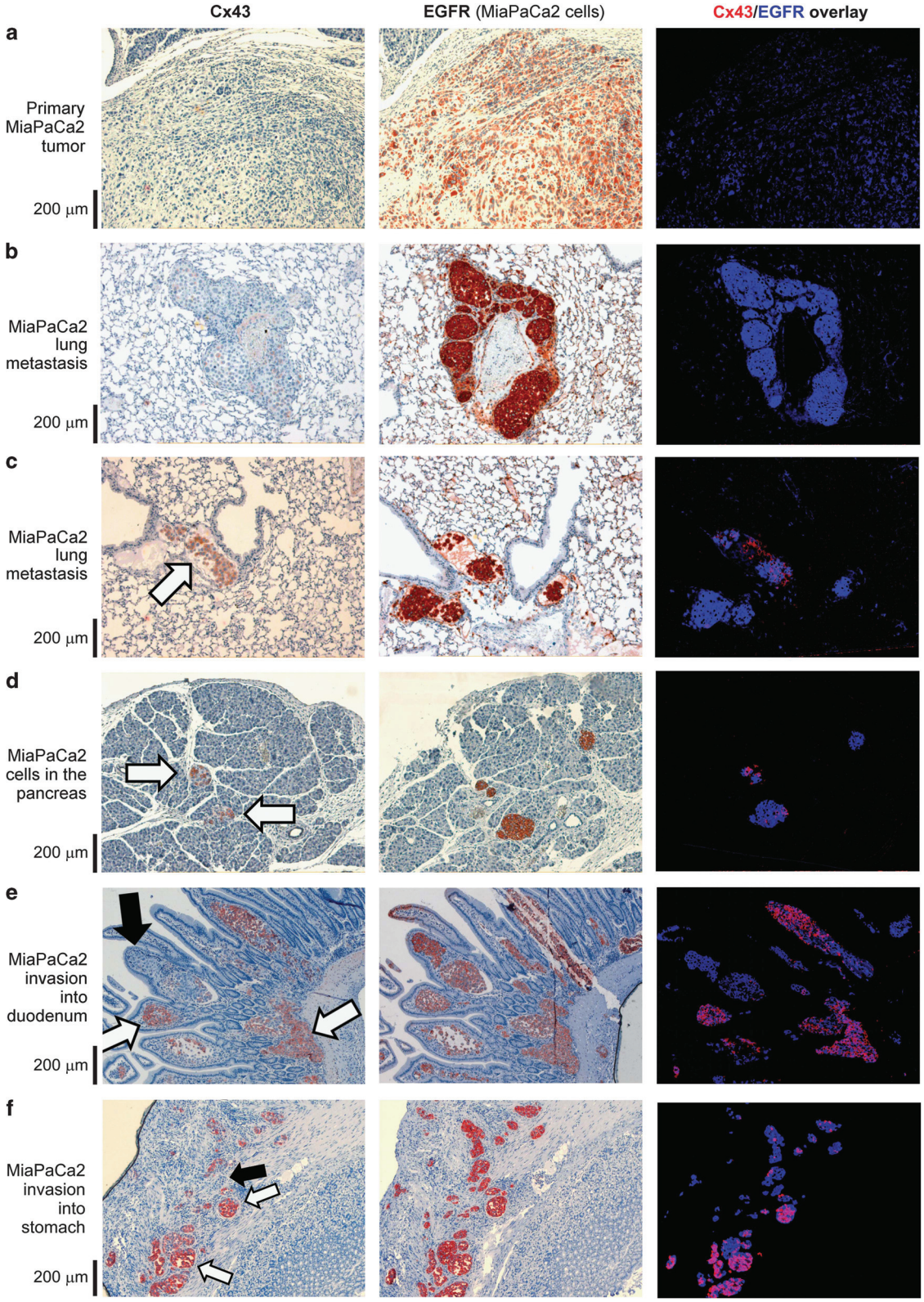


Figure 7. Cx43 immunoreactivity in MiaPaCa2 cells studied in orthotopic xenograft mouse models. Cx43 staining (left column) in sections of the primary tumour, invasion into adjacent tissues and sites of metastasis. Staining for human EGFR (middle column) identifies MiaPaCa2 cells. Overlay of Cx43 and EGFR immunoreactivity analysed by image-pair registration and colour filtering to identify staining (right column). (**a**) Cancer cells in the primary tumour remained Cx43 negative (overlay is blue, indicating EGFR signal only). (**b**) Example of a lung metastasis with absent Cx43 staining and (**c**) with more prominent Cx43 staining that co-localizes with an EGFR-positive cluster. (**d**) Clusters of Cx43-positive MiaPaCa2 cells (white arrows) within the host pancreas that co-localize with EGFR staining. MiaPaCa2 cell invasion into (**e**) mucosa of duodenum and (**f**) stomach muscularis, showing stronger and more uniform Cx43 staining (white arrows), but also a number of Cx43-negative clusters (black arrows). Clusters that are positive for both Cx43 and EGFR are indicated by purple colour on the overlay.

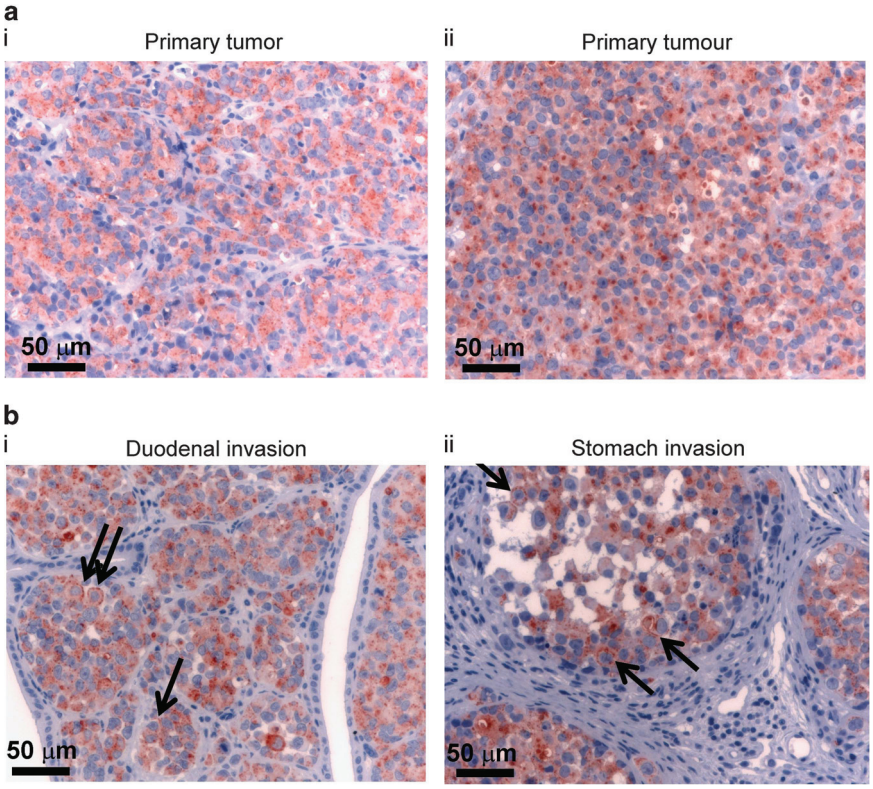


Figure 8. Distribution of LAMP2 in primary and invading MiaPaCa2 cells *in vivo*. (**a**) Diffuse LAMP2 staining in MiaPaCa2 cytoplasm but not at cell margins in sections of primary tumour. (**b**) In a subpopulation of MiaPaCa2 cells invading (i) duodenal mucosa and (ii) stomach muscularis, LAMP2 staining appeared more concentrated at cell margins, a marker of chronic extracellular acidosis.

to assemble into cell-to-cell conduits (Supplementary Figure S6). In 13 sections obtained from four mice, out of 547 clusters of EGFR-positive MiaPaCa2 cells, 109 clusters (20%) were strongly positive for Cx43 (Supplementary Figure S7A). The appearance of Cx43 staining in these clusters was predominantly uniform, arguing that these may have been established from a Cx43-positive clone. These findings may suggest that Cx43-positive cells are more invasive or better adapted for colonizing new niches. Increased Cx43 staining at the tumour/pancreas interface was also observed with orthotopically implanted PANC1 cells, another PDAC cell line with modest *in vitro* Cx43 expression (Supplementary Figure S8).

Chronic extracellular acidosis in under-perfused areas occupied by PDAC cells may be a factor favouring the junctional route over the pH_e-sensitive MCT mechanism. A recent study[9] has shown that over-expression and redistribution of lysosome-associated membrane protein 2 (LAMP2) towards the plasma membrane is a marker of acidotic niches. Results from four mice demonstrate that LAMP2 staining was diffuse in primary tumour regions (Figure 8ai and aii), as expected for the protein's normal lysosomal targeting. In contrast, invasions of the duodenum mucosa (Figure 8bi) and stomach muscularis (Figure 8bii) contained a subpopulation of MiaPaCa2 cells in which LAMP2 staining was concentrated near or at the plasma membrane. Analysis of 17 sections obtained from four mice showed LAMP2 staining at or near the plasmalemma in 39% of clusters containing MiaPaCa2 cells (Supplementary Figure S7B). In these niches, the acidic extracellular milieu would favour junctional lactate transmission.

DISCUSSION

Enhanced anaerobic glucose metabolism favours PDAC progression,[24] but sustaining an elevated glycolytic rate requires adequate pipelines for discharging lactate. PDAC cells express MCT1 and MCT4 proteins (Figure 1a),[24] which can shuttle lactate out of cells, provided that the transmembrane [lactate] and pH gradients are favourable. Through a process called metabolic symbiosis,[2,39] stromal cells can absorb extracellular lactate and hence facilitate lactate off-loading from glycolytic cancer cells. However, the extracellular milieu of solid tumours is commonly more acidic than cytoplasm[6–11] and this curtails MCT-dependent lactate efflux from cancer cells. *In vivo* evidence for this pH-related thermodynamic constraint is suggested by the appearance of the acidosis marker LAMP2[9] near or at the plasma membrane of invading PDAC cells (Figure 8). Strong diffusive coupling between PDAC cells attained by means of Cx43 channels (for example, Colo357, hypoxic BxPC3 or invading MiaPaCa2) provides an alternative route for exchanging metabolites across cellular networks. The magnitude of lactate traffic discharged junctionally and aboard MCTs can be compared in PDAC spheroids by exploiting the observation that these two fluxes evoke opposite pH_i responses (Figure 3). This difference is because MCT activity enforces a 1:1 stoichiometry between lactate and H^+ ions, whereas lactate anions penetrate junctions faster than highly-buffered H^+ ions (Figure 2d). In Colo357 spheroids, as many as 4-in-5 lactate anions are vented junctionally from the core (Figure 3), and a sizeable traffic of lactate through gap junctions was also recorded in non-PDAC spheroids (Supplementary Figure S5). Junctional transmission of lactate does not produce net electric current because connexin channels are also highly permeable to monovalents (for example, K^+, Cl^- present at ~100 mM), which promptly neutralize any potential difference between cells. Coupling by connexins improves overall lactate venting from clusters of cells by allowing lactate anions to dissipate across the cytoplasmic syncytium towards regions where off-loading by MCT is thermodynamically most favourable (that is, nearest to a blood

vessel). This was confirmed by biochemical assays, which demonstrated a smaller degree of intracellular lactate retention in junctionally coupled tissue growths (Figure 5d).

The dissipation of lactate anions (a chemical base) across the syncytial cytoplasm, down a gradient maintained by oxygen tension, has an alkalinizing effect on recipient cells (Figure 4). As this shift in pH_i comes at no energetic cost to recipient cells, it is favourable over secondary active pH_i regulators. Since high pH_i is permissive for growth,[27–29] proliferation in peri-hypoxic tumour regions could be stimulated by coupling onto lactate-supplying cells. An additional benefit of junctional lactate transmission is that it supplies normoxic cells with substrate for oxidative phosphorylation without having to rely on MCT activity. This is significant because metabolic symbiosis between lactate-generating hypoxic cells and lactate-catabolizing normoxic cells[2] facilitates PDAC progression.[24]

The role of gap junctions in transporting metabolites between cells is likely to have been understated in the past as a consequence of experimental designs based largely on monolayer culture. In monolayers exposed uniformly to culture media or superfusates, cell-to-cell solute gradients are collapsed and net junctional transmission cannot be observed. However, uniformity of solute concentration is not representative of tumours, where heterogeneity of pH and oxygenation establishes gradients that can drive metabolites through gap junctions.

Gap junctions are assembled from the protein products of at least 20 connexin genes, but the most commonly expressed isoforms in PDAC cells are Cx43, Cx45 and Cx26 (Figure 1bi). High Cx43 expression in cells such as metastatic Colo357 produced strong cell-to-cell coupling (Figure 1c). Comparable coupling and Cx43 expression were attained under hypoxia in BxPC3 cells (Figure 1). This hypoxic response may involve the binding of hypoxia-inducible factor to a putative hypoxia response element (GGCGTGAGG)[40] at 5094–5098 base pairs downstream of the start codon of *GJA1*. In contrast, hypoxic induction of Cx43 was not observed *in vitro* in MiaPaCa2 cells. Increased Cx43 positivity was, however, described in a subpopulation of MiaPaCa2 cells spreading into the host pancreas and at invasions of the duodenum and stomach of orthotopic PDAC mouse models, where one-in-five PDAC clusters were Cx43 positive (Figure 7). Chronic extracellular acidosis, demonstrated by the appearance of LAMP2 at or near the plasmalemma in 39% of invading clusters (Figure 8b), may explain the selective advantage of Cx43 channels over MCTs. On the basis of our junctional lactate handling model, we propose that Cx43-positive cells are better at colonizing new niches. This hypothesis is supported by the finding that Colo357 cells with high Cx43 levels segregated preferentially at the proliferating rim of spheroids (Figure 6). The metabolic advantage may explain the significant upregulation of Cx43 reported by others in three pancreatic cancer datasets: Bandea (3.5-fold, $P=10^{-9}$), Segara (4.1-fold, $P=0.001$) and Buchholz (1.6-fold, $P=0.02$; see Supplementary Information). Furthermore, higher Cx43 expression (3.6-fold, $P=0.003$) has been associated with tumours sensitive to inhibitors of EGFR.[41–43]

In summary, our results propose a novel metabolic role for Cx43-assembled gap junctions in handling lactate in networks of cancer cells. This junctional venting mechanism can be important in lieu of the canonical MCT-operated mechanism that is inhibited by the acidic tumour microenvironment. Considering the necessity of supporting a high glycolytic rate, Cx43 channels may be particularly advantageous for highly-proliferating cells at invasion fronts and distant metastases. Therapeutic approaches targeting lactate handling in tumours[44] need to be re-evaluated in light of the proposed junctional route in connexin-positive cancers.

MATERIALS AND METHODS

Connexin expression data

Microarray data for connexin isoform gene expression in 22 PDAC cell lines was obtained from http://biogps.org (dataset E-GEOD-21654). Gene expression in pancreatic tumours was obtained from the Pancreatic Expression Database (http://www.pancreasexpression.org/).

Cell lines

AsPC1, BxPC3, Capan1, MiaPaCa2, PANC1 and Colo357 were kindly provided by Holger Kalthoff (Kiel, Germany). NHDF-Ad fibroblasts were purchased from Lonza. HEK293.T cells were a kind gift from Adrian Harris (Oxford, UK). Cells were authenticated by STR profiling and tested for mycoplasma. AsPC1, BxPC3, MiaPaCa2, PANC1, Colo357, NHDF-Ad and HEK293.T cells were grown in bicarbonate-buffered DMEM (Sigma-Aldrich, Dorset, UK; D6546) containing 10% FBS (Sigma-Aldrich, F9665; Capan1 cells in 20%), 2 mM L-glutamine, 20 U/ml penicillin and 20 μg/ml streptomycin (Sigma-Aldrich) and 0.1 mg/ml Normocin (InvivoGen, San Diego, CA, USA). Cells were trypsinised with 0.1% Trypsin (Gibco, Bleiswijk, Netherlands, 15400-054) and passaged twice per week. Monolayers were plated in IBIDI or LabTek chambers (seeded at 50 000 and 70 000 cells, respectively) for real-time imaging, in 6 cm dishes (seeded at 600 000 cells) for 4 days for collecting adequate cell mass for biochemical assays, or in 6 cm dishes (seeded a 1 200 000 cells) for 3 days for immunoblotting. For pH imaging and co-culture experiments, spheroids were cultured using the hanging-drop method (400 Colo357 cells per 20 μl, 400 HEK293.T cells per 20 μl, 2000 NHDF-Ad cells per 20 μl) for 3 days. For biochemical assays, spheroids were grown in spinner flasks in 250 ml medium, seeded at 5 000 000 cells, for up to 120 h. MiaPaCa2 and PANC1 cells used for xenografting were cultured in DMEM/F12 with Glutamax, 10% FCS and 2.5% horse serum, and in high-glucose DMEM with 10% FCS, respectively. 25 mM galactose-containing medium was based on glucose-free DMEM; all other media contained 25 mM glucose.

GJA1 knockdown

HEK293T packaging cells were plated into 25T T/C flasks and grown to 50% confluency, and transfected ($CaPO_4$ method) with packaging plasmids pSPAX2, pMD2.G and shRNA construct (Genecopoiea, HSH007411-1-LVRU6GP, HSH007411-2-LVRU6GP, HSH007411-3-LVRU6GP and HSH007411-4-LVRU6GP; CSHCTR001-LVRU6GP was the scrambled control). Lentivirus-containing media were collected, filtered through 0.45 μm syringe filter and added to PDAC cells for 72 h. Transduced cells were selected with puromycin (6 μg/ml).

Immunoblotting

To measure protein levels under normoxic conditions, cells were incubated in an atmosphere of 21% O_2. To characterize the effect of stabilizing hypoxic signalling, cells were incubated with dimethyloxalylglycine (1 mM DMOG; in 0.1% DMSO) or incubated in 2% O_2 for 48 hours. Cells were then lysed in RIPA buffer containing protease/phosphatase inhibitors. Overall, 55 μg of total protein (BCA assay, Thermo, Rockford, IL, USA) was loaded per lane, separated using polyacrylamide gel electrophoresis and transferred onto PVDF membrane. Membranes were blocked in 5% skimmed milk and incubated with primary antibodies raised against human MCT1 (Millipore, Darmstadt, Germany, AB 3538P), MCT4 (Novus, Littleton, CO, USA, NBP1-00920), Cx43 and β-actin (Cell Signaling Technologies, Danvers, MA, USA, 3512, 5125), Cx26 and Cx45 (Abcam, Cambridge, UK, AB65969, AB78408) and mouse monoclonal antibody against human CAIX (M75, kind gift from Silvia Pastorekova, Bratislava, Slovakia). Membranes were then incubated with HRP-conjungated secondary antibodies (Novus NB7256, NB7185 or NB120-7061) and developed using ECL (Thermo). Blots were repeated three times on independent lysates.

Solutions and superfusion

5% CO_2/HCO_3^--buffered solution (in mM): 125 NaCl, 4.5 KCl, 11 glucose, 22 $NaHCO_3$, 1 $CaCl_2$, 1 $MgCl_2$. Hepes-buffered solution: $NaHCO_3$ replaced with 20 mM or 1 mM HEPES, and NaCl raised to osmolarity of 300 mOsm/kg. Lactate-containing solution: NaCl replaced with NaLactate. Ammonium-containing solution: NaCl replaced with NH_4Cl. pH adjusted to 7.4 with 4 M NaOH. Monolayers were superfused in the LabTek or IBIDI chambers. Spheroids were superfused in a Perspex chamber with a poly-L-lysine

treated coverslip. Dual microsuperfusion of monolayers using a double barrel micropipette is described previously.[34]

Confocal imaging

Cells were loaded with 10 μg/ml cSNARF1-AM (5 min for monolayers and up to 3 h for spheroids) or 4 μM calcein-AM (5 min). cSNARF1 fluorescence was excited at 555 nm, measured at 580 nm/640 nm and converted to pH using a calibration curve determined using the nigericin method. Calcein fluorescence was excited at 488 nm laser and measured >510 nm. Imaging was performed on a Zeiss LSM system (Jena, Germany). Pinhole for monolayer and spheroid experiments was 2.9 and 1.8 Airy units, respectively. Measurements on individual cells or cell clusters were repeated on different monolayers; measurements on spheroids were repeated at least four times on different batches seeded independently.

Mathematical algorithms

(a) FRAP analysis: Calcein fluorescence was normalized to signal in remote regions of the monolayer. Signal in the central (bleached) cell was best-fitted to a mono-exponential function to estimate the time constant τ. Calcein permeability, $P_{\mathrm{junc,calc}}$ (units: μm/s), was calculated as the perimeter of the central cell × area of central cell/τ. (b) Cytoplasmic H^+ diffusivity (D_H): $[H^+]$ was measured in ten regions of interest, offset to baseline, and fitted to a constant-source diffusion equation for over 30 s:

$$\mathrm{d}[H^+]/\mathrm{d}t = D_H \times \partial^2[H^+]/\partial x^2 + J(x),$$

where J is the rate of H^+ uncaging. (c) Junctional H^+ permeability, $P_{\mathrm{junc,H}}$. Mean $[H^+]$ was measured in the central cell and in all directly neighbouring cells. $P_{\mathrm{junc,H}}$ was calculated by best-fitting, over 60 s, to a system of equations for $[H^+]$ in the central ($[H^+]_c$) and neighbouring ($[H^+]_n$) cells:

$$\mathrm{d}[H^+]_c/\mathrm{d}t = P_{\mathrm{junc,H}} \times \rho_c \times ([H^+]_n - [H^+]_c) + J(x)$$

$$\mathrm{d}[H^+]_n/\mathrm{d}t = P_{\mathrm{junc,H}} \times \rho_n \times ([H^+]_c - [H^+]_n),$$

where ρ_c is the perimeter/area ratio of the central cell and ρ_n is the ratio of the central cell perimeter to the area of the ensemble of neighbouring cells.

Orthotopic xenografts

Animal experiments were approved by the administration of Lower Saxony (Germany). Animals were handled according to national guidelines (license 33.9-42502-04-13/1085). Orthotopic PDAC xenografts were obtained by transplantation of human MiaPaCa2 or PANC1 cells (10^6 cells in 20 μl PBS) into the proximal part of the pancreas of anaesthetized (15 mg/kg xylazine, 75 mg/kg ketamine) 10–20 week NMRI $Fox^{nu/nu}$ nude male mice (Charles River, Sulzfeld, Germany) as described previously.[45] Mice were sacrificed after ~90 days (MiaPaCa2) or ~115 days (PANC1) and only those that developed xenografts were used for sectioning. Lungs and pancreatic tumour excised with the stomach, duodenum and the rest of the pancreas were fixed in 4% formalin in PBS overnight before embedding in paraffin. For each cell line tested, multiple tissue sections were obtained from four animals in order to accurately establish the fraction of clusters that were positive for a tested epitope among a large number of PDAC-positive clusters. No comparisons were made between xenografts of different cell lines. Animal randomization was not required.

Immunohistochemical staining

Deparaffinised and rehydrated 2-μm sections of tissues were pre-treated at 98 °C for 20 min in citrate buffer (pH 6, Dako, Glostrup, Denmark) and incubated with 3% H_2O_2 for 10 min. For Cx43 and EGFR staining, sections were blocked with SEA BLOCK buffer (Thermo) for 20 min and directly incubated with the polyclonal rabbit anti-Cx43 antibody (Cell Signaling Technologies, 1:100) or with the monoclonal rabbit anti-human EGFR antibody (Life Technologies, 1:100; MA5-16359) overnight at 4 °C. For LAMP2 staining, tumour sections were incubated for 60 min with Mousestain kit reagent A (v-histofine, Nichirei Biosciences, Tokyo, Japan) and directly incubated with the monoclonal mouse anti-LAMP2 antibody (Abcam; ab119124, cl. H4B4, 1:200). Anti-Cx43 and anti-EGFR primary antibodies were revealed by Simple Stain rabbit Max PO (v-histofine, Nichirei Biosciences). Anti-LAMP2 antibody was revealed by reagent B and Simple Stain mouse Max PO of Mousestain Kit (Nichirei Biosciences). AEC staining was performed for 30 min and then sections were washed in water and counterstained for 20 s with Meyers hematoxylin. Sections were washed twice for 5 min in TRIS buffer between steps. To generate overlays, image pairs stained for EGFR and Cx43 were aligned ('registered') using 10–20 histological landmarks (ImageJ plugin: http://imagej.net/Landmark_Correspondences rigid non-linear least squares method). Staining patterns were extracted by filtering colour (IHC toolbox, https://imagej.nih.gov/ij/plugins/ihc-toolbox/index.html) and pseudocoloured to distinguish the Cx43 and EGFR channels (red and blue, respectively). Image pairs were overlaid for presentation, with co-localization appearing as purple pixels. Analysis of staining patterns was performed by two investigators independently. The identity of the epitope being visualized was known to the investigators.

Biochemical assays

Colo357 cells were grown as monolayers or spheroids. Measurements were repeated on six batches of lysates of monolayers or four batches of lysates of spheroids in a given size category. At the end of the incubation period, three aliquots of media and an aliquot of cell pellet (spun down at 1000 r.p.m. for 5 min to remove medium) were collected and cooled on ice to slow metabolism and membrane transport. In the case of spheroids, a small sample was extracted for microscopy to measure radius. Cells were lysed with 400 μl water (containing protease inhibitors) and two freeze-thaw cycles, and centrifuged (15 000 × g for 20 min at 4 °C) to remove cellular debris. [Lactate] and [glucose] were measured using an ABX Pentra 400 (Horiba, Northampton, UK) with the LDH and glucose PAP CP cassettes, respectively; osmolarity was measured by a Roebling freezing point osmometer (CamLab, Cambridge, UK); protein concentration was measured by standard BCA assay. Extracellular concentrations ($[\mathrm{lactate}]_e$, $[\mathrm{glucose}]_e$ and osmolarity) were measured in the aliquots of media. Intracellular concentrations were determined from lysates after correcting for the residual volume of medium that is inadvertently included with cells during collection. The lysate is a mixture of intracellular and residual medium volume fractions (v_i, v_e) and plus volume fraction of added water ($v_w = 1 - v_i - v_e$). Assuming osmotic equilibrium between cells and media in culture, the sum of v_i and v_e is estimated from the lysate-to-medium osmolarity ratio ($\mathrm{Osm_l/Osm_e}$). Lactate detected in lysates is from the intracellular fraction and residual medium. In contrast, lysate glucose is mainly from the residual medium because the majority of intracellular glucose is phosphorylated, and therefore not detected by the assays. Thus, glucose can be used as a marker of extracellular volume (v_e). The following equations relate intracellular (i), extracellular (e) and lysate (l) concentrations:

$$[\mathrm{Glucose}]_l \approx v_e \times [\mathrm{Glucose}]_e,$$

$$[\mathrm{Lactate}]_l = v_i \times [\mathrm{Lactate}]_i + v_e \times [\mathrm{Lactate}]_e.$$

Cell-derived lactate in the lysate (mmol $\mathrm{lactate_i}$/L lysate) is therefore equal to

$$[\mathrm{Lactate}]_l - [\mathrm{Glucose}]_l \times [\mathrm{Lactate}]_e/[\mathrm{Glucose}]_e.$$

This result was normalized to the concentration of soluble protein in the lysate (units: mmol $\mathrm{lactate_i}$/g protein); to convert this into units of mmol $\mathrm{lactate_i}$/L cell (that is, mM), the result was multiplied by ρ: the mass of soluble protein in a unit of intracellular fluid (g protein/L cell). ρ was determined to be 13.21 ± 1.78 g/l from the quotient of protein concentration (g protein/L lysate) and v_i (L cell/L lysate), calculated as:

$$v_i = \mathrm{Osm_l/Osm_e} - [\mathrm{Glucose}]_l/[\mathrm{Glucose}]_e.$$

CONFLICT OF INTEREST

The authors declare no conflict of interest.

ACKNOWLEDGEMENTS

We thank Bärbel Heidrich, Sabine Wolfgramm and Bettina Jeep for excellent technical assistance. We thank Vicky Ball for performing measurements on the ABX Pentra 400 system. This study is supported by the European Commission through the IONTRAC Marie Curie Initial Training Network (FP7-PEOPLE-2011-ITN Grant 289648), Royal Society and Worldwide Cancer Research (2012/0027).

REFERENCES

1 Gatenby RA, Gillies RJ. Why do cancers have high aerobic glycolysis? *Nat Rev Cancer* 2004; **4**: 891–899.
2 Sonveaux P, Vegran F, Schroeder T, Wergin MC, Verrax J, Rabbani ZN *et al.* Targeting lactate-fueled respiration selectively kills hypoxic tumor cells in mice. *J Clin Invest* 2008; **118**: 3930–3942.
3 Ullah MS, Davies AJ, Halestrap AP. The plasma membrane lactate transporter MCT4, but not MCT1, is up-regulated by hypoxia through a HIF-1alpha-dependent mechanism. *J Biol Chem* 2006; **281**: 9030–9037.
4 Halestrap AP, Price NT. The proton-linked monocarboxylate transporter (MCT) family: structure, function and regulation. *Biochem J* 1999; **343**: 281–299.
5 Le Floch R, Chiche J, Marchiq I, Naiken T, Ilc K, Murray CM *et al.* CD147 subunit of lactate/H+ symporters MCT1 and hypoxia-inducible MCT4 is critical for energetics and growth of glycolytic tumors. *Proc Natl Acad Sci USA* 2011; **108**: 16663–16668.
6 Vaupel P, Kallinowski F, Okunieff P. Blood flow, oxygen consumption and tissue oxygenation of human tumors. *Adv Exp Med Biol* 1990; **277**: 895–905.
7 Gillies RJ, Raghunand N, Karczmar GS, Bhujwalla ZM. MRI of the tumor microenvironment. *J Magn Reson Imaging* 2002; **16**: 430–450.
8 Ojugo AS, McSheehy PM, McIntyre DJ, McCoy C, Stubbs M, Leach MO *et al.* Measurement of the extracellular pH of solid tumours in mice by magnetic resonance spectroscopy: a comparison of exogenous (19)F and (31)P probes. *NMR Biomed* 1999; **12**: 495–504.
9 Damaghi M, Tafreshi NK, Lloyd MC, Sprung R, Estrella V, Wojtkowiak JW *et al.* Chronic acidosis in the tumour microenvironment selects for overexpression of LAMP2 in the plasma membrane. *Nat Commun* 2015; **6**: 8752.
10 Gatenby RA, Gawlinski ET, Gmitro AF, Kaylor B, Gillies RJ. Acid-mediated tumor invasion: a multidisciplinary study. *Cancer Res* 2006; **66**: 5216–5223.
11 Tannock IF, Rotin D. Acid pH in tumors and its potential for therapeutic exploitation. *Cancer Res* 1989; **49**: 4373–4384.
12 Kennedy KM, Dewhirst MW. Tumor metabolism of lactate: the influence and therapeutic potential for MCT and CD147 regulation. *Future Oncol* 2010; **6**: 127–148.
13 Kumar NM, Gilula NB. The gap junction communication channel. *Cell* 1996; **84**: 381–388.
14 Hulikova A, Black N, Hsia LT, Wilding J, Bodmer WF, Swietach P. Stromal uptake and transmission of acid is a pathway for venting cancer cell-generated acid. *Proc Natl Acad Sci USA* 2016; **113**: E5344–E5353.
15 Loewenstein WR, Kanno Y. Intercellular communication and the control of tissue growth: lack of communication between cancer cells. *Nature* 1966; **209**: 1248–1249.
16 Naus CC, Laird DW. Implications and challenges of connexin connections to cancer. *Nat Rev Cancer* 2010; **10**: 435–441.
17 McLachlan E, Shao Q, Wang HL, Langlois S, Laird DW. Connexins act as tumor suppressors in three-dimensional mammary cell organoids by regulating differentiation and angiogenesis. *Cancer Res* 2006; **66**: 9886–9894.
18 Mesnil M. Connexins and cancer. *Biol Cell* 2002; **94**: 493–500.
19 Lin JH, Takano T, Cotrina ML, Arcuino G, Kang J, Liu S *et al.* Connexin 43 enhances the adhesivity and mediates the invasion of malignant glioma cells. *J Neurosci* 2002; **22**: 4302–4311.
20 Elzarrad MK, Haroon A, Willecke K, Dobrowolski R, Gillespie MN, Al-Mehdi AB. Connexin-43 upregulation in micrometastases and tumor vasculature and its role in tumor cell attachment to pulmonary endothelium. *BMC Med* 2008; **6**: 20.
21 Ito A, Katoh F, Kataoka TR, Okada M, Tsubota N, Asada H *et al.* A role for heterologous gap junctions between melanoma and endothelial cells in metastasis. *J Clin Invest* 2000; **105**: 1189–1197.
22 el-Sabban ME, Pauli BU. Cytoplasmic dye transfer between metastatic tumor cells and vascular endothelium. *J Cell Biol* 1991; **115**: 1375–1382.
23 Zhang A, Hitomi M, Bar-Shain N, Dalimov Z, Ellis L, Velpula KK *et al.* Connexin 43 expression is associated with increased malignancy in prostate cancer cell lines and functions to promote migration. *Oncotarget* 2015; **6**: 11640–11651.
24 Guillaumond F, Leca J, Olivares O, Lavaut MN, Vidal N, Berthezene P *et al.* Strengthened glycolysis under hypoxia supports tumor symbiosis and hexosamine biosynthesis in pancreatic adenocarcinoma. *Proc Natl Acad Sci USA* 2013; **110**: 3919–3924.
25 Koong AC, Mehta VK, Le QT, Fisher GA, Terris DJ, Brown JM *et al.* Pancreatic tumors show high levels of hypoxia. *Int J Radiat Oncol Biol Phys* 2000; **48**: 919–922.
26 Maupin KA, Sinha A, Eugster E, Miller J, Ross J, Paulino V *et al.* Glycogene expression alterations associated with pancreatic cancer epithelial-mesenchymal transition in complementary model systems. *PLoS One* 2010; **5**: e13002.
27 Moll W, Gros G. Combined glycolytic production of lactate(−) and ATP(4−) derived protons (=dissociated lactic acid) is the only cause of metabolic acidosis of exercise—a note on the OH(−) absorbing function of lactate (1−) production. *J Appl Physiol* 2008; **105**: 365.
28 Grillo-Hill BK, Choi C, Jimenez-Vidal M, Barber DL. Increased H(+) efflux is sufficient to induce dysplasia and necessary for viability with oncogene expression. *Elife* 2015; **4**: e03270.
29 Putney LK, Barber DL. Expression profile of genes regulated by activity of the Na-H exchanger NHE1. *BMC Genomics* 2004; **5**: 46.
30 Deer EL, Gonzalez-Hernandez J, Coursen JD, Shea JE, Ngatia J, Scaife CL *et al.* Phenotype and genotype of pancreatic cancer cell lines. *Pancreas* 2010; **39**: 425–435.
31 Morgan RT, Woods LK, Moore GE, Quinn LA, McGavran L, Gordon SG. Human cell line (COLO 357) of metastatic pancreatic adenocarcinoma. *Int J Cancer* 1980; **25**: 591–598.
32 Schilling F, Duwel S, Kollisch U, Durst M, Schulte RF, Glaser SJ *et al.* Diffusion of hyperpolarized (13) C-metabolites in tumor cell spheroids using real-time NMR spectroscopy. *NMR Biomed* 2013; **26**: 557–568.
33 Swietach P, Rossini A, Spitzer KW. Vaughan-Jones RD. H+ ion activation and inactivation of the ventricular gap junction: a basis for spatial regulation of intracellular pH. *Circ Res* 2007; **100**: 1045–1054.
34 Richards M, Lomas O, Jalink K, Ford KL, Vaughan-Jones RD, Lefkimmiatis K *et al.* Intracellular tortuosity underlies slow cAMP diffusion in adult ventricular myocytes. *Cardiovasc Res* 2016; **110**: 395–407.
35 Hulikova A, Aveyard N, Harris AL, Vaughan-Jones RD, Swietach P. Intracellular carbonic anhydrase activity sensitizes cancer cell pH signaling to dynamic changes in CO_2 partial pressure. *J Biol Chem* 2014; **289**: 25418–25430.
36 San Martin A, Ceballo S, Ruminot I, Lerchundi R, Frommer WB, Barros LF. A genetically encoded FRET lactate sensor and its use to detect the Warburg effect in single cancer cells. *PLoS ONE* 2013; **8**: e57712.
37 Hulikova A, Vaughan-Jones RD, Swietach P. Dual role of CO_2/HCO_3(−) buffer in the regulation of intracellular pH of three-dimensional tumor growths. *J Biol Chem* 2011; **286**: 13815–13826.
38 Swietach P, Patiar S, Supuran CT, Harris AL, Vaughan-Jones RD. The role of carbonic anhydrase 9 in regulating extracellular and intracellular ph in three-dimensional tumor cell growths. *J Biol Chem* 2009; **284**: 20299–20310.
39 Whitaker-Menezes D, Martinez-Outschoorn UE, Lin Z, Ertel A, Flomenberg N, Witkiewicz AK *et al.* Evidence for a stromal-epithelial "lactate shuttle" in human tumors: MCT4 is a marker of oxidative stress in cancer-associated fibroblasts. *Cell Cycle* 2011; **10**: 1772–1783.
40 Mole DR, Blancher C, Copley RR, Pollard PJ, Gleadle JM, Ragoussis J *et al.* Genome-wide association of hypoxia-inducible factor (HIF)-1alpha and HIF-2alpha DNA binding with expression profiling of hypoxia-inducible transcripts. *J Biol Chem* 2009; **284**: 16767–16775.
41 Gadaleta E, Cutts RJ, Kelly GP, Crnogorac-Jurcevic T, Kocher HM, Lemoine NR *et al.* A global insight into a cancer transcriptional space using pancreatic data: importance, findings and flaws. *Nucleic Acids Res* 2011; **39**: 7900–7907.
42 Faller BA, Burtness B. Treatment of pancreatic cancer with epidermal growth factor receptor-targeted therapy. *Biologics* 2009; **3**: 419–428.
43 Oliveira-Cunha M, Newman WG, Siriwardena AK. Epidermal growth factor receptor in pancreatic cancer. *Cancers* 2011; **3**: 1513–1526.
44 Parks SK, Chiche J, Pouyssegur J. Disrupting proton dynamics and energy metabolism for cancer therapy. *Nat Rev Cancer* 2013; **13**: 611–623.
45 Saccomano M, Dullin C, Alves F, Napp J. Preclinical evaluation of near-infrared (NIR) fluorescently labeled cetuximab as a potential tool for fluorescence-guided surgery. *Int J Cancer* 2016; **139**: 2277–2289.

This work is licensed under a Creative Commons Attribution 4.0 International License. The images or other third party material in this article are included in the article's Creative Commons license, unless indicated otherwise in the credit line; if the material is not included under the Creative Commons license, users will need to obtain permission from the license holder to reproduce the material. To view a copy of this license, visit http://creativecommons.org/licenses/by/4.0/

© The Author(s) 2017

Supplementary Information accompanies this paper on the *Oncogene* website (http://www.nature.com/onc)

Connexin-43 channels are a pathway for discharging lactate from glycolytic pancreatic ductal adenocarcinoma cells

TH Dovmark, M Saccomano, A Hulikova, F Alves and P Swietach

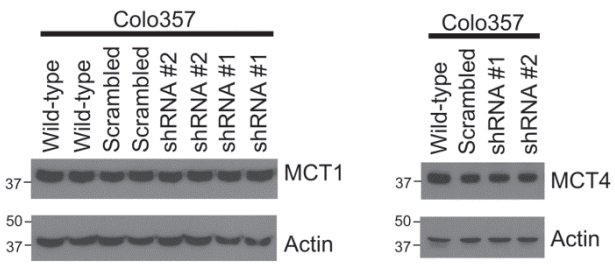


Figure S1. *MCT1/4 expression is unchanged by Cx43 knockdown.* Immunoblot showing that Colo357 cells infected with scrambled construct, shRNA #1 or shRNA #2 express MCT isoforms at comparable levels to wild-type cells.

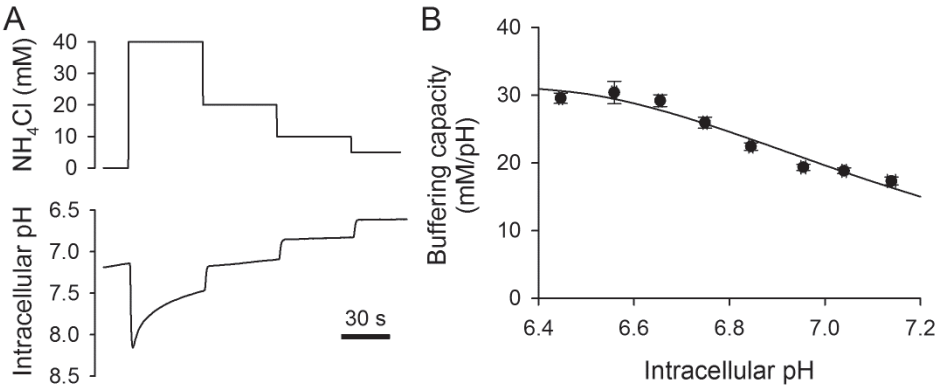


Figure S2. *Intrinsic buffering capacity.* (A) Colo357 monolayers, superfused in Hepes-buffered (CO_2/HCO_3^--free) solutions containing a range of [NH_4Cl] (iso-osmotically replacing [NaCl]), according to the protocol indicated in the upper panel. Measurements of intracellular pH show step-wise changes, coinciding with NH_4Cl removal; the amplitude of these is inversely related to buffering capacity. (B) Intrinsic buffering capacity as a function of intracellular pH, together with best fit curve. Each data point is mean±SEM from 20-35 cells.

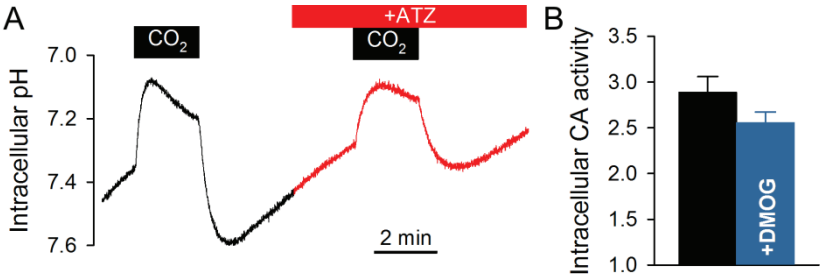


Figure S3. *Intracellular carbonic anhydrase activity.* (A) cSNARF1-loaded Colo357 monolayers under superfusion. Switching from Hepes-buffered to 5% CO_2/22 mM HCO_3^--buffered solution evokes CO_2 entry into cells and cytoplasmic CO_2 hydration, reported as a change in pH. The rate of the measured pH change depends on intracellular carbonic anhydrase activity. The uncatalysed hydration rate can be measured by repeating the protocol in the presence of acetazolamide (ATZ; 100 µM), a broad-spectrum carbonic anhydrase inhibitor. (B) Intracellular carbonic anhydrase activity in normoxic Colo357 cells and in cells with hypoxic signalling pathways stabilized with prior 48 hr incubation with 1 mM DMOG. CA activity is quantified as the measured CO_2 hydration rate constant divided by the uncatalysed rate constant; the result is dimensionless (a ratio of two first-order rate constants). Mean±SEM from 50 and 40 cells, respectively.

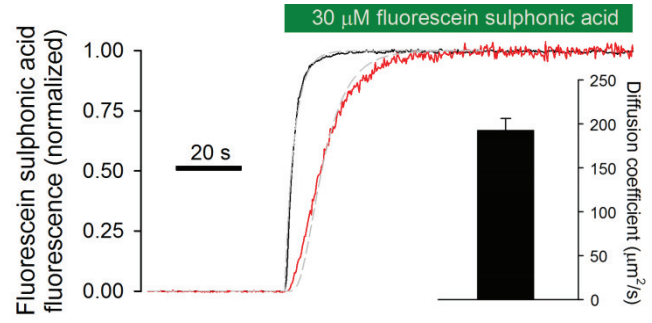


Figure S4. *Diffusive tortuosity in the extracellular compartment of Colo357 spheroids.* Colo357 spheroids (radius 110±5 µm) were superfused with Hepes-buffered solution at 37°C. At the point indicated (green bar), the superfusate was switched to one containing 30 µM fluorescein sulphonic acid, a membrane-impermeable fluorescent dye. Fluorescence was imaged across the equatorial plane of the spheroid. Black trace shows time course in the spheroid rim (layer of width=11 µm); red trace shows time course in spheroid core (radius=11 µm). Grey broken lines are model best-fit, as described in Hulikova & Swietach, 2015. The best-fit diffusion coefficient was determined from 9 spheroids; it was reduced by 70% relative to the diffusivity of fluorescein sulphonic acid in water at 37°C.

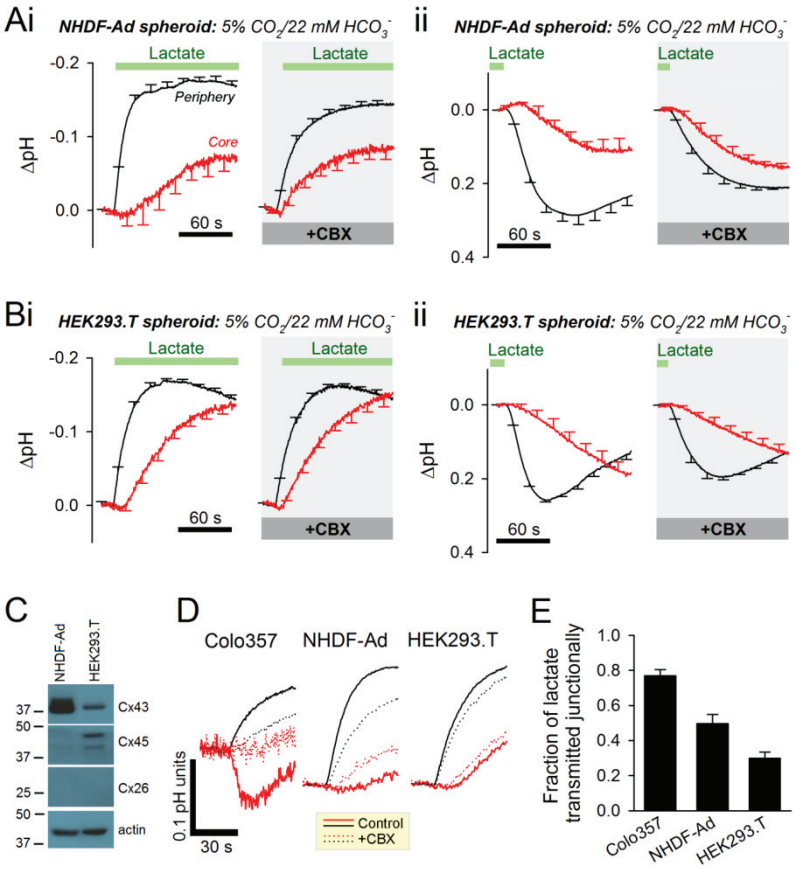


Figure S5. *Evidence for junctional lactate traffic in non-PDAC spheroids.* (A) NHDF-Ad (adult human fibroblast) spheroids (radius 101±2 μm) loaded with cSNARF1 and imaged across the equatorial plane for pH_i. Time courses show change in pH_i in the core *(red)* and rim *(black)*. Superfusion with 5% CO_2/22 mM HCO_3^--buffered solution (6 spheroids). Experiments also performed in the presence of 100 μM CBX to block gap junctions (7 spheroids). *(i)* pH_i response to superfusion with 40 mM lactate-containing solution and *(ii)* pH_i response to subsequent withdrawal of lactate. The pH_i time courses at the core and periphery appeared closer together under gap junctional inhibition. (B) Experiments repeated according to the above protocol on HEK293.T (human embryonic kidney cells) spheroids (radius 93±2 μm). (C) Immunoblot for Cx43, Cx45 and Cx26 expression in NHDF-Ad and HEK293.T cells. (D) pH_i time courses from Fig 3 (Colo357), S5A (NHDF-Ad) and S5B (HEK293.T), showing a range of responses. Colo357 spheroids demonstrated the greatest contribution from junctional lactate transmission, observed as a large alkalinising pH_i transient; the response was smaller in NHDF-Ad spheroids and weakest in HEK293T spheroids. These measurements correlated with Cx43 expression. (E) Fraction of lactate that is transmitted junctionally (see text).

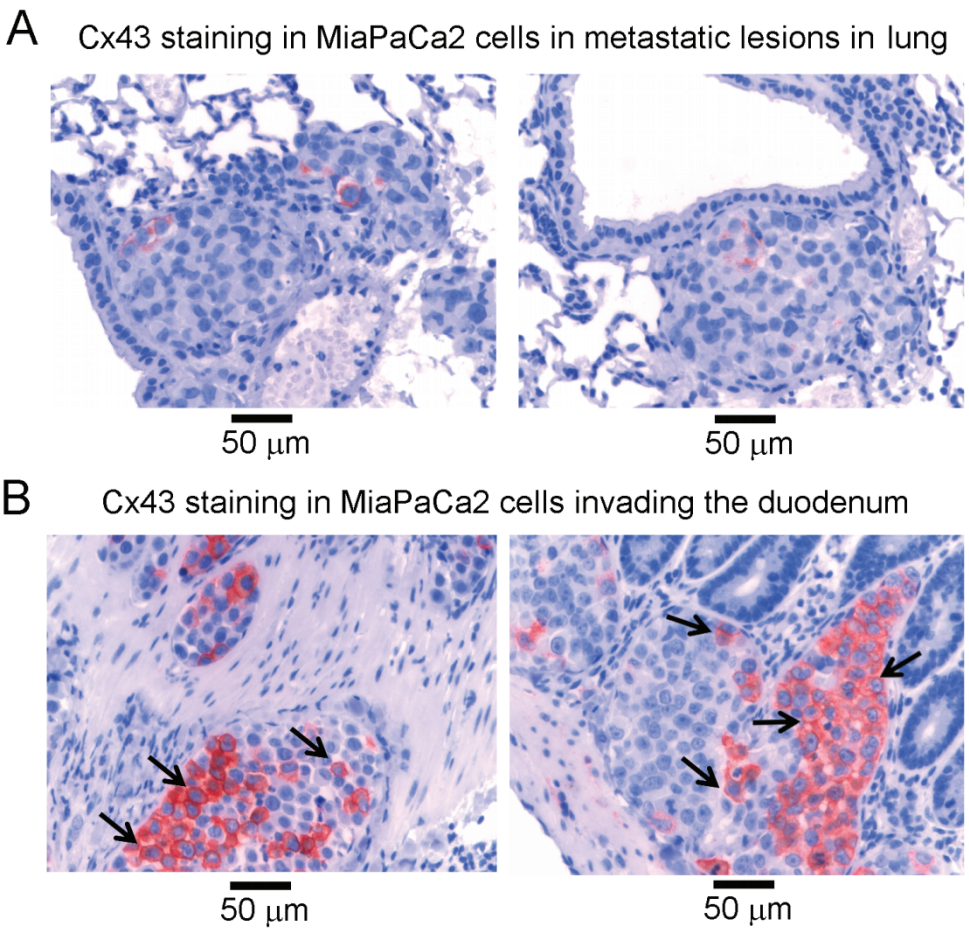


Figure S6. *Evidence for Cx43 staining at the membrane.* (A) Examples of two areas of lung (from different animals) with metastatic lesions containing MiaPaCa2 cells with sparse Cx43 staining. (B) Examples of two areas of duodenum (from different animals) containing clusters of invading MiaPaCa2 cells with strong Cx43 staining. Staining at cell-to-cell margins indicates surface membrane targeting, where Cx43 channels can form cell-to-cell conduits.

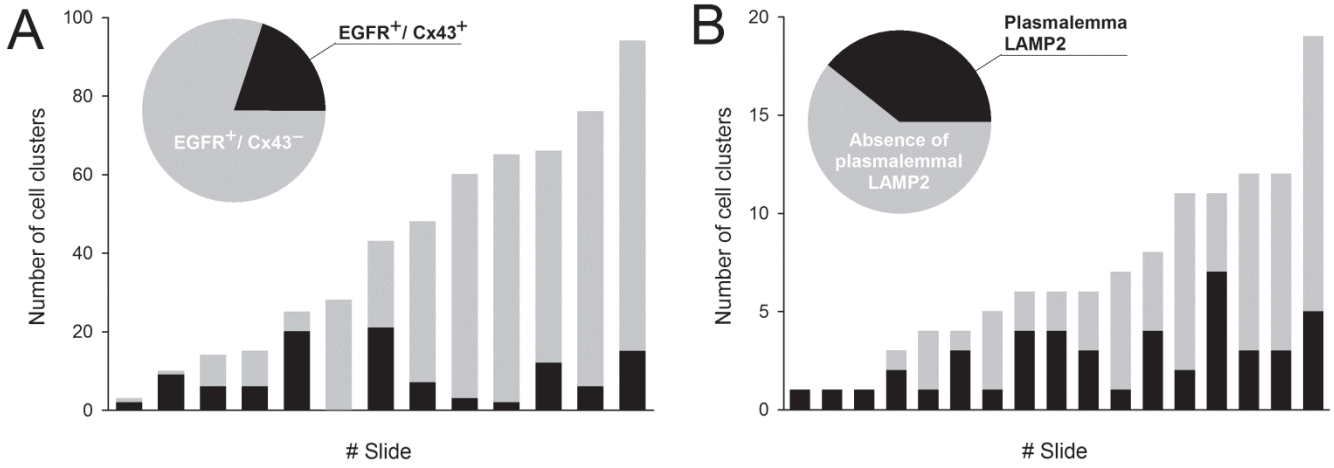


Figure S7. *Analysis of staining patterns in MiaPaCa2 cell clusters invading the gut or pancreas.* (A) Analysis performed on 13 sections of gut or pancreas from four different mice with orthotopic MiaPaCa2 xenografts. MiaPaCa2 cells were identified by positive EGFR staining. Out of a total of 547 clusters, 20% also showed strong Cx43 staining. (B) Analysis performed on 17 sections of gut or pancreas from four different mice with orthotopic MiaPaCa2 xenografts. MiaPaCa2 clusters were analysed for subcellular the pattern of LAMP2 staining. Out of 117 clusters, 39% included cells with LAMP2 staining near/at the plasmalemma, a marker of an acidotic niche.

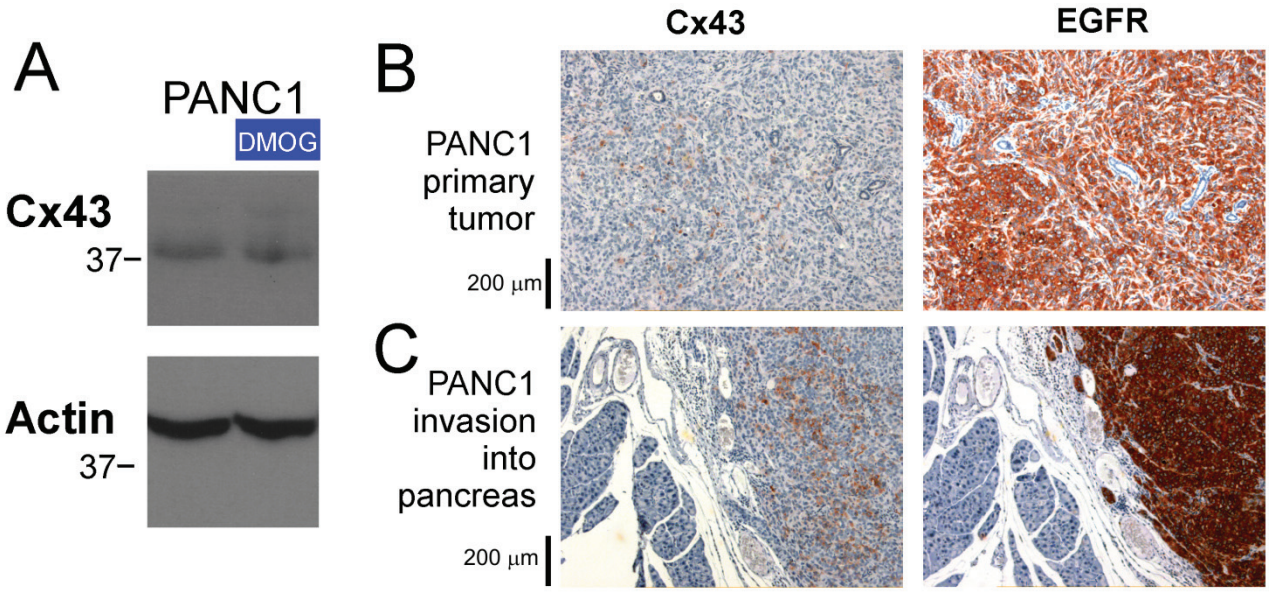


Figure S8. *Cx43 expression in PANC1 cancer cells in culture and* in vivo. (A) Low Cx43 expression in PANC1 cells cultured *in vitro* under normoxic conditions or in the presence of 1 mM DMOG (to stabilize hypoxic signalling). (B) Sparse pattern of Cx43 staining in regions of the primary tumour of PANC1 orthotopic xenograft mouse models. PANC1 cells are identified by positive staining for human EGFR. (C) Cx43 staining is increased in areas of invasion into the pancreas.

The FASEB Journal article fj.201700480R. Published online September 7, 2017.

Normoxic cells remotely regulate the acid-base balance of cells at the hypoxic core of connexin-coupled tumor growths

Tobias H. Dovmark,* Alzbeta Hulikova,* Steven A. Niederer,† Richard D. Vaughan-Jones,* and Pawel Swietach*,[1]

*Department of Physiology, Anatomy, and Genetics, University of Oxford, Oxford, United Kingdom, and †Division of Imaging Sciences and Biomedical Engineering, St. Thomas' Hospital, London, United Kingdom

ABSTRACT: ATP fuels the removal of metabolic end-products, including H^+ ions that profoundly modulate biological activities. Energetic resources in hypoxic tumor regions are constrained by low-yielding glycolysis, and any means of reducing the cost of acid extrusion, without compromising pH homeostasis, would therefore be advantageous for cancer cells. Some cancers express connexin channels that allow solute exchange between cells, and we propose that, *via* this route, normoxic cells supply hypoxic neighbors with acid-neutralizing HCO_3^- ions. This hypothesis was tested by imaging cytoplasmic pH in spheroidal tissue growths of connexin43-positive pancreatic cancer Colo357 cells during light-controlled H^+ uncaging at the hypoxic core. Cytoplasmic acid retention at the core was halved in the presence of CO_2/HCO_3^-, but this process requires a restorative HCO_3^- flux. The effect of CO_2/HCO_3^- was ablated by connexin43 inhibition or knockdown. In connexin-decoupled spheroids, 4,4′-diisothiocyano-2,2′-stilbenedisulfonic acid (DIDS), an inhibitor of HCO_3^- uptake, had no effect on cytoplasmic $[H^+]$ in the H^+-uncaging region, indicating that DIDS-sensitive transport is not an adequate pH-regulatory strategy therein. With intact connexin-coupling, acid retention at the core increased upon DIDS treatment, indicating that HCO_3^- ions are taken up actively by peripheral cells and then transmitted passively to cells at the hypoxic core. Thus, the energetic burden of pH regulation is offloaded from hypoxic cells onto metabolically altruistic normoxic neighbors.—Dovmark, T. H., Hulikova, A., Niederer, S. A., Vaughan-Jones, R. D., Swietach, P. Normoxic cells remotely regulate the acid-base balance of cells at the hypoxic core of connexin-coupled tumor growths. FASEB J. 32, 000–000 (2018). www.fasebj.org

KEY WORDS: homeostasis · gap junctions · bicarbonate transport · pancreatic cancer · metabolic altruism

Tumors, including pancreatic cancers (1, 2), commonly undergo metabolic reprogramming to maximize the synthetic and energetic resources available for proliferation under microenvironmental constraints, such as hypoxia (3). For instance, cancer cells switch to substrate-limited glycolysis to maintain a pipeline of ATP, even when oxygen is depleted (4). An inescapable consequence of reprogrammed glycolytic cancer metabolism is high-volume production of lactic acid, which challenges intracellular pH (pH_i) homeostasis. Pancreatic tumors *in vivo* receive blood-borne glucose at ~3 mmol/min per liter tumor volume (5). With ample supply of glucose, pancreatic ductal adenocarcinoma (PDAC) cells can generate 8–22 mmol lactate/min per liter of cell volume (6, 7), which is enough to acidify cytoplasm by 1 pH unit in just a few minutes. In its canonical form, pH_i regulation involves ATP-consuming active transport of H^+ (or H^+-equivalent) ions across the cell membrane (8, 9). In many examples of cancer cells, metabolic acids are titrated by HCO_3^- ions imported by secondary active transporters, such as Na^+-HCO_3^- cotransporters (NBCs) (10). This mechanism is proposed to be a major pH_i-regulatory strategy in PDAC (11), which develops from HCO_3^--secreting ductal epithelia with characteristically high levels of the NBCe1 isoform (12). As a tumor grows, and its blood perfusion becomes ineffective, diffusion distances expand, and the milieu surrounding cells in underperfused regions becomes hypoxic and acidotic (13, 14). Low extracellular pH (pH_e) compromises pH_i regulation because it

ABBREVIATIONS: AM, acetoxymethyl ester; ATZ, acetazolamide; CA, carbonic anhydrase; CAIX, carbonic anhydrase 9; CBX, carbenoxolone; cSNARF1, 5-(and-6)-carboxy SNARF-1; DMA, 5-*N*,*N*-dimethylamiloride; DIDS, 4,4′-diisothiocyano-2,2′-stilbenedisulfonic acid; DMOG, dimethyloxalylglycine; FS, fluorescein-5-(and-6)-sulfonic acid; MCT, H^+-monocarboxylate transport; HEPES, 2-[4-(2-hydroxyethyl)piperazin-1-yl] ethanesulfonic acid; NBC, Na^+-HCO_3^- cotransporter; NHE, Na^+/H^+ exchange; NVA, nitroveratraldehyde; PDAC, pancreatic ductal adenocarcinoma; pH_e, extracellular pH; pH_i, intracellular pH; ROI, region of interest; shRNA, short hairpin RNA; WGA-fluorescein, wheat germ agglutinin–conjugated fluorescein

[1] Correspondence: Department of Physiology, Anatomy and Genetics, University of Oxford, Parks Rd., OX1 3PT Oxford, United Kingdom. E-mail: pawel.swietach@dpag.ox.ac.uk

doi: 10.1096/fj.201700480R

This article includes supplemental data. Please visit *http://www.fasebj.org* to obtain this information.

Downloaded from www.fasebj.org to IP 129.67.119.187. *The FASEB Journal* Vol., No. , pp:, October, 2017

exacerbates the thermodynamic barrier for acid extrusion and can allosterically inhibit acid-extruding proteins (15). In the case of NBC, HCO_3^- uptake from an acidotic microenvironment would have to work against a considerable concentration gradient and thus require a major commitment of energetic resources. Indeed, in response to a uniform acid load applied to cultured 3-dimensional spheroidal tissue growths (spheroids), cells at the core demonstrate the slowest pH_i recovery and are thus most vulnerable to acid-base imbalance (15). Any means of improving pH_i control without raising its ATP cost would confer a selection advantage on these environmentally stressed cells.

Various mechanisms for assisting cancer cell acid-base homeostasis have been proposed, such as acid uptake by juxtaposed stromal cells (16), but these do not involve the direct provision of HCO_3^- ions to cancer cell cytoplasm. Although carbonic anhydrase (CA)-catalyzed intracellular CO_2 hydration produces HCO_3^- ions (17), it also loads cytoplasm with H^+ ions, which counters the objective of acid extrusion. A plausible route for supplying cytoplasm with solutes, including HCO_3^- ions, may involve passive permeation through gap junctional channels found in many tissues, including some tumors (18–22). We have demonstrated that connexin43 channels conduct a flow of lactate anions away from the hypoxic core of PDAC tissue growths (23). In contrast, H^+ ions, coproduced by glycolytic metabolism, are heavily buffered and therefore unable to diffuse freely through connexin43 channels (23, 24), which leaves hypoxic cells vulnerable to uncontrolled acidification. In the current study, we tested the extent to which HCO_3^- permeation through connexin-assembled gap junctional channels are able to supply hypoxic cancer cells with sufficient chemical base for titrating metabolic H^+ ions. Under this arrangement, active transport of HCO_3^- ions would be performed remotely (*e.g.*, by cells at the normoxic rim where thermodynamic conditions for this type of membrane transport are most favorable). The passive transmission of HCO_3^- ions through connexin channels comes at no energetic cost to the recipient cell because it occurs down a gradient of $[HCO_3^-]_i$. In pancreatic cancer, connexin43 immunoreactivity has been shown to increase with disease progression (25). Our recent study (23) demonstrated the presence of connexin43 in PDAC cell lines, such as Colo357, hypoxic BxPC3 *in vitro* and in invading or metastasizing MiaPaCa2 cells *in vivo* and also established a correlation between connexin43 levels and solute exchange between cells. Evidence of the loss of histone H3 methylation during subclonal evolution may provide a molecular mechanism for the upregulation of genes coding for connexins in PDAC metastases relative to the primary tumor (26).

To evaluate connexin channel permeation as a pipeline for HCO_3^- ions, we imaged pH_i dynamics in the syncytial cytoplasmic compartment of connexin43-coupled spheroids of Colo357, a cell line derived from PDAC metastasis. The ammonium prepulse method, used widely to interrogate acid handling (15), was not appropriate for studying junctional HCO_3^- handling, because this technique imposes near-uniform shifts in pH_i that collapse the driving force for junctional transmission and, furthermore, do not accurately replicate the heterogeneity of metabolic acid production in tumors. Because the ammonium prepulse maneuver evokes a substantial intracellular acidification, it emphasizes the importance of pH_i regulatory mechanisms triggered at low pH_i, over those operating nearer to resting pH_i. In response to these limitations, we designed a new method for studying acid handling in tissue growths. Acid loading of cells at the hypoxic core was evoked by photolytic H^+ uncaging applied to the spheroid's central region. By imaging the spatiotemporal responses of cytoplasmic $[H^+]$ to light-controlled acid loading, we were able to show that a substantial fraction of HCO_3^- ions in hypoxic areas is passively supplied by cell-to-cell diffusion through connexin43 channels. Ultimately, these HCO_3^- ions are sequestered into the syncytial cytoplasm by active transport taking place in cells at the normoxic rim, where energetic resources are less constrained. We thus showed that, in syncytial tissue growths, hypoxic cancer cells exploit the energetic resources of normoxic cells to provide a steady flow of HCO_3^- ions for titrating metabolic acids.

MATERIALS AND METHODS

Cell lines

AsPC1, BxPC3, MiaPaCa2, PANC1, and Colo357 cells were kindly provided by Holger Kalthoff (Christian-Albrechts-Universitaet, Kiel, Germany). Cells were grown in CO_2/HCO_3^--buffered DMEM (D6546; Millipore-Sigma, St. Louis, MO, USA) containing 10% fetal bovine serum (F9665, Capan1 cells in 20%; Millipore-Sigma), 2 mM L-glutamine, 20 U/ml penicillin, and 20 μg/ml streptomycin (Millipore-Sigma) and 0.1 mg/ml Normocin (InvivoGen, San Diego, CA, USA). Cells were trypsinized with 0.1% Trypsin (15400-054; Thermo Fisher Scientific, Waltham, MA, USA) and passaged twice per week. Monolayers were plated in Ibidi or LabTek chambers (seeded at 5×10^4 and 7×10^4 cells, respectively) for real-time imaging or in 6-cm dishes (seeded a 1.2×10^6 cells) for 3 d for immunoblot analysis. Spheroids were grown by using the hanging-drop method (400 Colo357 cells/20 μl) for 3 d.

Cell viability assay

Cells were plated in 96-well plates (at 60,000 AsPC1, and BxPC3 cells/well, and 45,000 $MiaPaCa_2$, PANC1, and Colo357 cells/well). After 24 h of culture in high-glucose DMEM supplemented with 10% fetal calf serum, medium was replaced with glucose-free DMEM containing 25 mM glucose, galactose, or 2-deoxy-D-glucose. Cell viability after a 24-h period was measured with the CellTiter Blue Assay (Promega, Southampton, United Kingdom).

Short hairpin RNA knockdown

GJA1 (connexin43-coding gene) knockdown clones and their scrambled controls were generated in a parallel study (23). In brief, HEK293.T packaging cells were plated into 25T tissue culture flasks, grown to 50% confluence, and transfected ($CaPO_4$ method) with packaging plasmids pSPAX2, pMD2.G, and a short hairpin RNA (shRNA) construct (GeneCopoiea, Rockville, MD, USA; HSH007411-1-LVRU6GP, HSH007411-2-LVRU6GP, HSH007411-3-LVRU6GP and HSH007411-4-LVRU6GP; CSHCTR001-LVRU6GP was the scrambled control). Lentivirus-containing media were collected, filtered through

Downloaded from www.fasebj.org to IP 129.67.119.187. *The FASEB Journal* Vol., No. , pp:, October, 2017

0.45-μm syringe filters and added to PDAC cells for 72 h. Transfected cells were selected with puromycin (6 μg/ml). Knockdown efficiency, determined from Cx43 immunoreactivity, was found to be 70% based on densitometry of 3 blots from independently prepared lysates.

Immunoblot analysis

To measure protein levels under normoxic conditions, cells were incubated in an atmosphere of 21% O_2. To characterize the effect of stabilizing hypoxic signaling, monolayers were incubated with the prolyl-4 hydroxyl domain protein inhibitor dimethyloxalylglycine (DMOG; 1 mM in 0.1% DMSO) or incubated in 2% O_2 for 48 h. Cells were then lysed in RIPA buffer containing protease and phosphatase inhibitors. Total protein (55 μg per lane) (bicinchoninic acid assay; Thermo Fisher Scientific) was loaded, separated on by SDS-PAGE and transferred onto PVDF membrane. The membranes were blocked in 5% skim milk and incubated with primary antibodies raised against β-actin and Cx43 (5125, 3512S; Cell Signaling Technology, Danvers, MA, USA), NBCe1 (H00008671-M01; Novus, Taipei, Taiwan), and mouse mAb against human carbonic anhydrase 9 (CAIX) (M75, gift from Silvia Pastorekova, Institute of Virology, Slovak Academy of Sciences, Bratislava, Slovakia) used in this study as a sensitive readout of downstream hypoxia-inducible factor signaling (27–29). Membranes were then incubated with horseradish peroxidase–conjugated secondary antibodies (Novus) and developed with ECL (Thermo Fisher Scientific). Blots were repeated 3 times on independently prepared lysates.

Solutions and superfusion

CO_2/HCO_3-buffered solution (5%) (mM): 125 NaCl, 4.5 KCl, 11 glucose, 22 $NaHCO_3$, 1 $CaCl_2$, 1 $MgCl_2$. 2-[4-(2-hydroxyethyl) piperazin-1-yl]ethanesulfonic acid (HEPES)-buffered solution: $NaHCO_3$ replaced with 20 mM HEPES; pH adjusted to 7.4 with 4 M NaOH. Ammonium-containing solution: NH_4Cl was added at 20 or 30 mM, replacing an equimolar concentration of NaCl to preserve osmolarity. Monolayers were superfused in the LabTek or IBIDI chambers, and spheroids were superfused in a Perspex chamber with a poly-L-lysine–treated coverslip.

Confocal imaging

Cells were loaded with 10 μg/ml 5-(and-6)-carboxy SNARF-1 (cSNARF1) acetoxymethyl ester (AM) (5 min for monolayers and up to 3 h for spheroids). cSNARF1 was excited at 555 nm, measured at 580/640 nm and converted to pH with a calibration curve determined by the nigericin method (17). Fluorescein sulfonic acid (FS) or wheat germ agglutinin-conjugated fluorescein (WGA-fluorescein) was excited at 488 nm and measured >510 nm and calibrated at solutions of various pH (5.5–8) (30). Hoechst 33342 and the hypoxic probe Image-iT Hypoxic Reagent (31) (Thermo Fisher Scientific) were coloaded into spheroids for 3 h at 10 μg/ml and 4 μM, respectively. Hoechst was excited at 405 nm and measured at 470 ± 40 nm; Image-iT was excited at 488 nm, and emission was collected >560 nm. All imaging was performed on an LSM 700 system (Zeiss, Jena, Germany). The pinhole for monolayer and spheroid experiments was 2.9 and 1.8 Airy units, respectively. Data were collected from at least 4 batches of monolayers, and the spheroids were grown independently.

Photolytic uncaging

To uncage H^+ ions from 6-nitroveratraldehyde (NVA; MilliporeSigma) in the central region of a spheroid and then image the evoked changes in $[H^+]$, excitation alternated, at a cycle length of 0.73 s, between 405 nm restricted to a small region 1/10th radius of spheroid at the center of spheroid and either 555 nm (for cSNARF1 imaging) or 488 nm (for FS imaging) across the entire field of view. For image analysis, fluorescence was averaged in regions of interest (ROIs) equivalent to layers (thickness equal to 1/10th of spheroid radius), each with a center of mass at the center of the uncaging region.

Generating the time course of H^+ titration onto buffers

Measurements of pH are a readout of free $[H^+]$. During a pH disturbance, the total amount of acid injected (Q) can be calculated as the product of the change in pH (ΔpH) and buffering capacity (β). In the absence of CO_2/HCO_3^-, cumulative Q can be measured from ΔpH and intrinsic buffering capacity (β_i). The light protocol releases the same amount of acid (Q) in the presence of CO_2/HCO_3^-, but some of the H^+ ions are titrated onto carbonic buffer (β_c), according to the relationship (Eq. 1):

$$\int_{t=0}^{t=T} \beta_i \times \left(\frac{dpH}{dt}\right)_{\mathrm{HEPES}} dt = \int_{t=0}^{t=T} \beta_i \times \left(\frac{dpH}{dt}\right)_{\mathrm{CO_2HCO_3}} dt + \int_{t=0}^{t=T} \beta_c \times \left(\frac{dpH}{dt}\right)_{\mathrm{CO_2HCO_3}}$$

$$\therefore \beta_c = \beta_i \times \left(\frac{(dpH)_{\mathrm{HEPES}}}{(dpH)_{\mathrm{CO_2HCO_3}}} - 1\right) \quad (1)$$

RESULTS

Glycolytic dependence and buffering capacity of PDAC cells

A cell's propensity to produce lactic acid depends on its glycolytic dependence, which was determined from the effect of replacing medium D-glucose with D-galactose, a substrate that yields no net ATP glycolytically (30), on redox chemistry and cell viability (CellTiter Blue assay). Results from 5 PDAC cell lines (32, 33) were normalized to measurements in 2-deoxy-D-glucose, which blocks carbohydrate catabolism. Under normoxic conditions, monolayers of MiaPaCa2 and BxPC3 cells (lines established from primary tumors), AsPC1 cells (established from ascites), and Colo357 cells (established from metastases) had significantly reduced viability in galactose (**Fig. 1*A***), indicative of the Warburg effect, with Colo357 cells having the most glycolytic phenotype. The net effect of glycolytic metabolism, when also taking into account ATP synthesis and hydrolysis, is the generation of lactate and H^+ ions in a ~1:1 ratio (34), equivalent to the production of lactic acid. This acid reacts chemically with intracellular buffers, categorized as either extrinsic (CO_2/HCO_3^-, also called carbonic) or intrinsic (*e.g.*, proteins). The fraction of H^+ ions titrated by a particular type of buffer depends on its buffering capacity. At equilibrium, carbonic buffering capacity (β_c) is mathematically related to intracellular

Downloaded from www.fasebj.org to IP 129.67.119.187.

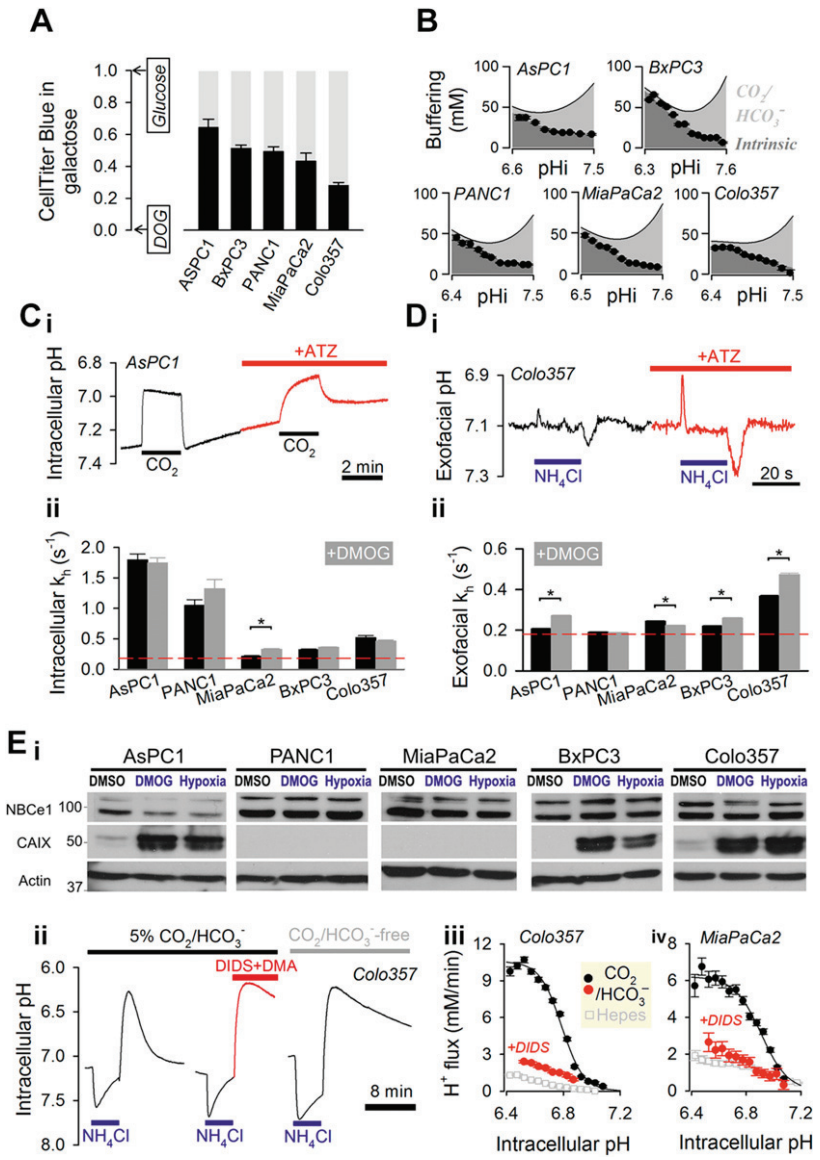


Figure 1. Characterizing the metabolic profile and carbonic buffering in PDAC monolayers. *A*) Cell viability measured in medium containing 25 mM galactose, expressed relative to reading in 25 mM glucose and the nonmetabolizable substrate 2-deoxyglucose (mean ± SEM of 9 repeats/line). *B*) Intrinsic buffering capacity measured by the ammonium removal method (mean ± SEM of 3–6 repeats/line). CO_2/HCO_3^- buffering was calculated. *C*) Intracellular carbonic anhydrase activity. *Ci*) cSNARF1-loaded monolayers (reports pH_i) superfused in HEPES-buffered solution; 2 min exposure to CO_2/HCO_3^- evoked CO_2 entry into cells and H^+-yielding intracellular hydration. Repeating in presence of ATZ (100 μM) interrogates spontaneous kinetics. *Cii*) Intracellular CO_2 k_h (hydration rate). Control, mean ± SEM of 3–6 repeats/line; DMOG pretreated, mean ± SEM of 3–5 repeats/line. Dashed red line is spontaneous k_h. *D*) Exofacial carbonic anhydrase activity. *Di*) WGA-fluorescein–labeled monolayers (reports pH_e) superfused in CO_2/HCO_3^- buffered solution; 30 s exposure to 30 mM NH_4Cl evoked a pH_e transient as a result of re-equilibration of NH_4^+/NH_3 secondary to transmembrane NH_3 flux. Size of transient is inversely proportional to speed of buffering. Repeating in the presence of ATZ (100 μM) determined spontaneous reaction kinetics. *Dii*) Exofacial k_h. Control, mean ± SEM of 3–5 repeats/line; DMOG pretreated, mean ± SEM of 3–4 repeats/line. Dashed red line: spontaneous k_h. *Ei*) Western blot for Na^+-$2HCO_3^-$ cotransporter NBCe1 under control conditions (DMSO vehicle) or after 48 h incubation with 1 mM DMOG or in 2% O_2 (hypoxia). CAIX induction was a proxy for the stabilization of hypoxia-inducible factor signaling in 3 cell lines (AsPC1, BxPC3, and Colo357). *Dii*) pH_i time course in cSNARF1-loaded Colo357 monolayer during a 20 mM NH_4Cl prepulse maneuver; recovery from intercellular acid load interrogates transmembrane H^+-equivalent flux. Recovery was inhibited with 30 μM DMA (blocker of Na^+/H^+ exchange) plus 150 μM DIDS (blocker of HCO_3^- transport); flux at pH_i 6.3 was reduced to 1.9 ± 0.4 mM/min *vs.* 10.5 ± 0.5 mM/min in the absence of drugs. Repeating protocol in absence of CO_2/HCO_3^- (HEPES buffer) measured the HCO_3^--independent component of flux. *Diii*) pH_i dependence of flux. DIDS (150 μM) blocked of HCO_3^- transport. Mean ± SEM of 5 repeats per condition, each representing 10–15 cells. *Div*) Similar measurements in MiaPaCa2 cells. Mean ± SEM of 5 repeats for each condition, each representing 10–15 cells.

$[HCO_3^-]$ (β_c = 2.303 × $[HCO_3^-]_i$), whereas intrinsic buffering capacity (β_i) must be determined empirically by the ammonium-removal method (9) under CO_2/HCO_3^--free conditions in cSNARF-1-loaded cells imaged for pH_i. Figure 1*B* compares β_c and β_i in the 5 PDAC cell lines. Over the alkaline range of pH_i, most of the buffering at physiologic (5%) pCO_2 is provided by CO_2/HCO_3^-, and the β_c-to-β_i ratio rises sharply with pH_i.

The spontaneous kinetics of buffering by CO_2/HCO_3^- are modest but can be accelerated by CA enzymes. The ensemble activity of intracellular isoforms was measured in cSNARF1-loaded cells from the pH_i response to a rapid change in pCO_2 (Fig. 1*Ci*) (17). Spontaneous reaction kinetics were determined by measurements repeated in the presence of acetazolamide (ATZ; 100 μM), a broad-spectrum CA inhibitor (17). The highest intracellular CO_2 hydration rate (k_h) was recorded in AsPC1 and PANC1 monolayers (Fig. 1*Cii*); activity in MiaPaCa2, BxPC3, and Colo357 cell monolayers was <3-fold the spontaneous rate. Induction of hypoxic signaling with DMOG (1 mM for 48 h) marginally increased intracellular CA activity in MiaPaCa2 monolayers only. The activity of exofacial CA isoforms was reported by membrane tethered WGA-fluorescein (30). To investigate the kinetics of extracellular CO_2/HCO_3^- buffering (hence exofacial CA activity), a pH_e disturbance was evoked at the outer surface of cells. Brief exposure to 30 mM NH_4Cl produces exofacial acidification, reported as a quenching of WGA-fluorescein that can be calibrated into units of pH_e by subsequent application with a series of buffers of known pH. The amplitude of pH_e transients was most sensitive to acetazolamide (100 μM) in Colo357 cells, indicating that

Downloaded from www.fasebj.org to IP 129.67.119.187. *The FASEB Journal* Vol., No. , pp:, October, 2017

these have high exofacial CA activity. Hypoxic signaling resulted in a modest increase in exofacial k_h in AsPC1, BxPC3, and Colo357 cells (Fig. 1*Dii*), which correlated with the hypoxic induction of CAIX, an extracellular-facing isoform (Fig. 1*Ei*).

To maintain adequate carbonic buffering capacity under sustained metabolic acid production, intracellular [HCO_3^-] must be restored by a matching flux. One such restorative mechanism involves HCO_3^- uptake from the extracellular fluid by transporters that are normally present in pancreatic ducts, of which NBCe1 is particularly important (12). NBCe1 expression was confirmed in monolayers of all 5 PDAC cell lines under normoxic and hypoxic conditions (Fig. 1*Ei*). The flux generated by HCO_3^- transporters was determined by acidifying the cytoplasm, by means of a 20 mM ammonium prepulse solution maneuver, and comparing the rate of pH_i recovery in the presence and absence of CO_2/HCO_3^- (Fig. 1*Eii*). In Colo357 cells, robust pH_i recovery was observed when HCO_3^- transporters were functional, and this effect was attenuated by the broad-spectrum HCO_3^- transport inhibitor 4,4′-diisothiocyano-2,2′-stilbenedisulfonic acid (DIDS; 150 μM; Fig. 1*Eiii*). Similar results were obtained in MiaPaCa2 cells (Fig. 1*Eiv*). In Colo357 monolayers, pH_i recovery was largely inhibited (82% reduction calculated at $pH_i = 6.3$) in the presence of 150 μM DIDS and 30 μM 5-*N*,*N*-dimethylamiloride (DMA; blocker of Na^+/H^+ exchange, NHE), which argues for a negligible contribution from DIDS-insensitive HCO_3^- transport.

An alternative pipeline for delivering HCO_3^- ions is passive permeation from neighboring cells *via* connexin channels. Connexin43-dependent coupling has been demonstrated in PDAC cells *in vivo* and *in vitro* (23) and thus may be characteristic of at least some stages of pancreatic cancer. The strength of cell-to-cell coupling was evaluated by fluorescence recovery after photobleaching of calcein (AM-loaded into monolayers), which serves as a diffusible cytoplasmic marker (**Fig. 2**). Calcein fluorescence in a cell of a confluent monolayer was bleached to 50% by 405 nm flashes, and any subsequent recovery of signal was measured over a 4 min period by confocal imaging. In relation to HEK293.T cells, a control for strong cell-to-cell coupling (Fig. 2*D*), cell-to-cell transmission of calcein was rapid in Colo357 (Fig. 2*C*) and BxPC3 (Fig. 2*B*) cells, but negligible in MiaPaCa2 cells (Fig. 2*A*). HCO_3^- ions, which are 10-fold smaller than calcein molecules, are expected to permeate connexin channels significantly faster and therefore supply recipient cells with a meaningful restorative flux of HCO_3^- ions. On the basis of strong connexin-coupling and glycolytic metabolism, Colo357 cells were selected for further imaging studies.

Spheroidal tissue growths show radial gradients of oxygen tension

Net flux of small solutes through connexin channels can occur only down cell-to-cell concentration gradients, which are notably absent in uniformly perfused monolayers but are highly significant in 3-dimensional tissue growths, where pO_2 nonuniformity establishes metabolite heterogeneity. Thus, to study connexin-dependent transport, spheroids were grown from Colo357 cells, a PDAC line with high levels of connexin43 (23). The spheroids were first seeded using the hanging drop method and then transferred to culture dishes for another 1–3 d to gradually increase the degree of cell–cell packing (*i.e.*, tortuosity, which favors steeper pO_2 gradients). Hypoxia was measured with a hypoxia-sensitive fluorescent probe (Image-iT hypoxia reagent) (31). Fluorescence emitted by the hypoxic probe increases as pO_2 falls. However, as a spheroid becomes more compact, light transmittance from its core becomes attenuated. To account for nonuniformity

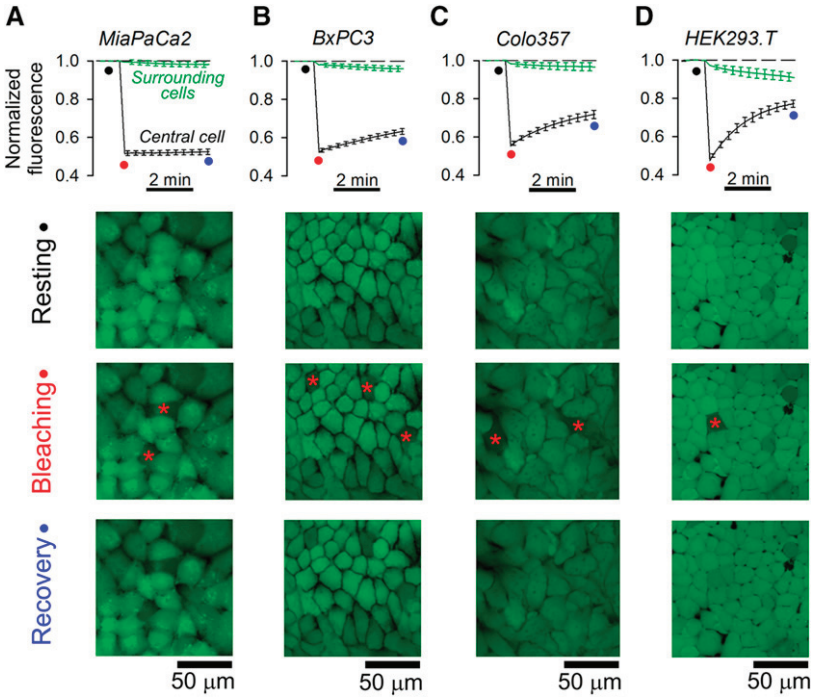


Figure 2. Characterizing junctional coupling in monolayers. Confluent monolayers were loaded with the diffusible cytoplasmic marker calcein. Cell-to-cell diffusive coupling was then measured by fluorescence recovery after photobleaching on monolayers of MiaPaCa2 (*A*), BxPC3 (*B*), Colo357 (*C*), and HEK293.T cells (*D*). Fluorescence in a central cell, indicated by asterisks (1–3 areas/field of view), was bleached to 50%, and the subsequent rate of signal recovery reports degree of coupling (*i.e.*, entry of calcein from neighboring cells). To correct for dye leakage, time courses were normalized to signal averaged in 5 remote cells elsewhere in the field of view. Note that fluorescence recovery in the central cell is associated with a decrease in signal measured in neighboring cells. Time courses show mean of 20–30 experiments obtained from at least 5 independently grown monolayers. Exemplar images of calcein fluorescence are shown below time courses.

Downloaded from www.fasebj.org to IP 129.67.119.187.

of fluorescence, spheroids were coloaded with Hoechst 33342, an oxygen-insensitive dye that penetrates spheroids passively. Hypoxic gradients were thus expressed as the ratio of fluorescence emitted by the hypoxic probe and by Hoechst, as a function of radial depth. Dual excitation/dual emission imaging was performed on spheroids superfused with normoxic buffer bubbled with 21% O_2 (**Fig. 3*Ai***). Paired experiments were performed under superfusion with hypoxic buffer bubbled with 100% N_2 and containing 1 mM dithionite, an oxygen scavenger, to confirm the hypoxic probe's responsiveness (Fig. 3*Aii*). Spheroids grown for longer periods produced more attenuated Hoechst fluorescence at the core (Fig. 3*Bi*, 3*Bii*), consistent with greater cell–cell packing. The hypoxic probe/Hoechst ratio reported a smooth pO_2 gradient that was steepest with +3-d spheroids, reaching a ratio that was 4-fold greater at the core, when compared with the normoxic rim (Fig. 3*Ci*). In hypoxic superfusates, the fluorescence ratio increased, confirming the dye's sensitivity (Fig. 3*Cii*). Of note, the ratio at the core of spheroids in normoxic superfusates reached the same level as that at the rim of spheroids imaged in hypoxic superfusates. Subsequent experiments for characterizing acid-handling were performed with +3-d spheroids, because these support substantial pO_2 gradients over a distance of ~100 μm, indicative of significant diffusional barriers.

Carbonic buffer greatly improves acid handling at the hypoxic core of tissue growths

In monolayers superfused with 5% CO_2/22 mM HCO_3^- buffer, the resting pH_i of Colo357 cells was 7.35 (variance 0.003, 109 cells from 4 monolayers) in normoxic incubation and only marginally different (7.33; variance 0.001, 92 cells from 4 monolayers), after 48 h of incubation with 1 mM DMOG to stabilize hypoxic signaling. In tissues, however, hypoxic regions tend to accumulate acidity as a result of

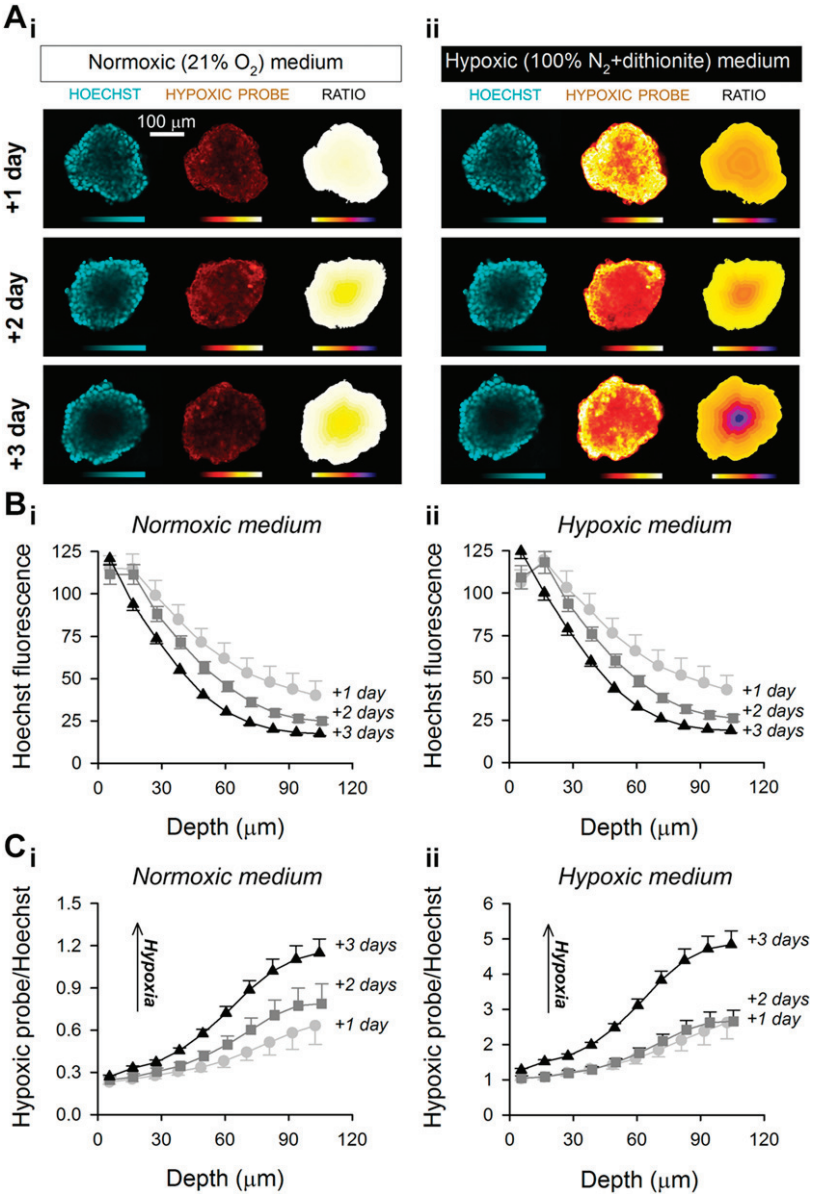


Figure 3. Gradients of O_2 in Colo357 spheroids. *A*) Spheroids were seeded by the hanging drop method and then transferred for growth in suspension for 1–3 d. Spheroids were collected at 1, 2, or 3 d, coloaded with Hoechst 33342 and a hypoxic probe, and imaged during superfusion. Images of Hoechst fluorescence (relates to compactness of spheroid) and hypoxic probe fluorescence (inversely related to O_2 tension) were measured in normoxic medium equilibrated with air (*Ai*) and medium bubbled with 100% N_2 and containing the oxygen-scavenger sodium dithionite [(*Aii*); 1 mM]. *B*) Radial profiles of Hoechst fluorescence in normoxic (*Bi*) and hypoxic (*Bii*) superfusates. Radial profiles of the hypoxic probe/Hoechst fluorescence ratio (inversely proportional to O_2) in normoxic (*Biii*) and hypoxic (*Biv*) superfusates. Mean ± SEM of 7, 12, and 16 spheroids collected at d 1, 2, and 3, respectively.

Downloaded from www.fasebj.org to IP 129.67.119.187. *The FASEB Journal* Vol., No. , pp:, October, 2017

long diffusion distances. The acid-handling mechanisms operating at the hypoxic core of tissue growths were investigated by measuring the pH_i response to a sustained and localized acid-loading that mimicked an elevated glycolytic rate. H^+ ions were uncaged photolytically at the core of Colo357 spheroids at intervals of every 0.73 s from NVA (500 μM), a membrane-permeable photolabile H^+ donor (Fig 4*A*). At 500 μM, this donor is less toxic than a previously used compound, 2-nitrobenzaldehyde, and can produce an equally high H^+ yield with a less damaging wavelength (405 *vs.* 361 nm) (24) (Supplemental Fig. S1*A*, *B*). By means of regional laser scanning, uncaging was restricted to a centrally positioned circular area of diameter equal to 1/10th of the spheroid diameter (**Fig. 4*Ai***, inset). Between uncaging events, pH-sensitive fluorescence (cSNARF1) was captured confocally across the equatorial plane of the spheroid and reported as $[H^+]_i$ time courses in 10 concentric ROIs of width equal to 1/10th of the spheroid diameter (the innermost ROI was also the uncaging area).

In the absence of CO_2/HCO_3^- (replaced with 20 mM HEPES), H^+ uncaging produced a saturating increase in $[H^+]_i$ that spread radially (Fig. 4*Ai*). Under this buffering regime, acid-extrusion across Colo357 cell membranes is very low (<1 mM/min over the relevant pH_i range; Fig. 1*Eiii*); therefore, the rate of acid injection by photolysis at the hypoxic core (J_{inj}) can be estimated from the product of pH_i change and β_i, integrated across the spheroid. J_{inj} was thus calculated to be 20.6 ± 1.2 mM/min over the 4 min uncaging protocol, which is within the range of lactic acid production rates reported in PDAC cells (6, 7). Repeating this uncaging protocol in spheroids superfused with CO_2/HCO_3^- buffer resulted in a substantially reduced $[H^+]_i$ response (Fig. 4*Aii*), as demonstrated by a 2.5-fold smaller radial $[H^+]_i$ profile measured at 4 min of uncaging (Fig. 4*Aiii*). This effect on cytoplasmic $[H^+]$ is intuitively explained by the provision of additional buffering. [Note that of CO_2/HCO_3^- did not meaningfully affect starting pH_i (Supplemental Fig. S2*A*).] However, at H^+-uncaging rates of ~20 mM/min, $[HCO_3^-]_i$ in hypoxic cells would become depleted in ~1 min, unless levels were restored by a source of HCO_3^- ions. The persistence of carbonic buffering is illustrated in Fig. 4*Aiv*, which compares the time course of H^+ ion titration onto intrinsic and carbonic buffers during photolysis (Eq. 1).

As a result of metabolic acid production, and similarly during H^+ uncaging, the spheroid's extracellular compartment also acidifies. Since low pH_e inhibits acid-extrusion from cells (15), extracellular acidification is likely to affect cytoplasmic acid-handling at the spheroid core. To measure the pH_e response, the H^+-uncaging protocol was performed on spheroids superfused with the membrane-impermeable pH-dye, FS, which is quenched at low pH_e (30) (Supplemental Fig. S1*C*). The FS fluorescence time courses, shown in Fig. 4*B*, were normalized to starting fluorescence to show changes in pH_e at different distances from the uncaging site (note the inverted *y* axis). During H^+ uncaging, the FS signal at the core decreased substantially (Fig. 4*Bi*), and this response was only modestly affected by total CA inhibition (100 μM ATZ; Fig. 4*Bii*; 2-way ANOVA: $P = 0.0015$ for effect of ATZ, and $P < 10^{-10}$ for effect of depth). CA inhibition resulted in a very modest steepening of the radial pH_e profile, which is consistent with weakened CO_2/HCO_3^- buffering (30). However, the small magnitude of the ATZ effect argues that catalytic activity is not greatly rate limiting and that spontaneous kinetics are sufficient to maintain carbonic buffering near equilibrium. The decline in FS signal was not related to photobleaching of the dye (Supplemental Fig. S1*D*). According to a calibration curve (Supplemental Fig. S1*C*), pH_e at the core was estimated to have fallen significantly (by >1 U; Fig. 3*Biii*). This pH_e response can be explained by local depletion of extracellular $[HCO_3^-]$, but also by accumulation of CO_2, the product of titration. However, CO_2 is not expected to be retained appreciably, because this gas diffuses more freely than the electrically charged HCO_3^- anions. To confirm this, CO_2 diffusivity was investigated in cSNARF1-loaded spheroids by measuring the time delays in pH_i responses to a step change in superfusate pCO_2 (Fig. 4*Ci*) (35). The delay in the pH_i response at the core was <4 s (Fig. 4*Ciii*), arguing for rapid CO_2 diffusivity.

To summarize, Colo357 spheroids have mechanisms for supplying a flux of HCO_3^- ions to the cytoplasm of hypoxic core, sufficient to maintain carbonic buffering power during sustained acid loading. This restorative flux was ~10 mM/min, as half of the uncaged H^+ ions were titrated onto carbonic buffer (Fig. 4*Aiv*). The major pipelines that may carry this flux are 1) uptake of extracellular HCO_3^- by transporters including NBCe1 and 2) cell-to-cell transmission of HCO_3^- *via* connexin channels from remote cells that actively import HCO_3^- ions (Fig. 4*D*). However, NBCe1 activity probed in monolayers near resting pH_i was only modest (<2 mM/min in the range pH_i >6.9; Fig. 1*Eiii*); moreover, the low pH_e attained during H^+ uncaging inhibits Na^+-HCO_3^- cotransport and depletes its substrate (15). These observations argue that direct extracellular HCO_3^- uptake alone may not provide an adequate flux under the conditions studied. The capacity of the connexin-dependent pipeline to restore $[HCO_3^-]_i$ in hypoxic regions was evaluated by studying the effects of pharmacological inhibition and genetic ablation of connexin43, the principal connexin isoform in Colo357.

Cells at the spheroid core obtain HCO_3^- ions from the normoxic rim *via* connexin channels

The magnitude of transcellular HCO_3^- flux reaching the cytoplasm of the spheroid core *via* connexin43 channels was interrogated from the effects of pharmacological inhibition (100 μM carbenoxolone, CBX) and knockdown of *GJA1*, the gene coding for connexin43 protein. [Unlike genetic knockdown, treatment with CBX produces a modest acidification of starting pH_i, which may relate to the partial inhibitory effect of CBX on lactate efflux on MCT (23) (Supplemental Fig. S2*A*)]. In the absence of CO_2/HCO_3^- (replaced with HEPES) treatment with CBX did

Downloaded from www.fasebj.org to IP 129.67.119.187.

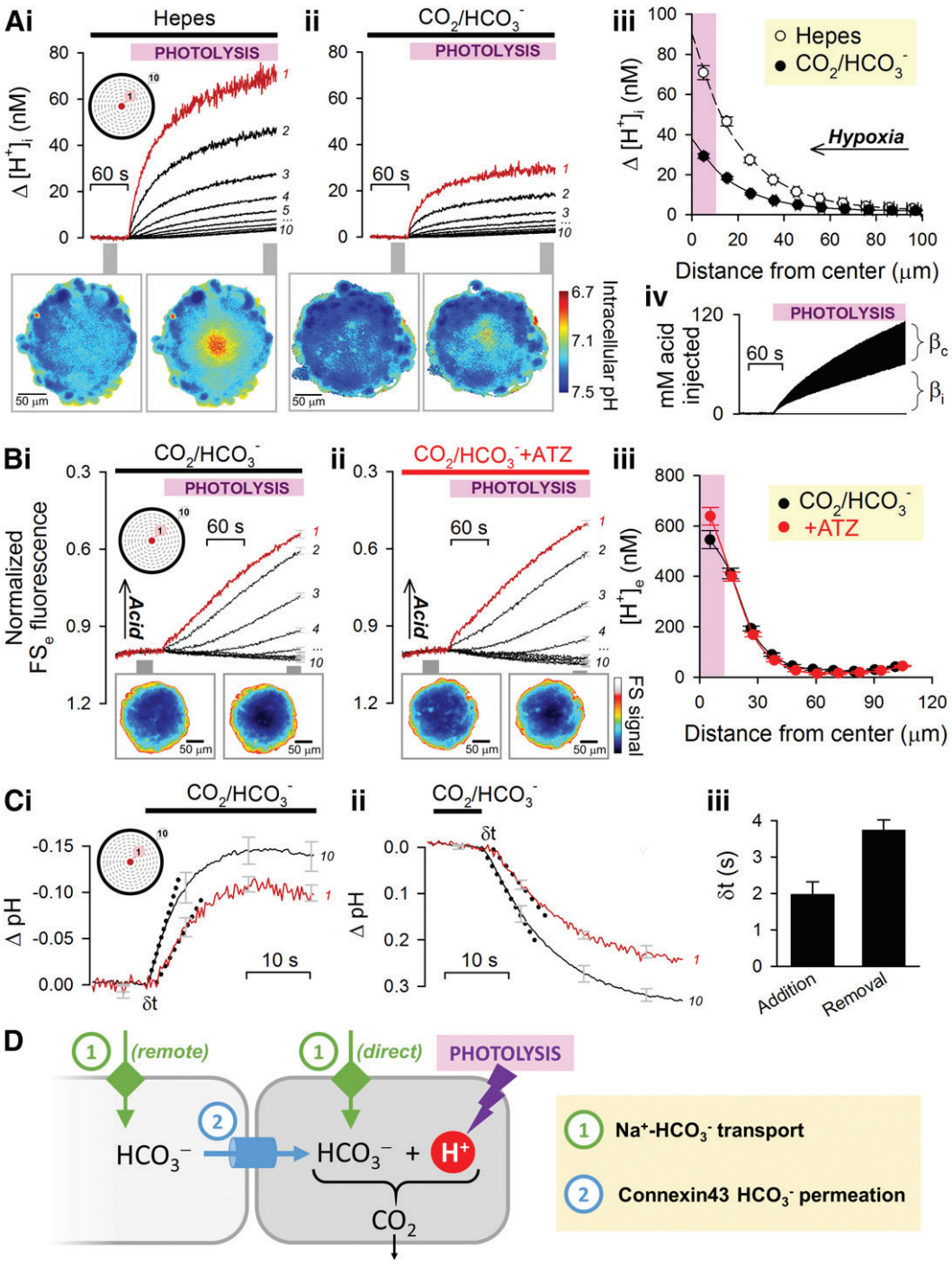


Figure 4. Acid handling in Colo357 spheroids. *A*) Time course of $[H^+]_i$ in the equatorial plane of cSNARF1-loaded Colo357 spheroids, reported in 10 regions (inset), during photolytic H^+ uncaging (0.5 mM NVA) under superfusion with HEPES (*Ai*; mean ± SEM of 22 spheroids) or CO_2/HCO_3^- buffer (*Aii* mean ± SEM of 25 spheroids). Pink bar indicates the period over which photolysis was repeated every 0.73 s to produce cumulative H^+ loading. Colored images through the equatorial plane of spheroids show the distribution of H^+ ions before and after 4 min of uncaging. *Aiii*) Radial profile of $[H^+]$ after 4 min of uncaging. *Aiv*) Calculated time course of uncaged H^+ ions titrated onto CO_2/HCO_3^- (β_c) and intrinsic (β_i) buffers. *B*) Colo357 spheroid superfused with FS (30 μM) to report pH_e. *Bi*) Time course of extracellular acidification during photolytic H^+ uncaging; repeated in ATZ (*Bii*). Colored images through the equatorial plane of spheroids show the distribution of FS fluorescence before and after 4 min of uncaging. *Biii*) Radial $[H^+]_e$ profile after 4 min of uncaging (mean ± SEM of 25 spheroids). *C*) pH_i response in cSNARF1-loaded Colo357 spheroid to addition (*Ci*) and removal (*Cii*) of CO_2/HCO_3^-. Delay (δt) in pH_i response at spheroid core relative to periphery (mean ± SEM of 25 spheroids). *D*) Supply routes for maintaining carbonic buffering capacity during photolytic H^+ uncaging.

not affect the time course (**Fig. 5*Ai***) nor the radial $[H^+]_i$ profile measured after 4 min of uncaging (Fig. 5*Aii*). These results indicate that the flow of noncarbonic (*i.e.*, intrinsic) buffers, such as dipeptides or phosphates, through connexin43 channels is not sufficient to meaningfully reduce the build-up of acidity at the hypoxic core. However, in the

Downloaded from www.fasebj.org to IP 129.67.119.187. *The FASEB Journal* Vol., No. , pp:, October, 2017

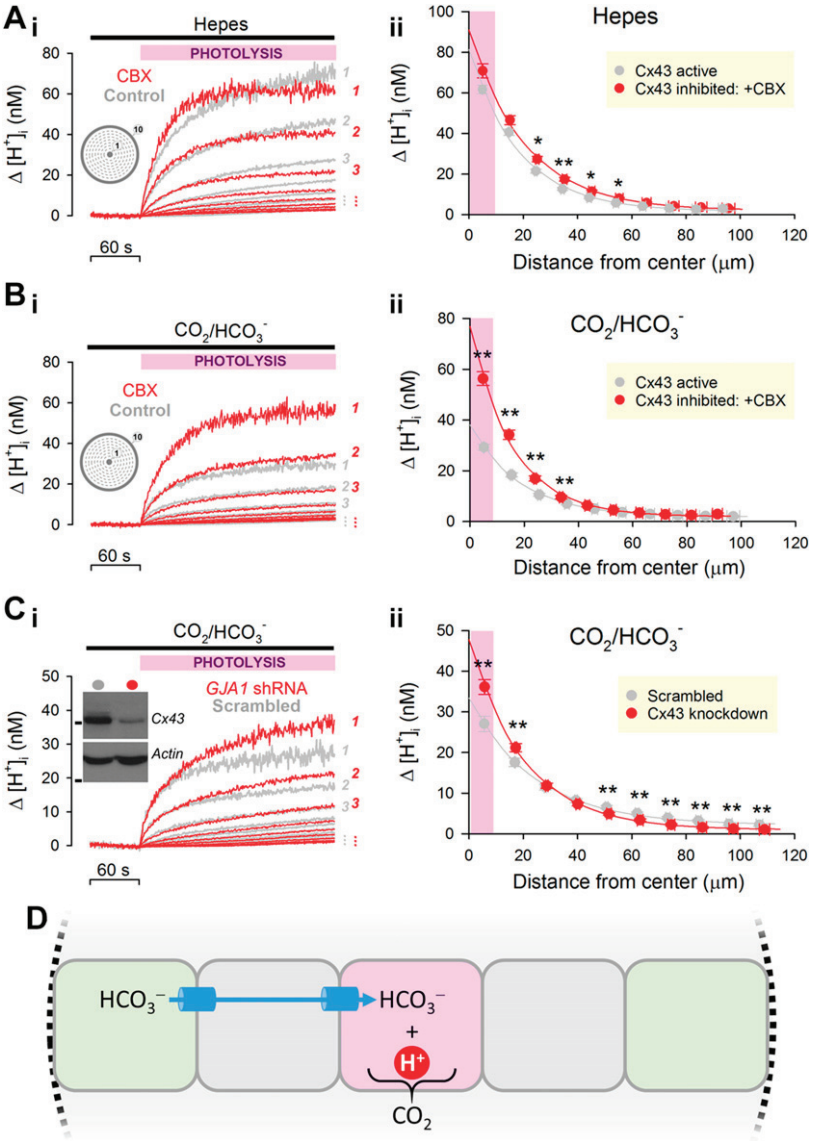


Figure 5. Assessing connexin-mediated HCO_3^- traffic in Colo357 spheroids. *Ai*) Time course of $[H^+]_i$ in 10 layers of cSNARF1-loaded spheroid, superfused in HEPES (CO_2/HCO_3^--free) buffer, in the absence (gray; data from Fig. 4*Ai*) and presence (red; mean ± SEM of 25 spheroids) of connexin-blocker CBX (100 μM). *Aii*) Radial $[H^+]_i$ profile after 4 min of uncaging. *B*) Experiment repeated in CO_2/HCO_3^- buffer. Time course of $[H^+]$ in 10 layers of Colo357 spheroids (*i*) and radial profile (*ii*) after 4 min of uncaging in absence (data from Fig. 4*Aii*) or presented (red; mean ± SEM of 24 spheroids) of CBX. Significant increase in cytoplasmic retention at core under connexin inhibition. *C*) Experiment performed on *GJA1* (connexin43-coding gene) knockdown spheroids (red; mean ± SEM of 25 spheroids) and scrambled controls (gray; mean ± SEM of 25 spheroids) in CO_2/HCO_3^- buffer. Time course of $[H^+]$ (*i*) and radial profile (*ii*) after 4 min of uncaging. Inset: Western blot for connexin43; knockdown efficiency, based on densitometric analyses of 3 blots, was 70%. Significant increase in cytoplasmic retention at core under connexin knockdown. $^*P < 0.05$, $^{**}P < 0.01$ (Student's *t* test with Bonferroni correction). *D*) Connexin43 channels (blue) provide a delivery route for intracellular HCO_3^- ions for neutralizing photolytically uncaged H^+ ions at the hypoxic core (shaded pink).

presence of physiologic CO_2/HCO_3^-, connexin43 inhibition with CBX (Fig. 5*B*) or its genetic ablation with shRNA (Fig. 5C) resulted in a substantial increase in cytoplasmic H^+ ion retention at the spheroid core during photolytic H^+ uncaging. Thus, the capacity of carbonic buffer to titrate a sustained metabolic acid load is attainable fully when connexin channels allow a restorative entry of HCO_3^- ions into cells at the hypoxic core (Fig. 5*D*).

Ultimately, the HCO_3^- ions that diffuse through connexin channels must be imported into the syncytial cytoplasm by membrane transport (Fig. 4*D*). From a thermodynamic viewpoint, the most favorable site for HCO_3^- uptake is at the normoxic rim, where good diffusive coupling maintains an ample supply of extracellular HCO_3^- and an alkaline pH_e which activate transporters such as NBCe1 (15). An analysis of the sensitivity to DIDS was performed to identify the location, within a spheroid, where cellular HCO_3^- uptake takes place during photolytic H^+ uncaging. In previous experiments on spheroids (15), we have shown that NBC activity, evoked by intracellular acidosis, can be blocked by DIDS, indicating that this drug is able to access the spheroid core.

In the absence of connexin coupling, DIDS-sensitive transmembrane uptake is the only plausible source of HCO_3^- for cells at the hypoxic core. However, in CBX-decoupled spheroids (100 μM), DIDS (150 μM) did not affect cytoplasmic $[H^+]$ during the photolytic protocol (**Fig. 6*Ai***) [DIDS did not meaningfully affect starting pH_i (Supplemental Fig. S2*B*)]. This result confirms that transporters, including NBCe1, at the hypoxic core are unable to generate an adequate uptake of HCO_3^- ions for neutralizing a sustained acid loading. As confirmation that uncaged H^+ ions are titrated onto carbonic buffer, inhibition of CA isoforms (with 100 μM ATZ) increased cytoplasmic $[H^+]$, as expected from a slowing of the reaction between HCO_3^- and H^+ ions (Fig. 6*Aii*) [ATZ produced a modest acidification of starting pH_i, which reflects the inactivation of CA-assisted CO_2 diffusion (36) (Supplemental Fig. S2*B*)]. The absence of a significant effect of DIDS on the radial $[H^+]$ profile was also observed in spheroids made of *GJA1* knockdown cells [*i.e.*, with genetically ablated coupling (Fig. 6*Aiii*)]. To summarize, DIDS, a drug that potently blocked secondary active HCO_3^- uptake into Colo357 monolayers (Fig. 1*Eiii*), had no effect on $[H^+]_i$

Downloaded from www.fasebj.org to IP 129.67.119.187.

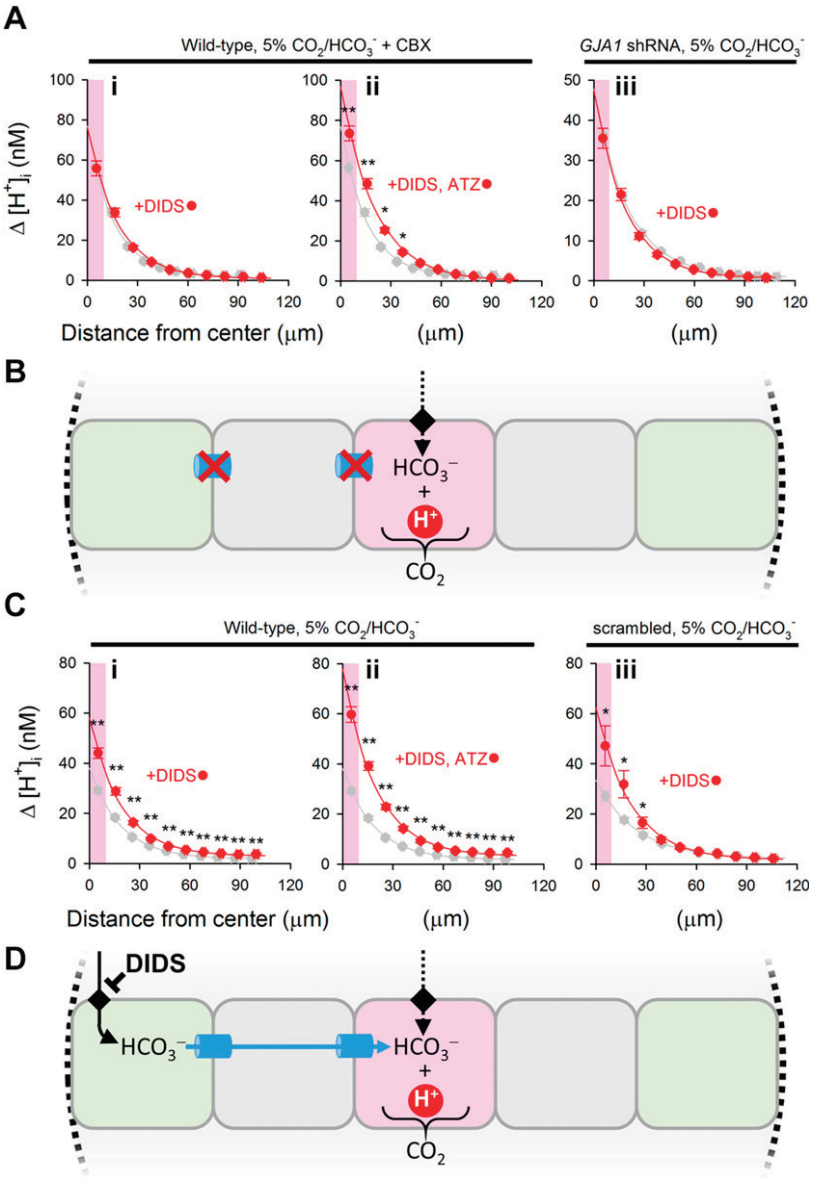


Figure 6. Interrogating the source of HCO_3^- ions for neutralizing cytoplasmic acidity at the hypoxic core of Colo357 spheroids. *A*) Radial $[H^+]_i$ profiles after 4 min of uncaging in uncoupled Colo357 spheroids. Gray traces are data from Fig. 5*Bii, Cii. Ai*) CBX-treated wild-type spheroids, showing lack of effect of 150 μM DIDS (blocks HCO_3^- uptake; mean ± SEM of 27 spheroids) but significant effect of 100 μM ATZ (blocks carbonic anhydrases; mean ± SEM of 39 spheroids) (*ii*). *Aiii*) *GJA1* knockdown spheroids, showing lack of effect of DIDS (mean ± SEM of 13 spheroids). Significant increase in cytoplasmic retention at core with ATZ. *B*) DIDS does not affect cytoplasmic $[H^+]$ retention at the hypoxic core of uncoupled spheroids, indicating that cellular HCO_3^- uptake at the core is ineffective. *C*) Radial $[H^+]_i$ profiles after 4 min of uncaging in connexin-coupled Colo357 spheroids. Gray traces are data from Fig. 5*Bii, Cii. Ci*) Wild-type spheroids, showing the effect of 150 μM DIDS (mean ± SEM of 19 spheroids) and (*Cii*) additional effect of 100 μM ATZ (mean ± SEM of 29 spheroids). *Ciii*) Scrambled control spheroids, showing effect of DIDS (mean ± SEM of 14 spheroids). Significant increase in cytoplasmic retention at core with application of DIDS±ATZ. *D*) DIDS increased cytoplasmic $[H^+]$ retention at the hypoxic core in connexin-coupled spheroids only, indicating that cellular HCO_3^- uptake takes place more peripherally, followed by transmission though connexin channels (blue).

responses at the hypoxic core of connexin-decoupled spheroids during photolytic H^+ uncaging. This finding argues for only a limited effectiveness of HCO_3^- transporters, such as NBCe1, at the spheroid core to regulate pH_i, which can be explained by the inhibitory effect of extracellular acidosis on Na^+-HCO_3^- cotransport (15).

In connexin-coupled spheroids, transmembrane HCO_3^- uptake into cells at the normoxic rim can provide a source of HCO_3^- ions destined for the hypoxic core. According to this model, sensitivity to DIDS would be manifested only in connexin-coupled spheroids. Indeed, during sustained acid-loading, cytoplasmic H^+ retention at the hypoxic core was elevated in the presence of 150 μM DIDS applied to connexin-coupled spheroids (Fig. 6*Ci*). A further increase in cytoplasmic H^+ retention was observed by slowing carbonic buffering kinetics with ATZ (Fig. 6*Cii*). [ATZ produced a modest acidification of starting pH_i (Supplemental Fig. S2*B*).] DIDS also increased cytoplasmic H^+ retention in spheroids transduced with scrambled shRNA [*i.e.*, cells that retain connexin43 coupling (Fig. 6*Ciii*); the control for the experiment in Fig. 6*Aiii*)]. A comparison of these results with the DIDS insensitivity observed in connexin-decoupled spheroids (Fig. 6*A*) indicates that secondary active Na^+-HCO_3^- cotransport takes place principally at the spheroid rim [*i.e.*, the least environmentally stressed region (Fig. 6*D*)].

Modeling the ATP-cost of secondary active transport of HCO_3^- ions

By obtaining HCO_3^- ions passively from normoxic neighbors *via* connexins, cells at the hypoxic core are able to conserve ATP resources that would have otherwise been consumed for direct secondary active Na^+-HCO_3^- cotransport. To estimate the magnitude of this ATP economy, the energetic cost of HCO_3^- uptake by NBCe1 was calculated by performing a "balance of fluxes" analysis, as shown in **Fig. 7*A***. At steady-state, in a cell that produces H^+ and lactate ions

Downloaded from www.fasebj.org to IP 129.67.119.187. *The FASEB Journal* Vol., No. , pp:, October, 2017

at a rate J_{met}, HCO_3^- influx on NBC must equal the passive entry (leak) of H^+ ions across the surface membrane (J_{leak}) plus the flux of metabolically generated H^+ ions that is not exported by MCT ($\alpha \cdot J_{met}$). If the cell's entire output of lactate were exported by MCT, scalar α would equal 0 and secondary active transport would be required to balance J_{leak}. In contrast, if lactate were catabolized or exported by an H^+-independent mechanism [*e.g.*, *via* connexin43 channels (23)], a greater secondary active transport flux would be necessary. J_{met} was taken to be 15 mM/min, the midpoint of the range of lactate production rates measured in PDAC cells (6, 7). To calculate J_{leak}, passive membrane permeability to H^+ ions (P_H) was measured in Colo357 cells (radius 8.78 ± 0.08 μm, surface area:volume ratio ρ = 0.342 μm^{-1}) that were dissociated from monolayers and superfused with solutions that block endogenous lactic acid production (glucose replaced with galactose) and inhibit membrane pH-regulatory transport (Cl^- replaced with gluconate, CO_2/HCO_3^- replaced with HEPES, and 30 μM DMA added to block Na^+/H^+ exchange). Exchanging solution at pH 7.4 for one at pH 6.4 evoked an intracellular acidification (Fig. 7*B*) that gave a readout of P_H according to the equation (where buffering capacity β was calculated from Fig. 1*B* at the point of solution exchange) (Eq. 2):

$$P_H = \frac{\beta \times \left(\frac{\delta pH_i}{\delta t}_{baseline} - \frac{\delta pH_i}{dt}_{evoked}\right)}{\rho \times (10^{-pH_e} - 10^{-pH_i})} \quad (2)$$

P_H was thus estimated to be 303 ± 5 μm/s. Given that the Na^+/K^+ ATPase consumes 1 ATP molecule for every 3 Na^+ ions exported, the cost of HCO_3^- uptake by NBCe1 (2 × HCO_3^- ions imported with Na^+) can be modeled as a function of pH_e, as shown in Fig. 7*C*. For cells in acidic niches, these ATP consumption rates are a significant fraction of the glycolytic yield, estimated to supply ~15 mM ATP/min (based on 1 ATP per lactate produced).

DISCUSSION

Metabolism is interwoven with pH_i homeostasis because its end-products are acidic. Continuously generated metabolic acids would eventually saturate all intracellular buffering moieties (15), including CO_2/HCO_3^- and intrinsic buffers, unless there is a mechanism for restoring the concentration of their weakly basic form. Indeed, HCO_3^- uptake by secondary active transport is generally recognized as a major pH_i regulatory mechanism in many types of cells. CO_2, the product of HCO_3^- titration, is a highly membrane-permeant gas (35), making CO_2/HCO_3^- a versatile choice of buffer for cellular pH homeostasis. Because CO_2/HCO_3^- is an open buffer system, fine tuned by the lungs and kidneys, it is in ample supply in the blood *in vivo*. Functional evidence for HCO_3^- uptake and for the underlying proteins has been established firmly in many types of cancer cells, including PDAC (8, 37). Moreover, at least some genes coding for HCO_3^- transporters are induced by tumor hypoxia (10). Our flux analyses on PDAC monolayers (Fig. 1*E*) show that HCO_3^--dependent transporters generate an acid-extrusion flux that is ~4 times greater than the flux produced by HCO_3^--independent transporters, such as NHE. This observation is consistent

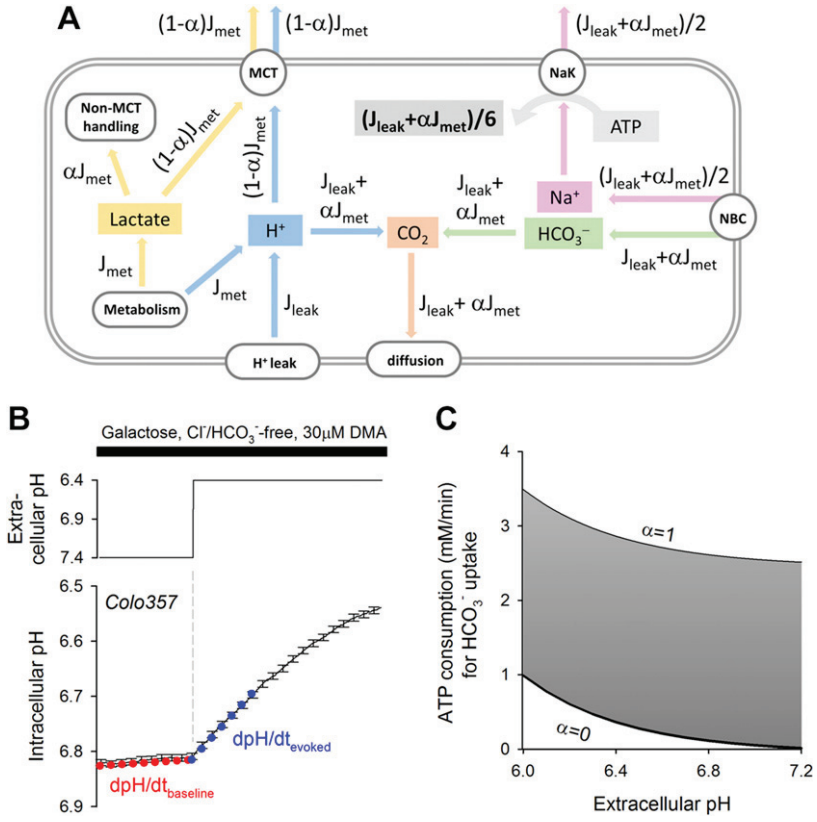


Figure 7. Modeling the ATP cost of HCO_3^- uptake by secondary active transport. *A*) Fluxes related to H^+ ions. Glycolytic metabolism produces an equimolar flux of lactate and H^+ ions. A fraction (1 − α) of lactate flux is exported, together with an equal flux of H^+ ions, by MCT. The remainder (α) of lactate is handled by other mechanisms, such as further catabolism or H^+-independent efflux (*e.g.*, transmission *via* connexin channels). An addition influx of H^+ ions arises from passive leak across the membrane (J_{leak}). Assuming that the NBCe1 is the major pH-regulatory mechanism, a HCO_3^- flux of J_{leak} + ($\alpha \cdot J_{met}$) is necessary to neutralize the H^+ flux. Assuming 1 Na^+:2 HCO_3^- stoichiometry of NBCe1 and a 3Na^+/ATP coupling of the Na^+/K^+ pump, the ATP consumption rate is modeled as [J_{leak} + ($\alpha \cdot J_{met}$)]/6. *B*) J_{leak} was measured experimentally from the rate of pH_i change, evoked by changing extracellular pH from 7.4 to 6.4, under conditions that minimize pH regulation (Cl^- and HCO_3^- replaced with gluconate and HEPES, respectively; 30 μM DMA blocked residual Na^+/H^+ exchange) and lactic acid production (glucose replaced with galactose). *C*) ATP consumption as a function of extracellular pH, modeled with measured values of J_{leak} and J_{met} for a range of values for α.

Downloaded from www.fasebj.org to IP 129.67.119.187.

with high expression levels of proteins such as NBCe1 in HCO_3^--secreting pancreatic ducts. Although NHE1 plays a smaller role in regulating bulk pH_i, it may serve specialized roles, for example, in the context of epidermal growth factor signaling (38). However, the downside of secondary active transport is that it requires an input of energy. With respect to the overarching importance of HCO_3^- uptake for tissue pH_i homeostasis, the present findings are in agreement with a previous study performed on spheroids that lack gap junctions (15). A key difference is that in junctionally coupled tissues (described herein), cells at the hypoxic core can obtain HCO_3^- ions passively from normoxic neighbors, which thereby take on the energetic burden of the additional active HCO_3^- uptake. In contrast, junctionally uncoupled tissues are unable to support such an altruistic relationship between cells.

A stable supply of ATP is necessary for the various biological functions performed by cancer cells. Somewhat counterintuitively, many cancer cells, including PDAC cells (Fig. 1*A*), are reprogrammed to rely on glycolytic metabolism which is a low-yielding means of harnessing energy from carbohydrates, although it has the advantage of making cells more resistant to hypoxia. Finite energetic resources force cancer cells to rationalize energy utilization (39), either by austerity, such as by inactivating certain biologic functions of the precursor cells (*e.g.*, epithelial transport), by favoring cost-effective alternatives, or by exploiting other cells, such as stromal cells. Among the many activities of cells, pH_i homeostasis must be prioritized because the acidic end-products of metabolism can rapidly accumulate in underperfused tumors, and proper cellular function is compatible with only a narrow band of pH_i in the alkaline range. The present findings show that Colo357 cells at the core of tissue growths can regulate their pH_i by sourcing chemical base (HCO_3^- ions) from neighboring cells by means of passive diffusion through connexin channels (Fig. 6*D*). In connexin-coupled tumors, which occur in at least some types of pancreatic cancers (23, 25, 26), the magnitude of this HCO_3^- pipeline can be sufficient to titrate excess acidity and maintain pH_i homeostasis in hypoxic regions (Figs. 4–6). The survival advantage of this arrangement is that it operates at no ATP cost to the environmentally stressed hypoxic cells. The significance of this ATP economy can be estimated from the anticipated cost of secondary active HCO_3^- transport, if it were solely responsible for pH_i regulation. According to the model presented in Fig. 7, maintaining pH_i at 7.3 in a microenvironment of pH_e 6.5 would require between ~2% (0.3 mM ATP/min) and 20% (3 mM ATP/min) of the glycolytic yield, depending on the fraction of lactate extruded by MCT. To put this range in a biological context, the replication of 3×10^9 bp of the human genome requires 5 fmol of deoxynucleoside trisphosphate in a cell of volume 3570 fl and is equivalent to merely several minutes of secondary active HCO_3^- transport activity. Thus, the ATP economy offered by connexin-mediated HCO_3^- entry can meaningfully increase energetic resources for rapidly proliferating cells in hypoxic niches.

From a whole-tissue perspective, transmission of HCO_3^- ions through connexin channels does not eliminate the requirement for secondary active HCO_3^- transport because, ultimately, these ions must be sequestered elsewhere in the cytoplasmic syncytium (Fig. 4*D*). In effect, connexin coupling transfers secondary active transport responsibility from environmentally stressed cells in hypoxic niches onto the more normoxic regions, where this process is a lesser energetic burden thanks to better substrate (HCO_3^-, O_2, and glucose) availability. Normoxic cells thus demonstrate metabolic altruism by committing their energetic resources to HCO_3^- uptake for the purpose of remotely regulating the pH_i of hypoxic cells. By extension of the conventional nomenclature describing transport processes as being primary or secondary active, this study makes a case for a distinct category of remote transport, in which proteins of one cell serve a homeostatic function for another.

Our observations were made by applying a novel approach to investigating the mechanisms of metabolic acid-handling in tumor growths. The methodology was designed to introduce a pH challenge that resembles, in as much as possible, the key characteristics of metabolic acid-loading in cancer cells and thereby ensures that physiologically relevant responses were being elicited (Fig. 3*A*, *B*). By triggering a sequence of H^+ uncaging events with light energy, a near-constant metabolic acid load was applied to the hypoxic core of spheroids (Fig. 4*A*). This photolytic protocol generates a weak acid, 6-nitroveratric acid, which ionizes fully at physiological pH and resembles the chemistry of lactic acidosis. The concentration of caged compound (500 μM) and photolytic rate (~1.4 s^{-1}) were adjusted to produce an acid-loading rate that was within the reported range of glycolytic fluxes (8–22 mM H^+ per minute) (6, 7) and of adequate magnitude to evoke resolvable [H^+] dynamics. The balance between photolytically driven H^+ uncaging and the endogenous pH_i-regulatory fluxes approaches a new steady-state that is more representative of the temporal stability of tumor pH. Overall, this approach has major advantages over the more traditional ammonium prepulse method (15), which uniformly reduces pH_i to very acidic levels and then interrogates the acid-handling mechanisms from the dynamic pH_i response, rather than the quasi steady state. The ammonium prepulse technique (15) would fail to fully recognize the importance of cell-to-cell solute exchange because a uniformly evoked cytoplasmic acidosis collapses net fluxes of ions through connexins. In addition, the ammonium prepulse maneuver selectively acidifies the intracellular compartment of tissue growths, which fails to fully replicate the concomitant acid loading of the intra- and extracellular fluids during metabolic acid production. In this respect, the H^+-uncaging protocol evokes a more realistic acid-base disturbance.

Adaptations that reduce the overall energetic burden of pH_i homeostasis would be positively selected for during the process of somatic evolution. Such selection may be observed in the induction of the connexin43-coding gene *GJA1* by hypoxia in BxPC3 cells or the emergence of connexin43-positive

Downloaded from www.fasebj.org to IP 129.67.119.187. *The FASEB Journal* Vol., No. , pp:, October, 2017

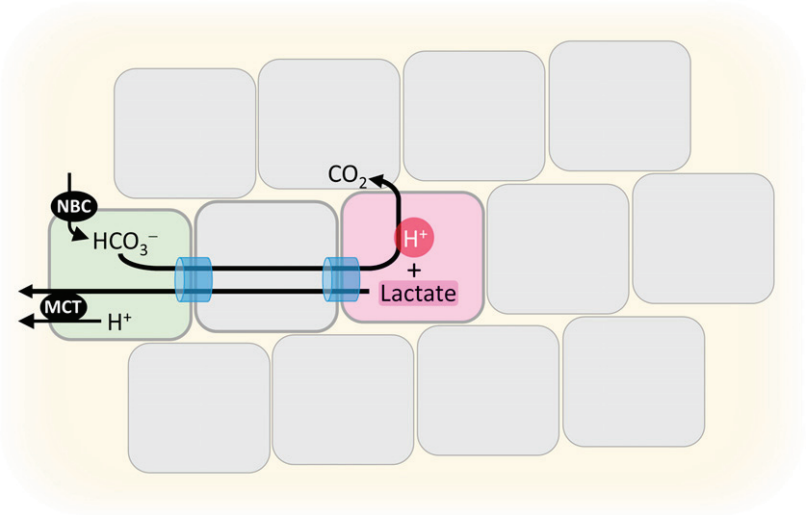


Figure 8. Integrated model of acid-base traffic through connexin channels in junctionally coupled tumors. Glycolytic metabolism in cells (shaded pink) at the hypoxic core of a tumor growth produces equimolar quantitites of H^+ and lactate ions. Connexin-assembled gap junctions (blue cylinders) transmit lactate anions down a concentration gradient toward normoxic cells (shaded green), where lactate is offloaded by MCT, together with an H^+ ion. Gap junctions also conduct a counter-flux of HCO_3^- ions, down a gradient between alkaline cells at the rim and acidic cells at the core, maintained by a continuous uptake of HCO_3^- into the former and chemical titration in the latter. HCO_3^- ions delivered to cells at the hypoxic core neutralize H^+ ions produced by glycolytic metabolism. Note that H^+ ions are heavily buffered in the syncytial cytoplasm and are therefore unable to freely diffuse through gap junctions. Ultimately, active HCO_3^- transport in normoxic cells regulates the pH_i of hypoxic cells, and supports lactate venting *via* connexin channels.

MiaPaCa2 cells in areas of invasion and metastasis (23), as well as a general induction of connexin-coding genes in metastasizing PDAC cells *in vivo* (25, 26). Furthermore, the shift from transmembrane to transcellular HCO_3^- provision would be accentuated by the inhibitory effect of low pH_e on HCO_3^- uptake transporters (15). The results of this study describe a novel role for connexin channels and explain how cell-to-cell coupling can produce a favorable phenotype under environmental stress developed in diffusion-limited niches. Combining the present work with our previous findings concerning lactate permeation through connexin43 channels (23), we propose an integrated model of lactic acid handling (**Fig. 8**), in which lactate anions are dissipated from hypoxic cells through gap junctions in exchange for a counterflux of HCO_3^- ions, which titrate H^+ ions coproduced with lactate by glycolytic metabolism. Emergence of this syncytial phenotype may bring resistance to therapies that selectively target secondary active acid-base transporters in hypoxic tumor regions, but could also underpin the therapeutic rationale for blocking connexin43 activity. FJ

ACKNOWLEDGMENTS

This work was supported by the European Commission through IonTraC Marie Curie Initial Training Network FP7-PEOPLE-2011-ITN Grant 289648, and the Royal Society (to P. S.) and Worldwide Cancer Research Grant 2012/0027 (to P.S. and A.H.). The authors declare no conflicts of interest.

AUTHOR CONTRIBUTIONS

T. H. Dovmark and A. Hulikova performed the research; P. Swietach designed the research and wrote the paper; S. Niederer developed the flux balance model; and all authors contributed to data analysis.

REFERENCES

1. Halbrook, C. J., and Lyssiotis, C. A. (2017) Employing metabolism to improve the diagnosis and treatment of pancreatic cancer. *Cancer Cell* **31**, 5–19
2. Ying, H., Kimmelman, A. C., Lyssiotis, C. A., Hua, S., Chu, G. C., Fletcher-Sananikone, E., Locasale, J. W., Son, J., Zhang, H., Coloff, J. L., Yan, H., Wang, W., Chen, S., Viale, A., Zheng, H., Paik, J. H., Lim, C., Guimaraes, A. R., Martin, E. S., Chang, J., Hezel, A. F., Perry, S. R., Hu, J., Gan, B., Xiao, Y., Asara, J. M., Weissleder, R., Wang, Y. A., Chin, L., Cantley, L. C., and DePinho, R. A. (2012) Oncogenic Kras maintains pancreatic tumors through regulation of anabolic glucose metabolism. *Cell* **149**, 656–670
3. Koong, A. C., Mehta, V. K., Le, Q. T., Fisher, G. A., Terris, D. J., Brown, J. M., Bastidas, A. J., and Vierra, M. (2000) Pancreatic tumors show high levels of hypoxia. *Int. J. Radiat. Oncol. Biol. Phys.* **48**, 919–922
4. Gatenby, R. A., and Gillies, R. J. (2004) Why do cancers have high aerobic glycolysis? *Nat. Rev. Cancer* **4**, 891–899
5. Komar, G., Kauhanen, S., Liukko, K., Seppänen, M., Kajander, S., Ovaska, J., Nuutila, P., and Minn, H. (2009) Decreased blood flow with increased metabolic activity: a novel sign of pancreatic tumor aggressiveness. *Clin. Cancer Res.* **15**, 5511–5517
6. Cheng, G., Zielonka, J., McAllister, D., Tsai, S., Dwinell, M. B., and Kalyanaraman, B. (2014) Profiling and targeting of cellular bioenergetics: inhibition of pancreatic cancer cell proliferation. *Br. J. Cancer* **111**, 85–93
7. Liu, M., Quek, L. E., Sultani, G., and Turner, N. (2016) Epithelial-mesenchymal transition induction is associated with augmented glucose uptake and lactate production in pancreatic ductal adenocarcinoma. *Cancer Metab.* **4**, 19
8. Swietach, P., Vaughan-Jones, R. D., Harris, A. L., and Hulikova, A. (2014) The chemistry, physiology and pathology of pH in cancer. *Philos. Trans. R. Soc. Lond. B. Biol. Sci.* **369**, 20130099
9. Hulikova, A., Harris, A. L., Vaughan-Jones, R. D., and Swietach, P. (2013) Regulation of intracellular pH in cancer cell lines under normoxia and hypoxia. *J. Cell. Physiol.* **228**, 743–752
10. McIntyre, A., Hulikova, A., Ledaki, I., Snell, C., Singleton, D., Steers, G., Seden, P., Jones, D., Bridges, E., Wigfield, S., Li, J. L., Russell, A., Swietach, P., and Harris, A. L. (2016) Disrupting hypoxia-induced bicarbonate transport acidifies tumor cells and suppresses tumor growth. *Cancer Res.* **76**, 3744–3755
11. Kong, S. C., Giannuzzo, A., Novak, I., and Pedersen, S. F. (2014) Acid-base transport in pancreatic cancer: molecular mechanisms and clinical potential. *Biochem. Cell Biol.* **92**, 449–459
12. Lee, M. G., Ohana, E., Park, H. W., Yang, D., and Muallem, S. (2012) Molecular mechanism of pancreatic and salivary gland fluid and HCO3 secretion. *Physiol. Rev.* **92**, 39–74

Downloaded from www.fasebj.org to IP 129.67.119.187.

13. Cruz-Monserrate, Z., Roland, C. L., Deng, D., Arumugam, T., Moshnikova, A., Andreev, O. A., Reshetnyak, Y. K., and Logsdon, C. D. (2014) Targeting pancreatic ductal adenocarcinoma acidic microenvironment. *Sci. Rep.* **4**, 4410
14. Gatenby, R. A., and Gillies, R. J. (2008) A microenvironmental model of carcinogenesis. *Nat. Rev. Cancer* **8**, 56–61
15. Hulikova, A., Vaughan-Jones, R. D., and Swietach, P. (2011) Dual role of CO2/HCO3(−) buffer in the regulation of intracellular pH of three-dimensional tumor growths. *J. Biol. Chem.* **286**, 13815–13826
16. Hulikova, A., Black, N., Hsia, L. T., Wilding, J., Bodmer, W. F., and Swietach, P. (2016) Stromal uptake and transmission of acid is a pathway for venting cancer cell-generated acid. *Proc. Natl. Acad. Sci. USA* **113**, E5344–E5353
17. Hulikova, A., Aveyard, N., Harris, A. L., Vaughan-Jones, R. D., and Swietach, P. (2014) Intracellular carbonic anhydrase activity sensitizes cancer cell pH signaling to dynamic changes in CO2 partial pressure. *J. Biol. Chem.* **289**, 25418–25430
18. Lin, J. H., Takano, T., Cotrina, M. L., Arcuino, G., Kang, J., Liu, S., Gao, Q., Jiang, L., Li, F., Lichtenberg-Frate, H., Haubrich, S., Willecke, K., Goldman, S. A., and Nedergaard, M. (2002) Connexin 43 enhances the adhesivity and mediates the invasion of malignant glioma cells. *J. Neurosci.* **22**, 4302–4311
19. Elzarrad, M. K., Haroon, A., Willecke, K., Dobrowolski, R., Gillespie, M. N., and Al-Mehdi, A. B. (2008) Connexin-43 upregulation in micrometastases and tumor vasculature and its role in tumor cell attachment to pulmonary endothelium. *BMC Med.* **6**, 20
20. Ito, A., Katoh, F., Kataoka, T. R., Okada, M., Tsubota, N., Asada, H., Yoshikawa, K., Maeda, S., Kitamura, Y., Yamasaki, H., and Nojima, H. (2000) A role for heterologous gap junctions between melanoma and endothelial cells in metastasis. *J. Clin. Invest.* **105**, 1189–1197
21. El-Sabban, M. E., and Pauli, B. U. (1991) Cytoplasmic dye transfer between metastatic tumor cells and vascular endothelium. *J. Cell Biol.* **115**, 1375–1382
22. Zhang, A., Hitomi, M., Bar-Shain, N., Dalimov, Z., Ellis, L., Velpula, K. K., Fraizer, G. C., Gourdie, R. G., and Lathia, J. D. (2015) Connexin 43 expression is associated with increased malignancy in prostate cancer cell lines and functions to promote migration. *Oncotarget* **6**, 11640–11651
23. Dovmark, T. H., Saccomano, M., Hulikova, A., Alves, F., and Swietach, P. (2017) Connexin-43 channels are a pathway for discharging lactate from glycolytic pancreatic ductal adenocarcinoma cells. *Oncogene* **36**, 4538–4550
24. Swietach, P., Rossini, A., Spitzer, K. W., and Vaughan-Jones, R. D. (2007) H+ ion activation and inactivation of the ventricular gap junction: a basis for spatial regulation of intracellular pH. *Circ. Res.* **100**, 1045–1054
25. Solan, J. L., Hingorani, S. R., and Lampe, P. D. (2012) Changes in connexin43 expression and localization during pancreatic cancer progression. *J. Membr. Biol.* **245**, 255–262
26. McDonald, O. G., Li, X., Saunders, T., Tryggvadottir, R., Mentch, S. J., Warmoes, M. O., Word, A. E., Carrer, A., Salz, T. H., Natsume, S., Stauffer, K. M., Makohon-Moore, A., Zhong, Y., Wu, H., Wellen, K. E., Locasale, J. W., Iacobuzio-Donahue, C. A., and Feinberg, A. P. (2017) Epigenomic reprogramming during pancreatic cancer progression links anabolic glucose metabolism to distant metastasis. *Nat. Genet.* **49**, 367–376
27. Wykoff, C. C., Beasley, N. J., Watson, P. H., Turner, K. J., Pastorek, J., Sibtain, A., Wilson, G. D., Turley, H., Talks, K. L., Maxwell, P. H., Pugh, C. W., Ratcliffe, P. J., and Harris, A. L. (2000) Hypoxia-inducible expression of tumor-associated carbonic anhydrases. *Cancer Res.* **60**, 7075–7083
28. Kaluz, S., Kaluzová, M., and Stanbridge, E. J. (2003) Expression of the hypoxia marker carbonic anhydrase IX is critically dependent on SP1 activity: identification of a novel type of hypoxia-responsive enhancer. *Cancer Res.* **63**, 917–922
29. Kaluz, S., Kaluzová, M., Chrastina, A., Olive, P. L., Pastoreková, S., Pastorek, J., Lerman, M. I., and Stanbridge, E. J. (2002) Lowered oxygen tension induces expression of the hypoxia marker MN/carbonic anhydrase IX in the absence of hypoxia-inducible factor 1 alpha stabilization: a role for phosphatidylinositol 3′-kinase. *Cancer Res.* **62**, 4469–4477
30. Swietach, P., Patiar, S., Supuran, C. T., Harris, A. L., and Vaughan-Jones, R. D. (2009) The role of carbonic anhydrase 9 in regulating extracellular and intracellular ph in three-dimensional tumor cell growths. *J. Biol. Chem.* **284**, 20299–20310
31. Zhang, S., Hosaka, M., Yoshihara, T., Negishi, K., Iida, Y., Tobita, S., and Takeuchi, T. (2010) Phosphorescent light-emitting iridium complexes serve as a hypoxia-sensing probe for tumor imaging in living animals. *Cancer Res.* **70**, 4490–4498
32. Deer, E. L., González-Hernández, J., Coursen, J. D., Shea, J. E., Ngatia, J., Scaife, C. L., Firpo, M. A., and Mulvihill, S. J. (2010) Phenotype and genotype of pancreatic cancer cell lines. *Pancreas* **39**, 425–435
33. Morgan, R. T., Woods, L. K., Moore, G. E., Quinn, L. A., McGavran, L., and Gordon, S. G. (1980) Human cell line (COLO 357) of metastatic pancreatic adenocarcinoma. *Int. J. Cancer* **25**, 591–598
34. Moll, W., and Gros, G. (2008) Combined glycolytic production of lactate(−) and ATP(4−) derived protons (=dissociated lactic acid) is the only cause of metabolic acidosis of exercise: a note on the OH(−) absorbing function of lactate (1−) production. *J. Appl. Physiol. (1985)* **105**, 365
35. Hulikova, A., and Swietach, P. (2014) Rapid CO2 permeation across biological membranes: implications for CO2 venting from tissue. *FASEB J.* **28**, 2762–2774
36. Swietach, P., Wigfield, S., Cobden, P., Supuran, C. T., Harris, A. L., and Vaughan-Jones, R. D. (2008) Tumor-associated carbonic anhydrase 9 spatially coordinates intracellular pH in three-dimensional multicellular growths. *J. Biol. Chem.* **283**, 20473–20483
37. Lee, A. H., and Tannock, I. F. (1998) Heterogeneity of intracellular pH and of mechanisms that regulate intracellular pH in populations of cultured cells. *Cancer Res.* **58**, 1901–1908
38. Cardone, R. A., Greco, M. R., Zeeberg, K., Zaccagnino, A., Saccomano, M., Bellizzi, A., Bruns, P., Menga, M., Pilarsky, C., Schwab, A., Alves, F., Kalthoff, H., Casavola, V., and Reshkin, S. J. (2015) A novel NHE1-centered signaling cassette drives epidermal growth factor receptor-dependent pancreatic tumor metastasis and is a target for combination therapy. *Neoplasia* **17**, 155–166
39. DeBerardinis, R. J., and Chandel, N. S. (2016) Fundamentals of cancer metabolism. *Sci. Adv.* **2**, e1600200

Received for publication May 23, 2017.
Accepted for publication August 14, 2017.

Downloaded from www.fasebj.org to IP 129.67.119.187. *The FASEB Journal* Vol., No. , pp:, October, 2017

Supplemental Data

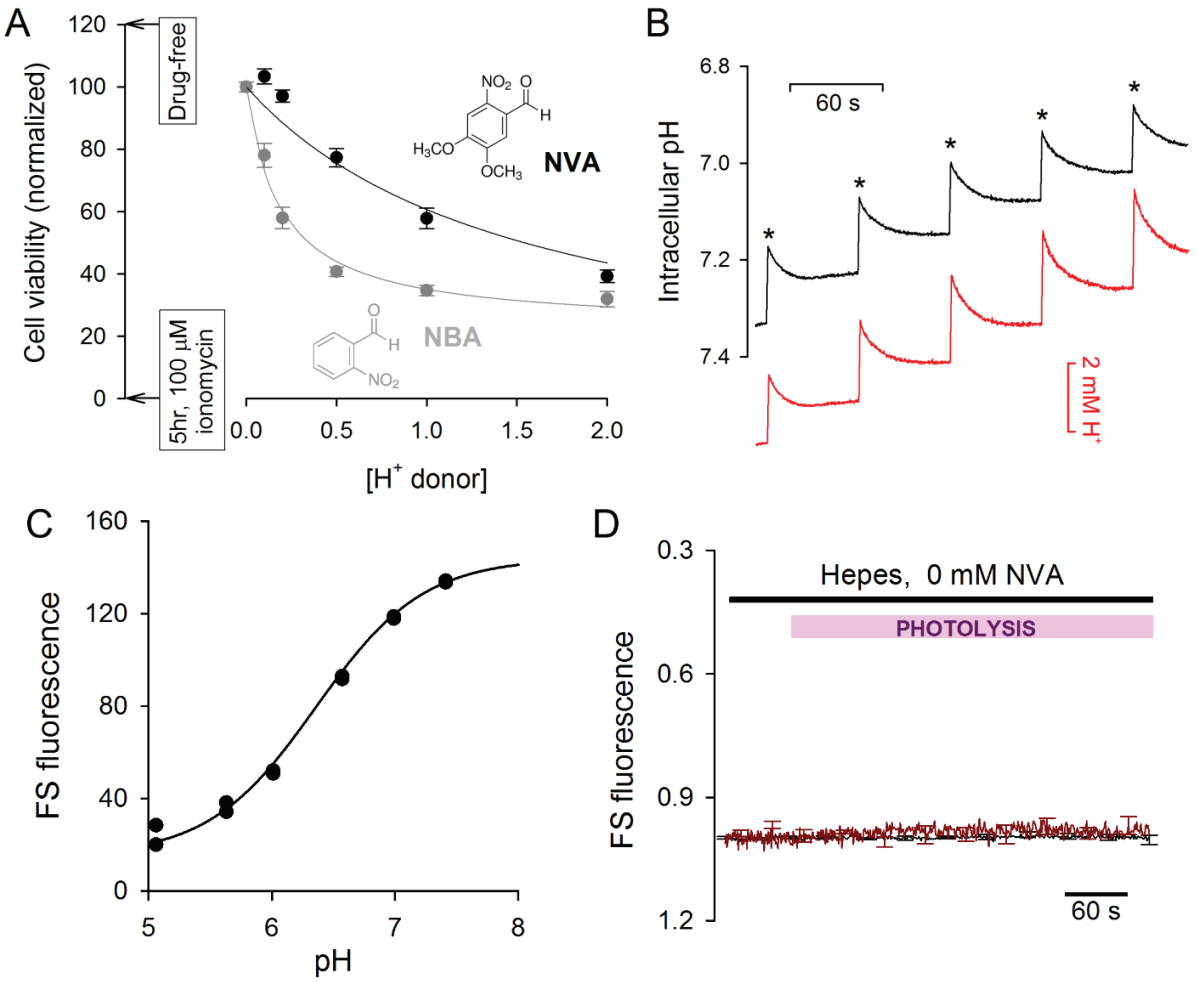


Figure S1: (A) Characterizing the caged H^+ compound. Cell viability, assessed by Cell Titre Blue assay, double-normalized to drug-free control and effect of 5 hr exposure to 100 µM ionomycin, a drug that triggers cell death. Colo357 cells were incubated for 5 hrs with various doses of 6-nitroveratraldehyde (NVA) or 2-nitrobenzaldehyde (NBA) dissolved in standard culture media. Insets show chemical structure of H^+-donor. NVA is less toxic than NBA. **(B)** Photolytic yield of uncaging from NVA. cSNARF-1oaded Colo357 monolayers were superfused with Hepes-buffered solution containing 0.5 mM NVA. Every 60 s, a train of four consecutive flashes of 405 nm light were applied, as indicated by asterisks (*) to drive the photolytic reaction. The pH_i response was converted, using buffering capacity, into concentration of acid injected *(red trace)*. The photolytic yield is ~100%. **(C)** Measurements with fluorescein sulfonic acid (FS). Calibration curve of 30 µM FS in 10 mM Hepes/10 mM Mes-buffered solution titrated to various levels of pH. Fluorescence was excited at 488 nm and collected >510 nm. Best-fit to the Grynkiewicz equation, with pK_a=6.3575, F_{max}=143.975 and F_{min}=15.1338. **(D)** Colo357 spheroid superfused with 20 mM Hepes solution at pH 7.4 containing 30 µM FS, but no caged H^+-compound. Fluorescence was measured in the core *(red)* and periphery *(black)* of the spheroid during the uncaging light protocol. In the absence of photolabile H^+-donor, FS signal remains constant, indicating that the dye was not photobleached as a result of 405 nm light used in other experiments for uncaging.

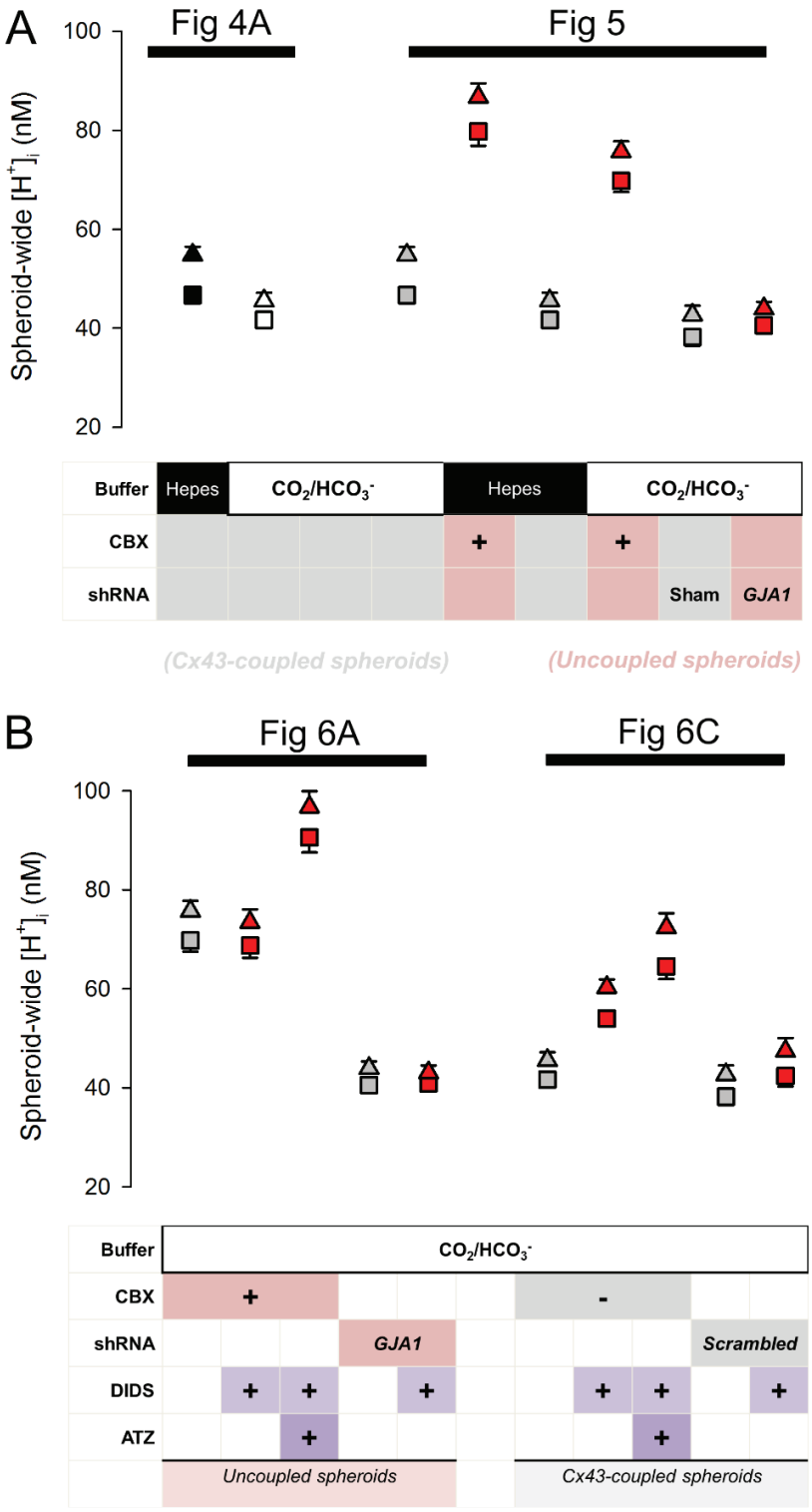


Figure S2: *Analysis of spheroid-averaged pH_i in photolysis experiments.* **(A)** Spheroid-average pH_i before uncaging *(squares)* and after 4 minutes of uncaging *(triangles)*. Data points relate to time courses shown in Fig 4A and Fig 5. **(B)** Data points relate to time courses shown in Fig 6A and Fig 6C.